Scale-up of Enface Electrochemical Reactor Systems

A Thesis Submitted by

Simon James Coleman

For the Degree of Doctor of Philosophy

School of Chemical Engineering and Advanced Materials

Newcastle University

August 2015

ABSTRACT

Photolithography, the standard pattern transfer technique, has many sustainable issues due to the application of a mask to the substrate. A 'maskless' pattern transfer method, called the Enface technique, has recently been proposed for metal plating and etching. This method introduces the idea of bringing a patterned tool and a substrate together in close proximity and a current or voltage is passed between them enabling metal to be selectively deposited or removed from the substrate. The process requires sufficient electrolyte agitation within a narrow inter-electrode gap and has previously been shown to hold in a vertical flow channel reactor. However, the process has to be adapted for tank-type systems for industrial implementation. Mass transfer during electrodeposition can be enhanced by ultrasonic waves. It has therefore been investigated whether this would be an appropriate agitation method for Enface.

In order to scale-up the process, 3 types of Enface reactors were investigated; a vertical flow cell, a 500 ml lab-scale tank-type cell and an 18 L ultrasound plating tank. The limiting current technique was used to study the mass transfer in these systems. Electrodeposition of copper pattern features in 0.1 M $CuSO_4$ was achieved in each of these geometries. The scalability was quantified by measuring the uniformity of deposit roughness and deposit thickness of the features across the substrate using profilometry.

The lab-scale tank-type cell with a 20 kHz ultrasound probe was used to investigate the effect of ultrasound agitation within narrow inter-electrode gaps. Mass transfer correlations showed that turbulent flow becomes fully developed when using ultrasound in this narrow geometry. Limiting current experiments showed that relatively low ultrasound powers of 9 – 18 W/cm^2 should be used and current distribution modelling showed that the ultrasound source should be placed no less than 30 mm from the substrate. Copper pattern features were deposited onto 10 mm diameter substrates and using long current pulses with bursts of ultrasound during the off-time was the most suitable plating mode. Specially designed electrode holders in the large-scale 18 L ultrasound tank was used to deposit copper patterns onto larger substrates. Features of μm-scale were deposited onto A7 size substrates, but there was an unacceptable variation in deposit thickness of ±80% due to the non-uniformity of the electrode gap across the plate. However, mm-scale features were successfully deposited onto A7 size substrates with an acceptable deposit thickness uniformity and deposit roughness uniformity of ±18% and ±40% respectively across the plate. Enface is therefore currently scalable for mm-scale features on substrates of this size.

ACKNOWLEDGEMENTS

I would like to sincerely thank the following people:

- My PhD supervisor, Prof. Sudipta Roy, for her exceptional guidance and constant support throughout the whole period of my PhD degree. She has provided excellent teaching, given me a lot of encouragement and offered many opportunities which have helped me greatly in the development of my research career
- My secondary PhD supervisor, Dr. Konstantin Vasilevsky, for the wet photolithography training and assistance in tool fabrication in the clean room
- Dr. Todd Green for dry photolithography training and useful discussions
- The School of Electrical and Electronic Engineering at Newcastle University for the use of their cleanroom and facilities
- The Advanced Chemical and Materials Analysis (ACMA) at Newcastle University, and Pauline for SEM measurements
- Dr. Jeet Varia for his assistance with the impedance measurements used for ohmic drop determination
- Iain Ditchburn for the building and fabrication of all the electrochemical cells and for useful advice and discussions on the cell designs
- Rob Dixon, Paul Sterling, Iain Strong, Stewart Latimer and all the technicians in the CEAM Mechanical Workshop for their assistance and advice
- The studentship support by EPSRC grant EP/J500288/1 and also support by EU "MESMOPROC" Grant 303550
- The Electrochemical Nanomaterials Group at Newcastle University, including Tri, Jeet, Naray, Mosaad, Swati, Susana, Priscila and Eden for their friendship and useful discussions in the lab
- All the students in my office C402 for a very friendly working environment
- My parents, Barrie and Anne, and my sisters, Emma and Eleanor, for their constant support and encouragement
- My girlfriend, Zsofia, for her brilliant support through the final stages of the degree which I am very grateful for

CONTENTS

LIST OF FIGURES

LIST OF TABLES

LIST OF SYMBOLS

a	Ion activity
A_a	Total exposed anode area
$a_{ads,e}$	Surface activity of the adsorbed ion
A_f	Total surface area of deposit features on the cathode surface
A_p	Area of probe
A_x	Cross-sectional area
c	Concentration of ionic species
c_0	Standard concentration
c_b	Bulk concentration of reacting species
c_i	Concentration of component i
c_k	Concentration of ionic species k
C_p	Heat capacity
c_s	Surface concentration of reacting species
D	Diffusion coefficient
d_c	Channel width
$d_{dep,\ 100\%,f}$	Nominal deposit thickness based on the area of cathode features and 100% current efficiency
$d_{dep,\ m}$	Deposit thickness measured from profilometry
$d_{dep,100\%}$	Deposit thickness based on the area of the anode features and 100% current efficiency
d_e	Equivalent diameter
d_H	Hydraulic diameter
D_k	Diffusion coefficient of ionic species k
d_p	Distance between the probe tip and the centre of the electrode
E	Applied potential
E^0	Standard electrode potential
$E^{0'}$	Formal potential
E_{cell}	Cell potential
E_e	Equilibrium potential
F	Faraday constant
g	Gravitational constant
Gr	Grashof number
h_0	Distance between the leading edge of the momentum and the

	concentration boundary layers
h_e	Distance between the anode an cathode
I	Current
i	Current density
i_f	Current density based on
i_{Lim}	Limiting current density
k	Constant
k_m	Mass transfer coefficient
L	Characteristic length
L_e	Entry length
M	Mass
M_w	Molecular Weight
n	Number of electrons transferred
$\vec{N}$	Flux
N_i	Flux of any species
$N_{i,\ convection}$	Convective flux
$N_{i,\ diffusion}$	Diffusion flux
$N_{i,\ migration}$	Migration flux
N_k	Flux of an ionic species k
n_p	Total number of data points from the profilometry used to calculate the roughness amplitude
p	Ultrasound power
p_{W/cm^2}	Ultrasound power in W/cm^2
$p_{W/L}$	Ultrasound power in W/L
$\nabla\phi$	Potential gradient
R	Gas Constant
r	Radius of the electrode
R_a	Roughness amplitude
r_c	Critical radius
Re	Reynolds number
R_k	Production rate of species k
r_n	Radius of the nucleus
Sc	Schmidt number
Sh	Sherwood number

T	Temperature
t	Time
U	Velocity of the flow of ultrasound far away from the electrode surface
u_k	Mobility of species *k*
w	Width of the electrode
x	Distance along the length of the electrode from the edge closest to the probe
y	Distance from electrode surface
y_i	Height of roughness irregularities
z_k	Charge of ionic species k
γ	Molar surface free energy (surface tension)
γ_i	Activity coefficient of component i
δ	Diffusion layer thickness
ΔG_{bulk}	Free energy change associated with formation of the bulk
ΔG_c	Critical free energy
$\Delta G_{surface}$	Free energy change associated with formation of the surface
ΔG_{total}	Total Gibbs free energy
ΔG_v	Free energy change per unit volume ($\bar{V}$)
δ_{min}	Minimum diffusion layer thickness
δ_N	Nernst diffusion layer thickness
ΔP	Pressure drop
ϵ	Dielectric constant of the solution
η	Overpotential
η_C	Concentration overpotential
η_S	Surface overpotential
η_{TOT}	Total overpotential
η_Ω	Ohmic overpotential
μ	Dynamic viscosity
ν	Kinematic viscosity
ρ	Density
σ	Conductivity
τ_i	Transition time
φ	Current efficiency
ω	Angular velocity

LIST OF ABBREVIATIONS

CUS	Continuous wave ultrasound
DC	Direct current
EcM	Electrochemical micromachining
EcP	Electrochemical printing
EHDA	Electrohydrodynamic atomization
EnFace	Electrochemical nano and micro Fabrication by Chemistry and Engineering
IC	Integrated circuits
LDI	Laser direct imaging
MEMS	Micro electrochemical or mechanical systems
PCB	Printed circuit boards
PTFE	Polytetrafluoroethylene
PUS	Pulsed Ultrasound
PVC	Polyvinyl chloride
US	Ultrasound
UV	Ultraviolet

Chapter 1. Introduction

1 Introduction

1.1 Background

Microfabrication is used in micro electrochemical or mechanical systems (MEMS), microfluidics, micro-optics, and other micro and nano technologies [1, 2]. It is widely used for the manufacture of electronic products such as Integrated Circuits (ICs) [2, 3] and Printed Circuit Boards (PCBs) [2, 4]. All these systems are gaining importance as the global market for this sector is increasing due to the high demand for electrical and electronic products.

Most microfabricated systems require a method of the fabrication of a pattern on a substrate. Currently the most popular method for pattern transfer is lithography [2], which is a fabrication process where a micro-meter size drawing of the device is delineated onto a substrate [5]. Types of lithography include electron-beam lithography, ion-beam lithography, and photolithography. The most commonly used method of these is photolithography [2], a very well-established method of pattern transfer. The first time it was applied to the manufacture of PCBs was in 1943, but it wasn't until 1961 when photolithography was used to produce the first commercial IC onto silicon [2]. The patterns made for ICs are currently almost all made by this method [2, 3].

There are a number of drawbacks for the use of the photolithography method which gave rise to the development of alternative methods for pattern transfer. This includes such techniques as laser direct imaging, inkjet techniques and electrohydrodynamic atomization [6]. There are also electrochemical pattern transfer techniques, such as electrochemical printing and micro-machining [6]. Another electrochemical process is the EnFace technique; an electrochemical method for sustainable pattern transfer. It was invented at Newcastle University by Prof. Roy and is currently under development. In this project, improvements to the EnFace method have been studied, focusing on the scale-up of the process for industrial application.

1.2 Photolithography technique

1.2.1 Description of the process of photolithography

Photolithography is the most common lithography method. The photolithography process can be explained with reference to the diagram displayed in Fig. 1.1. This figure illustrates the separate steps involved in photolithography. For manufacturing electronic devices, this process would take place on a substrate of a silicon wafer. Currently the resolution of this method using ultraviolet-light (UV) is 0.5 μm [5].

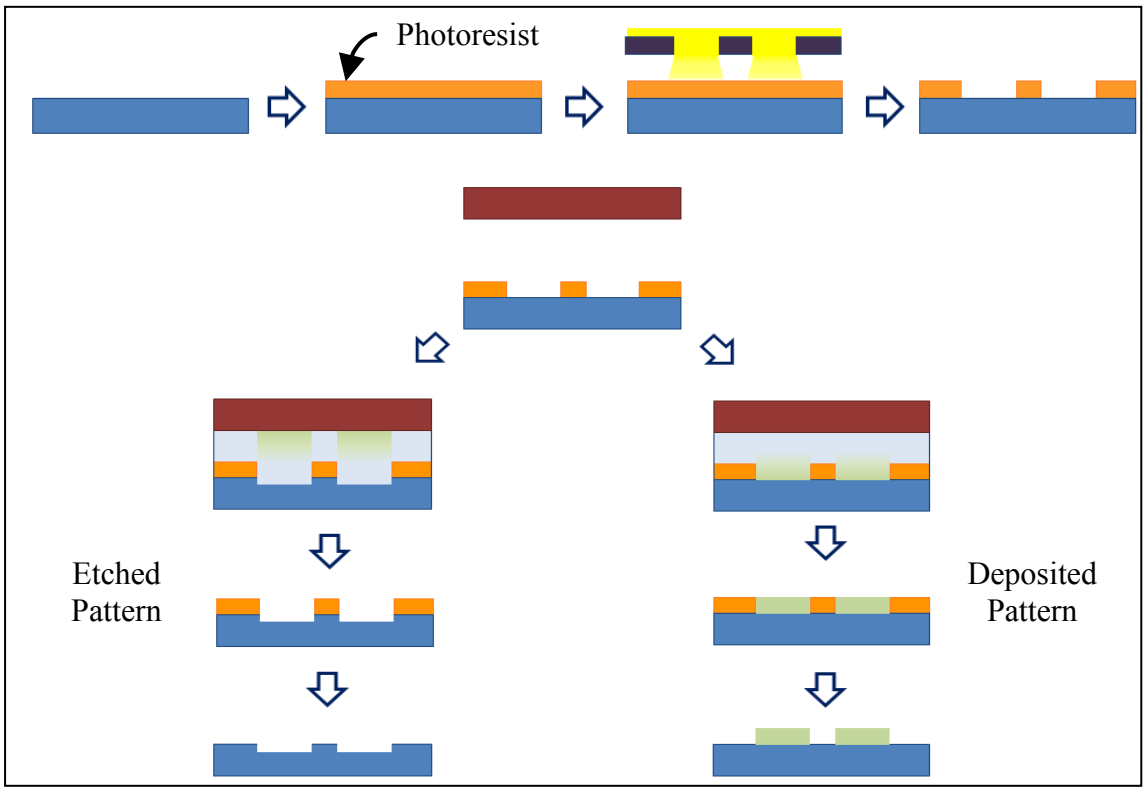

Figure 1.1 – Photolithography and pattern transfer process. Adapted from [7].

The description of each stage of the process is explained as follows:

1. A 1-4 μm thick layer of photoresist (a polymer that is sensitive to UV light) is applied to the substrate

2. The photoresist is then baked at 90^{o}C to harden the resist

3. A patterned stencil with micro-patterns, known as an optical mask, is placed over the top of the substrate. A typical mask would be a glass plate with sections of opaque patterns, selected depending on the type of pattern that is to be developed onto the substrate [8]

4. The material is then exposed to ultraviolet light.

5. The substrate is either rinsed or sprayed with developer solution (e.g. $(CH_3)_4N\ OH$). For a positive photoresist (as in this example), the sections of the photoresist exposed to UV light are removed from the substrate, leaving an image of photoresist in the pattern of the optical mask.

6. Two different stages can now occur depending on what is required
   - Substrate can either be etched with HF, removing exposed substrate
   - Or metal deposition can be carried out on the exposed substrate areas

7. Photoresist is removed by strong acids (H_2SO_4 or $H_2SO_4 - Cr_2O_3$)

1.2.2 Disadvantages of Photolithography

Despite this method being a well-established pattern transfer technique, there are several disadvantages that are concerned with its use. One of the main issues is a large number of steps are required with the preparation of the substrate and removal of photoresist [9]. Additionally, a different photoresist mask is required for each substrate which also creates a low efficiency for the manufacture of the components [6]. The current challenges are mainly due to throughput [10], illustrating that it is a relatively slow process to carry out.

The process has to be carried out in a very clean and controlled atmosphere which leads to a high operation cost. For patterns of a magnitude of 1 μm to 100 μm, any small particle in the air that landed on the substrate can create imperfections in the pattern [8]. A clean room is therefore a mandatory requirement for photolithography. The process also requires demanding safety protocols because of the use of hazardous concentrated acids; these include sulphuric acid, ammonium fluoride and hydrofluoric acid. Additionally, the removal of photoresist from the substrate is a waste product that needs to be disposed of properly as it can be harmful to the environment [11].

Despite all these issues, photolithography is still extensively used worldwide. This is not just because this method is well understood, but also because it is possible to create patterns of 0.5 μm resolution [6]. The fabrication of patterns of resolution within the nanometre range and is also under development [2]. Since the main issues with photolithography pattern transfer are mostly related to the application and removal of the photoresist mask onto the substrate surface, processes that do not require mask

fabrication would therefore eliminate these disadvantages. This has therefore given rise to the development of mask-less processes of pattern transfer.

1.3 Maskless processes

A pattern transfer method which does not require the application of a mask to the substrate is known as a mask-less process. These processes are capable of fabricating nanoscale devices. There are a number of different mask-less process which will now be described.

1.3.1 Laser Direct Imaging

The most commonly used mask-less technique is laser direct imaging (LDI), used to fabricate micro-pattern features onto PCBs, glass and epoxy [6]. A digital image of the desired pattern is defined onto the substrate using a laser device which focuses the image directly onto the surface of the substrate [6]. Deposition or etching of the pattern can be achieved either by a physical or chemical reaction. Chemical methods can be used to deposit metals, inorganic materials and also some organic entities [6].

The resolution of the LCI technique is 5-100 μm, which depends of the laser wavelength and the system optics [6]. The other issues which restrict the resolution there is a higher intensity in the centre of the laser beam compared to the edges. The disadvantages related to the use of this technique involve over-heating of the laser, driving photo-chemical reactions and the safety procedures required [6].

1.3.2 Inkjet techniques

Inkjet techniques are operated at a much lower temperature than LDI processes [6]. For this method an inkjet device is brought close to the substrate and multiple droplets of material are emitted from the head of the inkjet onto a particular area. The location of the substrate and inkjet head is operated by a computer control system. The process is used to fabricate etch resists, organic transistors and bioanalysis arrays.

There are two types of inkjet techniques; the ‘continuous charge and deflect method’ which produces droplet of sizes 50-500 μm, and the ‘dot on demand method’ which produces smaller droplets of sizes 20-100 μm. Inkjet patterning technology is inexpensive, operates at a low temperature and is considered to be environmentally friendly [12]. However, requires a lot of process optimization due to the physics and chemistry of the ink and nozzle and is therefore a complicated process to carry out [6].

1.3.3 Electrohydrodynamic atomization

Electrohydrodynamic atomization (EHDA) is a variation of the inkjet technique; however the operation of this method is different to inkjet printing. The material emitted from the nozzle is in the form of a jet, which is then broken up into droplets by an electrical field. The droplets are smaller than those which can be produced using the traditional inkjet technology [6]. However, it is difficult to maintain a stable jet as viscosity, electrical conductivity, flow rate and electric field have to be controlled [6]. The smallest features that have been fabricated with this technique are only 110 μm [13]. Additionally, as EHDA is a relatively new method it is currently only being used at the laboratory scale.

1.3.4 Electrochemical microfabrication techniques

Electrochemical methods of microfabrication use a localised electrochemical reaction to deposit or etch material on a substrate. Electrochemical printing (EcP) is one such technique used for electrodeposition of pattern features, which uses another variation of inkjet technology. An electrolyte solution is fed through the jet onto a local area on the substrate and a current is passed within that area where the metal is electroplated [6]. The EcP process has a low processing time [14], is easy to scale-up and can be used for a variety of substrate and deposit materials [6]. However, the highest resolution that has currently been achieved is only 300 μm [15] and the nozzle fabrication costs are high [6].

Electrochemical micromachining (EcM) is another electrochemical method, but is used for localised electrochemical etching of micropatterns on metals and semiconductors. The method is carried out by placing a tool in close proximity to the substrate and passing a high current between the cathode tool and the anode substrate [6].

EcM can be used in the metre, millimetre and micrometre scales [16, 17]. Photomasks or insulating masks are placed on the substrate and/or tool when carrying out EcM at the micrometre scale [16]. 10-30 μm features have been fabricated on a copper substrate using this method [18]. Nano-second voltage pulses can be used to achieve an even higher resolution. For example, 5 μm size structures have been fabricated on nickel substrates using this method [19]. However, this requires the gap between the anode and cathode to be ≤ 1 μm which is expensive and difficult to

achieve. This causes difficulties in scale-up for implementation of EcM in industry, as well as issues with control of generating accurate voltages within the nano-second range.

Another electrochemical microfabrication method is the Enface technique, described in the following section. This technique is currently being investigated for its feasibility on the industrial scale.

1.4 Enface Technique

The EnFace technique is an electrochemical microfabrication method devised by researchers at Newcastle University [6] which involves an electrochemical pattern transfer without the application of a mask onto the substrate. This method consists of an electrochemical reactor in which an anode acts as a tool and the cathode is the substrate. The technique has been named EnFace, which stands for **E**lectrochemical **n**ano and micro **Fa**brication by **C**hemistry and **E**ngineering, described in the next section.

1.4.1 Description of EnFace Method

The main difference in this system of transfer compared to photolithography is the fact that EnFace proposes the use of a maskless substrate. Instead of applying the pattern onto the substrate itself, the pattern to be transferred is put onto a tool which is brought into close proximity with the substrate. Metal can be plated or etched metal at the microscale using this patterned tool, when a voltage or current is passed between them. This tool can be used repeatedly therefore reducing the amount of removal of the photoresist, creating a procedure with less process steps [7].

The flow diagram for the EnFace technique is illustrated in Fig. 1.2. The electrode gap required for this process is less than 500 μm. The gap between the two electrodes is filled with an electrolyte containing the metal ions to be plated or etched. The fresh electrolyte is supplied to the electrodes by circulating the electrolyte through the channel gap, allowing by-product removal as well delivering fresh solution to the electrodes [6].

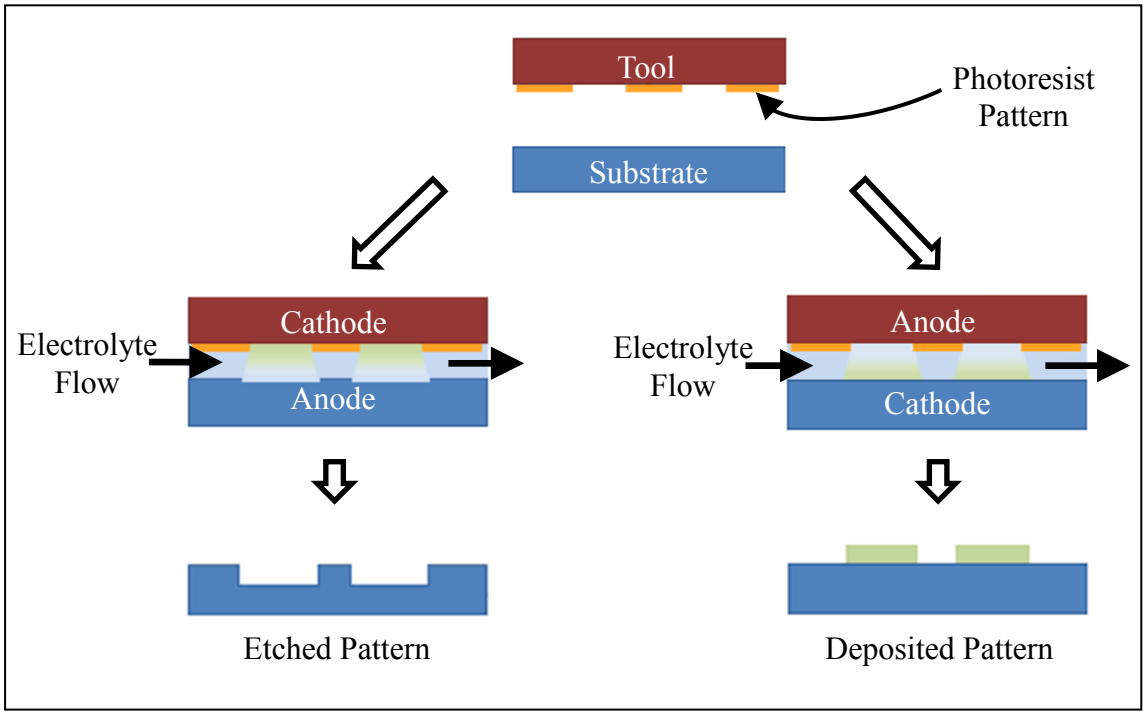

Figure 1.2 - EnFace patterning process, adapted from [7].

The advantages of the EnFace method are as follows.

- The tool can be used repeatedly; previously it has been shown that 20 – 25 pattern transfers can be made with one tool creating a much faster process [7, 11]
- EnFace is a safer and more environmentally friendly method to carry out than photolithography [7] due to the decrease in amount of hazardous chemicals required, such as mask removing solvents, and less waste disposal
- There is also a reduction in energy costs due to less usage of the clean room

1.4.2 Previous Work on EnFace

The initial investigations of the EnFace technique were carried out by Schönenberger and Roy [11] in an electrochemical flow cell with copper disc electrodes placed at an inter-electrode distance of 300-500 µm. Patterns of microscale patterns of size 5 to 100 µm were etched on the copper substrate.

This study found that conditions that ensured good pattern transfer were low conductivity electrolytes and an optimum value of inter-electrode distance. The

importance of the inter-electrode gap was illustrated by good pattern transfer occurring in the centre of the electrodes, but not as clear at the edges. This is due to the electrode being thicker at the centre due to polishing conditions. Direct current experiments carried out in 0.1 M $CuSO_4$ + 0.1 M Na_2SO_4 produced etchings with a roughness of 100 – 150 nm. Additional pulse plating experiments were carried out that produced etchings with a lower average roughness of 50 nm. The reproducibility of the tool also proved to be successful.

One of the problems highlighted during this study was related to trapped bubbles within the inter-electrode gap, which did not allow the pattern to be replicated. Schönenberger claimed that these trapped bubbles have evolved from the reaction, however, the large size of the bubbles suggest that they have actually been formed from trapped air from elsewhere in the flow system. In any case, these bubbles hindered the electrodeposition reaction, therefore a control of hydrodynamics is also needed for good pattern transfer.

Nouraei and Roy [9] developed a model to simulate the anodic dissolution of copper during pattern transfer etching. Comparisons to the experimental results of Schönenberger and Roy [11] were similar in terms of physical characteristics of the pattern transferred. The model simulation showed there was a difference in topography for different electrolytes; a rectangular shape was etched for non-acidic electrolyte, and a sinusoidal shape was etched for acidic electrolyte. The simulations showed that the electrode gap was a crucial parameter, with optimum ratio of feature size to inter-electrode gap of 1:3, suggested that the optimum electrode gap distance is 300 μm.

Pattern transfer by electrodeposition of copper was found to be feasible in a study by Wu, Green and Roy [20]. The importance of forced convection was realised via limiting current experiments carried out at varying electrode gaps. This revealed that the narrowest gap of 300μm gave the highest limiting current of 78 mA/cm^2 at a flow velocity of 6 cm/s.

Copper line patterns were transferred onto a nickel cathode of 0.9-1.2cm diameter using an electrolyte of 0.1 M $CuSO_4$ and a patterned anode with exposed line patterns, 100 μm in width. An increase in the lateral dimension of at least 20% occurred when transferring these features due to current spreading. Similar issues to Schönenberger's study, with pattern transfer differing in quality at different radial positions [11], was also evident in this work with wider line widths at the electrode

edges for the same reasons as above. Pulse plating experiments were also carried out for comparison to the direct current plating experiments. The roughness of the patterns of deposited copper was noticeably reduced by pulse plating, but current spreading was still an issue.

There after an investigation using a more a conventional tank-type geometry was carried out. These studies were carried out to determine (a) the generality of Enface for different metals, and (b) effectiveness of the process in non-agitated tank-type systems. Widayatno [21] studied deposition of nickel patterns onto 10 mm diameter electrodes facing each other within a beaker-type cell under stagnant conditions.

The findings of the experiments by Widayatno [21] are as follows:

- 0.19 M nickel sulfamate was found to be the most suitable electrolyte for the deposition of nickel patterns using the Enface technique
- There was a different current density for each pattern size
- 1 mm x 5 mm patterns and 300 μm size patterns were deposited using a manual fabricated tools (using a Kapton tape mask)
- 1 mm x 5 mm patterns had a deposit thickness of 0.54 μm and were 50-100% wider than anode tool pattern due to current divergence
- 300 μm features with a deposit thickness of 0.37 μm were 105 – 250% larger than the tool pattern
- When using tools fabricated by photolithography, only larger features of ≥ 500 μm were deposited and were only greater than the tool feature by 16-35%
- The current efficiency of the deposition of nickel patterns was 90%

The main issue that were observed during these deposition experiments was related to hydrogen bubble evolution, since this is an accompanying reaction during the nickel deposition reaction. It was observed that bubbles of gas were entrapped between the electrodes, thereby hindering deposition. It was also observed that the hydrogen evolution caused an increase in pH within the electrode gap which degraded the photoresist during a deposition time of 300 s. This illustrated the issues related to restriction of mass transfer within the inter-electrode gap. An agitation method was therefore established which directs agitation towards the narrow gap.

1.4.3 Current Mass Transfer Issues in the Development of EnFace

Improving mass transfer in a tank-type tank system is vital if the Enface process is to be confirmed as a feasible technique for use in industry. An enhancement in mass transfer with the narrow electrode spacing in a tank-type geometry could enable process scale-up. If standard agitation techniques for tank systems are used, for example pumped flow and eductors, not enough agitation will be achieved in the volume of fluid within the inter-electrode gap. This is because the majority of the fluid flowing from the eductors would by-pass the narrow gap.

The problem could be solved by using an agitation regime that can be directed precisely within the electrode gap increasing the mass transfer. One such type of agitation is ultrasound (US) agitation, a form of agitation which is well known for its mass transfer enhancement capabilities [22, 23]. Providing agitation via ultrasound could be economically advantageous for the EnFace process as the energy required for ultrasound agitation is a lot less than the energy required to power a clean room used in photolithography. A clean room would require 88 kWh to produce 100 patterned substrates [24], whereas ultrasound agitation would only require only 8 kWh to produce the same number of substrates.

In order to investigate if US agitation is a useful agitation technique for the scale-up of the Enface process a system with a 500 ml lab-scale tank-type cell and a US probe was investigated, which consisted of 10 mm diameter electrodes. Following these investigations a larger scale 18 L US plating tank with A7 size electrode plates was used. The mass transfer in these systems was studied using the limiting current technique and Sherwood correlations were developed. Electrodeposition of copper pattern features from 0.1 M $CuSO_4$ was carried out in each of these geometries, characterized by deposit thickness and roughness using profilometry to test the scalability of the process.

1.5 Aims and Objectives of Current Work

The initial aim of the project was to investigate the effect ultrasound agitation has on the mass transfer of Cu^{2+} ions within a narrow electrode gap during electrodeposition of copper in the lab-scale cell. Following from these results, the main objective is to test whether it is possible to scale-up the process to pattern onto larger substrates. The project objectives were as follows.

1. Perform mass transfer experiments with ultrasound agitation within a narrow electrode gap in a lab-scale Enface system

2. Compare the mass transfer of the lab-scale ultrasound Enface system with the previous flow cell system to observe whether ultrasound can provide similar mass transfer enhancement

3. Study the effect of ultrasound parameters (ultrasound power and ultrasound source distance) on the mass transfer within the narrow electrode gap and find the optimum operating conditions for using ultrasound in the Enface system

4. Perform pattern deposition experiments in the lab-scale cell to obtain the most suitable plating mode for applying the current and ultrasound for Enface

5. Design an 18 L ultrasound tank and electrode holders for patterning onto larger substrates by utilizing the results from the small-scale Enface experiments

6. Carry out experiments on A7 size substrates in the 18 L US tank reactor to verify the scalability of the Enface process by achieving the following:
   (i) Develop mass transfer correlations for both ultrasound systems to assess whether the mass transfer enhancement that is achieved with ultrasound on a small-scale can also be attained on a larger scale
   (ii) Perform pattern deposition of mm-scale features on A7 substrates to prove that patterns of this magnitude could be deposited on substrates of this scale
   (iii) Perform pattern deposition of smaller μm-scale linear features onto A7 substrates to test the resolution of the process on this larger scale
   (iv) Measure the quality of the deposit patterns. The process will be scalable if the deposit thickness uniformity and deposit roughness uniformity is within ±20% and ±40% across the plate respectively. This is what is acceptable for industrial application

In this chapter, the standard patterning methods and maskless processes have been discussed, along with the benefits and challenges of the Enface technique. Before investigating the effects of ultrasound agitation on the mass transfer in the Enface system, it is important to first understand the common agitation methods and techniques used in electrochemical systems. A literature survey for different agitation schemes were therefore undertaken, which are presented in chapter 2.

Chapter 2. Literature Review: Agitation in Electrodeposition

2 Literature Review: Agitation in Electrodeposition

2.1 Agitation Techniques in Electrodeposition

2.1.1 Natural Convection

When current flows through an electrochemical system, stirring occurs in the region of fluid adjacent to the electrode surface due to natural convection flows, brought about due to the hydrodynamic movement of the fluid. For example, during current flow between two flat plates, the movement of ions towards the electrode is brought about by concentration gradients existing between the surface and bulk solution. This creates convection flows known as natural convection.

The Sherwood correlation for laminar free convection at vertical plate electrodes is shown in equation (1.1) [25-27], for the conditions described in equation (1.3). Sh is the Sherwood number, Sc is the Schmidt number, Gr is the Grashof number represented by equation (1.2) where g is the gravitational constant, ρ is the density, L is the characteristic length and ν is the kinematic viscosity. Equation (1.1) was derived experimentally using the limiting current technique. This experimental technique involves gradually increasing the potential and observing the current. A current plateau is formed indicating the region where the rate of mass transfer of ions to the electrode surface has reached its limit. This current density where the plateau is formed is called the limiting current density (i_{Lim}). This can be used to calculate the diffusion layer thickness for development of mass transfer correlations.

$$Sh = 0.67(Gr\,Sc)^{\frac{1}{4}} \tag{1.1}$$

$$Gr = \frac{g\Delta\rho L^3}{\rho\nu^2} \tag{1.2}$$

$$5 \times 10^6 < Gr\,Sc < 5 \times 10^{12} \tag{1.3}$$

However, natural convection only produces limited agitation which may be insufficient when high rates of mass transfer are needed. Microfabrication requires electrodeposition of metals including copper, nickel, gold, silver and tin; many of which are limited by mass transfer of metal ions, which is a function of the flow of the electrolyte solution. This is why the reduction and elimination of mass transfer limitations is important and is the reason for additional external agitation in electrochemical systems.

2.1.2 Forced Convection Stirring

Applying agitation to electrochemical systems is a common feature of most electrochemical reactions, with the desired function of increasing the mass transfer rate of the metal ion towards the electrode surface. This is achieved by reducing the thickness of the diffusion layer situated close to the electrode surface. A thinner diffusion layer means a thinner layer for the ionic species to transport through, therefore increasing the rate at which ions are moving from the bulk towards the surface. A comparison of diffusion layer thickness in 'Still' and 'Stirred' systems are illustrated in Figure 2.1. Stirring can be applied in a variety of ways, including magnetic stirrers, pump flow and eductors.

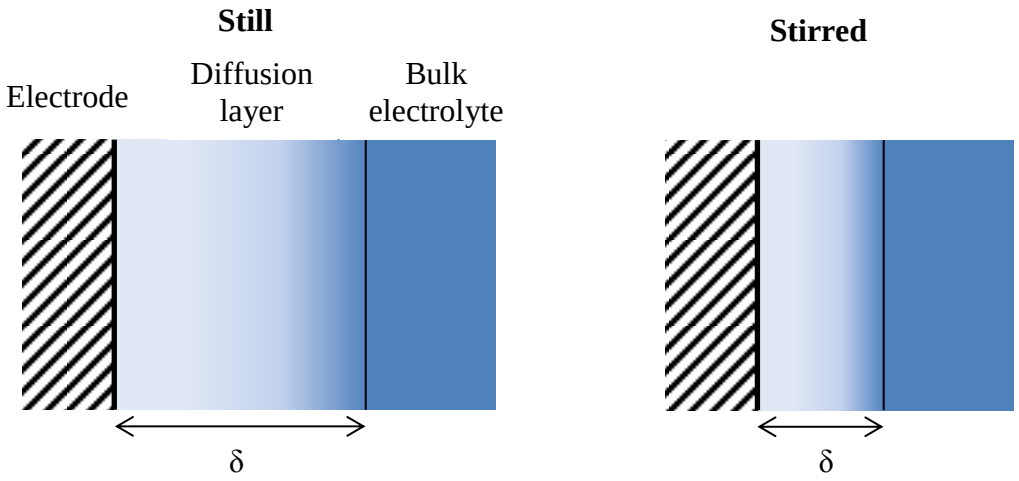

Figure 2.1 - Change in diffusion layer in stirred systems. Adapted from [28].

2.1.3 Electrode Stirring

In electrochemical systems, the electrolyte can also be agitated by mechanical movement of the electrode itself with the use of a motor. Both rotating disc and rotating cylinder electrodes are commonly used in electrochemical studies. Rotating disk fluid flow is a well understood technique associated with electrochemical studies involving centrifugal forces which push the fluid near the electrode surface out radially [29]. The arrows in Figure 2.2 illustrate the movement of the fluid during disk rotation.

Fluid from the bulk, perpendicular to the disk is brought towards the surface, thereby replacing the radially flowing fluid. This regime means that a uniform axial velocity towards the disc is created, therefore achieving uniform mass transfer rates across the disc [30]. Rotating electrodes have the ability to produce laminar flows close to the electrode surface, and can be controlled easily by altering the rotation speed. The Sherwood correlation for a rotating disk electrode can be represented by equation (1.4), derived theoretically [31, 32].

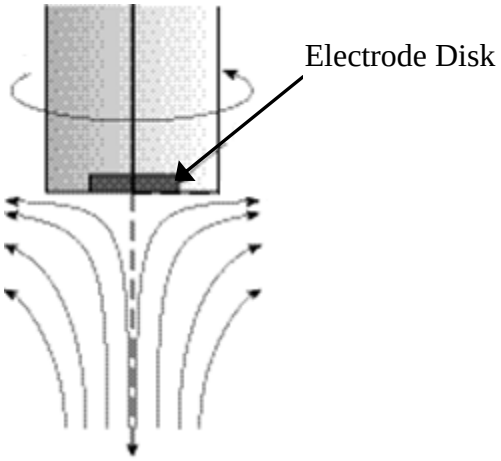

Figure 2.2 – Fluid flow adjacent to a rotating disk electrode. Adapted from [33].

$$Sh = 0.621\, Re^{\frac{1}{2}}\, Sc^{\frac{1}{3}} \qquad (1.4)$$

$$Sh = \frac{rk}{D} \qquad (1.5)$$

$$Re = \frac{\omega r^2}{\upsilon} \qquad (1.6)$$

$$Re < 2.7 \times 10^5 \qquad (1.7)$$

Although rotating electrodes agitate the solution close to the surface, they can be difficult to incorporate into systems which require the electrodes to be stationary. It is therefore common to stir the electrolyte solution externally.

2.1.4 External stirring

External agitation in electrochemical systems exists in many varieties, for example; mechanical stirrers, air sparging, eductors and pumped flow. An example of mechanical stirring could be an impeller immersed within the solution, creating turbulence within the cell resulting in an increase in mass transfer rates. The typical flow regime of a mechanical propeller stirrer in solution is shown in Figure 2.3.

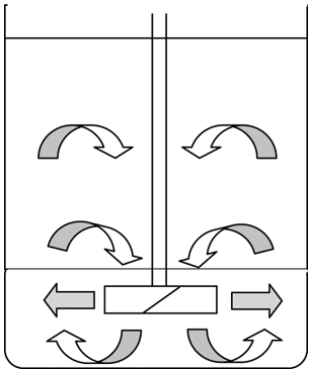

Figure 2.3 - Flow Diagram of Propeller Stirrer.

However, it has been reported that at low revolutions not enough turbulence is produced [34]. This suggests that an optimum revolution speed needs to be found to successfully improve the reaction rate. In this same paper, it was found that cathode height, with respect to the impeller, has an effect on the limiting current density. The limiting current for copper deposition in a mechanically stirred tank varied from 2 – 10 mA/cm^2 depending on the location of the electrode [34], illustrating the importance of the orientation of the impeller.

A common form of agitation in plating systems is a series of eductors placed within the plating tank. Eductors are essentially venturi tubes which pressurized fluid (> 10 psi) is pumped through, and fluid emerges as a high velocity jet, enabling a flow of solution within the tank. An example of the flow regime from an educator placed within a tank is shown in figure 2.4.

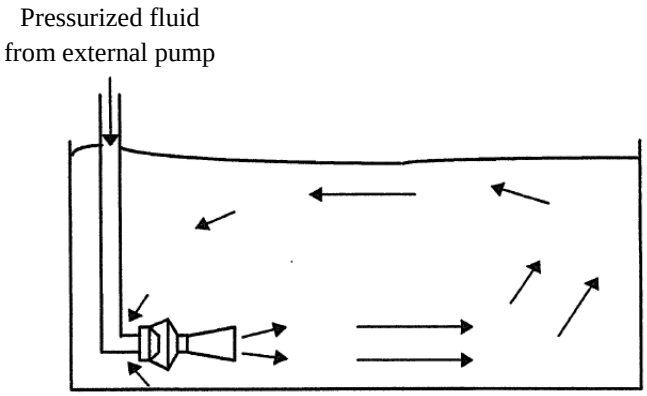

Figure 2.4 – Schematic of electrolyte flow around a process tank using eductor agitation. Adapted from [35]

The advantage of using eductors is that good flow rates can be achieved, they are devoid of oxygen and can be placed anywhere in the tank. Also, the direction of flow can be altered for different applications. However, they have relatively high power consumption and have also been shown to cause non-uniformity in the conductivity of the electrolyte solution within the tank [36].

An example schematic for an electrochemical pump flow system is shown in figure 2.5. The force from the pump pushes the electrolyte solution through the electrochemical cell and provides further movement of the ions within the hydrodynamic boundary layer creating forced convection flows. The flow of electrolyte solution means that reactants can move faster towards the surface, and also has the potential of transporting any bi-products away from the surface.

A Sherwood correlation can be used to express the flow in forced convection regimes. Equation (1.8) illustrates the Sherwood number for flow between two parallel plates [37], derived theoretically. Similar correlations were also developed for flow in an annular channel by Bazan and Arvia [38].

$$Sh = 0.85\left(Re\,Sc\,\frac{d_e}{L}\right)^{\frac{1}{3}} \quad (1.8)$$

$$for \quad Gr < 920 \quad (1.9)$$

$$75 < Re < 3000 \quad (1.10)$$

$$600 < Sc < 12\,000 \quad (1.11)$$

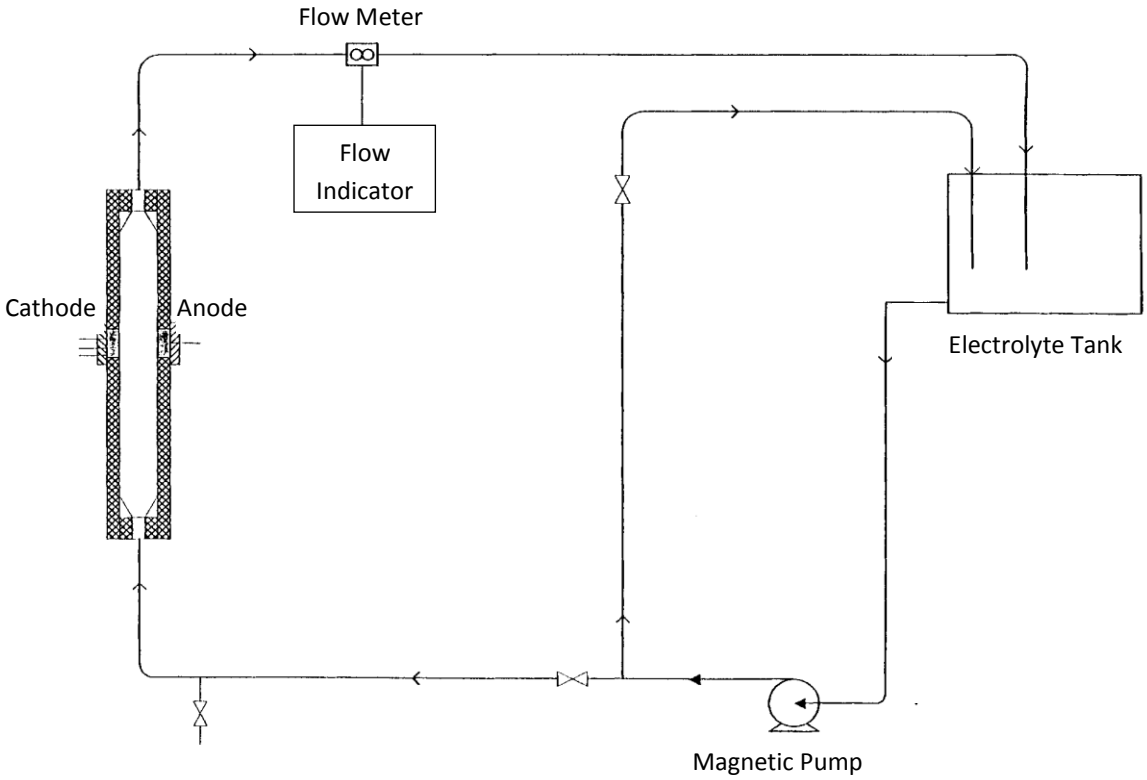

Figure 2.5 - Schematic of flow system for an electrochemical flow cell. Adapted from [39].

2.2 Limitations of these stirring techniques

Although all these stirring techniques are fairly common in electrochemical processes, there are a number of limitations that they possess. For example, the disadvantage of using mechanical agitation is that the anode and cathode placement is restricted due to the propeller placement within the electrochemical cell. Additionally, a significant flaw is that mechanical agitation cannot induce agitation close to the electrode surface.

Flow cells are useful for some applications due to the control of the flow velocity near the electrode surface. However, there is the risk of inducing high pressure within the system and there will also be a pressure drop (ΔP) along the length of the reactor (L) with the relationship $\Delta P \propto L^3$. Additionally, there is the possibility of additional costs due to pump energy requirements and additional filtration systems.

2.3 Methods of stirring in enclosed spaces

The Sherwood correlation in equation 1.8, describing the flow between two plates in an electrochemical flow cell, has been used extensively [40, 41], but is only valid for electrodes which are far apart from each other. Only a few investigations have been carried out which develop mass transfer correlations for forced convection within a narrow electrode gap between two parallel electrodes [39, 42]. The majority of work in thin gap cells includes studies on electrochemical growth [43], surface adsorption [44] and analysis [45, 46] within horizontal flow channels.

Studies which have carried out steady state electrochemical deposition in thin gap cells without external agitation have shown that instabilities in mass transport can occur [47, 48]. A system with parallel plate electrodes positioned 8 mm apart was used to electrodeposit copper from 0.1 M $CuSO_4$ showed signs of concentration instabilities as the mass transport limit was approached [47]. An electrochemical cell with an even narrower inter-electrode gap of 1 mm was used to deposit silver onto silver electrodes from 0.01 M $AgClO_4$ where the constriction of boundary layers close to the electrode surface resulted in oscillations in the transfer of ions [48].

Studies with flow cells with narrow gaps of 3 mm [49, 50] and 0.3 mm [20] allowed electrolyte solution to flow through the narrow channel between the electrodes. It was stated that turbulent forced convection occurred close to the electrode surface for the cell with the 3 mm inter-electrode gap [49, 50]. No mass transfer correlations were developed for either of these narrow gap systems. Sherwood correlations have only been developed for gaps that are 100 mm [39] and 25 mm [42] gaps.

A flow cell with an electrode gap of 100 mm was used to deposit copper onto a 10 mm diameter recessed copper electrode, with electrolyte flow velocities ranging from 0.75 to 4 cm /s. The correlation for this system is shown in equation 1.12, the value of the exponent of the *Re* illustrates that developing turbulence was present when using higher flow rates [39]. In the same study, a correlation was developed for laminar forced convection at a rectangular flat plate shown in equation 1.13.

$$Sh = 0.153 \left(Sc \, \frac{d_e}{L} \right)^{1/3} Re^{0.72} \tag{1.12}$$

$$Sh = 1.71 \left(Re \, Sc \, \frac{L}{d_e} \right)^{0.359} \tag{1.13}$$

A mass transfer study was also carried out using a flow cell with a smaller electrode gap of 25 mm, a copper electrode of length 75 mm and an electrolyte flow velocity of 0.7 cm/s. The δ at the lower section of the plate was calculated during copper deposition from experimental data. It was found that the δ matched well with the correlation for laminar forced convection shown in equation 1.14 [42].

$$Sh = 1.23\left(Re\ Sc\ \frac{L}{d_e}\right)^{1/3} \tag{1.14}$$

The stirring required in this EnFace process requires agitation within a much narrower gap than the studies above, using an inter-electrode gap of 0.3 mm. Since ultrasound agitation is a forceful form of agitation which can be directed towards such narrow spaces, it is suggested that applying ultrasound is an appropriate form of agitation to achieve this [51].

2.4 General Principles of Ultrasound

Ultrasound itself can be defined as "a sound transmitted through a medium via a pressure wave, therefore causing excitation in the medium in the form of enhanced molecular motion" [28]. The measurement of sound is described by the dimensions of the wave formed; the amplitude (height of the wave) and the frequency (waves per second) measured in Hz.

The frequency of human hearing is within the range of 10 Hz to 20 kHz and the range of ultrasound is above that of human hearing. The range of ultrasound associated with sonochemistry is known as power ultrasound, and is normally within the range of 20-100 kHz [28].

The intensity of ultrasound can be defined as the power dissipation into the system per unit area of irradiation [52]. The ultrasound power is measured in Watts, and can be represented by equation (1.15) [53, 54]. The intensity of the ultrasound is measured as the power per unit area and has units of W/cm^2. The ultrasound intensity can be represented by equation (1.16) [53, 54].

$$p = \left(\frac{dT}{dt}\right) C_p M \tag{1.15}$$

$$p_{W/cm^2} = \frac{p}{A_p} \quad (1.16)$$

Where p is the ultrasound power in Watts, T is the temperature (K), t is the time (seconds), C_p is the heat capacity of solvent (J kg^{-1} K^{-1}), M is the mass of solvent used (kg), p_{W/cm^2} is the ultrasound power in W/cm^2, and A_p is the area of probe tip (cm^2).

For an ultrasonic transducer, a vibrating solid is the source which has a certain characteristic known as the piezoelectric effect, discovered towards the end of the 1800s [55]. The piezoelectric effect is the interaction between mechanical force and electrical charge. When a potential is applied to a piezoelectric material, there is a conversion of electrical energy to mechanical energy. Figure 2.6 illustrates the effect, where a fluctuation in applied potential results in a mechanical movement of alternating compressions and extensions. The mechanical movement is so fast that it acts as a high frequency vibration, therefore producing what is known as ultrasound frequency [28].

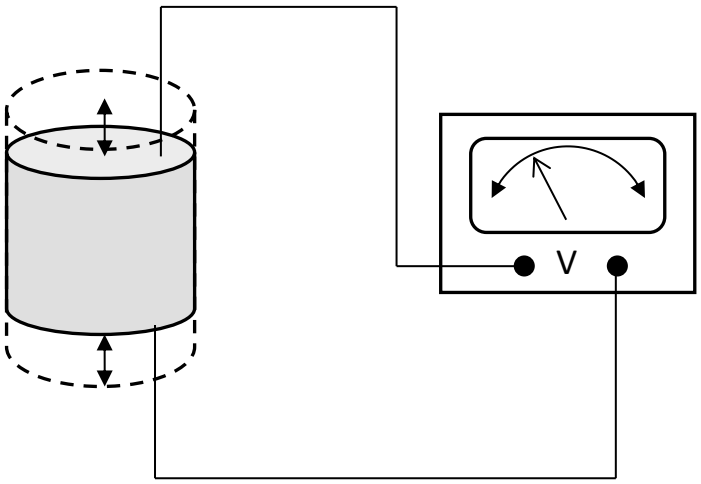

Figure 2.6 - Diagram of piezoelectric effect (Effect has been greatly exaggerated for explanation)

This vibration is passed on by a movement of a set of compressed air layers forming a moving wave that is transmitted through the air via variations in pressure [28]. Figure 2.7 shows how ultrasound is transmitted through a medium in a series of compression and expansion cycles [56].

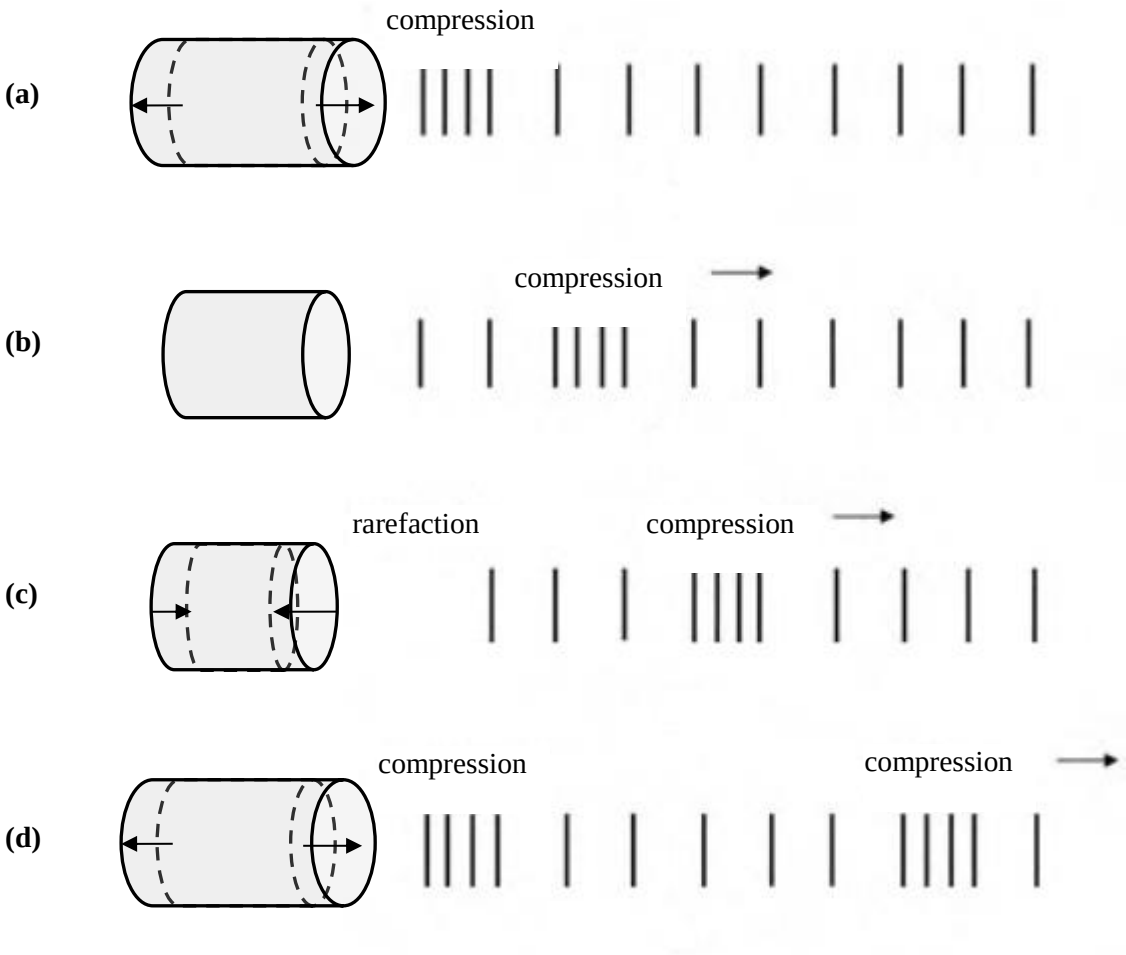

Figure 2.7 - Waves in air caused by a vibrating solid; (a) First expansion of solid; (b) Solid back in orginal position; (c) First compression of solid; (d) Second expansion of solid. Adapted from [28].

Ultrasound technology has been coupled with a variety of processes including; ultrasonic cleaning and degreasing, acoustic filtration, hard brittle material processing, biological cell disruption and solids dispersion [28]. The realisation for combining ultrasound technology specifically with chemical reactions however began around 1940.

In electrochemistry applications, the ultrasound sources available have different ways of transmitting the sound to the electrode surface. The sources can be split into two major categories; ultrasound baths and ultrasound probes/horns. Ultrasound probes are transducers which can be placed directly in the solution that requires agitation. The probe tips are commonly made from a titanium alloy. An example of an ultrasound probe applied to liquid within a small beaker is shown in figure 2.8a illustrating that the flow regime from an ultrasound probe tip is similar to a jet of flow from a pipe of the same diameter [57].

An ultrasound bath consists of a large container with a number of transducers placed underneath or on the walls of a tank which transmit the sound through the bath walls and then to the liquid it contains. The locations of the transducers are shown in figure 2.8b. Implementing an ultrasound bath in electrochemistry involves either filling the bath with distilled water, and immersing a glass electrochemical cell within it [23] or using the entire bath as the cell itself [58]. This is achieved by coating a layer of non-conductive material on the inside of the basin and filling the bath with electrolyte solution into which the electrodes are placed.

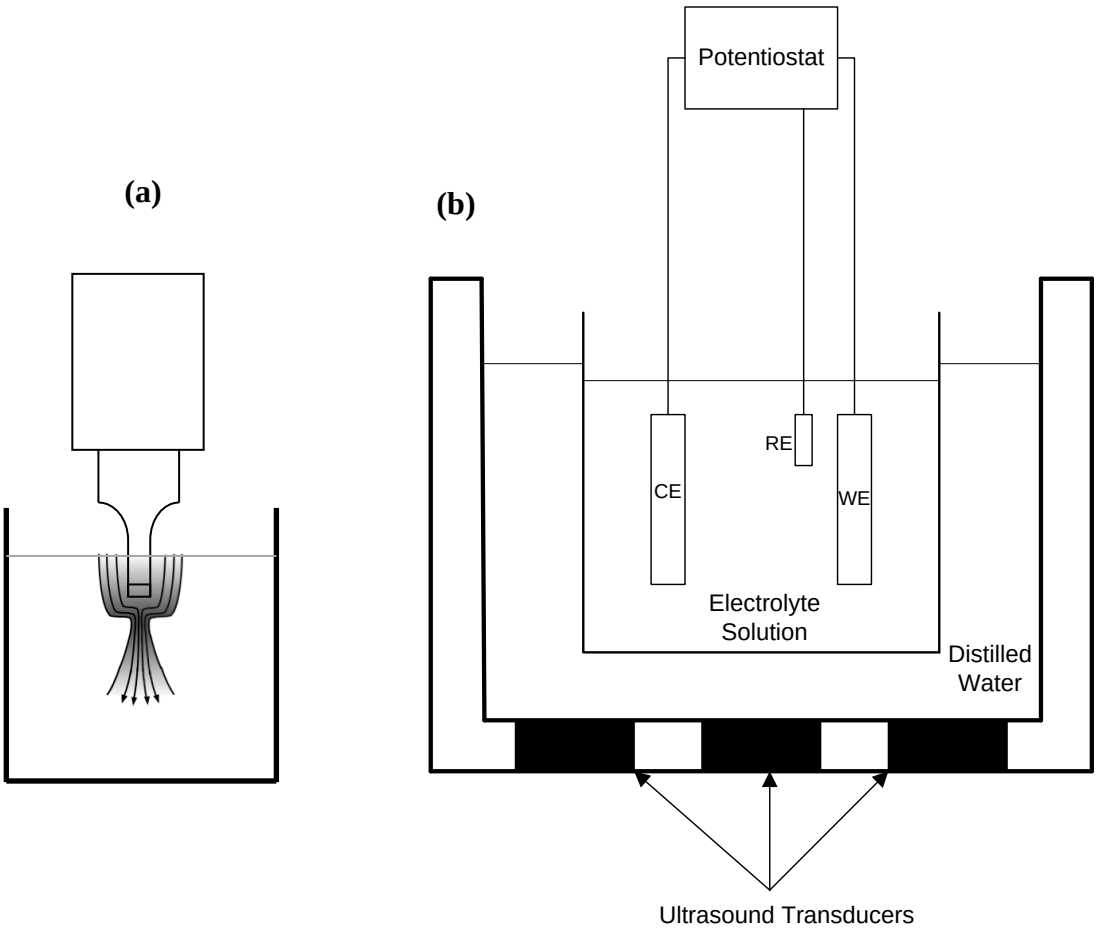

Figure 2.8 – (a) Example of an ultrasound probe applied to a beaker of liquid, (b) Diagram of an ultrasound bath with electrochemical cell.

2.5 Cavitation Bubbles and their behaviour

A major characteristic associated with ultrasonic agitation in liquid is the formation of bubbles formed by a phenomenon known as cavitation. If an ultrasonic pressure wave is traversing through the liquid at high intensity, a rupture of the liquid

takes place, allowing gaseous voids to be formed resulting in the formation of cavitation bubbles [59]. The bubbles are known to move in the direction of the ultrasonic wave, growing in size as this occurs [60].

An early investigation by Yeager and Hovorka [61] combined a copper deposition reaction with 200 – 1000 kHz of ultrasound with a power of 1 W/cm^2 and by using the Schlieren Technique it was found that the gas bubbles on the electrode surface periodically changed in size. These bubble oscillations have been investigated further in a more recent study where bubbles formed from a 1.3 mm diameter titanium ultrasound horn at 20 kHz were filmed by a digital camera as they came into contact with a Petri dish placed 10 mm from the probe. Pictures of both spherical and hemispherical shaped bubbles were discovered, along with a range of bubble diameters between 0.8-15 μm [62].

The movement of the bubbles produced via ultrasonic agitation enhance stirring due to the large shear forces which exist in the region of fluid directly adjacent to the bubble, [28]. This will assist with mixing in the hydrodynamic boundary layer, resulting in a thinning of the diffusion layer, therefore enhancing mass transport of ionic species.

Increasing the intensity of the ultrasound (i.e. ultrasound power) has various effects on the cavitational activity, outlined in the following list by Gogate, Wilhelm and Pandit [52],

- Maximum size of the cavitation bubbles increases
- Initial increase in bubble size is large (about 30%), but after a certain intensity the increase is not as much (<10%)
- Increase in bubble lifetime
- Bubble wall pressure at the collapse point decreases with increasing intensity

Interestingly, the pressure pulse generated from the collapse of a single cavity is lower when the US intensity is increased. However, the number of cavitation events increases with increasing power dissipation which is more significant than the decreasing in collapse pressure. This means that there is an overall increase in the pressure pulse and also an increase in cavitation yield when increasing the ultrasound power [52]. There is a certain limit of power dissipation that is reached where no further increase in number of cavitation bubbles occurs. At this point the negative effect of

decreasing collapse pressure dominates, therefore reaching an optimum ultrasound intensity [52].

2.5.1 Bubble Collapse and micro-jets

Typical cavitation bubble lifetimes have been measured to be less than 70 ms [62]. At the moment when bubble collapse occurs near an electrode surface, temperatures and pressures can be of the magnitude of 10000K and 500atm [63, 64], allowing for the possibility of chemical activation [28]. If ultrasonic cavitation bubbles are collapsing near to a surface, then there is a possibility of a phenomenon known as micro-jetting occurring which can have considerable surface effects.

A micro-jet can be formed when a bubble collapses. The first detection of microjets during bubbles collapse was found by the use of special photography detection equipment [65]. The bubble collapses are assymetric due to the travelling pressure wave. This results in micro-jet formation as shown in figure 2.9; as the bubble starts to tear apart a large amount of pressure is projected outwards from the bubble in the form of a jet. These liquid jets can reach velocities up to 280 m/s [66].

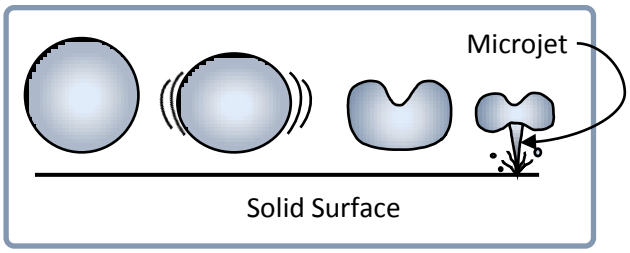

Figure 2.9 - Schematic diagram showing the occurrence of a micro-jet when a bubble collapses close to a surface [67], originally adapted from [62]

The diagram shows the occurrence when the bubble is in close proximity to a solid surface, the movement of the jet is projected towards the solid surface. The presence of these micro-jets in ultrasonic applications has been recorded in many sonochemistry investigations at the electrode surface [68-70]. The high pressures and forces of micro-jets, resulting from bubble collapse, at an electrode can damage either the substrate or deposited metal in terms of pitting or erosion [62, 63, 68, 69]. Despite this, many investigations have suggested that the effects of cavitation phenomena contribute to the enhancement of stirring in electrochemical systems [22, 23, 28, 54, 61, 62, 70, 71].

2.6 Effect on ultrasound agitation mass transfer

The earliest mass transfer experiments with ultrasound carried out by Roll [72] analysed the effect of ultrasound on the polarization of electrodeposition reactions. A low intensity ultrasound at a power of 0.3 W/cm^2 was applied to the electrochemical deposition of nickel, copper and silver reactions. The same depolarization effects seen with other forms of agitation occurred; but considerably smaller concentration gradients were observed compared to conventional agitation regimes. More advanced ultrasonic mass transfer studies were carried out by Bard [73] on the electrodeposition of silver onto a platinum gauze working electrode. It was found that using 30 Watts of 1 MHz ultrasound agitation caused a greater improvement to the efficiency of mass transfer than the more traditional agitation of nitrogen stirring.

2.6.1 Ultrasound probes

The majority of investigations that show the improvement of mass transfer by ultrasound are in systems with ultrasound probes where electrodes are far apart from each other [22, 54, 57, 74, 75], but no information is available for cases where ultrasound is applied within a narrow gap between parallel electrodes. Additionally, the effect of US agitation has been most extensively studied by probes orientated face-on to the working electrode surface [22, 54, 57], illustrated in Figure 2.10(a).

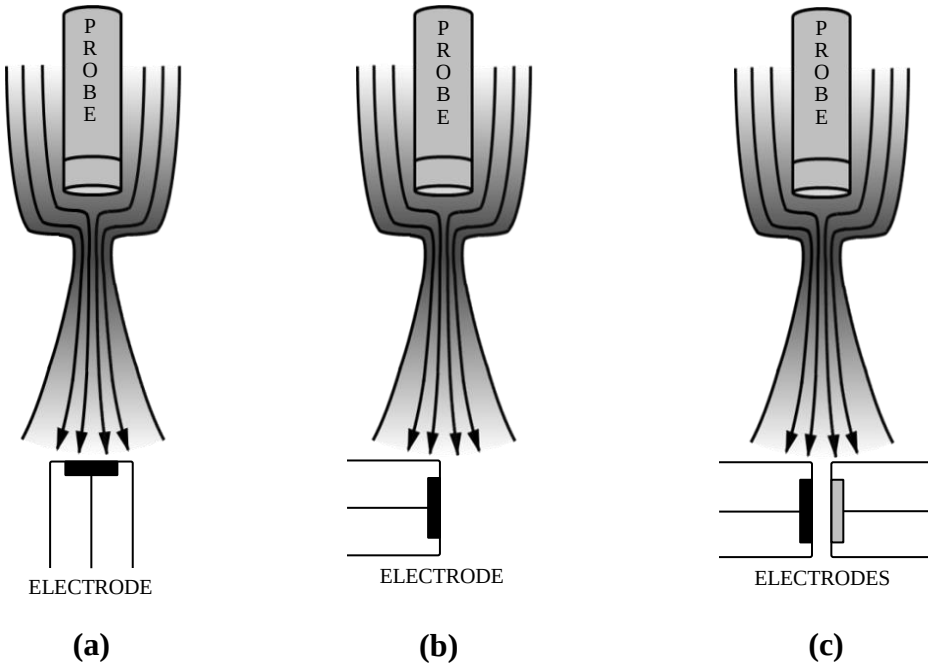

Figure 2.10 - US probe orientations relative to an electrode. (a) Face-on; (b) Side-on; (c) Side-on with narrow electrode gap. Adapted from [57]

The limiting current can be significantly increased with the application of ultrasound agitation. Compton et. al [22] investigated the oxidation of ferrocene in acetonitrile agitated by a 13 mm diameter ultrasound horn vibrating at 20 kHz and a power of 44 W/cm^2. The horn was placed 42 mm above, and face-on towards, a platinum electrode of small radius 13.6 μm. Figure 2.11b and 2.11a show the potential-current plots with and without ultrasound respectively illustrating an increase in limiting current by approximately a factor of 7.

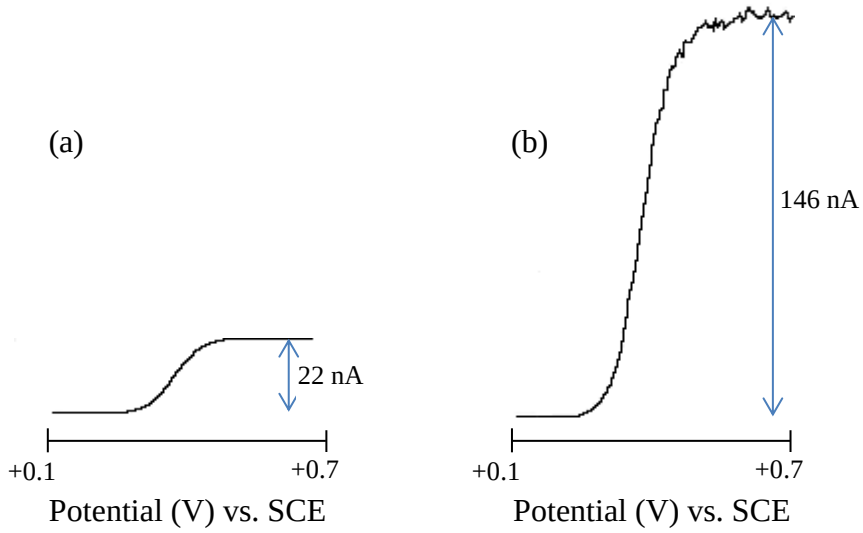

Figure 2.11 - Voltammograms for the oxidation of Cp_2Fe (2.0mM) in acetonitrile/0.1M TBAP at a scan rate of 20 mV/s, recorded in; (a) the absence of ultrasound; (b) the presence of ultrasound (20 kHz; intensity 44 ±5 W/cm2). Adapted from [22]

2.6.2 Face-on probe orientation

2.6.2.1 Effect of probe distance

An investigation studying the reduction of $Ru(NH_3)_6^{3+}$ at a working electrode placed face-on to a 13 mm diameter ultrasound probe operating at 20 kHz and power of 33 W/cm^2 illustrated the importance of the distance between the probe tip and the centre of the electrode surface (d_p). Figure 2.12 presents the limiting currents at varying values of d_p from 30 mm to 2 mm, showing a significant increase in limiting current at very close probe distances of less than 20 mm [57]. The limiting current (i_{Lim}) is shown to be approximately $i_{Lim} \propto 1/d_p^{1/3}$. This was attributed to the narrower jet of flow close to the probe tip compared to distances further away [57], as shown in figure 2.10a. The intensity of the mixing at the electrode surface is therefore increased as the probe tip is brought closer to it.

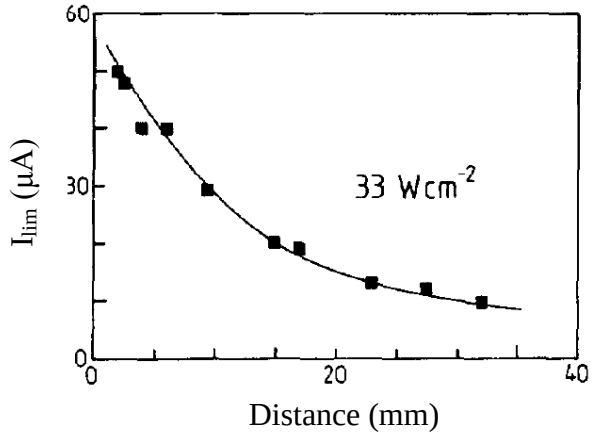

Figure 2.12 - Plot of the change in the limiting current for the sonovoltammetric reduction of 1mM $Ru(NH_3)_6^{3-}$ (33 W/cm^2, 1mm diameter Pt) with electrode-to-horn distance. Adapted from [57].

2.6.2.2 Effect of ultrasound power

Various investigations have studied the effect of the US power on the mass transfer [22, 54, 75]. Figure 2.13 shows the diffusion layer thickness (δ) with varying ultrasound power for a ferrocene oxidation reaction at a platinum electrode. There is a decrease in δ with increasing US power because the increase in the intensity of the flow of ultrasound waves and also the increase in cavitational activity. The diffusion layer thickness (δ) is approximately $\delta \, \alpha \, 1/p^{1/3}$ [22], but there appears to be a minimum diffusion layer thickness beyond a certain power. This is mainly due to the limiting

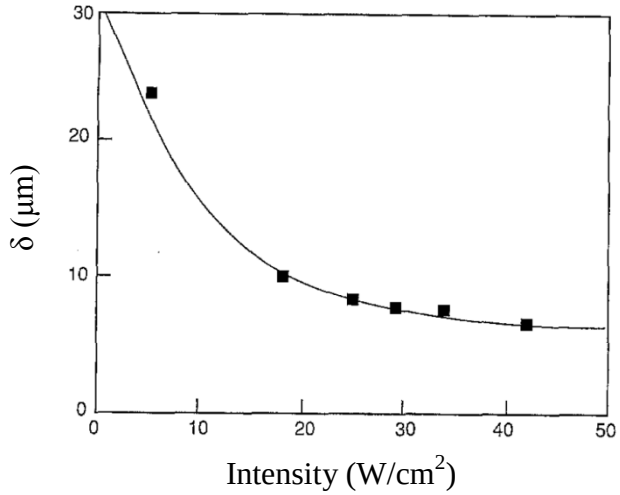

Figure 1 - Variation of the diffusion layer thickness (δ) with the intensity of incident ultrasonic power at macroelectrodes of radius of 0.39 cm, as inferred from the voltammetry of Cp_2Fe. Adapted from [22].

conversion of ultrasound energy to turbulent liquid flow [57], but also because a certain power is reached where no further increase cavitational activity occur therefore reaching an optimum ultrasound power intensity [52].

2.6.3 Side-on probe orientation

Only one investigation has studied the side-on ultrasound geometry [76] illustrated in Figure 2.10(b), which investigated the mass transfer during ferrocene oxidation at a square platinum plate electrode with a 'side-on' 13 mm diameter 20 kHz probe US probe, 32 mm from the electrode centre. The similarity of jet-flow from a pipe to the flow from the tip of an US probe meant that forced convection systems where fluid flowed past the electrode surface [77] could be used to develop a theoretical analysis for the side-on probe orientation. A comparison between the model of 'flow over a plate' and experimental results proved that the model was a good approximation for a side-on probe arrangement.

The 'flow-past' regime means that a thinner diffusion layer is likely to form at the edge of the electrode closest to the probe compared to the edge furthest away. A δ of 10-12 μm at the edge furthest from the electrode have been reported for the side-on probe placement [76], whereas an approximately uniform δ of 6-7 μm is formed at electrodes with the face-on probe system at the same p and d_p (Compton et. al 1994 ; Compton et. al 1995a ; Compton et. al, 1995b Lee et. al, 1995). The non-uniform diffusion layer formation over the electrode surface is the main reason why the side-on arrangement is not used among many electrochemists [76].

2.6.3.1 Theory of ultrasound agitation in side-on arrangement

Eklund et. al [76] described the limiting current at an electrode when US agitation takes place using a US probe positioned in the side-on arrangement. It is known that the flow regime from an ultrasound probe tip is similar to a turbulent jet of flow from a pipe of the same diameter [57]. Furthermore, Eklund et al. [76] proposed that the flow of ultrasound waves over an electrode surface from a 'side-on' probe is analogous to flow over a plate. Based on this assumption, these researchers used an analysis proposed by Levich [77] for forced convection to derive equation 1.17 describing the limiting current at an electrode when such a forced US agitation takes place for a side-on arrangement [76].

$$I_{sono} = \frac{0.34\,F\,D^{2/3}\,U^{1/2} w\,c_b}{\nu^{1/6}} \times \int_{h_0}^{h_0+2r} \frac{1}{x^{1/2}\left[1-\left(\frac{h_0}{x}\right)^{1/3}\right]^{1/3}}\,dx \qquad (1.17)$$

In equation 1.17, *F*, *D*, c_b and *v* are the Faraday constant, diffusion coefficient, bulk concentration of reacting species and the kinematic viscosity respectively. The parameter *w* is the width of the electrode, and the parameter *x* is the distance along the length of the electrode from the edge closest to the probe. In equation (4) h_0 is the distance between the leading edge of the momentum and the concentration boundary layers. The limits of the integral are set at h_o and h_o+2r since the deposition reaction occurs at the metal surface (see figure 4.7b in experimental section).

The only unknown parameter in the equation is *U*, the velocity of the flow far away from the electrode surface. For US agitation, *U* is related to the ultrasound power and is the limiting solution velocity at a large distance from the plate. The effect of bringing the probe tip closer is governed by changing the parameter 'd_p', which is defined as the distance between the centre of the electrode to the US probe tip. It has been shown in earlier experiments that a distance between the probe and electrode of > 3 cm is sufficiently far from the electrode surface for equation 1.17 to hold [22, 76].

Eklund et al. [76] carried out experiments using a 20 kHz probe placed side-on and 34 mm away from a platinum plate electrode where ferrocene was oxidised electrochemically. However, this data was difficult to use, and fig. 2.14 was developed by this author. In the figure, experimentally measured limiting currents were used to

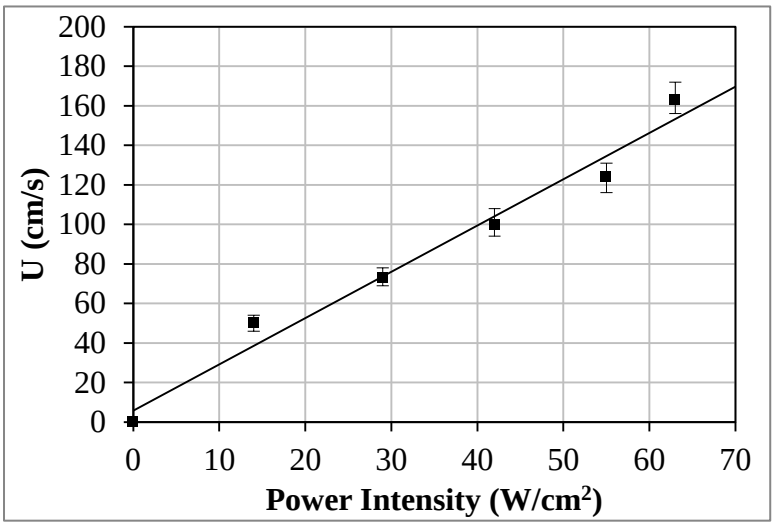

Figure 2.14 - A graph of *U* (best-fit value) obtained from the data (black square) published by Eklund et al. [76]. The distance between the probe and the centre of the electrode was 34 mm.

calculate values of *U* using equation 1.17 at various ultrasound intensities. This analysis showed that *U* was linearly proportional to US power, which is displayed in figure 2.14. This proved that 'flow over a plate' was a reasonable model for this side-on probe system.

2.6.4 Issue of potential interaction of an US probe

Some issues arise within an electrochemical system when using an US probe. When a titanium probe is immersed within the electrolyte solution of an electrochemical cell, the probe enters into the potential field of the system. This causes an interaction in potential of the probe between itself and the other electrodes. Marken and Compton [78] stated that when the probe is placed in the electrolyte solution of a typical 3 electrode cell system, the probe will implement a potential towards the reference electrode. The potential of the probe vs. reference electrode will be similar to the potential applied to the working electrode. This is because the probe and working electrode will be connected to each other through the earth. This interaction can cause problems due to the possibility of a large flow of current to the titanium probe. This could have a consequence for the potentiostat, causing an error or failure due to detection of high currents.

There are a number of techniques of reducing or eliminating the interaction in potential of the probe. Marken and Compton [78] suggest that a non-conducting material could be used for the probe tip; this would mean there is no electrical connection between the tip and the rest of the ultrasound device. Glass tips are available for some ultrasound probes.

Another way of disconnecting the titanium tip from the rest of the probe is to isolate the tip; therefore the titanium tip will no longer be connected to the working electrode through ground. This has been achieved in a fairly recent experiment by Garbellini, Salazar-Banda and Avaca [79] where the titanium tip of an ultrasound probe was insulated from the rest of the probe by use of a Teflon disc.

Marken and Compton [78] solved the issue of the electrochemical interaction of the probe by controlling the potential of the probe via a bipotentiostat. The probe was connected to the circuit as a second working electrode and then grounded. The bipotentiostat was then used to fix the probe at a certain potential which eliminated current flow through the probe, although a bi-potentiostat is an expensive instrument. In

this regard, laboratory scale apparatus cannot be easily implemented in industrial systems.

2.7 Ultrasound Tank Systems

In addition to the difficulties mentioned in the previous section, when ultrasound is incorporated on large-scale industrial processes, the ultrasound bath geometry is usually incorporated in a fashion shown in figure 2.8b. The ultrasound intensity in bath configurations is not as high as the intensity produced from other ultrasound sources [68]. This is because the ultrasound is first transmitted through the bath wall, which absorbs and reflects some of the vibrations. In electrochemical applications, where a cell is placed within a bath, the ultrasonic vibrations have to be passed through the electrochemical cell wall before they can reach the electrode surface. These issues means that cell placement within the bath has a major effect on the intensity being applied to the electrochemical cell [23].

However, the main advantage of using ultrasound tanks is their ability to produce a reasonably uniform distribution of the ultrasound agitation. This is because of the uniformity of the cavitational distribution. This is ideal for applications which require similar mass transport rates in all regions of the tank.

The intensity of the ultrasound wave is at its maximum near the irradiating surface (i.e. the tank wall) and decreases with increasing distance from the transducer [80]. However, the distribution of agitation is much more uniform in an US tank compared to an US probe [81], as US probes cannot transmit acoustic energy into large volumes [80]. Also, the cavitational activity can be distributed over a much larger area in an US tank which makes it an ideal geometry of reactor for scale-up purposes. There can be a wide variation of cavitational activity in the bulk [80], but this can be avoided with careful design of the transducers in the US tank. Maximum and uniform cavitational activity can be achieved by using a number of transducers operating at either the same or different frequencies positioned in such a way that the US wave patterns overlap [80].

The comparison of the distribution of agitation between a US tank and US probe system was carried out by Csoka, Katakhaye and Gogate [81]. A model reaction of potassium iodide oxidation was used to predict the pressure field distribution of a 21 mm diameter 20 kHz US probe in a 300 mL cell and a 204 kHz US cleaning tank with a

volume of 3.3 L. The prediction of the cavitational distribution for the probe and the tank are shown in the figures 2.15 and 2.16 respectively, illustrating the more uniform pressure distribution in the US tank. The probe had 30% higher iodine liberation due to the larger power dissipation. However, it is difficult to make a reasonable comparison of these systems due to the difference in power dissipation, which was 800 W/L and 66.7 W/L for the probe and bath respectively. This study showed that it is better to have a large area of irradiation as this gives a better pressure field distribution [81].

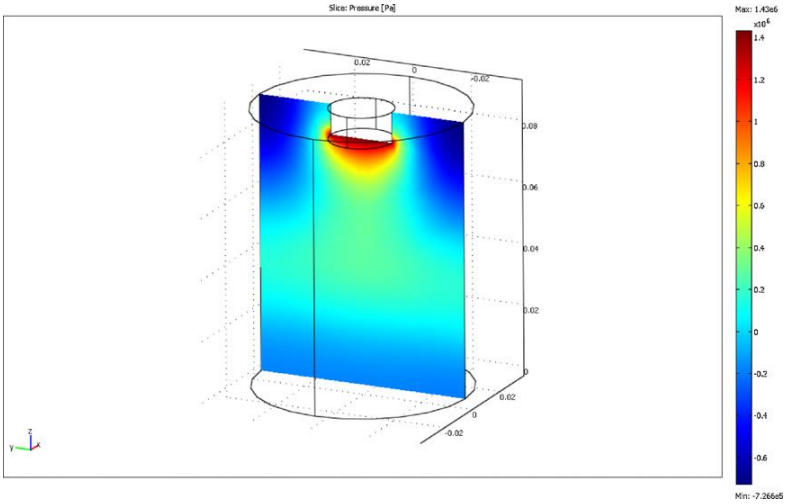

Figure 2.15 - Prediction of the cavitational activity distribution in the case of ultrasonic horn. Taken from [81].

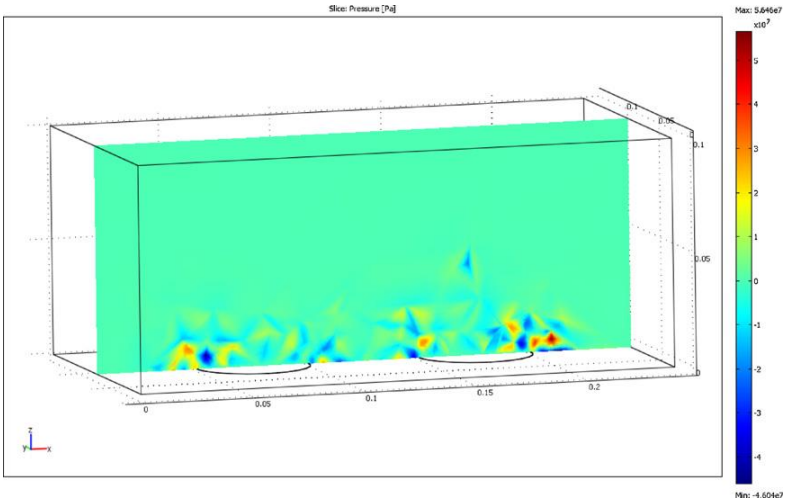

Figure 2.16 - Prediction of the cavitational activity distribution in the case of ultrasonic bath. Taken from [81].

Another study which compared US probe and bath systems investigated a 22.7 kHz probe operating at a power of 240 W through area of 81 mm^2, and a 500 mL 22 kHz US bath with dimensions 15 x 15 x 15 cm operating at 120 W with 2 transducers attached to the base of a steel tank. The calculation of 'Power dissipated in the liquid' /

‘Electric power supplied to the system’ was used to calculate the energy efficiency for each system which was < 10% and 43% for the probe and bath respectively. The bath is more energy efficient due to uniform dissipation of the ultrasound over a wider area as opposed to the probe’s concentrated energy dissipation.

Another study which compared US probe and bath systems investigated a 22.7 kHz probe operating at a power of 240 W through area of 81 mm^2, and a 500 mL 22 kHz US bath with dimensions 15 x 15 x 15 cm operating at 120 W with 2 transducers attached to base of steel tank. The calculation of ‘Power dissipated in the liquid’ / ‘Electric power supplied to the system’ was used to calculate the energy efficiency for each system which was < 10% and 43% for the probe and bath respectively. The bath is more energy efficient due to uniform dissipation of the ultrasound over a wider area as opposed to the probe’s concentrated energy dissipation.

A recent article by Sutkar and Gogate [80] have stated that although there is many applications that have been proved in laboratory scale acoustic reactors, there is a limited amount of research on large-scale industrial applications. Strategies to develop suitable ultrasound reactor designs and scale-up from successful laboratory-scale processes are therefore required. In particular, the higher energy efficiency of US tanks compared to US probes makes it more suitable for industrial applications. A further method of reducing energy costs for industrial electrodeposition purposes would be to pulse the agitation in the form of short bursts of ultrasound. This would reduce the amount of power required for the process and reduces the time of exposure of US to the electrode surface in order to decrease damaging effects of cavitation on the surface and the deposited metal.

2.8 Pulsed agitation

Pulsed processes in electrochemical applications are most commonly provided by pulsing either the potential or the current [82, 83] and have been used to create metallic deposits [84-87] and nanoscale materials [82, 88-90]. Mass transfer improvement adjacent to the electrode can be achieved with pulse deposition due to the dual diffusion layer which is formed using this technique when applying very short millisecond range pulses [91-94]. If pulses of current are applied in the second range, the typical effects associated with pulse plating cannot occur. This is mainly due to limited solution agitation, it is therefore suggested that hydrodynamic pulses can be combine with current pulses.

Applying external agitation using hydrodynamic pulsing has previously been used to improve an alloy deposition process with a rotating disk electrode [95, 96]. It was shown both theoretically [96] and experimentally [95] that co-deposition of two metal ions using a flow modulation altered the partial current for the metal that is plated under mass transfer limitation. This formed a composition modulation in the deposit. Pulsing agitation may also be applied to compositionally modulated alloy deposition processes where solution agitation could be introduced during the plating of the noble material. This is advantageous for processes where the rate of deposition is limited by the deposition rate of the more noble material [97].

Pulsed agitation may also be favourable for the Enface process [6, 11, 20], requiring solution agitation within narrow electrode gaps of 0.3 mm. Pumps and eductors would be unsuitable, not only because the majority of fluid would by-pass the narrow gap but also because providing hydrodynamic pulses using this kind of agitation have large time constants. The 'time constant' can be defined as the time needed for a dynamic process to reach 90% of its steady state value [98], i.e. the time required for the momentum boundary layer to reach 90% of its thickness at steady state. Providing changes in hydrodynamics using pistons or pumps may require 10 seconds to be applied to the fluid due to pump start-up and additional time to transfer the agitation to the electrode surface. Ultrasound agitation however, has a much lower time constant and also higher fluid velocities than these mechanical agitation techniques.

2.9 Pulsed US agitation

Transducers in an US tank are controlled by electrical signals which can be switched on and off rapidly within a second, therefore making it possible to provide rapid hydrodynamic pulses to a fluid. The agitation is immediately transferred to the electrolyte solution as the transducers are attached to the walls of the tank. The fact that relatively fast fluid velocities and uniform agitation is achieved at a distance of 30-40 mm from vibrating wall [76, 99] ensures that agitation reaches the electrode surface within approximately 1 second. This therefore suggests that US agitation would be suitable for applications which require fast hydrodynamic pulsing and also for combining with pulse deposition.

The application of pulsed ultrasound has been used previously to improve surfactant degradation [100-102] where the degradation of sodium dodecylbenzenesulfonate was enhanced by 119% when pulsed US was applied using a

US pulse of 100 ms and an on/off ratio of 1:50 [102]. The only electrochemical studies which have combined pulsed US and pulsed current have used pulses < 1 s in order to create metal [103] and alloy [104] nanoparticles with the use of an ultrasonic probe acting as both a cathode and ultrasonic transducer. An example of a combined pulse regime used to produce nanoparticles is shown in figure 2.17.

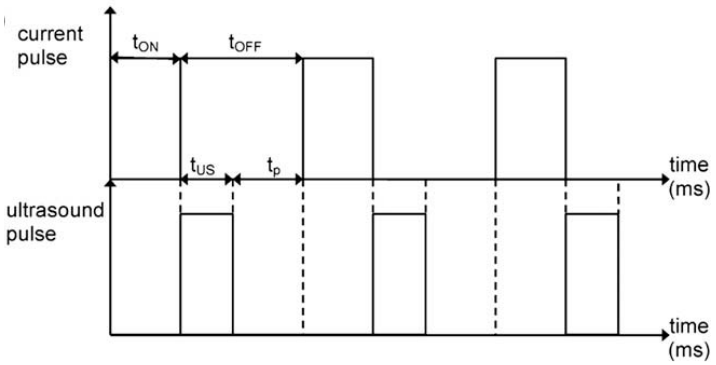

Figure 2.17 – Representation of electrochemical and ultrasound pulses [104]

2.10 Concluding Remarks

The standard agitation methods have been discussed and the work on ultrasound agitation has been described. Investigations on the use of pulsed US with deposition of metallic films have not been carried out until recently. A pulsed US study carried out by the author investigated the deposition of metallic films using the effect of combining the pulsed US agitation with long current pulses for the first time [67, 105, 106].

There has also been no exploration into the effect of US agitation on the mass transfer within a narrow gap between two parallel plates. The author has studied the combined geometry of a ‘side-on’ probe and narrow inter-electrode gap [51], a geometry which had not yet been investigated. This work assisted in determining whether ultrasonic technology will provide enough stirring for the Enface process and also to find the optimum ultrasound parameters in order to scale-up the process. The results of these papers will be presented in this thesis.

Although, US probes are useful for lab-scale experiments and optimization studies before scaling up the process, they cannot be used on a large-scale for industrial applications. An investigation into the use of US tanks was therefore also required for this work. Before describing the experiments that were carried out to achieve this it is first important to understand the fundamentals of electrodeposition, described in the following chapter.

Chapter 3. Electrodeposition Fundamentals

3 Electrodeposition Fundamentals

3.1 Electrode potential

The equation which represents a basic electrochemical reaction is shown in equation (3.1), displaying a reversible redox reaction.

$$Oxd^{n+} + ne^{-} \leftrightarrow Red \tag{3.1}$$

The electrode potential is the potential difference between an electrode and a reference electrode. The standard electrode potential (E^0) is the electrode potential of an electrode reaction when all components are in their standard states. This is conventionally measured against a standard hydrogen electrode, the data of which is well known and can be found in literature [107]. The equilibrium potential (E_e) is the electrode potential when the components are in equilibrium with each other. In other words, when the forward and backward reaction rates are equal to each other and therefore there is no current being passed. The Nernst equation is used to calculate the equilibrium potential, shown in equation (3.2).

$$E_e = E^0 + \frac{RT}{nF} ln\left(\frac{a_{Oxd}}{a_{Red}}\right) \tag{3.2}$$

Where R is the gas constant, T is the temperature, n is the number of electrons transferred, F is Faraday's constant and a is the ion's activity. As ion activity is difficult to measure, therefore an activity coefficient (γ_i) is used which is related to the concentration of the component i (c_i) as shown in equation (3.3), where c_0 is the standard concentration (typically 1 M). Substituting eq. (3.3) into eq. (3.2) gives eq. (3.4), and after re-arrangement gives eq. (3.5). Incorporating the γ_i into the E^0 gives what is known as the formal potential ($E^{0'}$) shown in eq. (3.6), therefore the Nernst equation in terms of ion concentrations is given in eq. (3.7).

$$a_i = \gamma_i \frac{c_i}{c_0} \tag{3.3}$$

$$E_e = E^0 + \frac{RT}{nF} ln\left(\frac{\gamma_{Oxd} c_{Oxd}}{\gamma_{Red} c_{Red}}\right) \tag{3.4}$$

$$E_e = E^0 + \frac{RT}{nF} ln\left(\frac{\gamma_{Oxd}}{\gamma_{Red}}\right) + \frac{RT}{nF} ln\left(\frac{c_{Oxd}}{c_{Red}}\right) \tag{3.5}$$

$$E^{0\prime} = \frac{RT}{nF} ln\left(\frac{\gamma_{Oxd}}{\gamma_{Red}}\right) \tag{3.6}$$

$$E_e = E^{0\prime} + \frac{RT}{nF} ln\left(\frac{c_{Oxd}}{c_{Red}}\right) \tag{3.7}$$

Equation 3.7 is the electrode potential for an ideal system, however in a real system the measurement of the electrode potential measured experimentally is likely to be different from that calculated from equation 3.7. This is due to presence of other species in the electrolyte, occurrence of other side reactions or external characteristics of the electrochemical cell which could all influence a change in the electrode potential.

3.2 Electrodeposition process

The basic equation for representing an electrodeposition reaction is shown in equation (3.8). It displays the reduction of the ion M^{n+} by electron transfer on an electrode surface, where M represents a metal, for example copper Cu^{2+}.

$$M^{n+} + ne^{-} \leftrightarrow M^{0} \tag{3.8}$$

Figure 3.1 shows the diagram of an electrodeposition reaction in a system with aqueous electrolyte solution, working electrode, counter electrode, reference electrode and a power supply. The electrolyte solution will contain dissolved metal ions which are reduced at the cathode surface due to the gain of electrons supplied by the power supply. If the anode is made from the metal being deposited on the cathode, then the anode is oxidised therefore allowing more metal ions to be dissolved into the solution. The cell potential (E_{cell}) is measured between the counter and working electrodes and the electrode potential is measured between the working and reference electrodes.

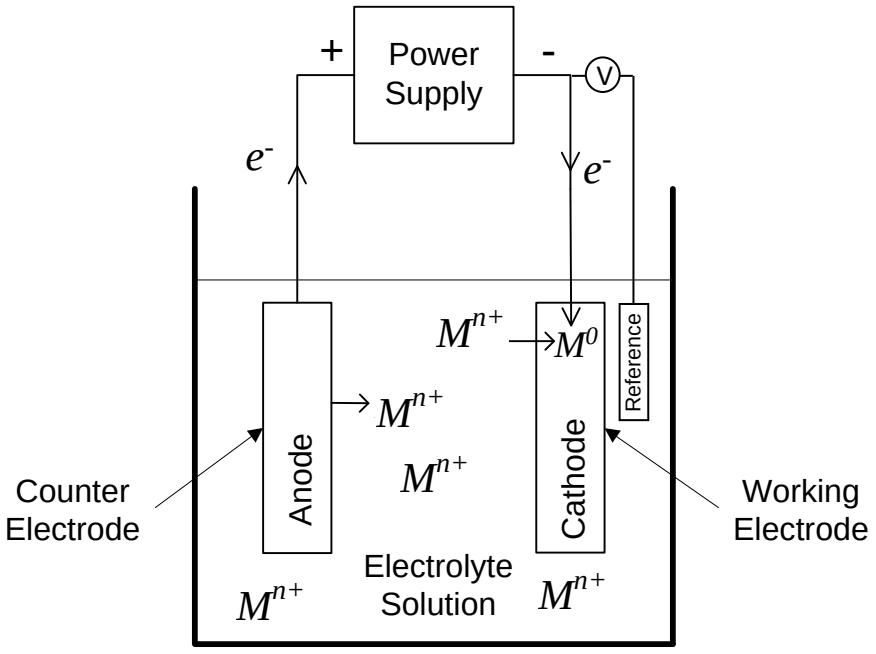

Figure 3.1 - Simple diagram of an electrodeposition process in a 3 electrode system.

The electrodeposition process occurs through various stages as follows:

1. Mass transport of ionic species from the bulk solution to the solution/electrode interface
2. Adsorption of ions on electrode surface
3. Charge transfer at the electrode surface (i.e. reduction of M^{z+} to M^0)
4. Nucleation of metal on the electrode surface
5. Incorporation into metal lattice

For the electrodeposition process to begin a potential is applied (E) to the working electrode. When this occurs there is a difference between the electrode potential and its equilibrium potential known as the overpotential (η), shown in equation 3.9. The sign of the η effects the electrode reaction, i.e. if overpotential is positive anodic current flows and an oxidation reaction takes place. If overpotential is negative, as for electrodeposition processes, cathodic current flows, supplying electrons and electron transfer takes place resulting in a reduction reaction on the electrode surface, leading to metal deposition.

$$\eta = E - E_e \tag{3.9}$$

The rate of the slowest step governs the overall rate of the electrodeposition process. In cases where the electron transfer reaction at the surface is faster than the transport of ions from the bulk solution to the electrode surface, the system is mass transport controlled. Since this work pertains to improving mass transfer by US agitation, fundamental aspects of material transport and associated measurement techniques are explored further in the forth-coming sections.

3.3 Mass Transfer Theory in Electrodeposition

The transport of reacting ions from the bulk solution to the electrode surface causes natural stirring in the form of free convection, creating an upwards flow near the electrode surface in vertical electrode plate electrochemical systems. This supplies convective transport of the ionic species from the bulk solution towards the diffusion layer [29]. Ion movement can occur via migration flux, convective flux or diffusion flux, which contribute to the overall flux of the ionic species shown in equation 3.10.

$$N_i = N_{i,migration} + N_{i,convection} + N_{i,diffusion} \quad (3.10)$$

N_i = Flux of any species

$N_{i,migration}$ = Migration Flux

$N_{i,convection}$ = Convective Flux

$N_{i,diffusion}$ = Diffusion Flux

$N_{i,migration}$ is related to the charge of the species located within the electric field. The direction of movement is dependent in the charge of the ion; anions migrate towards the positive electrode, and cations migrate towards the negative electrode. $N_{i,convection}$ depends on the hydrodynamic movement of the fluid. Concentration gradients located near the electrode surface cause a movement of ions towards the surface, resulting in a movement of ions in the bulk known as convection flows. $N_{i,diffusion}$ is dependent on a concentration boundary layer, called the diffusion layer, formed at the surface due to a difference between the rate of transport of ions to the surface and the rate of reaction of the ions at the surface. The thickness of this boundary layer is related to the change in the concentration of reacting species near the electrode surface.

3.4 Diffusion Boundary Layer

If the overpotential is steadily applied to the system, the reaction rate at the electrode surface increases due to the increase in current, resulting in a decrease in metal ion concentration at the electrode surface. If overpotential is increased further, the reaction rate at the surface increases, until the process reaches a point where the supply of reactant from bulk may not be sufficient, causing there to effectively be zero concentration at the surface. At this point the process is limited by the rate of mass transfer of species through a diffusion layer from the bulk solution to the surface. The current that this occurs at is known as the limiting current. A diagram of the concentration profile and diffusion layer is shown in figure 3.2.

The thickness of the boundary layer is dependent on the the concentration gradient. The actual thickness of the diffusion boundary layer (δ) is at the distance from the surface where the concentration starts to decrease from the value of the bulk concentration, indicated in figure 3.2.

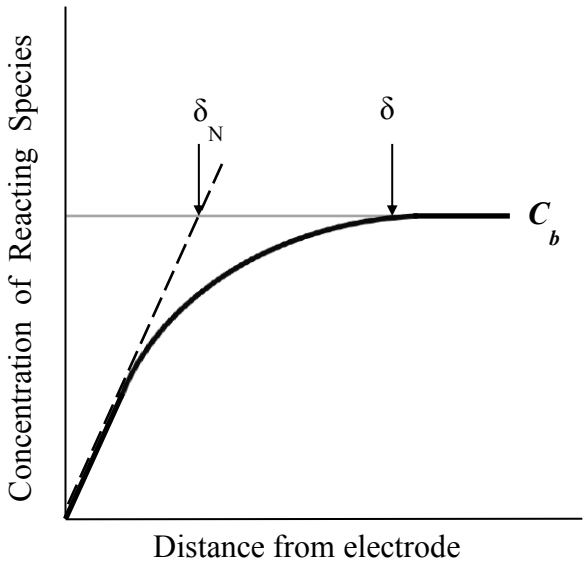

Figure 3.2 - Concentration profile at an electrode at the limiting current showing boundary layer thickness. δ = Actual Diffusion Layer Thickness; δ_N = Nernst Diffusion Layer Thickness. Adapted from [30].

3.4.1 Nernst Diffusion Layer

Nernst [108] created a model to calculate the diffusion layer thickness on the basis of two assumptions.

(1) Linear Concentration profile of reacting species

(2) Stagnant Diffusion Layer

This approximated thickness is called the Nernst diffusion layer thickness (δ_N, in figure 4) and is used in many standard calculations. Experiments have been carried out that prove that there is reasonable concurrence between the values of calculated Nernst diffusion layer thickness (δ_N) and actual layer thickness (δ) [109]. The Nernst diffusion layer thickness is calculated using the value of limiting current.

Pure diffusion of the mass transport of reacting ions is assumed when the reaction of the ions on the electrode surface are much faster than the rate of diffusion of ions. Pure diffusion is therefore usually considered for use in developing a model for the limiting current. The equation for total flux for pure diffusion is given in equation (3.11).

$$\vec{N} = -D \cdot \nabla c \qquad (3.11)$$

$\vec{N}$ = Flux

D = Diffusivity

c = Concentration of ionic species

$$\vec{N} = -D\frac{dc}{dy}\bigg|_{y=0} \qquad (3.12)$$

y = distance from electrode surface

Equation (3.12) shows equation of flux towards the electrode surface written in one dimension. This equation states that an increase in the concentration gradient (described earlier) will increase the flux of the species towards the surface of the electrode. The negative sign simply indicates that the direction of flux is in the opposite direction to the concentration gradient. This flux is equal to that given in equation (3.13), which can be rearranged with the current (i) as the subject in equation (6).

$$\vec{N} = \frac{\vec{i}}{nF} \qquad (3.13)$$

$\vec{i}$ = Current density of reduction reaction

n = Charge on reacting species

F = Faraday Constant (96485 A/mol)

$$\vec{i} = nF\,\vec{N} \qquad (3.14)$$

$$\vec{i} = nF\left(D\left(\frac{dc}{dy}\right)\right)\bigg|_{y=0} \qquad (3.15)$$

In relation to equation (3.12), ‘dc’ can be replaced by the difference in the bulk concentration (c_b) and surface concentration (c_s), and ‘dy’ can be replaced with ‘δ_N’. Equation (3.12) is then substituted into equation (3.14). This gives the vector equation for the limiting current density, equation (3.15), shown in terms of scalar quantities in equation (3.16). Equation (3.17) is the equation for the mass transfer coefficient (k_m). If equation (3.17) is applied to (3.16), and c_s is assumed to be zero, then the equation is simplified to equation (3.18).

$$i_{Lim} = \frac{nFD(c_b - c_s)}{\delta_N} \qquad (3.16)$$

$$k_m = \frac{D}{\delta_N} \qquad (3.17)$$

$$i_{Lim} = nFk_m c_b \qquad (3.18)$$

These equations can be used with limiting current density values from experimental data to calculate the diffusion boundary layer thickness.

3.5 Limiting Current Technique

The limiting current can be achieved by gradually increasing applied potential and observing the change in current. The result of an experiment such as this has been displayed in Figure 3.3 for a cathodic reaction. The current-potential diagram in Figure 3.3 shows a large increase of current density with the initial increase in applied potential from 0 V. At the point where the concentration of the surface is zero, a situation is reached where any further increase in potential cannot increase the flux of the reactant, and correspondingly the current density. A current plateau is therefore formed where this mass transfer limitation dominates, the current density at this plateau is called the limiting current density (i_{Lim}). After a large increase in cathodic potential, the current density begins to increase again due to other reactions occurring at the electrode surface, e.g. hydrogen evolution.

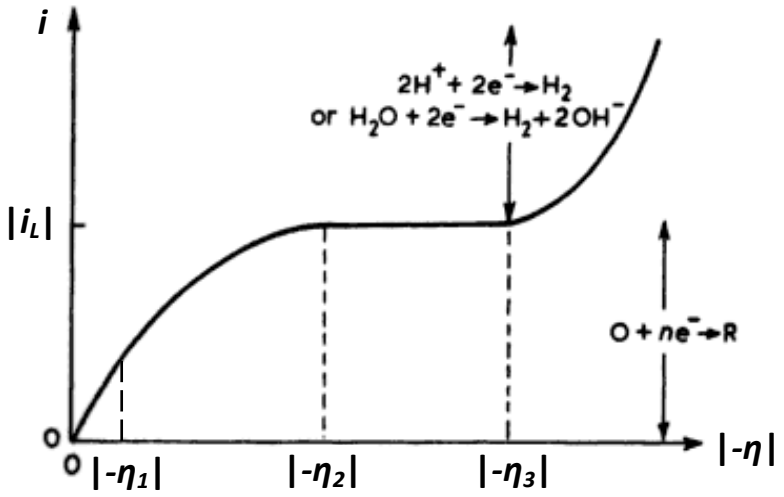

Figure 3.3 - Current-overpotential plot for a cathodic reaction. Adapted from [110].

3.6 Overpotential Curve

The shape of the current-potential curve in figure 3.3 can be described by changes in overpotentials. The overpotential consists of three components; concentration overpotential (η_C), surface overpotential (η_S), and ohmic overpotential (η_Ω). The total overpotential can be described as the sum of these three values, shown in equation (3.19). The shape in the overpotential-current curve depends on the contribution of each of these overpotentials.

$$\eta_{TOT} = \eta_S + \eta_C + \eta_\Omega \qquad (3.19)$$

The η_Ω depends on the resistance through the solution. A decrease in the distance between the reference and working electrode will decrease the value of ohmic overpotential. The η_S is caused by the characteristics and the rate of the surface reactions on the electrode and is also dependent on the surface properties, for example changes in the structure of the deposit surface during metal deposition. The η_C depends on the surface and bulk concentrations of ionic species and is defined as the amount of electrode potential that is increased so that the required current density is reached [111].

The depletion of Cu^{2+} that occurs immediately adjacent to the electrode is related to the concentration overpotential. When the surface concentration of Cu^{2+} goes to zero, this time is called the transition region. The transition time is calculated using the Sand equation, shown in equation 3.20 [112] and is defined as the time taken for the Cu^{2+} ion concentration to become effectively zero at the cathode surface after current is switched on.

$$\tau_i = \frac{\pi D_i n_i^{\,2} F^2 c_{i,b}^2}{4 i_i^2} \qquad (3.20)$$

where D_i is the diffuse ion coefficient, n_i is the number of electrons, F is the Faraday constant, $c_{i,b}$ is the concentration of Cu^{2+} ions in the bulk, and i_i is the plating current density.

The shape of the overpotential curve in figure 3.3 can be explained by changes in the η_S and η_C. It should be noted that the overpotential in figure 3.3 is negative as this is cathodic overpotential. In the region '0 to $|-\eta_1|$', the rate of reaction is controlled by kinetics, therefore the majority of the overpotential consists of the η_S. As the '$|-\eta_1|$ to |-

$\eta_2|$' region is reached, the η_C becomes increasingly more significant. The '$|-\eta_1|$ to $|-\eta_2|$' region is known as the transition region as the overall overpotential is controlled jointly by kinetics and mass transfer and consists of a mixture of η_S and η_C. The region of '$|-\eta_2|$ to $|-\eta_3|$' is where mass transfer limitation dominates and the η_C becomes greater than the η_S. For potentials greater than η_3 another electrochemical reaction has started to take place (e.g. H_2 evolution) and the reaction is no longer in the mass transfer controlling region.

When employing the limiting current technique, the measurement of the current plateau is made less difficult if the is a large separation between '$|-\eta_2|$ to $|-\eta_3|$', i.e. the region where mas transfer dominates. This means a more well-defined plateau and therefore a better accuracy in measurement.

3.7 Electrocrystallization

Other aspects that are affected by mass transfer (hence surface concentration) are nucleation and the growth of the crystal lattice. Before this is discussed, the thermodynamics during electrocrystallization should first be described, explained previously by Pletcher [113].

3.7.1 Thermodynamics of electrochemical phase formation

The equilibrium of electrochemical phase formation is established by the electrode transfer reaction shown in equation 3.8. To describe the thermodynamics of the electrocrystallization process it is assumed that (1) there is a negligible contact area between nuclei and the electrode surface, (2) small spherical nuclei are formed on the electrode, (3) the electrode surface is made from a foreign material, (4) the electrode transfer process is simplified to equation 3.8.

At the equilibrium potential (E_e) described by the Nernst equation, in equation 3.2, the surface activity of the adsorbed ion is $a_{ads,e}$. If the electrode potential is increased, the surface activity of the adsorbed ion can be described by equation 3.21. The Gibbs free energy of the phase formation is shown in equation 3.22

$$\frac{a_{ads}}{a_{ads,e}} = exp(-nF\eta/RT) \tag{3.21}$$

$$\Delta G_v = \frac{nF\eta}{\bar{V}} \tag{3.22}$$

Where ΔG_v is the free energy change per unit volume ($\bar{V}$) associated with the formation of the bulk phase. $\bar{V} = M_w/\rho$, therefore equation 3.22 becomes equation 3.23, where M_w is the molecular weight of the deposited material and ρ is the density of the deposited material.

$$\Delta G_v = \frac{nF\eta\rho}{M} \tag{3.23}$$

The total Gibbs free energy (ΔG_{total}) for a nucleus resting on an electrode surface is shown in equation 3.24. For a spherical nucleus on an electrode surface, ΔG_{bulk} and $\Delta G_{surface}$ can be described by equations 3.25 and 3.26 respectively, which gives equation 3.27.

$$\Delta G_{total} = \Delta G_{bulk} + \Delta G_{surface} \tag{3.24}$$

$$\Delta G_{bulk} = \frac{4\pi {r_n}^3 \Delta G_v}{3} \tag{3.25}$$

$$\Delta G_{surface} = 4\pi {r_n}^2 \gamma \tag{3.26}$$

$$\Delta G_{total} = \frac{4\pi {r_n}^3 nF\eta\rho}{3M} + 4\pi {r_n}^2 \gamma \tag{3.27}$$

Where r_n is the radius of the nucleus, and γ is the molar surface free energy (surface tension). The critical radius (r_c), equation 3.29, and the critical free energy (ΔG_c). i.e. the maximum free energy, depends on both the value of overpotential and the differentiation of equation 3.27 with respect to r_n, shown in equation 3.28. Equation 3.28 shows that the ΔG_c is inversely proportional to η^2 in electrochemical nucleation.

$$\Delta G_c = \frac{16\pi M^2 \gamma^3}{3n^2 F^2 \eta^2 \rho^2} \tag{3.28}$$

$$r_c = \frac{-2M\gamma}{nF\eta\rho} \tag{3.29}$$

The phase growth will not only continue on the surface of the electrode, but will also continue on previously deposited layers of material. This contributes to the formation of the crystal lattice.

3.7.2 Formation of the crystal lattice

The growth of the crystalline lattice involves the incorporation of atoms at various lattice sites. The growth on a crystal surface involved a number of different sites [114]. The various different sites are shown in figure 3.4, the incorporation of the atoms is associated with a different energy for each site. The growth of the metal lattice is mainly influenced by the rate of electron transfer and the diffusion of ions to the cathode surface and is therefore effected by the concentration of ions at the electrode surface and therefore the current density.

For example, at low current densities, the diffusion of ions is stable and ions would tend to form on preferred lattice sites, leading to the formation of a layered structure of the deposit. These favourable sites are those with a higher value if m in figure 3.4, which results in a layered deposit structure. When operating at higher current densities however, the limiting current density is approached and the ion diffusion is not as stable. This means the absorbed ions are less likely to be incorporated into the lattice at the favourable sites, and different structures will be formed, for example dendritic growth [115].

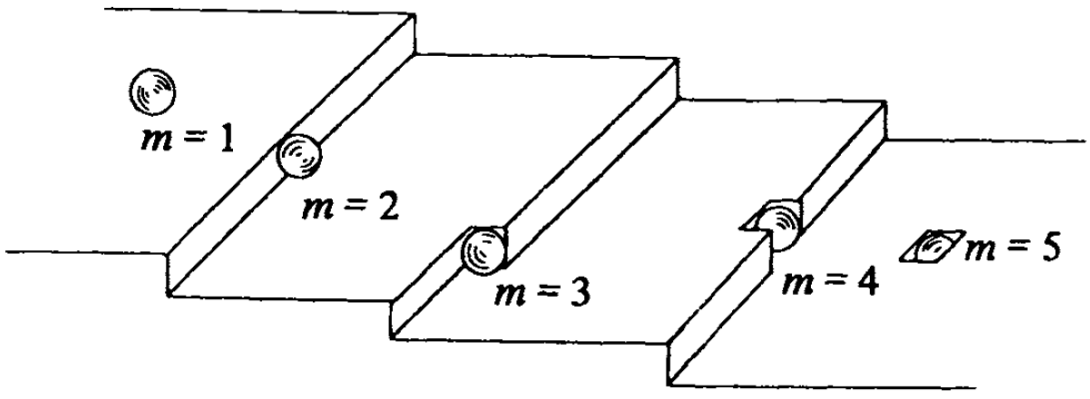

Figure 3.4 – The cubic sites considered in the Kossel-Stranski theory of phase growth. Surface sites (m=1), edge sites (m=2), kink sites (m=3), edge vacancies (m=4), surface vacancies (m=5). Adapted from [113]

3.7.3 Nucleation and Growth

When metallic ions are reduced on a metal electrode surface and nuclei formation occurs, there is an initial increase in cathodic current at the start of deposition, shown in figure 3.5. This is due to the initial increase in surface area that occurs where the nucleation is involved [116].

Two limiting nucleation mechanisms can occur; (1) instantaneous nucleation which is when there is a slow growth of nuclei on a small number of active sites activated at the same time, which can then be followed by (2) progressive nucleation which consists of fast growth of nuclei on many active sites which are all activated during electrochemical reduction [117].

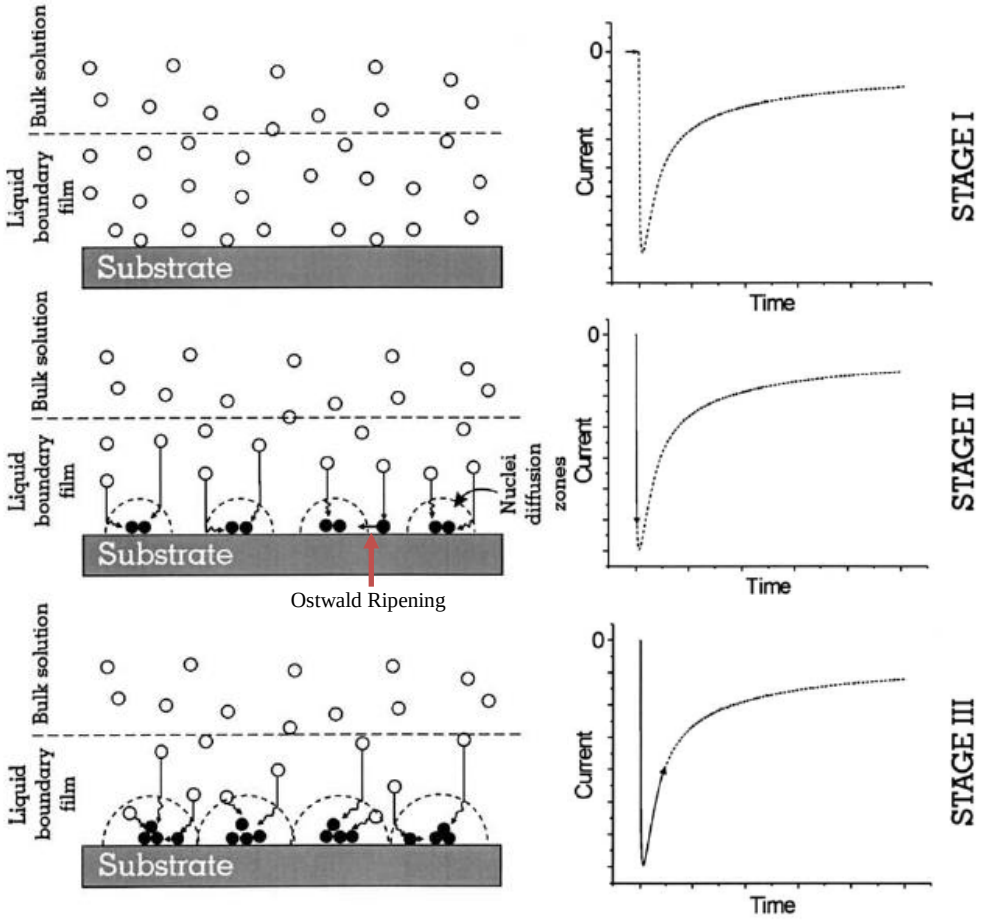

Figure 3.5 - Schematic presentation of phenomena involved during copper nucleation at various stages of chronoamperometric experiment for a low concentration of metal ions. Depicted stages are (I) prior to electroreduction, (II) state at the onset of reduction and (III) steady state of electroreduction. Adapted from [116]

During the progressive nucleation stage the nuclei tend to begin overlapping because each nucleus develops its own diffusion zone which is much larger than the size of the nuclei itself. Eventually these diffusion zones will overlap covering the entire electrode area, as shown in figure 3.5 [116]. Once this has been achieved then the copper deposition reaction is said to be mass transfer controlled. At this point, either more nuclei formation occurs on active sites or copper nuclei growth, which will be followed by the incorporation and growth of the metal lattice.

It is possible for the growth of nuclei to occur via a mechanism known as Ostwald ripening [118] which is a crystal growth phenomenon defined as larger crystals growing at the expense of smallest crystals [119]. An example of this phenomenon is shown in figure 3.5 indicated by the red arrow. Ostwald ripening can be explained in further detail with the use of the schematic shown in figure 3.6, illustrating the scenario when a small and a large spherical crystal is in close proximity to each other.

The crystals must slightly dissolve due to the requirement of equilibrium. There is therefore a difference in concentration that surrounds the crystals, this is shown as a 'spherical halo' in figure 3.6. If these two zones intersect, which would occur at small values of X, a concentration profile is formed between the two crystals. This results in mass transfer from the small crystal to the large crystal, causing the large crystal to grow and may continue until the small crystal disappears [119].

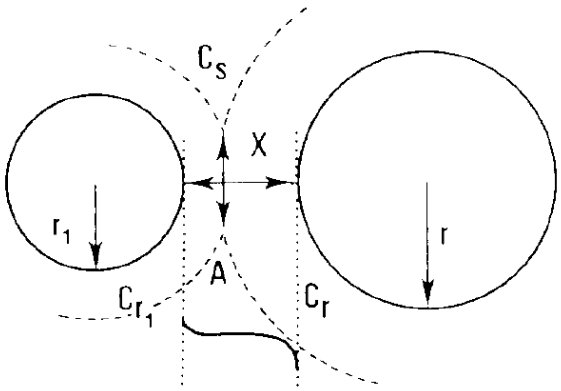

Figure 3.6 – Schematic representation of the solute transfer from the smallest to the largest crystal during Ostwald ripening, where r and r_1 = radii of the crystal or nuclei ; C_s = bulk concentration ; C_r = concentration within the halo of the larger crystal ; C_{r1} = concentration within the halo of the smaller crystal ; X = distance between the crystals ; A = cross-sectional area where the concentration spheres intersect [119]

3.8 Effect of US on electrodeposition

3.8.1 Effect of US on nucleation

Ultrasound agitation can affect the nucleation process and also the morphology of electrodeposited materials [69, 120-123]. It was previously shown that ultrasound agitation can affect the deposit surface due to pit formation in the deposited metal, caused by cavitation bubble collapse close to the electrode surface. However, the cavitation effects of ultrasound have also been shown to effect nucleation during deposition.

Floate et. al [121] investigated the effect of ultrasound on the morphology of cobalt deposited on a glassy carbon electrode with an ultrasound probe operating at 65.7 W cm^2 at a distance of 10 mm. The results from cyclic voltammetry, linear stripping voltammetry, chronoamperometry, and atomic force microscopy experiments indicated that instantaneous nucleation was favoured when using ultrasound. It was suggested that this was due to the stripping of poorly adhered nuclei from the substrate and also the enhancement growth of existing nuclei [121].

Ultrasound has also been shown to effect nucleation so that a finer grain structure is produced. The pulse reverse deposition of a Ni–Co/Al_2O_3 composite coating was carried out by Chang et. al [120] under silent and US conditions. When using US, the composite coating becomes uniform, compact and had finer grains as the effect of cavitation and acoustic streaming can interrupt crystal growth and form new nucleation sites. Alternatively, the high pressures associated with a cavitation bubble collapse would cause local super-cooling, decreasing the r_c of the nuclei, resulting in a promotion of the nucleation rate [120]. If nucleation rate becomes larger than crystal growth rate finer grain formation will occur.

Ultrasound had a different effect on nuclei formation during deposition of a nanocomposite coating of Co–W/MWCNTs onto a copper plate electrode, carried out in an ultrasound bath by Su et. al [123]. A large number of nano and micro nuclei were found to appear on the surface of the coating when using US. Despite this a more even surface coating was observed. Additionally, nodular structures of size 5-10 μm that were observed when using mechanical agitation were also observed when using US but with a size of 5-25 μm. When the US power was increased the nodular size became

more uneven. This illustrates the importance of the choice of US power in order to get the desired morphology of the deposit.

3.8.2 Other effects of US on electrodeposition

In addition to nucleation effects, US can also have a chemical effect. The energy from the disintegration of a cavitation bubble can result in the formation of free radicals [69]. An investigation by Mason, et. al [69] studied the effect of US frequencies on the surface modification of material which consisted of a blend of polypheylene oxide and polystyrene which resulted in both chemical and physical changes caused by the US. Physical effects were caused by bubble collapse and micro-jetting resulting in deposit erosion. A decrease in weight loss was observed as the US frequency was increased.

Chemical changes occurred due to the decomposition of water by the effect of cavitation bubble collapse. This caused oxidation on the surface of the polymeric material resulting in the formation of hydroxyl or carbonyl groups. The surface oxidation increased with increasing US frequency, however at frequencies >1000 kHz a sudden decrease in the cavitation energy arises, reducing both the physical and chemical effects and therefore practically no surface oxidation occurs. Studies prior to this have observed that mechanical effects were more significant at low frequencies (35 kHz) whereas only radical reactions is occurring at higher frequencies (>500 kHz) [124].

Another effect of US is its influence on the rate of electrodeposition, which has been shown to increase with the use of ultrasound in some cases [120, 125, 126]. Deposition rates have been observed to increase by 10% when using ultrasound during copper deposition [125] and even increases of 3-fold have been observed for nickel deposition when using ultrasound agitation compared to silent conditions [126]. The deposition rate of cobalt has also increased with the application of sonication, apart from when short probe-electrode distances were used which increased the ablative effect of ultrasound Floate et. al [121]. This demonstrates that the optimum values of the ultrasound parameters need to be established for each application in order to enhance the deposition process while avoiding or diminishing the negative effects of using US.

This chapter has explained the fundamentals of the electrodeposition process; including electrocrystallization, electrode potential measurement, mass transfer theory and the electrochemical techniques used to measure the mass transfer in electrochemical systems. The effects of ultrasound on the electrodeposition process have also been described.

To test whether US is a suitable from of agitation for the scale up of the Enface process, ultrasound was first applied to a lab-scale Enface system using a US probe. Ultrasound parameters were tested in order to achieve optimum conditions to achieve the best deposit patterns as well as enhanced mass transfer. These results were used to design a large scale ultrasound tank for pattern transfer onto A7 size substrates. This large-scale system was then used to investigate the scalability of the Enface process in terms of both the mass transfer and quality of deposit pattern features. A description of the apparatus that was used for these investigations and the details of experimental techniques used will now be explained.

Chapter 4. Experimental Systems

4 Experimental Systems

4.1 Vertical flow cell

Initially, experiments were carried out in a vertical electrochemical flow cell. It was designed and constructed for copper deposition onto 20 mm diameter substrates based on a flow system used previously for 10 mm diameter substrates [11, 20]. The new cell was used to illustrate the problems of scaling up the flow cell system by demonstrating the issues of depositing patterns onto larger substrates than previous flow cell studies [11, 20]. The mass transfer was also measured for comparison with the US Enface systems.

A schematic of the flow system is shown in figure 4.1 and a photograph of the flow cell and electrolyte tank is shown in figure 4.2. The system has an addition of a filter after the centrifugal pump and just before the flow cell. This has two functions; to filter out any copper that had been etched at the anode, and also to reduce and preferably prevent bubbles formed during pump start-up entering the vertical flow system. This is because large bubbles had previously been lodged between the electrodes causing hindrance to the deposition. [20].

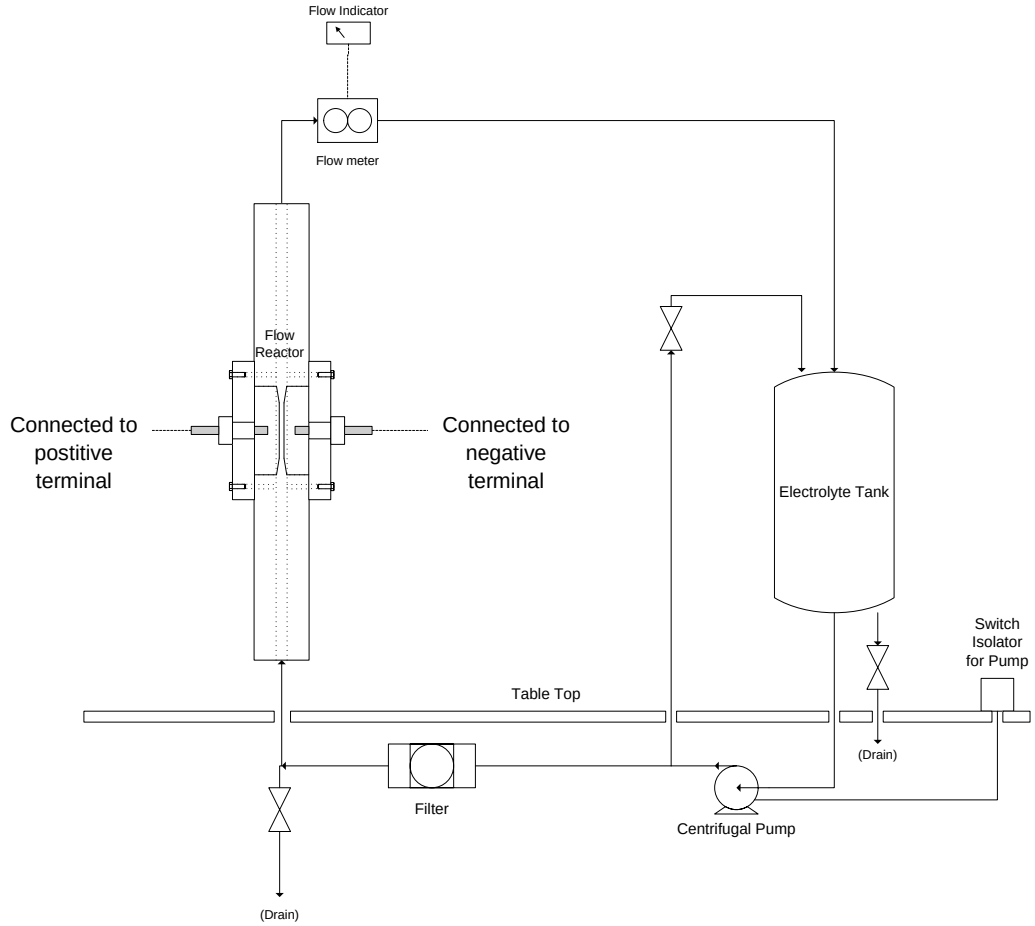

Figure 4.1 – Schematic of the flow system for the vertical flow cell

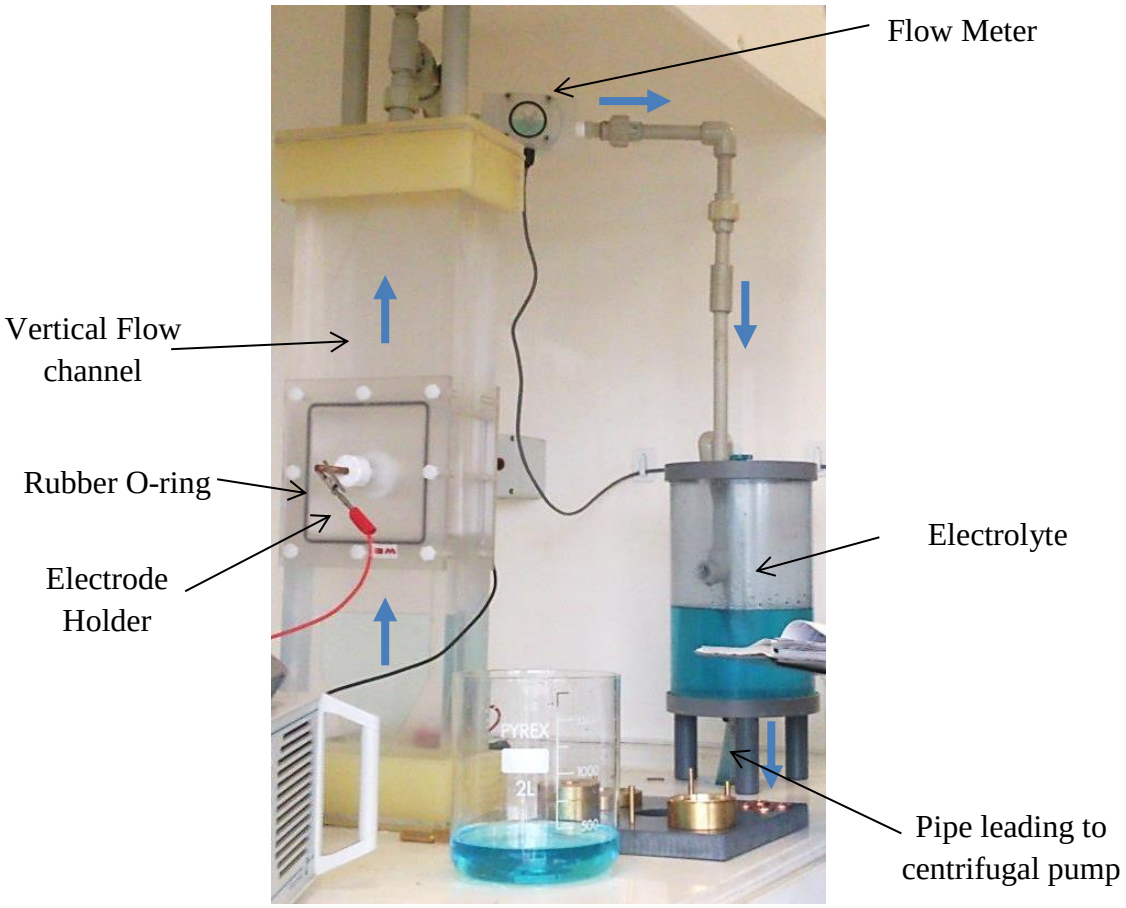

Figure 4.2 – Photo of the vertical electrochemical flow cell, with flow indicator and tank of electrolyte solution. Blue arrows indicate direction of electrolyte solution flow

The design of the Perspex electrode holders is shown in figures 4.3, used for both the anode and cathode. The electrode disc slots into a PTFE 'cup' which is then inserted into the Perspex electrode holder. The electrodes were 20 mm diameter polished copper discs with a surface area of 3.14 cm^2 and a thickness of 2 mm. Tools for loading the electrode discs were created in order to push the electrode discs into the PTFE 'cup'. The electrodes were slightly recessed in the holders, as this position gave the best results in terms of deposit uniformity and low roughness in previous deposition studies [20, 39]. Tools were also fabricated to load and unload the electrodes without anything coming into contact with the surface of the electrodes to prevent any damage to the deposits or resist.

A PTFE screw with a copper rod running through it and a beryllium copper alloy spring, pictured in figure 4.3, was screwed into the back of the holder. The spring allowed for a good electrical connection to the copper rod which the terminals were attached to, as shown in figure 4.2, and connected to a Thurlby Thander power supply.

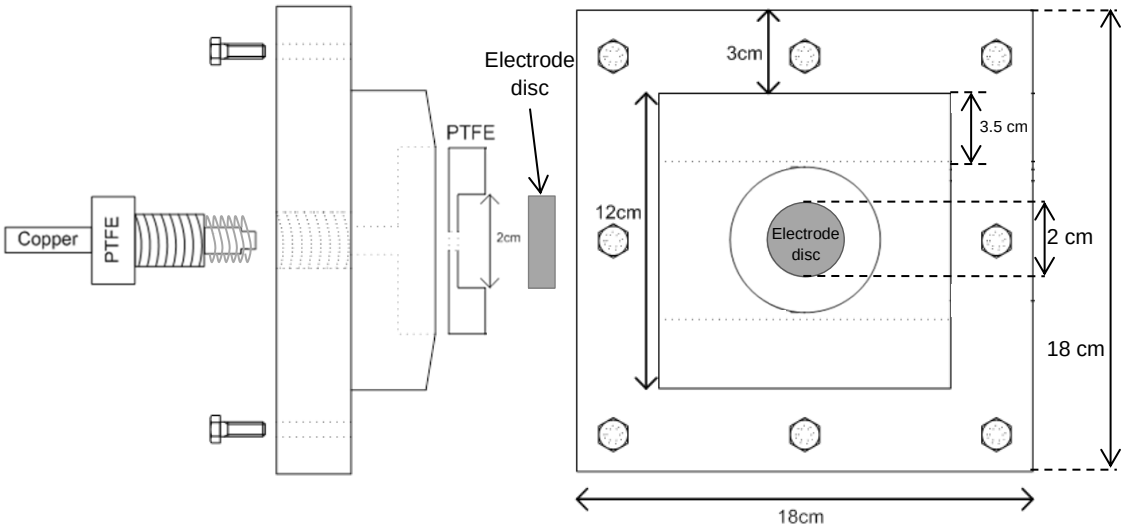

Figure 4.3 – Drawing of Electrode holder viewed from the side and the front, with electrical connection screw at the back of the electrode

Rubber O-rings were placed around both the copper rod and the entire holder, shown in figure 4.2. This sealed any gaps around the edges of the holders when they were screwed into place to prevent leakage through the back while solution is flowing through the flow channel. The design of the vertical flow channel, based on previous studies [11, 39], is shown in figure 4.4, with a total flow length of 58 cm, a width of 12 cm and a channel gap of 0.3 cm. This is much shorter and wider than the original flow cell used previously [11, 20, 39]. The channel width of 12 cm was used so that electrode holders could incorporate electrodes larger than 1 cm diameter. The length of the cell was designed so that forced convection flows were fully developed at the electrode surface, calculated using eq. (4.1).

$$\frac{L_e}{d_c} \approx 0.022Re \qquad (4.1)$$

For a maximum Re for laminar flow (2000) and a channel width (d_c) of 0.03 cm, the entry length (L_e) required is 13.2 cm. The flow cell in this study was approximately double this length to ensure that flows were fully developed, and conical entrances were incorporated to prevent eddy formation.

Figure 4.4 also shows how the electrode holders slot into the vertical channel. When the holders have been positioned and screwed into place, the chamfers on both holders narrow the flow channel so that the electrodes themselves are approximately 0.03 cm apart from each other. This is shown schematically in figure 4.5.

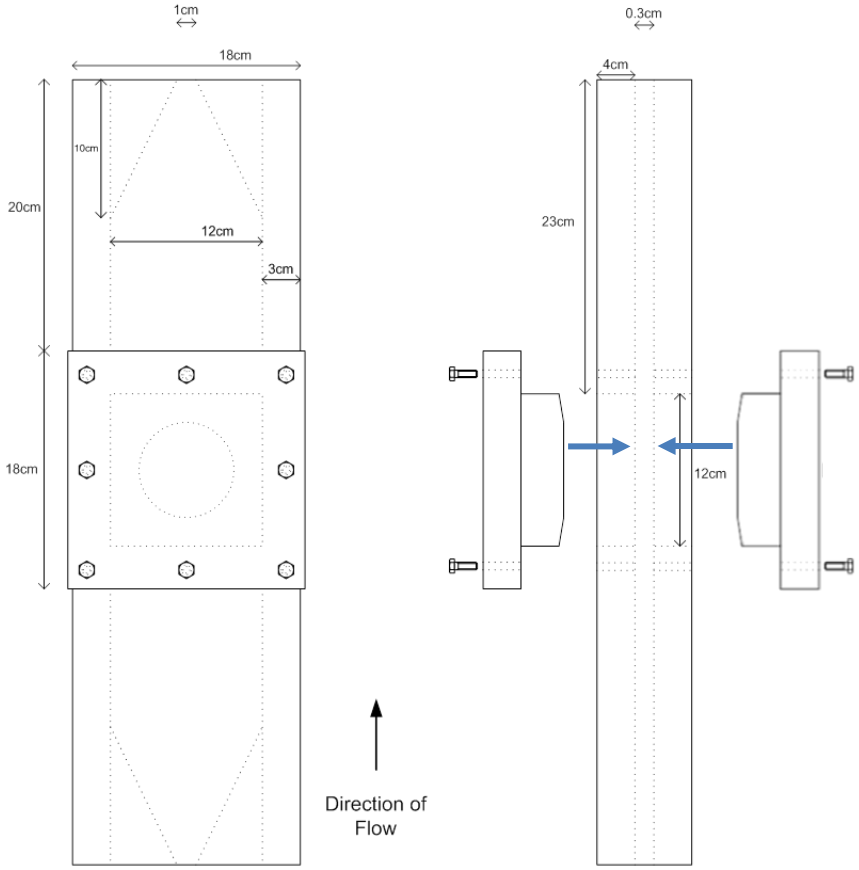

Figure 4.4 – Diagram of the vertical flow cell with a 0.3 cm wide flow channel showing how the electrode holders slot into the sides of the module so they face each other

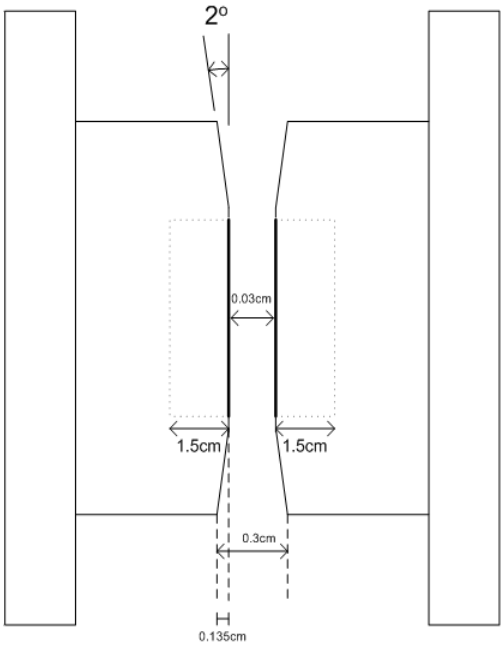

Figure 4.5 – Drawing of electrode holders when positioned within the vertical flow channel illustrating the angled chamfers which brings the flow channel gap from 0.3 cm to 0.03 cm

4.1.1 Electrode preparation

The 20 mm diameter copper disc cathodes were prepared by polishing with #2400 and #4000 SiC paper on a Struers polishing machine until a mirror-like finish was achieved. They were then rinsed with deionized water before being dried under a standard hair dryer. Deionized water was provided by a Purite Select Analyst 40 – L2G water purification dispenser system.

4.1.2 Tool fabrication

The same copper discs and surface preparation was used for the copper anode tools. These discs were then washed in acetone and transported to the cleanroom for the photolithography of a patterned resist on the surface, carried out as follows.

1. Copper discs were dried thoroughly with a nitrogen gun
2. AZ-5214E liquid photoresist was dropped onto the disc surface using a pipette and the disc was spun at 2000 rpm for 40s distributing the photoresist evenly across the surface using the EMS 5000 Spin Coater shown in fig. 4.6(a)
3. Discs were baked at 90 ^{o}C for 10 mins in a Gallenkamp oven
4. A chrome mask with a linear pattern of 100 μm parallel lines was placed over the top of the disc in the UV mask aligner, shown in fig. 4.6(b), and exposed to 3 mW/cm^2 of UV light for 45 s
5. The disc was then submerged in AZ-326 developing solution for 70 s, rinsed in deionized water and then dried thoroughly with a nitrogen gun. A pattern of 100 μm wide lines of exposed copper with 500 μm spacing was therefore fabricated on the copper disc, which were then stored under dark conditions

After the surface preparation and careful loading of the electrodes into their holders, the holders were then screwed into place and the flow system was operated for 5 minutes at approximately 60 cm^3/s in order to flush the system of air before any current was applied. The flowrate was then adjusted to 40 cm^3/s for all experiments, corresponding to a flow velocity of approximately 14 cm/s at the electrode surface.

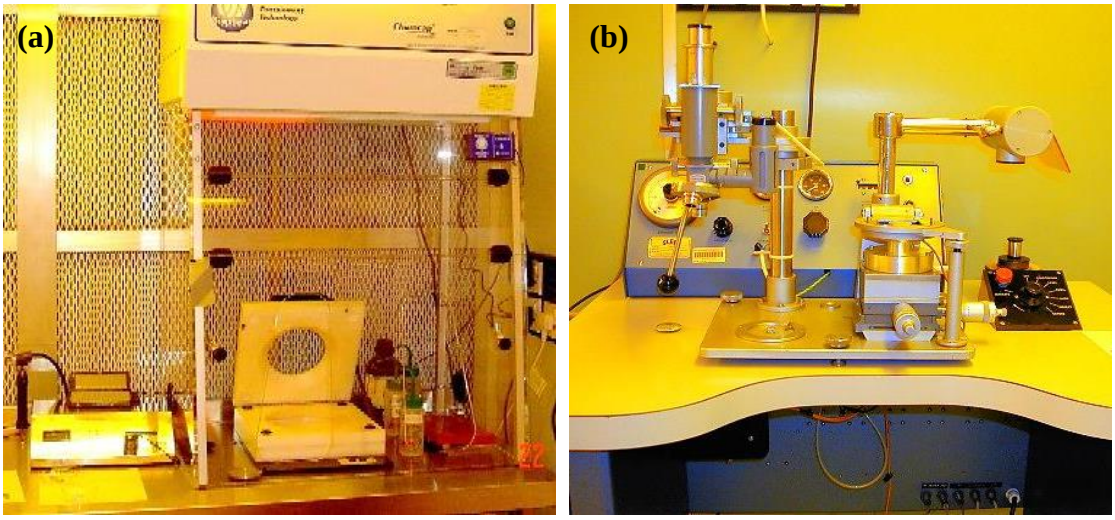

Figure 4.6 – (a) EMS 5000 Spin Coater in cleanroom used for spinning liquid photoresist onto the copper discs. (b) SLEE Co. Mask Aligner used for UV light exposure for photolithography of liquid resist on the copper discs

4.1.3 Experimental procedure for mass transfer experiments

First, limiting current experiments were carried out using a 2-electrode system which consisted of a fully exposed copper anode and copper disc cathode. Different current densities were applied using the power supply, ranging from 5 to 170 mA/cm^2. A multimeter was used to measure the cell potential 30 s after each current was applied to allow the system to reach steady-state. Three experimental repeats were carried out.

4.1.4 Experimental procedure for deposition experiments

The initial deposition experiments were carried out at 46 mA/cm^2 for 300 s using a fully exposed copper anode and a copper disc cathode, both with a surface area of 3.14 cm^2. DC deposition experiments were then carried out using an anode tool with linear patterns with 28 lines, each with a width of 100 μm. The exposed anode area was 0.39 cm^2, measured using a confocal optical microscope were 46 mA/cm^2 and 94 mA/cm^2, for plating times of 300 s and 147 s respectively. This would plate up Cu metal to a thickness of 5 μm for the nominal current efficiency of 100% based on the anode area.

4.2 Small-scale laboratory cell

A diagram of the cell used for the lab-scale experiments with the US probe is shown in figure 4.7. This consists of a 500 ml cylindrical PVC cell with two polished electrode discs 10 mm in diameter acting as a cathode and anode, facing each other separated by an electrode gap. Screw gauges on each electrode holder could be used to alter the distance between the electrodes from 0.3 mm to 10 mm.

A *SONICS Vibra-Cell VC505 Processor* connected to a 20 kHz US probe with a 13 mm diameter titanium alloy tip was used, operated at US powers of 9 to 29 W/cm^2, the power calibration is shown in Appendix A. The probe was placed above the gap in a side-on orientation (Fig. 2.9b), and the d_p could be varied from 15 - 30 mm. The probe tip was submerged into the solution by 4 mm for every probe-electrode distance.

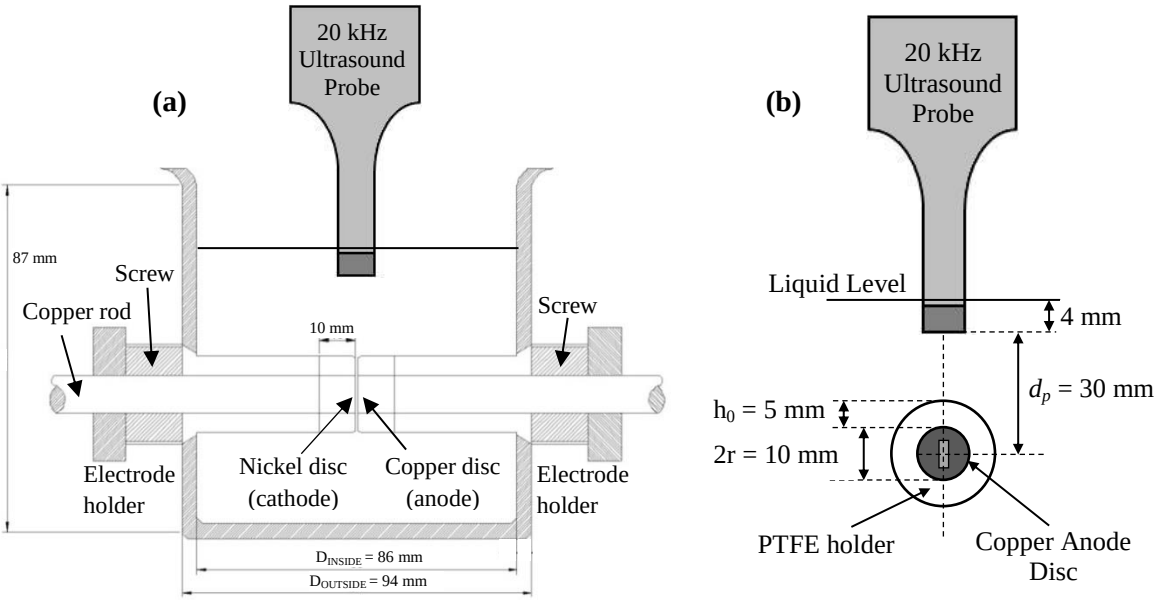

Figure 4.7 - (a) Side-view of experimental set-up of the electrochemical cell used in this work. (b) Frontal-view of anode surface; dark grey circle = Masked area; light grey rectangle = Area of exposed copper [106]

Electrode surfaces were prepared using the following procedure:

1. Wash with deionised water
2. Polish at 250 rpm for 20 seconds with #2400, then #4000 grade SiC sandpaper, corresponding to grain sizes of 9 and 3 μm respectively. (If polishing did not remove previous deposit, then #1200 grade (grain size of 15.3 μm) SiC sandpaper was used first for 10 seconds, then polished with #2400 and #4000 grade)
3. Wash with deionised water again

4.2.1 Experimental procedure for mass transfer experiments

A three electrode system was used for the limiting current experiments using copper discs for both the anode and cathode and a copper wire reference electrode wrapped in PTFE tape with only the tip exposed, placed approximately 0.5 cm from the cathode surface, above and to the side of the electrode gap. Copper has been proven to be a stable reference electrode in acidified $CuSO_4$ electrolytes in previous polarisation experiments [39, 127]. 0.1 M $CuSO_4$ in 0.1 M H_2SO_4 was used as the electrolyte solution used as the electrolyte solution. The pH was 1.0 (±0.05) and conductivity 59.8 mS/cm (±0.05 mS/cm), measured using a Mettler-Toledo S47 SevenMulti^{TM} dual pH and conductivity meter measured at room temperature (18-22 ^{o}C).

For the silent experiments (where there is no US agitation), linear potential scans were applied using an *Eco Chemie Autolab Potentiostat (PGSTAT30)* and *NOVA 1.7* software was used to input scan settings and data recording. The scans were carried out from the OCP to -1V at a scan rate of 5 mV/s. For the ultrasound agitation experiments, all linear potential scans scans were carried out at a scan rate of 5 mV/s from the OCP (after probe switched on) to -0.9V. The probe was then removed, solution was emptied, and the probe and electrodes were prepared for the next experiment. The following washing procedure was carried out for the probe tip for each experiment.

1. Washed with deionised water
2. Wiped with paper towel until deposit from previous experiment was removed
3. If deposit could not be removed by hand, the probe was placed in a beaker of distilled water and switched on for 10 seconds, which removed deposit from the probe surface.
4. Washed with deionised water and then dried with paper towel

4.2.2 Ohmic Potential Drop Experiments

Measurements of the ohmic resistance between the copper wire reference and the working electrode (ohmic drop) were carried out under silent conditions. The ohmic potential drop was obtained from impedance experiments. The impedance data was only used to acquire the value of ohmic drop within the cell.

The cell was set to an electrode gap of 10 mm and filled with 0.1 M $CuSO_4$. An impedence experiment under silent conditions was completed for 4 different potentials; -0.1V, -0.25V, -0.5V and -1V. The ohmic drop was obtained for each potential, this data was then applied to the data from the silent linear scans obtained from the experiment explained above to produce current-potential plots with ohmic drop compensated. The calculation procedure for this is shown in Appendix B.

4.2.3 Experimental procedure for deposition experiments

The cell shown in figure 4.7 was also used to deposit copper patterns. These were carried out as a two electrode system, with a 10 mm diameter nickel cathode and 10 mm copper anode tool, as shown in figure 4.7a. The electrodes were polished with SiC paper using the same preparation procedure described above. An electrolyte solution of 0.1M $CuSO_4$ solution was used which had a pH of 4.3 (±0.05) and a conductivity of 8.1 mS/cm (±0.05 mS/cm).

4.2.4 Tool Fabrication

The copper anode tools were prepared by simply masking them with a non-conductive tape (Kapton tape), which had a thickness of 60-65 μm. A surgical blade was then used to cut out a 1 x 5 mm rectangle from the tape with a tolerance of ±0.075 mm in width. The area of exposed copper, shown in figure 4.8, was the pattern that was desired to be transferred to the nickel substrate. The anode tool was rinsed with deionized water and screwed into the electrode holder.

The electrodes were then positioned at a distance of 0.3 mm from each other using a spacer, ensuring that the rectangular pattern was positioned in the upright position, shown in figure 4.7b. The 20 kHz ultrasound probe was positioned 30 mm above the electrode gap and was operated at a power of 9 W/cm^2.

Four deposition modes were tested; (1) Direct current deposition under silent conditions, (2) Direct current deposition under constant wave US, (3) Long current pulses under silent conditions, (4) Long current pulses combined with pulsed US.

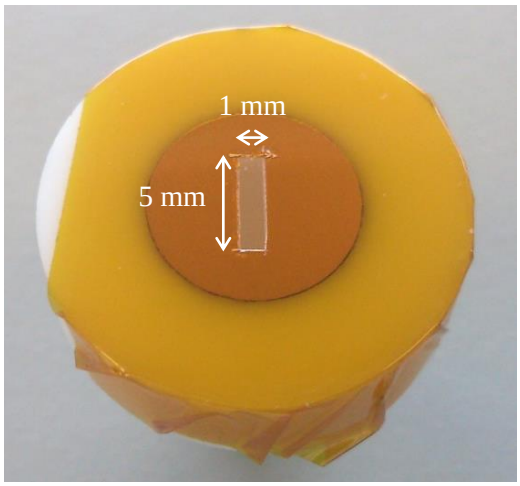

Figure 4.8 – Photograph of 10 mm diameter copper anode tool, masked with non-conductive tape with a 1 x 5 mm linear feature of exposed copper surface

The pattern transfer deposition experiments were carried out by applying direct current (DC) galvanostatically using an *Eco Chemie Autolab Potentiostat (PGSTAT30)* with the working electrode terminal connected to the nickel substrate and both the counter and reference terminals connected to the copper tool. *NOVA 1.7* software was used to input the settings for the current plating experiments and also recorded the potential response during plating. A chronopotentiometry procedure was set up in the *NOVA 1.7* software to apply the desired direct current; these DC experiments were carried out either under silent conditions or with constantly applied US agitation.

When applying long current pulses an automatic procedure was set-up in *NOVA* which involved alternating chronopotentiometry procedures with periods where no current was applied, therefore creating a series of long current pulses. For these experiments the current was applied for 150 s, meaning that plating proceeded under (virtually) DC conditions. When plating with 50% of the limiting current (i_{Lim}) and 75% i_{Lim}, three chronopotentiometry procedures were applied, each with a time of 200s and 150s respectively, and both with a current off-time of 25 s. When combining long current pulses with ultrasonic agitation, the ultrasound source was switched on and off manually and applied for 10 s at the start of each off-time. An example of the combined pulse sequence for current and US is shown in figure 4.9.

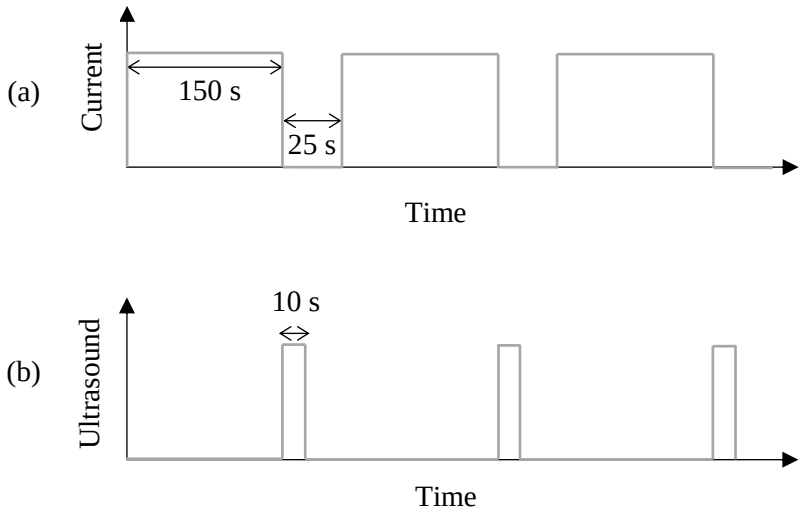

Figure 4.9 - Current (a) and ultrasound (b) pulse waves used for pulsed ultrasound electrodeposition in small-scale cell. The off-time is inserted for replenishment of reactants near the electrode surface. When US is used, this replenishment should occur faster than solely diffusion controlled conditions. [67]

4.2.5 Current distribution modelling of the small-scale cell

In order to understand the issues arising due to overpotential changes induced by the inclusion of a metallic probe, current distribution within the lab-scale cell was also studied. A primary current distribution model of copper electrodeposition was carried out with ElSyca software, (ElSy, SA) using a two dimensional model of the cell in figure 4.7a. The surface of the probe was modelled as a second cathode. The software was used to analyse the potential and current distribution for 0.5 to 0.15 cm electrode gaps and a probe distances of 1.5 to 3 cm.

A uniform concentration gradient of ions in the solution and a constant electrolyte conductivity was assume for the model calculation. The equation for the flux of an ionic species *k* (N_k) was used, shown in equation (4.2).

$$N_k = -D_k \nabla c_k + c_k v - z_k u_k F c_k \nabla \phi \qquad (4.2)$$

where u_k is the mobility of species *k* ($cm^2 mol/J.s$) and $\nabla\phi$ is the potential gradient (V). The accumulation of species *k* can be expressed by equation 4.3.

$$\frac{\partial c_k}{\partial t} = -\nabla . N_k + R_k \quad (4.3)$$

where R_k is the production rate of species k (mol/s). Substituting equation 4.2 into equation 4.3 gives the mass balance equation shown in equation (4.4).

$$\frac{\partial c_k}{\partial t} + v.\nabla c_k = z_k F \nabla.(u_k c_k \nabla\phi) + \nabla(D_k \nabla c_k),\ k = 1....n \quad (4.4)$$

The velocity of an incompressible fluid flow in electrochemical systems is described by the well-known Navier-Stokes equation, shown in equation 4.5, with constant density and viscosity

$$\nabla . v = 0 \quad (4.5)$$

The Poisson equation, shown in equation 4.6, describes the electric potential (Φ), which can be replaced with the electroneutrality expression in equation 4.7 as the bulk electrolyte solution is electrically neutral.

$$\nabla^2\phi = -\frac{F}{\epsilon}\sum_k^n z_k c_k \quad (4.6)$$

$$\sum_k^n z_k c_k = 0 \quad (4.7)$$

where ϵ is the dielectric constant of the solution (Farad/m).

The current density (i) can then be described by equation 4.8. If equation 4.3 is substituted into N_k is substituted by equation 4.2, then the current density can be expressed in terms of diffusion, convection and migration. Taking the conductivity (σ) into account (equation 4.7), along with the condition of electroneutrality (equation 4.9), then the current density can be expressed by equation 4.10.

$$i = F\sum_k^n z_k N_k \quad (4.8)$$

$$\sigma = F^2 \sum_k^n z_k u_k c_k \quad (4.9)$$

$$i = -\sigma\nabla\phi - F\sum_k^n z_k D_k \nabla c_k \quad (4.10)$$

Equation 4.4 can be omitted for steady-state conditions. If there is a continuous stirring of the solution, it can be assumed that convection is dominant and concentration gradients can also be omitted. Equation 4 can therefore be simplified to equation 4.11, the Laplace equation therefore the current density can be expressed as equation 4.12.

$$\sigma \nabla^2 \phi = 0 \tag{4.11}$$

$$i = -\sigma \nabla \phi \tag{4.12}$$

ElSyca software is used to solve this model using the Boundary Element Method. The boundary conditions stated in equations 4.13 and 4.14 state that the current density at each point at the insulating walls of the cell and the top surface of the solution is zero. This means that the current flows to the electrodes only; in this case the anode and cathode as well as the US probe placed in solution.

$$i_y = i \,.\, 1_y = -\sigma \, \nabla \phi \,.\, 1_y = -\sigma \frac{\partial \phi}{\partial y} \tag{4.13}$$

$$\frac{\partial \phi}{\partial y} = 0 \tag{4.14}$$

where *y* denotes the normal distance from the surface.

A constant temperature of 293 K was used and the electrolyte conductivity used was 59.8 mS/cm, taken from a measurement of the solution of 0.1 M $CuSO_4$ in 0.1 M H_2SO_4 with a conductivity probe during experimentation. The dimensions of the US probe were modelled as a rectangle with a width and of height 13 mm and 4 mm respectively, placed above the electrode gap. 30 elements were used on both the cathode and anode, 120 elements were used on the surface of the probe facing the electrodes and 30 elements on the side of the probe. This was the same number of elements that was used in previous simulations of this electrochemical cell, a higher number of elements would cause too small mesh spacing and would therefore lead to a non-convergence calculation [128]. The convergence of the current density calculation was achieved when the current residual reached a value of < 0.001 mA/cm^2 and the calculation was completed within 6 iterations (at maximum number of iterations of 20).

4.3 Large-scale ultrasound tank cell

As mentioned, pattern transfer experiments with A7 size substrates (105 x 74 mm) were carried out in an 18 L tank. This tank size is 50% (by volume) of a standard plating tank in industry (40 L). Electrode holders were specially designed to hold the large scale A7 size substrates and tools together and opposite each with an inter-electrode gap of either 0.3 mm or 1.5 mm maintained uniformly across the electrode plates. Figure 4.10 shows a diagram of the electrode holders which consist of two polyvinyl chloride (PVC) blocks, one for each electrode, with a recess for a 1 mm thick A7 size electrode plate to sit in. These can be screwed together so they face each other using the plastic bolts in each corner.

For deposition experiments, electrode spacers made from 0.3 mm thick Polytetrafluoroethylene (PTFE) sheet were placed in each corner ensuring there is gap of 0.3 mm between the electrodes and also holds the electrode in its recess. The curvature of the plates dictated that a spacer had to be placed in the centre to maintain the electrode gap across the electrode surface and also to prevent the plates to touch resulting in a short circuit.

The measurement of the electrode gap at various locations was carried out by applying silicone sealant at various locations across the electrode plate, as shown in figure 4.11a. The spacers were positioned and the electrode holders were screwed together. Once the silicone had dried, the holders were taken apart. A confocal optical microscope was used to measure the thickness at various locations on the plate shown in figure 4.11b. For mass transfer experiments, an inter-electrode gap of 1.5 mm was used by stacking five 0.3 mm PTFE sheets on top of each other in the same locations.

The electrical connection was made from the back of the holder via a copper block inset into the PVC holder. A screw hole was cut through the top of the holder and into the copper block so that a copper rod could be screwed into the top allowing for an electrical connection to be attached to the top of the rod. The electrode plate is pressed tightly against the copper block when the holders are screwed together ensuring that there is a good electrical connection. The copper rod was covered in electrical insulation to prevent any exposure to the electrolyte solution. A Perspex rod was attached to the other side of the holder to the copper rod for extra support. These rods were fastened to a support bar so the electrode holder could be suspended securely. Figure 4.12 shows a photo of the electrode holder screwed together with support rods and support block.

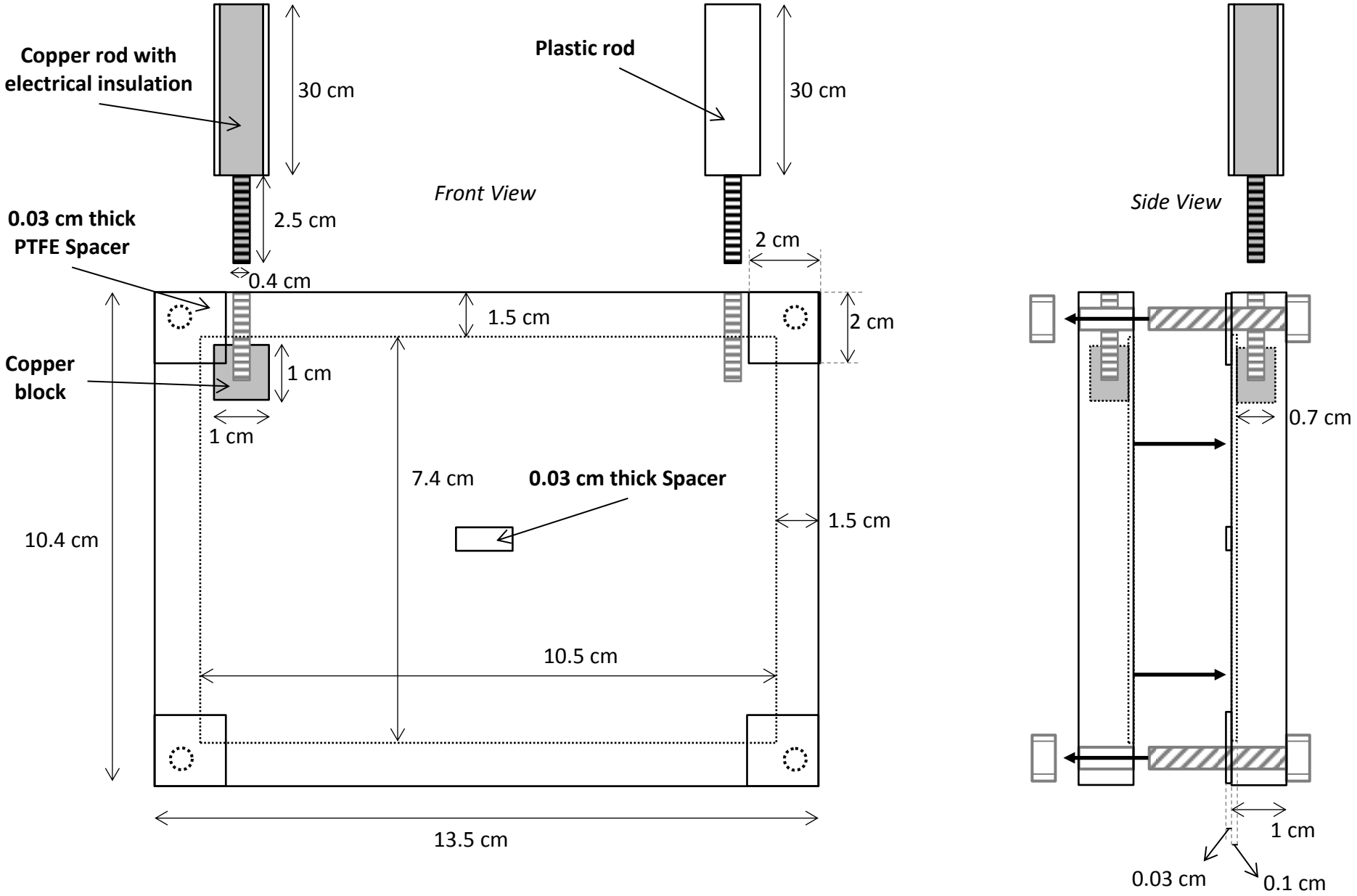

Figure 4.10 - Diagram of Enface Electrode Holder Design for A7 size electrode plates

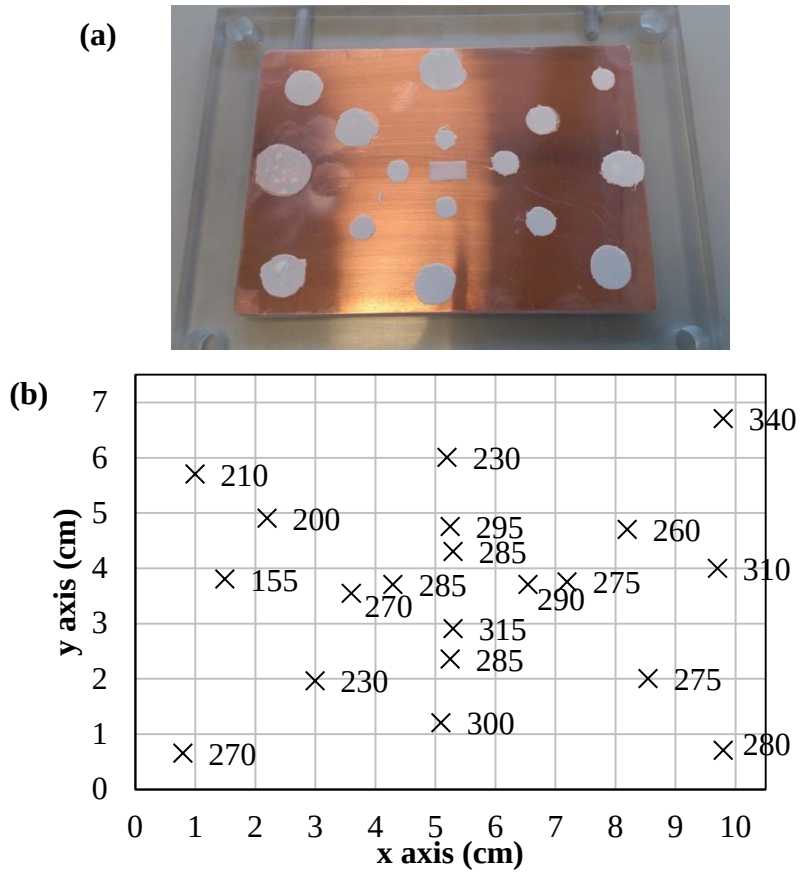

Figure 4.11 - Measurement of the electrode gaps at different locations across the plate when two copper plates are screwed together within the electrode holders with spacers placed in–between the plates, (a) Copper plate with silicone sealant applied at various locations on the electrode surface, (b) Thickness of silicone on the copper plate measured using an optical microscope.

Figure 4.12 – Photo of the Enface electrode holder for A7 size substrates with support rods and support block

The photos in figure 4.13a shows the ultrasound tank (left) and the generator with the control panel (right). Figure 4.13b shows the placement of the transducers, with 5 transducers on each side-wall and 4 at the bottom. They operate at a fixed frequency of 30 kHz. The amplitude of the transducers can be varied via control of the ultrasound generators to vary the ultrasound power delivered to the solution in the tank between approximately 30 to 145 W/L, the US power calibration procedure is shown in the appendix. There are 3 ultrasonic generators; each one controls a group of transducers on one wall of the tank. All three generators were used for all the plating experiments.

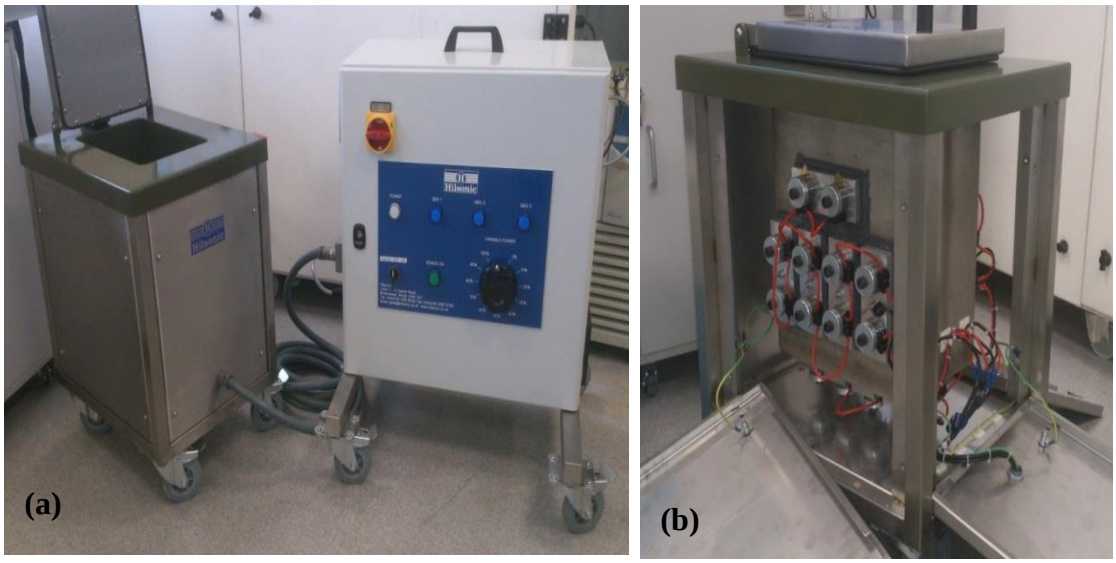

Figure 4.13 – Photo of 18 L ultrasonic tank, (a) Ultrasonic tank (left) connected to ultrasonic generators with control panel (right), (b) Ultrasonic tank with outer protective walls removed to display placement of ultrasound transducers, 5 on two of the side-walls and 4 at the bottom.

The electrode holder was submerged within the 18 L ultrasound tank constructed by *Hilsonic*, the design of which is described in figure 4.14, showing the placement of the holder. There is a higher intensity of stirring at distances less than 3 mm from the ultrasonic source. In this case the walls were attached to transducers. If the electrodes are placed within this region the agitation will not be uniform across the plate, therefore the holder is placed at distances further than 30 mm from the walls of the tank to get the most uniform agitation occurring across the electrode plates. There is also a lip on the

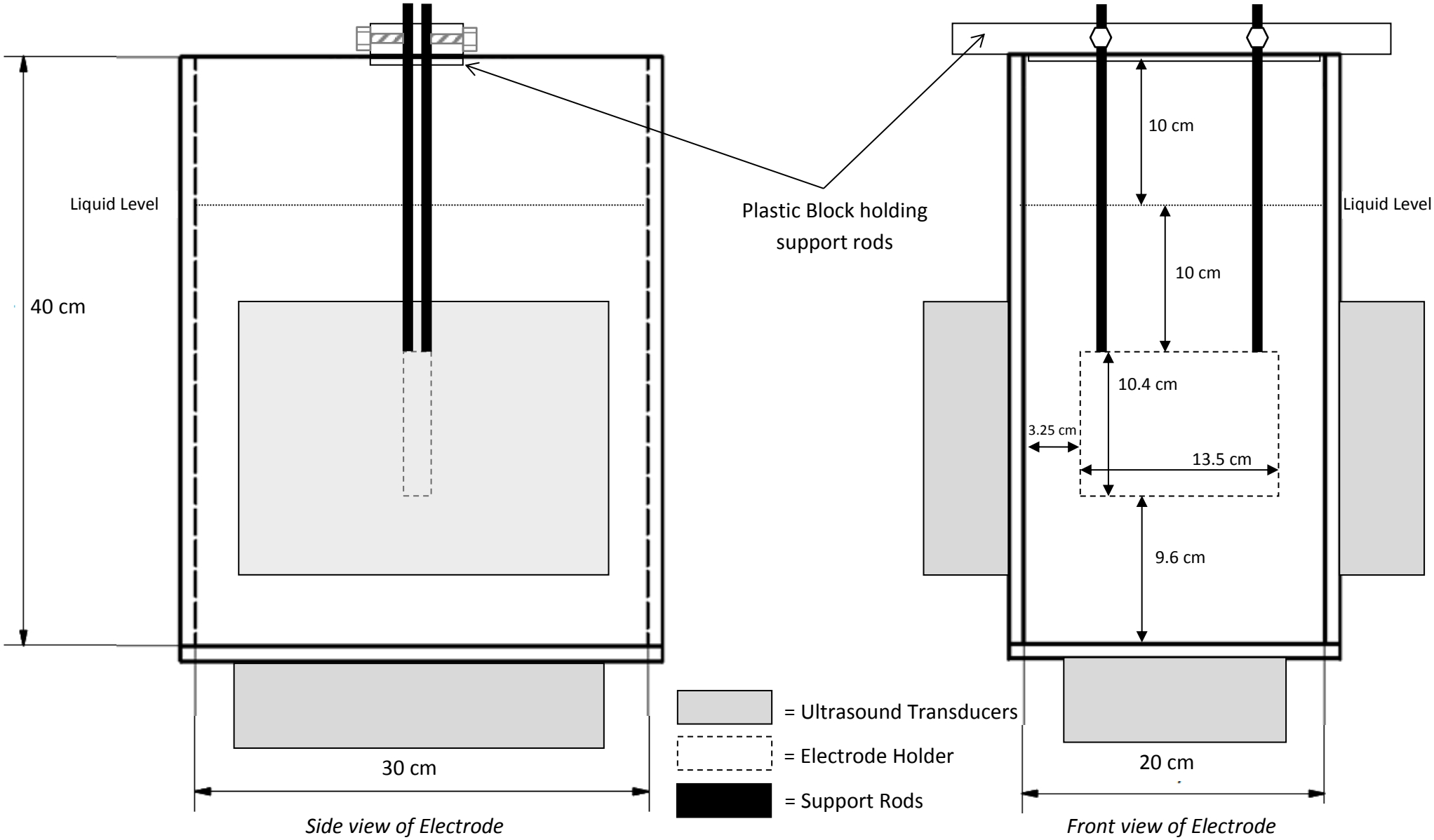

Figure 4.14 - Diagram of Enface Ultrasonic Tank showing position of ultrasonic transducers and placement of Electrode Holder

Perspex bar to prevent any movement of the electrode holder towards the side walls. The tank walls were coated in a layer of hard enamel to prevent electrolyte solution coming into contact with the steel tank walls. Figure 4.14 also shows the locations of the ultrasound transducers around the walls of the tank so that when the electrode holder is in position the transducers are located around the sides of the holder.

Ultrasound could either be applied as a continuous wave (CW) or in pulsed ultrasound mode which allowed the agitation to be applied in short bursts. The pulsed regime involved switching the generators on and off in a sequence with a 10 second on-time and 5 second off-time automatically.

4.3.1 Mass transfer experiments

Mass transfer within the tank under US conditions was estimated using limiting current experiments. Due to the size of the electrodes as well as the proximity of anode and cathode, potentiostatic experiments were not possible. Therefore, a two-electrode DC, galvanostatic method for limiting current measurement was employed. In addition, the large size of the electrode could lead to varying limiting current at different locations.

A tool was fabricated in order to carry out limiting current experiments in the ultrasound tank. It was specially designed so that the limiting current could be measured at different places across the electrode plate. The tool is made from a 1 mm thick Perspex sheet with 10 mm x 10 mm squares cut out from it where copper squares can be slotted into. The squares are in the same position as those for the spray resist tool. A diagram of the tool is shown in figure 4.15.

The copper squares could be connected up individually to the electrical connection at the back of the tool via a copper foil which was placed behind the Perspex sheet when positioned into the electrode holder. Experiments were carried out with the square in the corner at position B and in square in the centre at position F only. Using this arrangement, current only flowed to a specific location and it was therefore enabled measurement of the mass transfer across the plate at a particular location on the substrate.

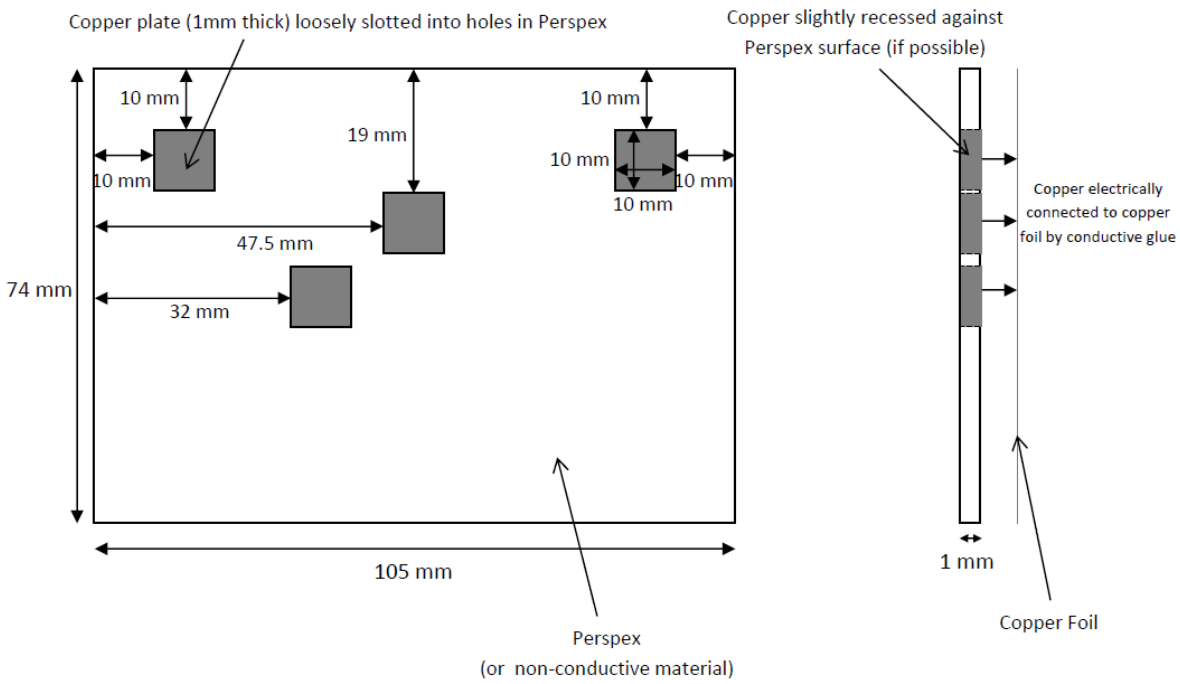

Figure 4.15 – Diagram of the tool used for limiting current experiments in the ultrasound tank with the A7 size substrates

Before each experiment the copper square was polished with #1200, #2400 and #4000 grit SiC paper on a *Struers polishing machine* and rinsed with deionized water. The copper square was then dried with a nitrogen gun and then pushed into the Perspex sheet which was then positioned into the PVC electrode holder. An A7 copper plate was polished and prepared with the same procedure as for the deposition experiments and placed into the opposite holder. Five spacers with a thickness of 0.3 mm on top of each other in each corner and in the centre to create an electrode gap of 1.5 mm and the electrode holders were screwed together and submerged into a solution of 0.1 M $CuSO_4$ with 0.1 M H_2SO_4.

The terminals of the *Thurlby Thander* power supply was connected up so that the copper square was the anode the copper plate was the cathode. Current densities between 10 and 140 mA/cm^2 were applied for 30 seconds and the cell potential was measured using a multimeter. Experiments were carried out with all three generators operating under continuous wave conditions with ultrasound powers of 30, 40 and 60 W/L and each experiment was repeated three times.

4.3.2 Pattern transfer experiments

Two different sets of tools were manufactured to deposit pattern features. The first set was used to transfer mm-scale patterns, which had 10 x 10 mm size exposed areas, created using spray photoresist. The second set was used to transfer linear μm-scale sized features which were manufactured using standard dry photolithography.

Both the substrate and tools for the large scale plating experiments in the 18 L ultrasound tank were made from 99.99% purity high conductivity oxygen-free copper plates (Advent), cut into A7 size rectangles. The substrate plates were washed thoroughly with diluted Decon 90 solution and polished by hand with #1200, #2400 and #4000 grit SiC paper. They were then rinsed with deionized water and dried thoroughly using a nitrogen gun. The fabrication procedures for the two different tools are described as follows.

Preparation of Enface A7 Enface Spray Photoresist Tool:

1. Copper plate was rinsed with deionized water and polished with #1200, #2400 and #4000 grit SiC paper until a mirror-like finish was achieved
2. Rinsed thoroughly with deionized water
3. Dried thoroughly with nitrogen gun
4. Copper tape was used to mask areas of the copper plate surface with large squares of 10 x 10 mm at locations A to H, shown in figure 4.16
5. Electrolube Positive Photoresist was sprayed over the entire surface
6. Photoresist was dried using a hair dryer for 5 – 10 minutes
7. Tape was carefully removed from the plate
8. Plate was baked in an oven at 50^{o} for 20 minutes
9. Any spray photoresist that remained within the square areas where there should be exposed copper surface was selectively dissolved with acetone using a cotton bud stick
10. The plate was then thoroughly rinsed with deionized
11. Dried thoroughly with a nitrogen gun
12. Stored within a dark area until it was ready for use

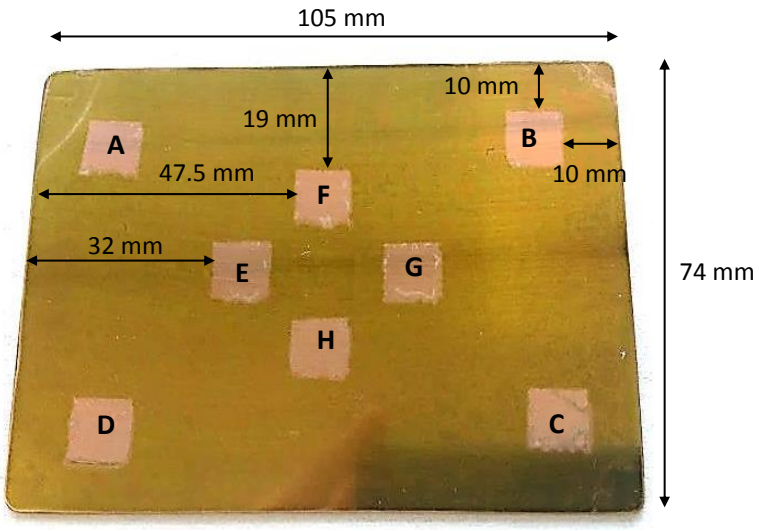

Figure 4.16 – Photo of Spray resist tool with 8 squares of exposed copper squares of dimension 10 mm x 10 mm

Dry resist tool fabrication:

1. Copper surface was wiped with isopropanol

2. Dried thoroughly with a nitrogen gun

3. Lamination of a 35 μm layer of *Laminar E9230 Dry Film Photoresist* (Eternal Chemical Co. Ltd) onto the copper surface with at 110 ^{o}C using the laminator shown in figure 4.17

4. A photomask of the desired line pattern, shown in figure 4.18(a) was placed over the resist layer which was then exposed to UV light for 15s in the UV exposure unit shown in figure 4.17

5. Developing solution was prepared by diluting 23 ml of *Chestech Developer* (Trimite Technologies Ltd) developing solution with 980 ml of deionized water and heating to 30 ^{o}C

6. The substrate was submerged developing solution for 13 minutes agitating the solution by hand every 30 seconds to assist the developing procedure

7. Rinsed thoroughly with deionized water

8. Dried thoroughly with nitrogen gun. An optical microscope image of the developed photoresist pattern is shown in figure 4.18(b), and a photo of the tool in figure 4.19.

9. Stored under a dark environment until ready for use

Figure 4.17 – Equipment used for dry photolithography with a lamination device (left) for applying the photoresist and a UV light box (right) for exposing the photoresist to ultraviolet light through a photomask

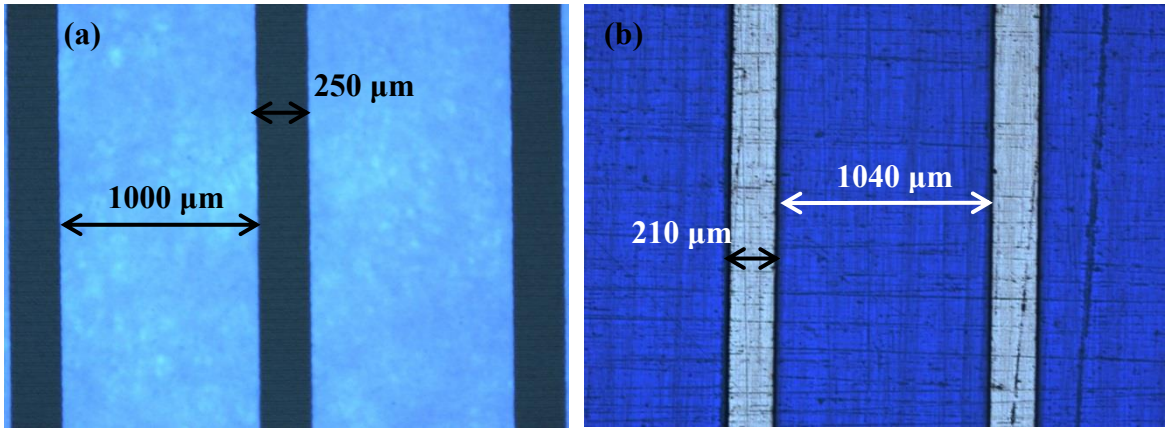

Figure 4.18 – Optical microscope images of (a) photomask and the (b) developed photoresist pattern on a polished copper plate

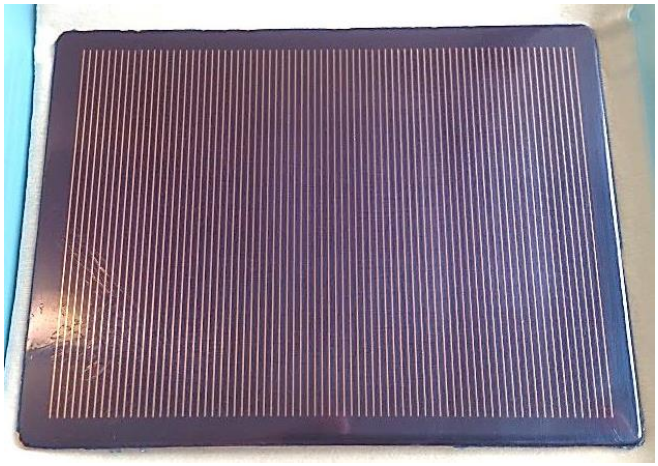

Figure 4.19 – Photo of A7 size dry resist tool with linear pattern features

4.3.3 Experimental procedure for deposition experiments in US tank

For each pattern deposition experiments, the A7 size copper substrates were washed with diluted Decon 90 solution and polished with #1200, #2400 and #4000 grit SiC paper until a mirror-like finish was achieved. The plates were then dried thoroughly using a nitrogen gun. They were then placed in the electrode holder and the copper rods were screwed into the top. The electrical connection from the rod to the plate was checked with a multimeter before positioning the electrode spacers and screwing both the holders together. After the electrodes were clamped together with the spacers, a multimeter was connected between the copper rods to ensure that the plates weren't electrically in-contact with each other. The Perspex support rods were then screwed into the top of the holder and the Perspex support bar was positioned over the support rods to the desired height and fastened into position with screws.

The ultrasound tank was filled with 18 L of 0.1 M $CuSO_4$ solution, the ultrasound generators were then switched on at 30 W/L for 5 minutes to let the ultrasonic tranducers stabilize. The electrode holder was then lowered slowly into the solution, ensuring that no air got trapped within the inter-electrode gap. The terminals of the *Thurlby Thandar* power supply were connected to the anode tool and the cathode substrate. A multimeter was connected between the connection rods to monitor the cell potential during the plating.

For the plating experiments, all three ultrasound generators were used and were either operated as a continuous wave (CUS) or pulsed ultrasound (PUS). When operating in CUS mode, ultrasound powers of 30, 40 or 60 W/L was used throughout the plating period.

4.3.3.1 Deposition experiments of square mm-scale features

Each CUS plating experiment was carried out under DC conditions with a plating time of 677 seconds at a current density of 20 mA/cm^2. This would achieve a nominal deposit thickness of 5.0 μm based on the anode area. A ruler was used to measure the size of the exposed copper square features; the total exposed anode area (A_a) of each tool was 8 cm^2. This area was also used to calculate the value of current to apply in order to apply a current density of 20 mA/cm^2. A current of 160 mA was therefore applied for each experiment.

When using PUS, 40 W/L of ultrasound power was used with an on-time of 10 seconds and an off-time of 5 seconds. A current density of 20 mA/cm^2 was used for each pulse which was applied by switching the current on and off manually using the power supply, with an off-time of 10 seconds and an on-time of 5 seconds. The combined current and ultrasound pulse is described in figure 4.20, which was repeated for 34 minutes. The total current on-time for the PUS experiments was the same as for the plating time used for the CUS experiments of 677 s, to achieve the same nominal thickness based on the anode area.

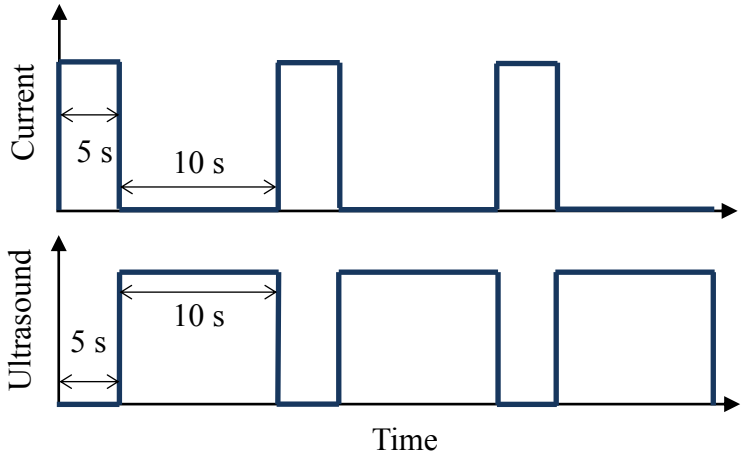

Figure 4.20 – Current and ultrasound pulse waves used for pulsed ultrasound electrodeposition in the ultrasound tank with A7 size substrates

After plating was complete, the ultrasound generators were switched off and the electrode holder was removed from the bath and immediately placed into a deionized water rinse bath. The electrode holder was then dismantled by removing the screws and the substrate was removed using a thin metal piece to push it out of its recess. The patterned substrate was rinsed thoroughly with deionized water and then dried thoroughly with a nitrogen gun.

The total surface area of deposit features on the cathode surface (A_f) was larger than the anode features due to current spread and variations in current distribution across the plate. The area of each deposit square feature was estimated from feature width measurements, taken from feature profiles. The sum of the area of all the square features on the plate gave the value of A_f for that experiment. The A_f used to calculate the actual applied current density based on the area of cathode features (i_f), which could be used with the Faraday equation to find a more accurate nominal deposit thickness ($d_{dep,\,100\%,f}$) for each deposition mode.

4.3.3.2 Deposition experiments of linear µm-scale features

Deposition of linear features was carried out using the tool in figure 4.19 under 40 W/L of CUS. The same plating conditions as for the square features, with a plating time of 677 seconds at a current density of 20 mA/cm^2, again achieving a nominal deposit thickness of 5.0 µm based on the anode area. Deposition of linear features was also carried out using PUS with the same conditions as described in figure 4.20 with 40 W/L.

The area of exposed copper anode surface (A_a) was measured by measuring the widths of the linear features using a confocal optical microscope at all locations (A-H) across the plate. The average width of the exposed copper lines was 210 µm and the length of each line was 66 mm. The average area of one line feature was therefore 0.14 cm^2, and the area of all 77 lines was 10.6 cm^2. A current of 211 mA was applied for each experiment to achieve approximately 20 mA/cm^2.

Current spreading again caused a larger total surface area of deposit features on the cathode surface (A_f) compared to the anode features. The total area of all the linear deposit features was estimated by measuring the line widths at all locations using an optical microscope. The average width of the deposit line features was then used with the length of the deposit lines, measured with a ruler, to determine an estimation of the A_f. The value of A_f was then used to calculate the actual nominal deposit thickness ($d_{dep,\ 100\%,f}$) for each experiment.

4.4 Deposit characterization

4.4.1 Optical Microscope, SEM, ESEM and EDX

The surface of the copper deposited features were also analysed by an Olympus BX41 microscope within the magnification range of 5 to 50 times. For more detailed analysis of the surface morphology, Scanning Electron Microscopy (SEM) was carried out using a Jeol JSM-5300LV SEM for magnifications of x35 and for further detail Environmental Scanning Electron Microscopy (ESEM) was carried out using a XL30 ESEM-FEG to capture images of magnification up to x2000. The analysis of the surfaces of the copper deposits was carried out with energy dispersive X-ray (EDX) analysis using the SEM machine which was equipped with an EDX detector. The EDX spectroscopy could be used to carry out elemental mapping analysis.

4.4.2 Profilometery

Profilometry was carried out to measure the thickness of the deposit features ($d_{dep,\,m}$). This was required for the analysis of deposit thickness uniformity at both the feature-scale (i.e. across a feature) and also at the substrate (i.e. across the substrate plate). It is essential to check the uniformity of thickness of the deposit features as this is important for microfabrication where $d_{dep,\,m}$ is monitored. The current efficiency can also be calculated from the $d_{dep,\,m}$.

The roughness of the deposits was calculated from the surface of the deposit feature profiles. This is another important parameter in microfabrication and will also be an indication of the current distribution across the substrate. Measurement of both the deposit thickness uniformity and deposit roughness uniformity across the A7 size substrates will test the process's scalability.

4.4.2.1 Profilometry of deposits plated in small-scale cell

Each deposition experiment was repeated 3 times, and either a *Dektak Profilometer* or a *Tencor P-1 Long Scan Profilometer* was used to measure the profiles across the width of the deposited copper feature. The length of each profile scan was 5 mm with a speed of 100 μm/s and a stylus force of 20 mg. A profile was measured across the top, centre and bottom of the deposited linear feature. The average height across a 1000 μm region in the centre of the profile gave the deposit thickness of the feature.

4.4.2.2 Profiles of square mm-scale features plated in large-scale US tank

Profiles of each deposit were measured using a *Tencor P-1 Long Scan Profilometer* across the middle of the deposit pattern feature. The length of each profile scan was 13 mm with a speed of 0.4 mm/s and a stylus force of 20 mg. The thickness of the deposit was taken as the average height of the profile in the centre of the deposit over a 7 mm region. However, some manipulation of the deposit profiles was required before this measurement could be made.

Levelling of the deposit profiles was needed as the plate was not entirely flat during measurement. The total length of the measurement of the profile was over a large

distance of 13 mm, this meant that the natural curvature of the plate resulted in curved profile shapes, shown in figure 4.21a. In order to eliminate this issue, a profile of the surface of the plate near to the deposit feature was measured to obtain the equation for the curvature in that region of the plate. This equation was then subtracted from the profile of the deposit, which resulted in a flatter profile shape, similar to the profile shown in figure 4.21b.

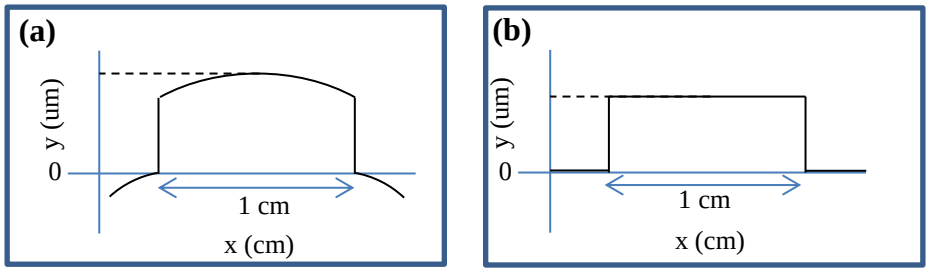

Figure 4.21 – Diagram of subtracting curvature of the copper plate from profiles of copper deposit features. (a) Before subtracting curvature of plate, (b) After subtracting curvature of plate

An example of the plate curvature subtraction from a copper feature profile is shown in figure 4.22. A profile of the surface of the copper plate was measured where there was no copper deposit. Figure 4.23 shows a profile measured directly below where the copper feature was deposited, illustrating a significant plate curvature in this region. A polynomial line of regression was extracted from this data, shown in equation (4.16). This line was then subtracted from the profile data in figure 4.22a to obtain the corrected profile shown in figure 4.22b.

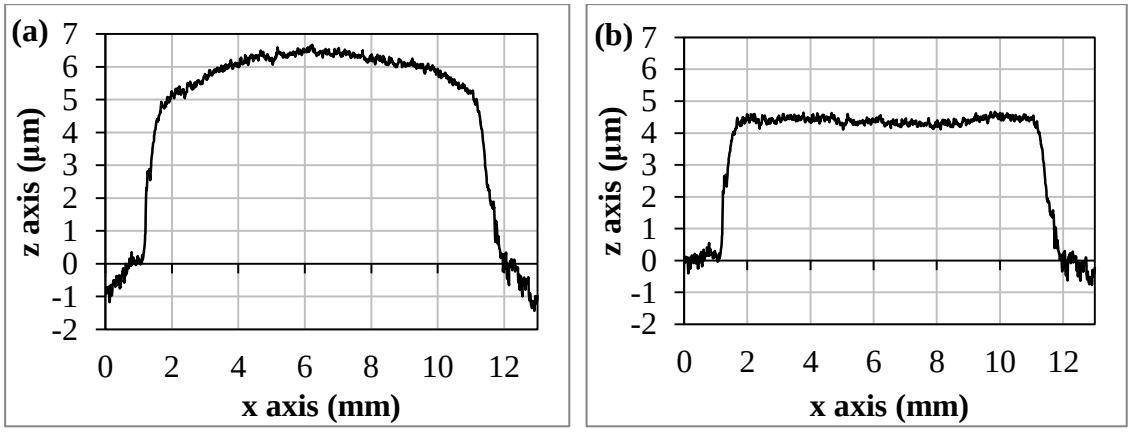

Figure 4.22 – Example of subtraction of curvature of the copper plate from a profile of copper deposit feature plated at 20 mA/cm^2 for 677 seconds with 30 W/L of CUS. (a) Before subtracting curvature of plate, (b) After subtracting curvature of plate

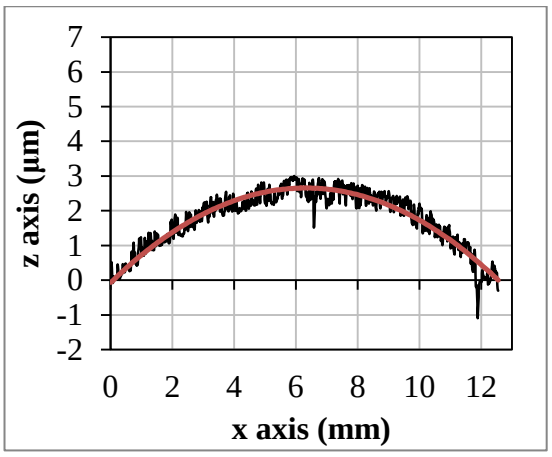

Figure 4.23 – Example of profile of the copper plate surface measured just below the feature of the profile shown in figure 13. Black line = Profile data, Red line = Polynomial line of regression, shown in equation (4.16)

$$z = (-0.070)x^2 + 0.879x - 0.074 \quad (4.16)$$

4.4.2.3 Profiles of linear µm-scale features plated in large-scale US tank

The profiles of the lines were measured over two linear features at the same locations as each of the squares (i.e. ABCDEFGH). The length of each profile scan was 2600 µm with a speed of 25 µm/s and a stylus force of 20 mg. The thickness of each feature was taken as the average height across centre of the linear feature over a 500 µm region.

4.4.3 Current Efficiency

The current efficiency (φ) can be used to measure the deposition performance, defined as the percentage of charge consumed by the desired reaction of interest. The current efficiency for metal electrodeposition is shown in equation (4.17), where Q_r is the charge required for the desired reaction and Q_T is the total charge that was applied. The Q_r is related to the amount of deposited metal, therefore the weight of deposited metal can be measured and compared to that which is expected at 100% current efficiency using Faraday's law.

$$\varphi = \frac{Q_r}{Q_T} \times 100 \quad (4.17)$$

For very thin deposits, such as those deposited in this study, deposit weight measurement would be difficult. This is because the weight of the 1 mm thick copper

plate is very large compared to the 5 μm thick deposit copper features, and therefore the difference in weight would be undetectable. For this reason, the measurement of deposit thickness was used to calculate the current efficiency, as shown in equation 4.18.

$$\varphi = \frac{d_{dep,m}}{d_{dep,100\%}} \times 100 \tag{4.18}$$

where $d_{dep,m}$ is the deposit thickness measured experimentally from deposit feature profiles. $d_{dep,100\%}$ is the deposit thickness assuming 100% current efficiency. The $d_{dep,100\%}$ is also the desired thickness of the deposit and was used to calculated the required plating time, calculated using equation (4.19).

$$t = \frac{A_a\, n\, F\, \rho\, d_{dep,100\%}}{I\, M_w} \tag{4.19}$$

where n is the charge on reacting species, F is Faraday's constant, ρ is the density of the plated metal (ρ of copper metal is 8.92 g/cm^3), M_w is the molecular weight of the deposited metal (M_w of copper is 63.546 g/mol) and I is the current applied. A_a is the estimated area of the copper deposit feature on the substrate taken as the area of exposed copper surface on the anode tool. This calculation assumes the following:

(1) 100% current efficiency
(2) The shapes of the deposits are rectangular, i.e. cuboid in shape
(3) The area of the plated metal feature is the same as the area of exposed copper surface on the anode tool (A_a)

Assumption (3) is only appropriate for estimating the deposition time (t) for a desired deposit thickness. It is also sufficient for calculating the current efficiency when the sizes of the plated features are very close to the size of the anode features. However, when the area of deposited is much larger than the anode feature due to the effect of current spreading, it would result in thin deposits, thereby giving considerably lower values of current efficiency.

The actual area of the plated pattern features therefore needed to be taken into account in order to find the deposit thickness at 100% efficiency based on the actual area of the plated features ($d_{dep,100\%,f}$). This can be calculated using equation (4.20).

$$d_{dep,100\%,f} = \frac{I\, t\, M_w}{A_f n F \rho} \tag{4.20}$$

where A_f is the area of the plated features calculated by measuring the sizes of the features using an optical microscope. The current efficiency would therefore be calculated by equation (4.21).

$$\varphi = \frac{d_{dep,m}}{d_{dep,100\%,f}} \times 100 \tag{4.21}$$

4.4.4 Deposit roughness measurement

The R_a (roughness amplitude) of each deposit plated in the small scale cell was calculated over a 1000 μm region in the centre of each profile using equation (4.22), where n_p is the total number of data points. The height of roughness irregularities (y_i) were calculated as the vertical distance from the i^{th} data point to the mean line, which was a quadratic regression line.

$$R_a = \frac{1}{n_p}\sum_{i=1}^{n_p}|y_i| \tag{4.22}$$

Equation (4.15) was also used to calculate the R_a for the features plated on the A7 substrates. For the square mm-scale features, the R_a of each deposit feature was calculated over a 3000 μm region, and was measured in 3 locations of each profile; near the left side, near the right side and in the centre of the profile. Each deposition experiment was repeated 3 times and the average R_a of these 3 repeats gave the average deposit roughness across the feature.

For the linear μm-scale features the R_a of a linear feature was calculated over a 500 μm region. The R_a of the linear features was measured for two line features within the same locations that the square features were deposited (i.e. ABCDEFGH), and two lines were measured within each location. The average deposit roughness of the linear features was calculated as the average R_a of the 3 experimental repeats.

This chapter has provided a description for each of the three systems that were used in this investigation. The experimental techniques for both the mass transfer and pattern deposition experiments carried out in each system have also been described. The results from these experiments will now be reported. The observations from the mass transfer experiments will first be discussed.

Chapter 5. Results:- Mass transfer experiments

5 Results:- Mass transfer experiments

5.1 Mass Transfer in the flow cell

Limiting current experiments were carried out during copper deposition on a 20 mm diameter copper disc using a fully exposed copper anode with an inter-electrode gap of 0.3 mm. Both electrodes were polished to a mirror-like finish. Current densities were applied from 5 to 170 mA/cm^2 using a power supply and a multimeter was used to measure the cell potential 30 s after each current was applied to allow the system to reach steady state. The flowrate was set to 40 cm^3/s for each experiment and three experimental repeats were carried out. Standard limiting current experiments are carried out with the use of a reference electrode, however the cell potential was measured in these flow cell experiments as opposed to the electrode potential. This is because of the difficulty of including a reference electrode in this system experienced in previous experiments using a similar flow cell [20, 39].

The cell potential vs. current density plots are shown in figure 5.1. A limiting current plateau is barely observable, but a small increase in potential can be noticed at approximately 120 mAcm^2 before the hydrogen evolution region is reached at potentials greater than 1.2 V. The unobservable current plateau and the high linearity in the current vs. potential plot is likely to be due to a large amount of Ohmic overpotential. Another reason for this could be due to the occurrence of a potential shift which occurs because of potential distortions that occur when using this narrow electrode gap. This will be discussed and explained in more detail in the following chapter.

The method of approximating the limiting current was carried out by the bisection of the lines shown in figure 5.1. The limiting current was therefore approximately 125 mA/cm^2 when using a 20 mm diameter electrode and a volumetric flowrate of 40 cm^3/s, which is equivalent to a flow velocity of 14 cm/s near the electrode surface. Equation 5.1 can be used to calculate the diffusion layer thickness using a diffusion coefficient of 7.15 x 10^{-6} cm^2/s, calculated from the limiting current equation [129].

$$i_{Lim} = \frac{n\,F\,D\,(c_b)}{\delta} \tag{5.1}$$

where n is the charge on the reacting species, F is the Faraday constant, D is the diffusivity of the reacting species, c_b is the bulk concentration of reacting species and δ is the diffusion layer thickness.

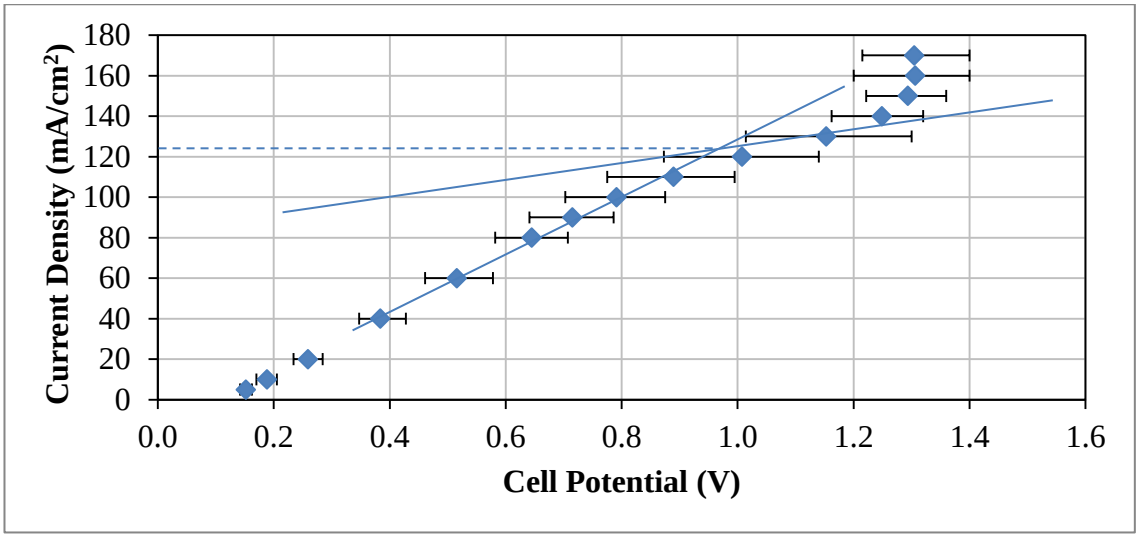

Figure 5.1 - Limiting current experiments in vertical flow cell with 0.1 M $CuSO_4$ electrolyte, with 20 mm diameter copper electrodes and an unpatterned anode surface. The inter-electrode gap is 0.3 mm and the electrolyte volumetric flow rate 40 cm^3/s.

The diffusion layer thickness was calculated to be 11 µm. These results are similar to previous limiting current experiments carried out by Wu, Green and Roy [20] in a similarly designed flow cell with 10 mm diameter copper electrodes, at the same electrode gap of 0.3 mm and using the same electrolyte solution of 0.1 M $CuSO_4$. A limiting current of 78 mA/cm^2 was measured when using a flow velocity of 6 cm/s. This is equivalent to a diffusion layer thickness of 18 µm.

Previous investigations using similar designed flow cells stated that turbulent forced convection occurred near to the electrode for narrow inter-electrode gaps of 3 mm [49, 50]. However, mass transfer correlations were not developed for this system or the flow cell with the 0.3 mm electrode gap [20]. To the best of the author's knowledge, no correlations have been developed for this narrow gap. However, a prediction of the correlations can be made by referring to mass transfer investigations with larger electrode gaps [39, 42] can be used.

A mass transfer study using a flow cell with a 25 mm electrode gap, a copper electrode of length 75 mm and an electrolyte flow velocity of 0.7 cm/s calculated the δ during copper deposition from experimental data matched at the lower section of the plate. It was found that the δ matched well with the correlation for laminar forced convection shown in equation 5.2 [42].

$$Sh = 1.23\left(Re\,Sc\,\frac{L}{d_e}\right)^{1/3} \qquad (5.2)$$

Another copper deposition investigation using a flow cell with a larger electrode gap of 100 mm has also been studied. A 10 mm diameter recessed copper electrode and electrolyte flow velocities ranging from 0.75 to 4 cm/s were used. A correlation was developed for this system which showed that when using the higher flow rates developing turbulence was present. This is shown in the correlation in equation 5.3 [39]. In the same study, a correlation was developed for laminar forced convection at a rectangular flat plate shown in equation 5.4

$$Sh = 0.153\left(Sc\ \frac{d_e}{L}\right)^{1/3} Re^{0.72} \tag{5.3}$$

$$Sh = 1.71\left(Re\ Sc\ \frac{L}{d_e}\right)^{0.359} \tag{5.4}$$

In order to compare our results with those predicted by equations 5.2, 5.3 and 5.4, for the case of a 20 mm diameter electrode and a flow velocity of 14 cm/s (as is the case in our experiments) the values of δ were evaluated. The calculated values of δ were 1575 μm, 103 μm and 50 μm for equations 5.2, 5.3 and 5.4 respectively. The value of δ calculated from equation 5.4 is the closest to the δ calculated from equation 5.1 using the experimental limiting current data. Equation 5.4 is therefore a reasonable prediction for the mass transfer correlation for this flow cell system and suggests that laminar forced convection may be occurring.

It is important to note that the diffusion layer will not be uniform over the electrode surface. This is partly due to the flow regime as mass transfer will differ at the bottom of the electrode compared to the centre. A previous flow cell investigation with assisting forced convection flow showed that the diffusion layer can be 50% larger at 10 mm from the bottom of the electrode compared to the very bottom edge [42].

There may be non-uniformity in the electrode spacing which will create differences in mass transfer across the electrode. Previous flow cell experiments estimated a variation of ±25 μm of the inter-electrode gap across a 10 mm diameter electrode. This is mainly due to the curvature of the disc due to polishing which is unavoidable. The distance between the 20 mm diameter electrodes in this investigation was measured using a micrometer to determine the distance from the surface of the holder to the electrode surface, since the electrodes were slightly recessed. This was measured in 5 different locations across the disc for both electrode holders. The two

distances were then summated, along with the distance between the holders (0.3 mm) to give the estimation of the distance between the electrodes in the middle and edges of the electrode. The average electrode spacing of the 20 mm diameter electrodes was 400 μm with a variation of ±30 μm, slightly more than the 10 mm electrodes.

The variation in the electrode spacing for 3 experimental runs was ±60 μm due to the slight differences in each electrode and also the difficulty in levelling the electrode during loading into its holder. This difference in electrode gap will cause differences in mass transport across the disc, resulting in variations in diffusion layer thickness across the disc. These issues, along with the time consuming loading and unloading procedure for this flow cell, means that this geometry is not suitable for the scale-up of the Enface system.

5.2 Mass transfer in the small-scale cell

5.2.1 Linear polarization scans in 0.1 M $CuSO_4$

A linear polarization scan for copper deposition at a cathode substrate under silent conditions in 0.1 M $CuSO_4$ with a 10 mm electrode gap is shown in figure 5.2. The current-potential plots in figure 5.2 have the characteristic sigmoidal shape curve for electrochemical reactions in the reduction region. As the negative potential is increased from the OCP the curve begins to plateau towards the limiting current (i_{Lim}). Further increases in potential result in a curve towards higher current densities due to the presence of the hydrogen evolution reaction. A limiting current of -14.5 mA/cm^2 is reached under silent conditions. This corresponds to a δ of 95 µm calculated using equation 5.1, using a diffusion coefficient of 7.15 x 10^{-6} cm^2/s [129].

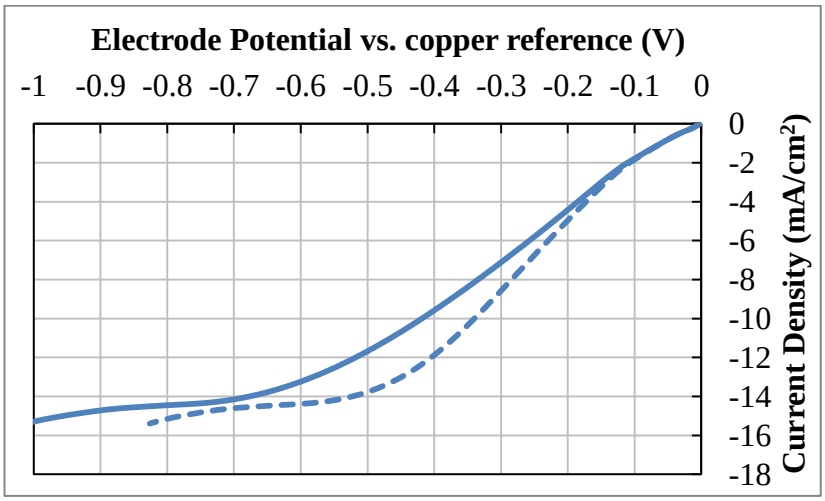

Figure 5.2 - Silent linear scans in 0.1 M $CuSO_4$; Scan rate = 5 mV/s ; Inter-electrode gap = 1 cm ; Solid blue - without compensated ohmic drop ; Dotted blue – with compensated ohmic drop)

The dotted line is the silent linear scan with compensated ohmic drop. The calculation for the determination of ohmic drop is shown in Appendix B. It can be observed that the largest ohmic potential drop within the region below the limiting current was approximately 0.1 V. This is reasonably high compared to most electrochemical systems. However, the value of the limiting current was unaffected by the ohmic potential drop, therefore the values of limiting current were valid to use in mass transfer calculations and comparisons in this system.

The current-potential plot of a linear scan at 5 mV/s in 0.1 M $CuSO_4$ with ultrasound at a power of 18 W/cm^2 is shown in Figure 5.3. The limiting current plateau is undetectable due to the high linearity of the current-potential response. The sudden increase in current which usually occurs during hydrogen evolution at higher potential does not appear in figure 5.3, suggesting that when using a vibrating US probe during a linear scan, the limiting current plateau is being 'masked' by the hydrogen reaction, seen previously [130].

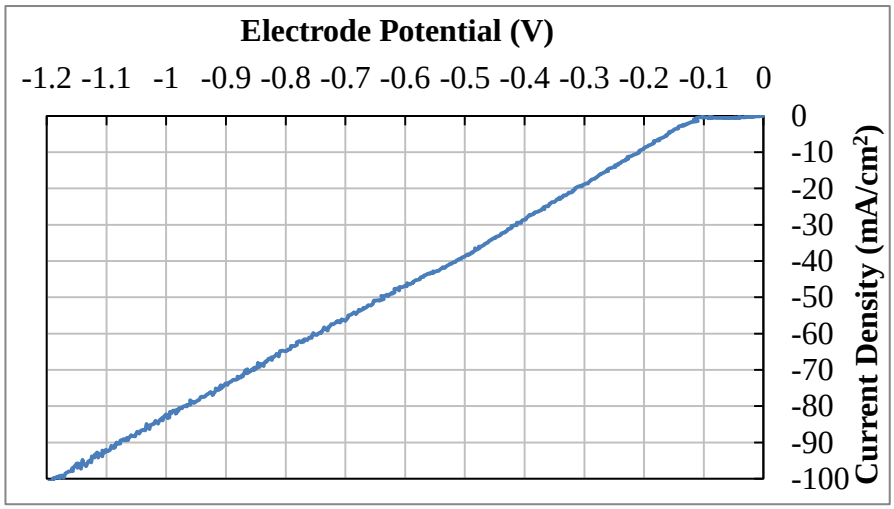

Figure 5.3 - Linear Scan with Ultrasound at 35% Amplitude. 0.1 M $CuSO_4$ electrolyte ; Scan Rate = 5 mV/s ; Inter-electrode gap = 10 mm ; Probe-electrode = 15 mm.

5.2.2 Silent linear polarization scans with 0.1 M $CuSO_4$ in 0.1 M H_2SO_4

In order to solve the problem of the undetectable limiting current, an acidic electrolyte of 0.1 M $CuSO_4$ in 0.1 M H_2SO_4 was used. A silent linear scan with an inter-electrode gap of 10 mm using this acidic electrolyte is shown in figure 5.4. The limiting current with the acidic electrolyte is -10.5 mA/cm^2, corresponding to a δ of 130 μm, using a diffusion coefficient of 7.07 x 10^{-6} cm^2/s [129]. This is larger than the δ of the non-acidic electrolyte because adding sulphuric acid significantly decreases the effect of migration as a consequence of a decrease in the electric field, therefore resulting in a reduction in the rate of mass transport of Cu^{2+} ions [29].

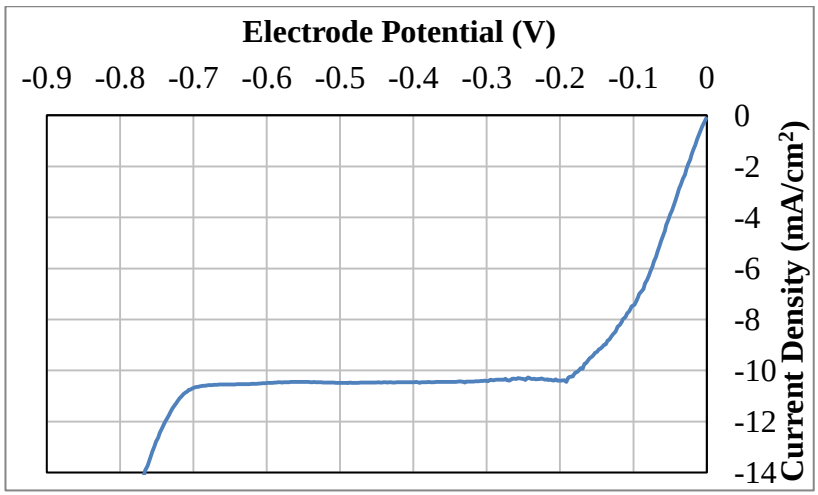

Figure 5.4 – Silent linear scan in acidic electrolyte, 0.1M $CuSO_4$ + 0.1M H_2SO_4 ; Scan rate = 5 mV/s ; Inter-electrode gap = 10 mm ; d_p = 30 mm.

The limiting current is reached at a much lower potential of -0.2 V with the acidic electrolyte compared to -0.75 V with a non-acidic electrolyte, observed by comparison of figures 5.4 and 5.2 respectively. The conductivity of acidic electrolytes is higher than less acidic electrolytes due to the presence of more H^+ ions. This decreases the resistance of the solution, therefore reducing the ohmic resistance. This causes the reduction reaction to occur at lower potentials, therefore the limiting current is reached at a less negative potential. The H_2 evolution reaction also begins at a lower potential of -0.7 V for the acidic electrolyte, indicated by a sharp increase in negative potential.

Additionally, figure 5.4 clearly shows that the limiting current plateau is observable over a much larger potential region in the acidic electrolyte compared to the non-acidic electrolyte. The limiting current plateau is present over a potential range of 0.5 V and 0.1 V in acidic and non-acidic electrolytes respectively. The wider potential range of the current plateau and also the lower potential at which the limiting current is reached when using acidic electrolytes means that the 0.1 M $CuSO_4$ in 0.1 M H_2SO_4 is more suitable for detecting limiting currents in this system. This electrolyte was therefore used for the subsequent experiments with US agitation. The following experiments were recorded in a previous paper by the author [51].

5.2.3 Linear polarization scans at varying ultrasound intensities

Linear polarization scans with ultrasound agitation are shown in Figures 5.5a-c. The limiting current plateaux are visible, however noisy fluctuations in current are present due to cavitation bubble movement and oscillations and bubble collapses

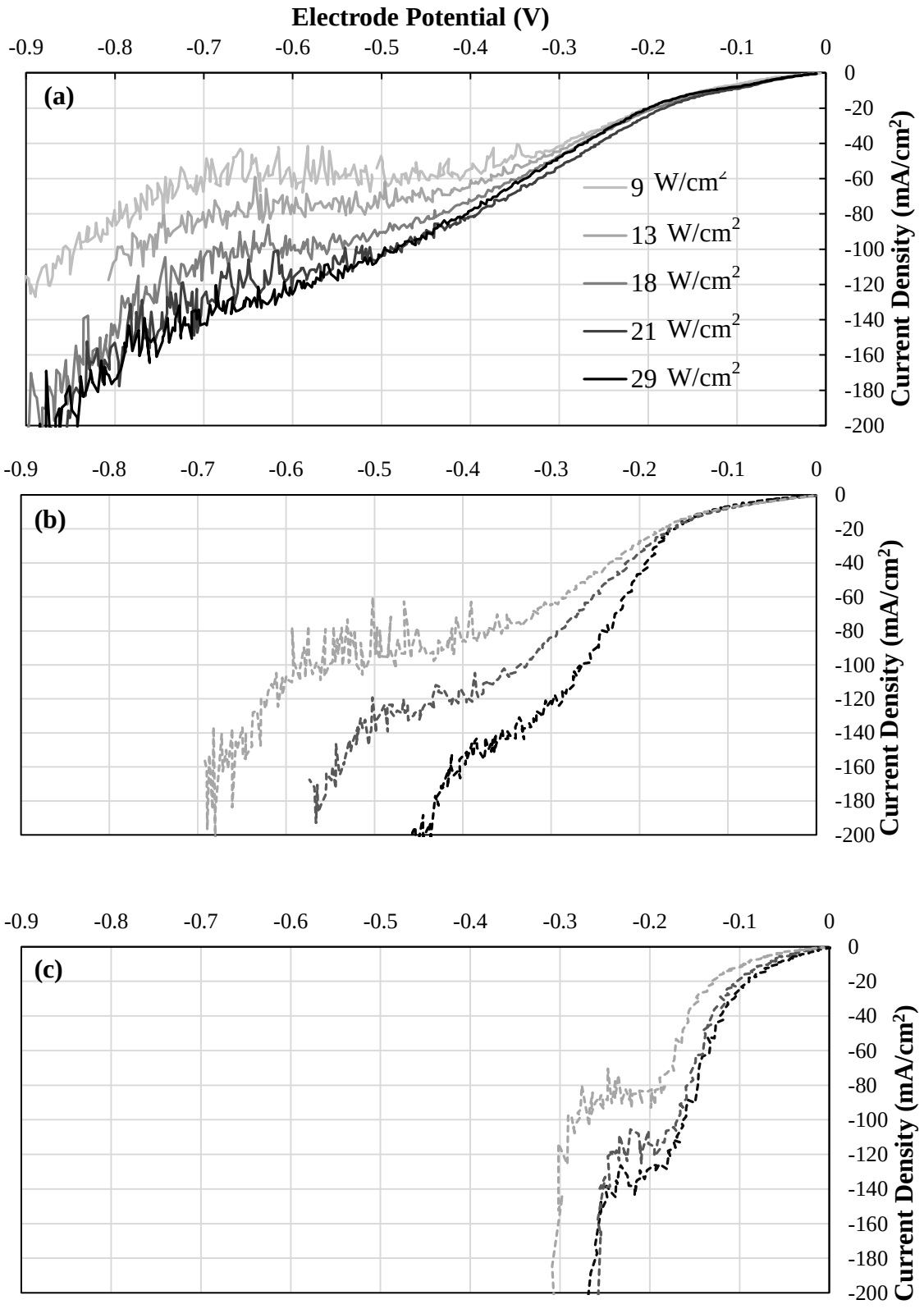

Figure 5.5 - Linear Potential scans with a 0.1 M $CuSO_4$ + 0.1 M H_2SO_4 electrolyte; Scan Rate = 5 mV/s. (a) at varying ultrasound intensities (9 - 29 W/cm^2), h_e = 10 mm ; d_p = 30 mm. (b) h_e = 5 mm ; at varying d_p of 30 mm (dashed light grey), 20 mm (dashed grey) and 15 mm (dashed black) at fixed p of 18 W/cm^2. (c) h_e = 1.5 mm, with same ultrasound conditions as for 'b' and varying d_p at distances of 30 mm (dashed light grey), 20 mm (dashed grey) and 15 mm (dashed black). [51]

causing micro-jetting resulting in sudden current peaks. This has been observed in previous investigations in both the side-on [76] and face-on [22, 57] probe arrangements.

Figure 5.5a shows the limiting current data for an inter-electrode gap of 10 mm with varying ultrasound powers, from 9-29 W/cm^2. The values of i_{Lim} range from -57 to -130 mA/cm^2, significantly larger than the i_{Lim} measured under silent conditions for the same electrode gap shown in figure 5.2. This shows that the rate of mass transfer of Cu^{2+} ions towards the cathode is considerably increased by ultrasound agitation. This increase in limiting current with increasing US intensity has been reported in several previous investigations [22, 54, 76].

5.2.4 Effect of inter-electrode gap and probe-electrode distance under US conditions

Figure 5.5b and 5.5c show linear polarization scans for smaller inter-electrode gaps less than 10 mm with varying probe-electrode distances. These plots display narrower current plateau regions and hydrogen evolution apparently occurring at lower potentials, this causes a difficulty in the detection and measurement of the i_{Lim}.

However, despite these issues the limiting current measurements in figure 5.5b and 5.5c can still be used to make a reasonable comparison for the difference in mass transfer at varying inter-electrode gaps and d_p. Figure 5.5b shows that the values of i_{Lim} are approximately 90, 122 and 140 mA/cm^2 for d_p values of 30, 20 and 15 mm respectively, when using a 5 mm inter-electrode gap. This illustrates the effect of increasing the mass transfer as the probe-electrode distance is decreased, reported previously in other ultrasound investigations [22, 54, 57]. It is suggested that this is due to both the higher cavitational activity near the probe tip [81] and a higher flow velocity at smaller probe-electrode distances [57].

Figure 5.5c displays linear potential scans with varying probe-electrode distances for a very small inter-electrode gap of 1.5 mm. The values of i_{Lim} are almost the same for both electrode gaps of 5 and 1.5 mm, illustrating that ultrasound is still a useful agitation technique and still effective at very narrow electrode gaps. However, the measurement of the limiting current is more difficult at the narrowest gap due to the very small plateaux region due to the distortion in polarisation data. A shift in the polarization also occurs when shortening the distance between the probe and the

electrode surface (d_p). The largest value of d_p used in these experiments, i.e. 30 mm, is therefore said to be sufficiently far from the electrode surface for this system.

5.2.5 Effect of US agitation on the diffusion layer thickness

The diffusion layer thickness (δ) at the cathode was calculated from equation (5.1) using the i_{Lim} data in figure 5.5. The δ at different US intensities and two different electrode gaps, 10 mm and 1.5 mm, using a constant probe-electrode distance of 30 mm, is shown in figure 5.6. The boundary layer is large at lower US intensities and is thinner when using higher intensities.

An increase in δ occurs when inter-electrode gap is decreased from 10 mm to 1.5 mm. This is thought to be due to a constriction in convection flows which occurs as the electrode surfaces are brought closer together. There is a higher decrease in δ for the narrower electrode gap, most evident at US powers between 9 and 18 W/cm^2. At powers higher than 18 W/cm^2 the decrease in δ with increasing power is less for both gaps until a minimum diffusion layer thickness (δ_{min}) of 10 μm is reached. This shows that when using lower ultrasound powers the effectiveness of using US is high and the effectiveness of US diminishes as the power is raised. It has been suggested that this is mainly due to the limiting conversion of ultrasound energy to turbulent liquid flow [57].

For the narrowest electrode gap of 1.5 mm, the value of δ under silent conditions is 136 μm; which can be reduced to a thickness of 16 μm when using US agitation provided by the US probe operating at 18 W/cm^2. This illustrated the usefulness of US agitation in constricted geometries.

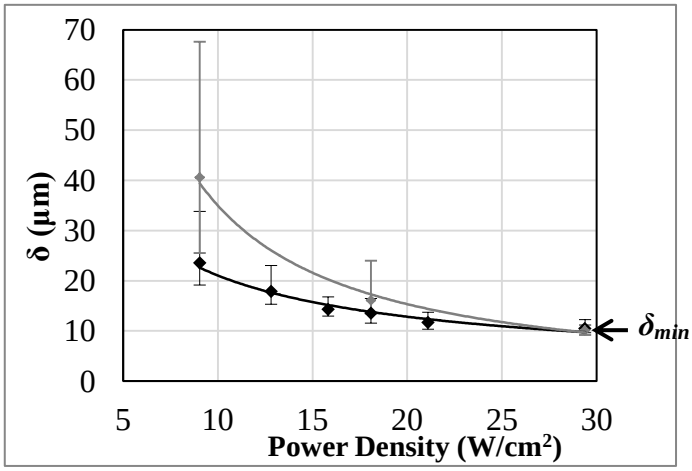

Figure 5.6 - Diffusion layer thickness (δ) calculated using experimental limiting currents and equation (5) as a function of US power density. h_e = 1.5 mm (grey), 10 mm (black) ; d_p = 30 mm. [51]

5.2.6 Mass transfer correlations

The comparison of the agitation within the electrode gap was analysed in more detail by developing Sherwood number (*Sh*) correlations. In order to calculate these correlations the flow velocity (*U*) of the 'jet-like' ultrasound flow from the probe tip was required. The value of *U* would be very difficult to measure in this system and was therefore calculated using an estimation from the relationship of US power and U, shown in figure 2.13, which was formulated by Eklund et al. [76]. This is a suitable estimation as the study by Eklund et al. [76] used a similar US probe with an electrode placed at a similar distance of 34 mm from the probe tip to this study.

Equation 5.5 was used to calculate the Reynolds number (*Re*) using the values of U calculated from relationship shown in figure 2.13.

$$Re = \frac{(U\ d_H)}{\nu} \tag{5.5}$$

where d_H is the hydraulic diameter and ν is the kinematic viscosity.

The calculation of the hydraulic diameter is shown in equation (5.6). For the dimensionless, the electrode dimensions were simplified to 10 mm square electrodes, shown in figure 5.7. A_x is the cross-sectional area of the channel between the electrodes, r is the radius of the electrode and h_e is the electrode gap.

$$d_H = \frac{4A_x}{(4r+2h_e)} \tag{5.6}$$

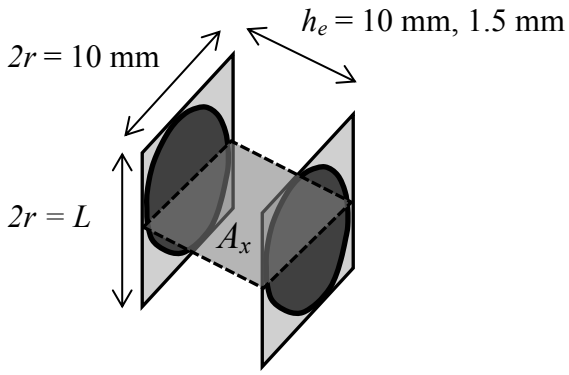

Figure 5.7 - Schematic of electrode gap for calculation of d_H with assumption of square electrodes. 2r = Characteristic Length, A_x = Cross-sectional Area, h_e = electrode gap.

The calculated *Re* are shown in table 5.1, showing that the range of *Re* were 700 – 2000 and 2700 – 7400 for the small and large electrode gaps respectively. *Sh* correlation for the narrow gap occurrence of fully developed turbulence, therefore the

efficacy of US is higher even when *Re* values are smaller. The Re values at 29 W/cm^2 for the small and large gap are approximately 2000 and 7400, respectively, however the thickness of δ is practically the same.

Table 5.1 – Calculated Reynolds numbers at varying powers for two difference electrode gaps, with values of U at each power, obtained from figure 2.13. [51]

Electrode gap (mm)	Power (W/cm2)	Velocity, U (cm/s)	Re
10	9	27	2690
	18	48	4800
	29	75	7430
1.5	9	27	700
	18	48	1250
	29	75	1940

Figure 5.8 shows the Sherwood-Schmidt-Reynolds mass transfer correlations which were developed for the small and large electrode gaps. The line of best-fit was used to calculate the values shown in the correlations displayed in equations 5.7 and 5.8 for electrode gaps of 10 mm and 1.5 mm respectively.

$$Sh = 1.7 \times 10^{-3} \left(Re\, Sc\, \frac{d_e}{L} \right)^{0.82} \tag{5.7}$$

$$Sh = 9 \times 10^{-6} \left(Re\, Sc\, \frac{d_e}{L} \right)^{1.38} \tag{5.8}$$

Comparing these equations to equation 2.8, the correlation for forced convection flow between two parallel electrodes, then it can be observed that the value of *b* for the 10 mm electrode gap is 0.82. This implies that there is an onset of turbulent flow occurring when using the larger gap. When using the smaller gap of 1.5 mm the value of *b* is 1.38 indicating the occurrence of fully developed turbulent flow. The reason for added turbulence could be the ultrasound jet-flow from the probe coming into contact with the top section of the PTFE electrode holder. This possibly causes the formation of eddies at the top of the electrode holder when narrower electrode gaps are used.

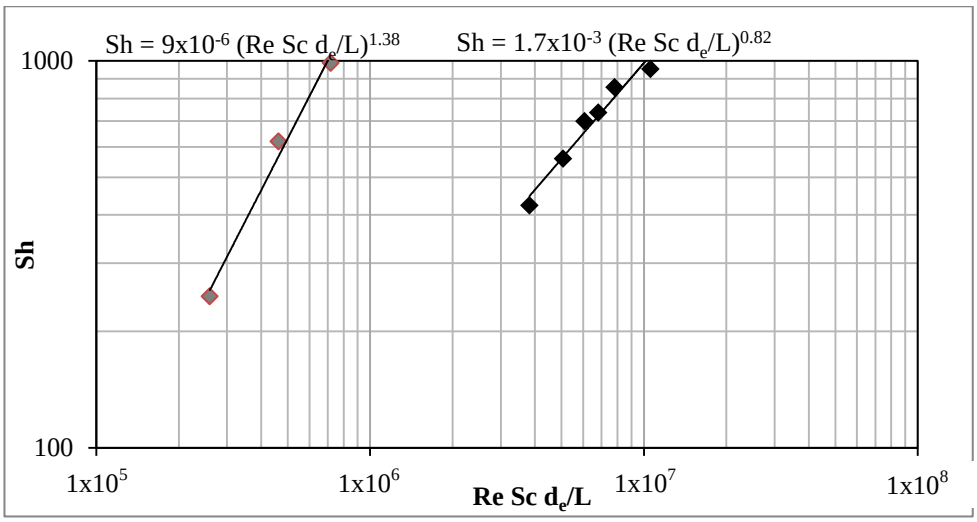

Figure 5.8 - Mass transfer correlations using US agitation. Data shown for US power 18 W/cm^2 and probe-electrode distance of 30 mm, where the US source is far away from the electrode. Inter-electrode gaps of 1.5 mm (grey) and 10 mm (black). [51]

5.2.7 Limiting current at 0.3 mm gap with patterned anode

The flow regime of the flow of US waves between two 10 mm diameter electrodes separated by a narrow electrode gap of 1.5 mm has now been analysed. However, the electrode gap required for the Enface technique is 0.3 mm, and in order to deposit patterns using Enface the anode surface requires a pattern feature with a smaller exposed surface area than the cathode area. Furthermore, a non-acidic electrolyte should be used, rather than the electrolyte with 0.1 M H_2SO_4, as used above. This is because acidic electrolytes have a higher conductivity; resulting in further divergence of current lines between the anode and cathode. An investigation was therefore carried out to assess the improvement of mass transfer using US agitation for a system under the conditions required for the Enface process.

Limiting current experiments were carried out with a 0.3 mm electrode gap, 0.1 M $CuSO_4$ electrolyte solution and a 1 mm x 5 mm rectangle of exposed anode area. These experiments were also used to calculate the plating current density required to carry out copper pattern deposition with this system. The potential-current plots for both silent and ultrasound conditions are shown in figure 5.9. The current density was based on the area of anode that was exposed; which was 5.0 ± 0.5 cm^2. The limiting current is reached at small potentials of approximately -0.06 V. The reason for the small narrow potential range of these limiting current plots is due to the use of the narrow inter-electrode gap, explained in a later chapter.

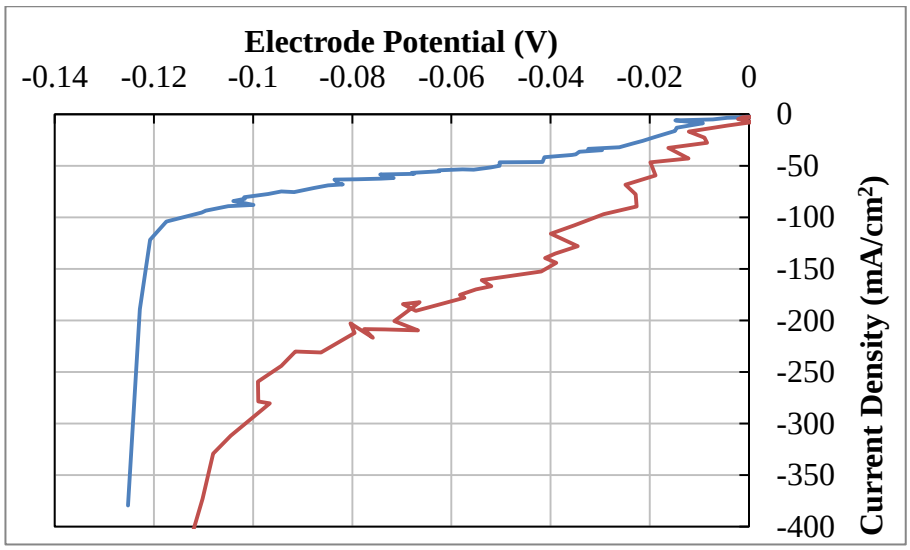

Figure 5.9 - Linear potential scans with a 1 x 5 mm rectangular pattern of exposed anode area. 0.1 M $CuSO_4$ electrolyte ; Scan Rate = 2 mV/s ; Inter-electrode gap = 0.3 mm ; d_p = 30 mm ; Blue = Silent ; Red = With ultrasound, p = 9 W/cm^2

The bisecting lines method of measuring the i_{Lim}, as used previously in fig. 5.1, was used to estimate the i_{Lim} from the plot in fig. 5.9. A i_{Lim} of -80 mA/cm^2 was observed under silent conditions with a 1 x 5 mm rectangle of exposed anode area. The limiting current with ultrasound agitation at 9 W/cm^2 at a probe-electrode distance of 30 mm was approximately -200 mA/cm^2. This therefore shows a significant increase in limiting current by just over a factor of 3 when ultrasound is used. Ultrasound can therefore successfully increase the rate of mass transfer of ions under the constraints of the conditions required for Enface.

The i_{Lim} measured under silent conditions, shown in figure 5.9, is much higher than the i_{Lim} under silent conditions with a fully exposed 10 mm diameter anode and a 1.5 mm electrode gap with a value of -13 mA/cm^2. The reason for the difference in the measured current density between the fully exposed anode system with the 1.5 mm gap and the patterned anode system with the 0.3 mm gap is unclear. However, it is thought to be mainly due to distortions in current flows which occur at very narrow electrode gaps and also the current flow to the metallic probe. The measurement of the current will be effected in these narrow geometry systems as the copper reference electrode is placed in the region where these current distortions occur. This will be explained further in the discussion section in chapter 8.

5.3 Mass transfer in ultrasound tank

Limiting current experiments were carried out in the 18 L ultrasound tank at ultrasound powers of 30, 40 and 60 W/L. The units of ultrasound power are different to those used for the ultrasound power for the ultrasound probe; this is due to the difference in the calibration calculations for the two systems. The ultrasound probe is calculated per square cm of irradiating ultrasound area (i.e. area of the probe tip), whereas the standard method of calculating the power in ultrasound baths is per litre of solution within the bath.

The conversion from W/cm^2 to W/L can be simply achieved by taking the power transferred from the ultrasound probe to the solution and dividing it by the volume within the cell (500 mL). A plot of the conversion between the two power units is shown in figure 5.10, and can be calculated using equation 5.8.

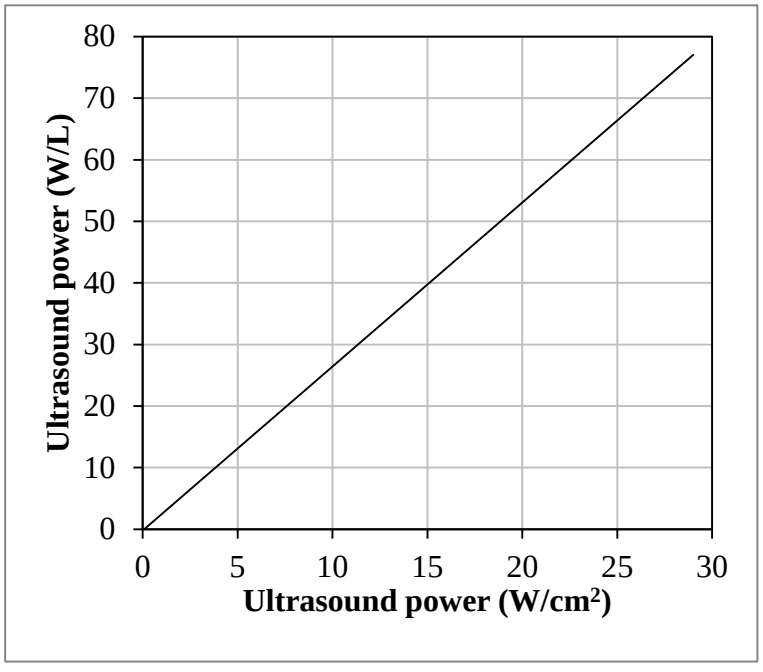

Figure 5.10 – Conversion of ultrasound power from W/cm^2 to W/L

$$p_{W/L} = 2.66\, p_{W/cm^2} - 0.20 \qquad (5.8)$$

The electrode holder that was designed to plate patterns onto A7 size substrates was used to carry out the limiting current experiments in the 18 L ultrasound tank. A specially designed tool with 10 x 10 mm square features was used so that the mass transfer could be measured at different locations across the plate. The limiting current was measured at locations B and F, shown in figure 5.11. The experiments were carried out by applying a current density and recording the cell potential. The cell potential was measured as opposed to the electrode potential due to the difficulty of the inclusion of a reference electrode as mentioned previously. All experiments were carried out with an electrode gap of 1.5 mm for comparison with mass transfer experiments in the small-scale cell which was the narrowest gap for which the limiting current could be measured in this system.

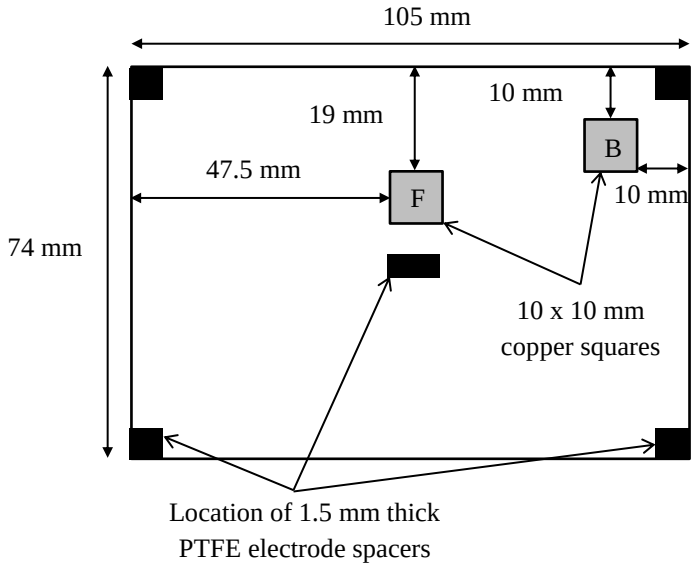

Figure 5.11 – Diagram of the position of the copper anode squares on the tool used for the limiting current experiments in the ultrasound tank with the A7 size electrode holder with locations of the placement of 1.5 mm PTFE electrode spacers.

Figure 5.12 and 5.13 shows the plots of the cell potential vs. current density for the limiting current experiments carried out in the ultrasound tank using an electrolyte of 0.1 M $CuSO_4$ with 0.1 M H_2SO_4 and an electrode gap of 1.5 mm. This was similar to the conditions for the limiting current experiments carried out in the 500 ml cell. Figure 5.12 shows the results from the limiting current experiments carried out with only the middle square (position F) used as the anode. Figure 5.13 shows the results of the limiting current experiments carried out with a tool with only the corner square (position B) connected up to the anode terminal.

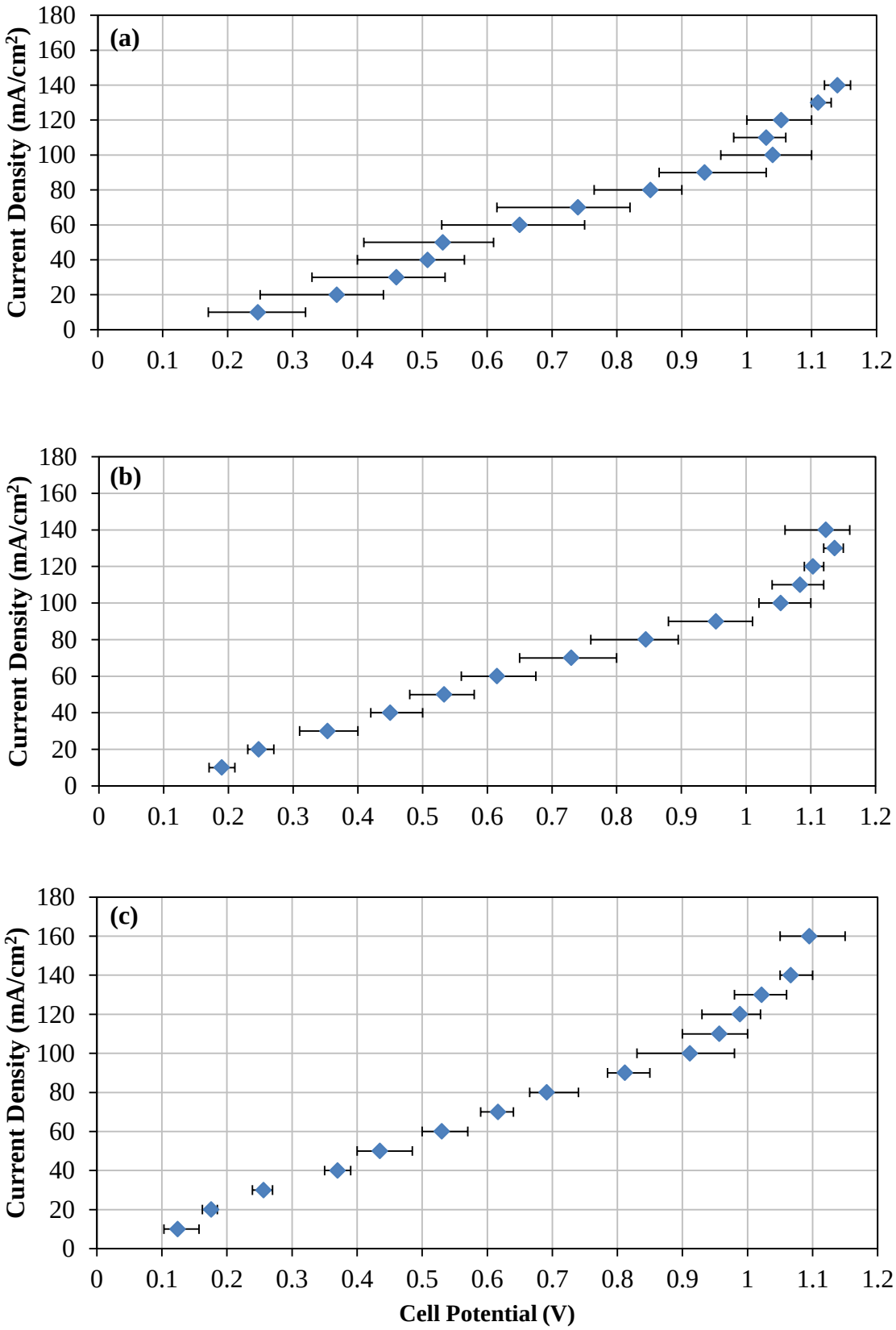

Figure 5.12 – Limiting current experiments in ultrasound tank with 0.1 M $CuSO_4$ + 0.1 M H_2SO_4 electrolyte, using a tool with middle square (position F), using an inter-electrode gap of 1.5 mm and with ultrasound operating as a continuous wave at ultrasound powers of (a) 30 W/L, (b) 40 W/L and (c) 60 W/L.

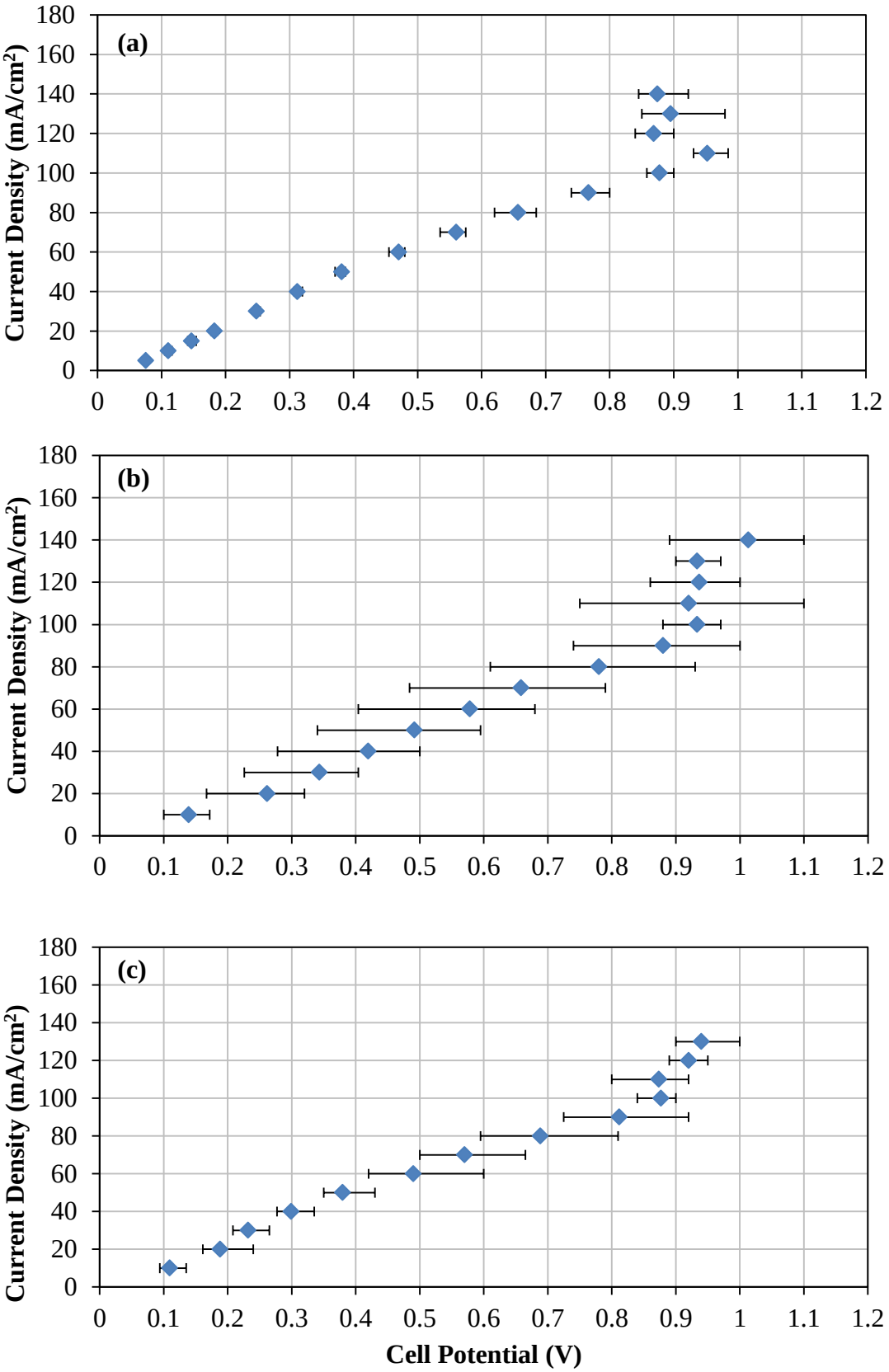

Figure 5.13 – Limiting current experiments in ultrasound tank with 0.1 M $CuSO_4$ + 0.1 M H_2SO_4 electrolyte, using a tool with corner square (position B), using an inter-electrode gap of 1.5 mm and with ultrasound operating as a continuous wave at ultrasound powers of (a) 30 W/L, (b) 40 W/L and (c) 60 W/L.

The limiting current plateaux are not particularly well-defined due to the distortions in potential at this narrow electrode gap, described by the current distribution modelling for the 500 ml cell system discussed in chapter 8. Another reason for the lack of definition in these limiting current plateaus has been stated previously by Ibl and Schdegg [131]. The current distribution across a deposit feature will not be uniform when current densities are below the i_{Lim}. As the current is increased, the i_{Lim} will first be reached at the edges of the feature and therefore deposit roughness will also develop along the feature edges. This means that the average i_{Lim} across the square feature can increase before the conditions of i_{Lim} are reached for the entire area of the feature, resulting in a narrow potential range for which the limiting current can be measured.

It is interesting to note that most of plots of cell potential vs. current density appear to shift to lower potentials at currents higher than the i_{Lim}. This can be seen in figures 5.12a, 5.12b, 5.13b and most predominantly in figure 5.13a. This observation has been witnessed in other limiting current experiments [131]. It is thought that this shift towards lower potentials is due to an increase in surface area, caused by the roughening of the deposit surface when the i_{Lim} is reached.

Despite these issues, the limiting current plots that were obtained can still be used to measure a limiting current within approximately ±5 mA/cm^2 by using the line bisection method used in figure 5.1. According to the plots in figure 5.12, the i_{Lim} at a square feature in the middle of the plate when using ultrasound powers of 30, 40 and 60 W/L is approximately 70, 80 and 90 mA/cm^2 respectively. This demonstrates the increase in the mass transfer of Cu^{2+} ions with increasing ultrasound power, as stated in chapter 5.2. The diffusion boundary layer thickness was calculated to be 15 – 19 μm; similar to the thickness observed in the small-scale cell when using the ultrasound probe at similar powers. This shows that the same enhancement to mass transfer of Cu^{2+} can be achieved using this ultrasound tank geometry.

When using the square anode in position B in the corner however, there doesn't appear to be a significant change in the i_{Lim} at varying ultrasound powers. The plots in figure 5.13 shows that the i_{Lim} is approximately 80 mA/cm^2 for all three ultrasound powers that were tested, suggesting that varying the ultrasound power does not have a significant effect on the mass transfer in the narrow electrode gap near corners of this A7 size tool. This may be caused by a lower cavitational activity in this area or a lower flow rate of the ultrasonic waves as the forced convection flows could be more

restricted in this region. An illustration of an example of what the fluid flow could look like within the inter-electrode gap across the A7 electrode plate, based on the location of the transducers, is shown in figure 5.14. The observation of flow patterns on some of the deposits also provided evidence for this flow regime.

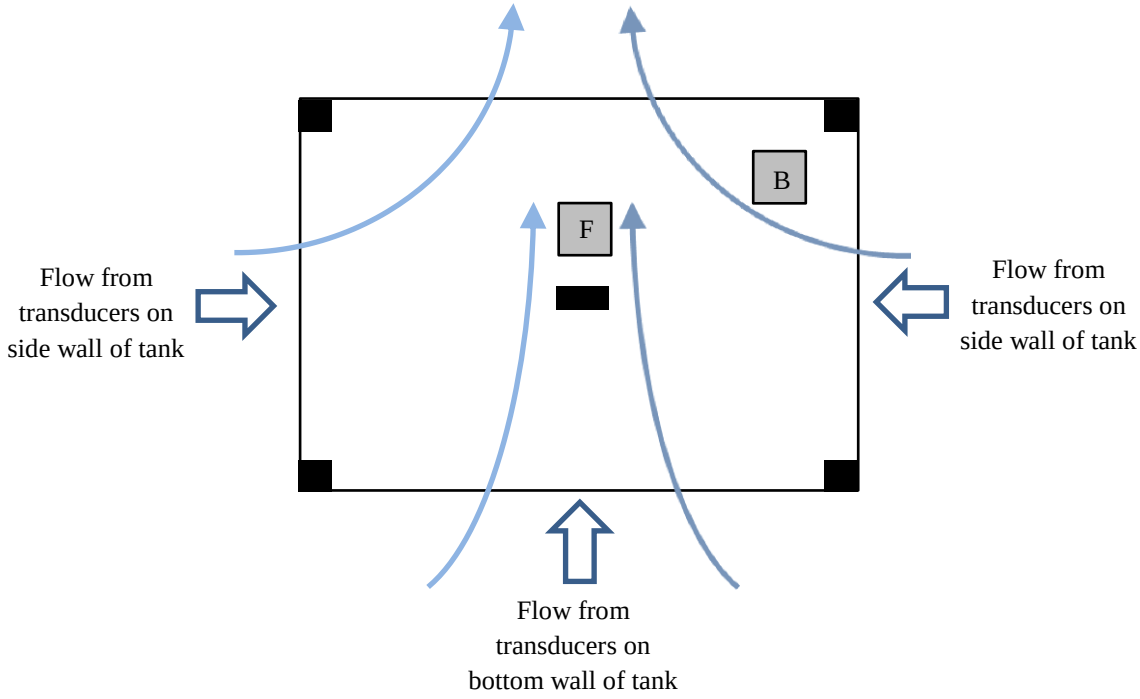

Figure 5.14 – Example of the flow regime across the electrode plate within the inter-electrode gap in the 18 L ultrasound tank

The diffusion layer thickness at varying US powers for both the probe system and the US tank system is shown in figure 5.15. There appears to be less dependence of ultrasound on the thickness of the diffusion layer when using the US tank. However, thinner diffusion layers are formed in the US tank compared to the using the US probe when operating at the same powers. When using higher US powers the probe provides slightly smaller diffusion layer thicknesses. This possibly due to the focused jet-like flow of the ultrasound compared to the uniform agitation provided by the US tank. In any case, it is more beneficial to use the lower powers as stated in the previous chapter.

The mass transfer can be analysed further with the use of dimensionless analysis allowing for a comparison between the two ultrasound systems. The values of the diffusion layer thickness were used for dimensionless analysis calculations. This was carried out by using the same diffusion coefficient (D) and kinematic viscosity (ν) used for the dimensionless analysis for the small-cell and ultrasound probe with values of

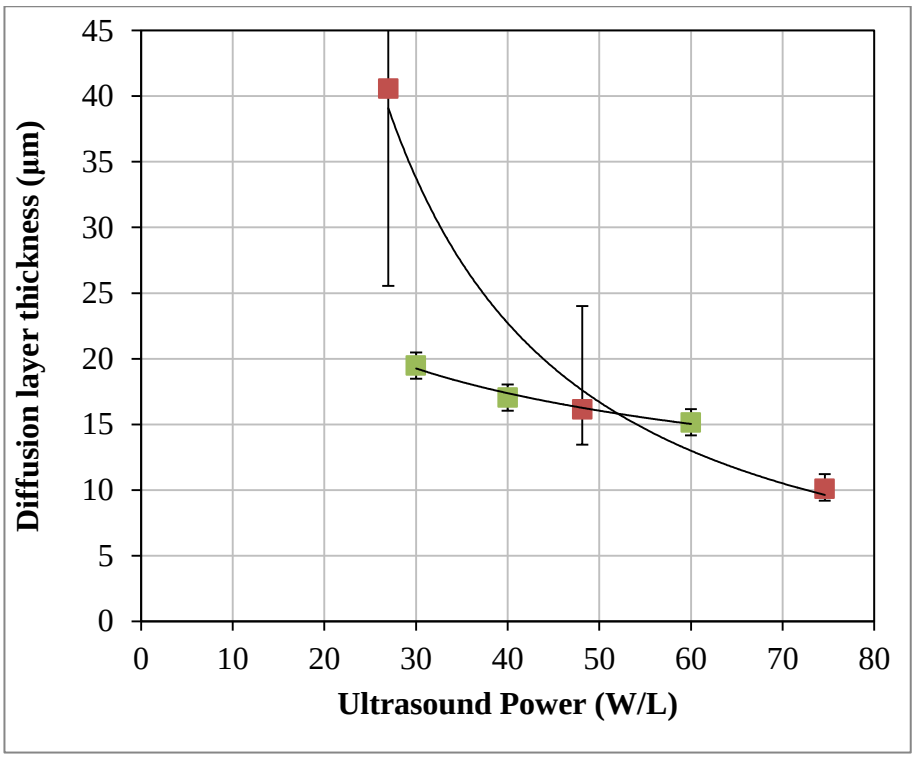

Figure 5.15 - Diffusion layer thickness (δ) calculated using experimental limiting currents as a function of US power for US probe system (Red) and US tank system (Green) at the same electrode gap of 1.5 mm.

7.07 x 10^{-6} cm^2/s and 1.00 x 10^{-2} cm^2/s respectively. The Schmidt number was therefore also the same with a value of 1420. The hydraulic diameter (d_H) was calculated using the same method as before, and due to similar dimensions this is also the same value as in the small-cell, 0.261 cm. The same electrode gap of 1.5 mm was used and therefore the analysis will enable a suitable comparison between the two systems.

Some studies have measured changes in pressure within ultrasound tanks using hydrophones [80] as well as the cavitational activity in different areas of an ultrasound tank [81, 132], but to the best of the author's knowledge there are no studies which have calculated or simulated the fluid flow within an ultrasound tank. Even if this was the case, each ultrasound tank has different flow regimes due to the differences in transducer placement. The same relationship for the fluid velocity for an ultrasound probe by Eklund [76] that was used in the previous chapter was therefore used for the US tank. The values of fluid velocity and Reynolds number are shown in table 5.3.

It is important to note that the fluid velocities provided by Eklund's relationship (in figure 2.13 will be different from the actual fluid velocities within the ultrasound

tank due to different geometries. Eklund's geometry is a 'free electrode' whereas this system is a narrow channel. Therefore, instead of the fluid flowing past the electrode surface and then freely flowing into the bulk of the electrolyte solution from any direction, the fluid is forced through a narrow channel. This causes other turbulences to form due to the interaction between both of the momentum boundary layers formed at either electrode.

In order to develop a dimensionless analysis for the tank system some assumptions were made in order to calculate the flow velocity at varying powers in the US tank. It was assumed that the flow velocity of US in the tank was uniform throughout the volume of the tank, apart from within 30 mm from the tank wall due to information from the US tank manufacturers. Power calibration tests were carried out by placing a thermocouple at various locations within the tank, which confirmed the uniformity in power dissipation throughout the tank and detected higher powers at distances less than 30 mm from the tank wall.

It was also assumed that the fluid velocity at a distance of 30 mm from the ultrasound probe is the same as the fluid velocity at distances > 30 mm from the US tank wall when operating at the same ultrasound power. This is a reasonable assumption, as the probe tip and tank wall are both acting as a vibrating surface which are vibrating at a very similar frequency. The calculation of the flow velocity (U) in the tank was therefore estimated by first converting the ultrasound power in the tank from W/L to W/cm^2, and then the relationship in figure 2.14 was used to calculate the corresponding velocity, shown in table 5.2. As there is no data available concerning the flow velocity within US tanks, this was the most suitable way in which to calculate a reasonable estimate.

Table 5.2 - Diffusion layer thickness, calculated fluid velocity and dimensionless numbers at various ultrasound powers in the 18 L ultrasonic tank

Power (W/L)	Power, converted to W/cm^2	Diffusion layer thickness, δ (μm)	Sh	Velocity, U (cm/s)	Re
30	11	19.5	513	32	840
40	15	17.0	587	41	1070
60	23	15.1	660	59	1530

The Sherwood-Schmidt-Reynolds number correlation for copper deposition within the 1.5 mm with the large electrodes in the US tank at position F is shown in figure 5.16 alongside the correlation for the same electrode gap in the small cell within a similar range of US powers. The correlation equations for the small and large electrodes are shown in equations 5.10 and 5.11 respectively, calculated from the line of best fit.

It is important to note that the mass transfer correlations are based on the velocity of the flow of ultrasound waves, and do not incorporate turbulences from the flow from high number of individual cavitation bubble collapses due to the large amount of cavitational activity that is present. It is possible that the collapse of a cavitation bubble can produce liquid jet velocities of 280 m/s [66].

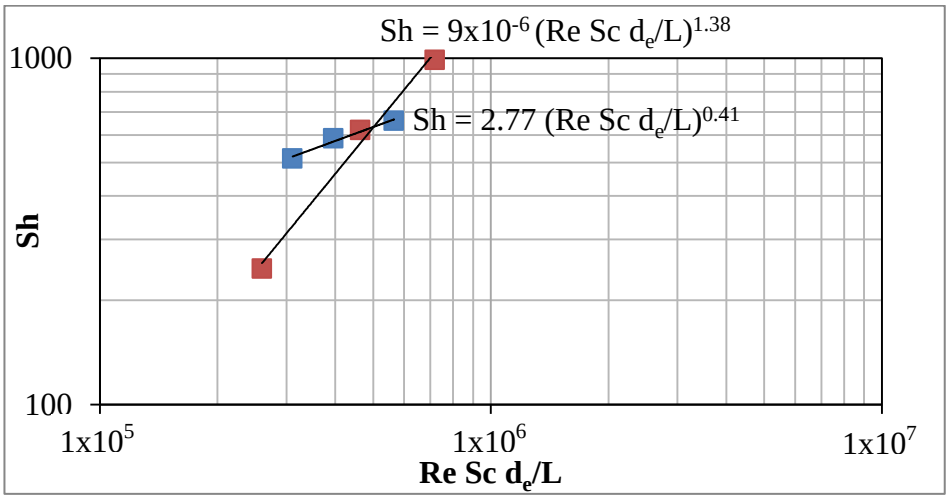

Figure 5.16 – Mass transfer correlations using US agitation with an electrode gap of 1.5 mm, in the small-cell with and US probe (red) and in the US tank (blue).

$$Sh = a\left(Re\ Sc\ \frac{d_e}{L}\right)^b \qquad (5.9)$$

$$Sh = 9 \times 10^{-6}\left(Re\ Sc\ \frac{d_e}{L}\right)^{1.38} \qquad (5.10)$$

$$Sh = 2.77\left(Re\ Sc\ \frac{d_e}{L}\right)^{0.41} \qquad (5.11)$$

In any case, by comparison of the correlations it appears as though that the small-scale US probe system has fully developed turbulence and the large scale ultrasound tank system has developing turbulence, with regard to the value of b in

equations 5.10 and 5.11. These differences are due to the different flow regimes for probes vs. tanks and also the geometry of the electrode systems. The small-scale system is essentially a short electrode, with the ultrasound source providing forced convection flow from the top. The large-scale system is a long electrode, with flow from the bottom and the sides of the electrode gap. In these ultrasound systems, the high fluid velocities and intense agitation cause the natural convection flows to become negligible compared to the forced convection. These systems are therefore mainly controlled by the turbulent forced convection flows provided by the ultrasound. A more detailed explanation of the comparison of the mass transfer in these systems is presented in the discussion in chapter 7.

The experiments proved that ultrasound agitation is suitable for the Enface process in terms of its mass transfer enhancement. Ultrasound agitation significantly improved mass transfer by increasing limiting currents by a factor of 10 compared to silent conditions in the Enface system. Relatively low ultrasound powers of 9 – 18 W/cm^2 provided the most effective agitation. Decreasing the probe-electrode distance increased stirring at the electrode surface. However, the ultrasound source should not be placed closer than 30 mm due potential interactions that can occur.

Mass transfer correlations showed that ultrasound agitation from an US probe provides developing turbulence and fully turbulent flow occurs within larger and narrower electrode gaps respectively. Developing turbulent flow was shown to be present between the A7 plate electrodes in the large-scale system. Turbulent flows are required for the Enface system to ensure sufficient agitation of the electrolyte within the narrow gap. Similar diffusion layer thicknesses were measured in the flow cell, small-scale cell and large scale US tank systems. Additionally, similar values of limiting current were observed in the middle of the plate to the corners of the plate showing that agitation is relatively uniform across the A7 electrode plate.

It has been shown that the mass transfer conditions provided by ultrasound agitation were suitable for the scale-up of Enface. Pattern deposition experiments were then carried out to assess the scalability of the Enface process in terms of the quality of the pattern deposits that could be achieved with the use of ultrasound.

Chapter 6. Results: Deposition of patterns on small-scale substrates

6.1 Deposition experiments in the Flow cell

6.1.1 Deposition with fully exposed copper anode

The first deposition experiments in the flow cell were carried out with a fully exposed copper anode, the results of which are shown in figure 6.1. The photo in figure 6.1(b) shows the copper deposit obtained after applying 46 mA/cm^2 for 300 s with an electrolyte flowrate of 40 cm^3/s. This was the current density and flowrate which achieved good pattern transfer of copper deposits in a previous study [20].

Holes were observed in the deposit which are most likely to have been formed due to the lodging of bubbles between the electrodes therefore hindering the deposition in that region. Optical microscope images of these holes, such as the image in figure 6.1(a), showed that the holes ranged from sizes of 100 – 500 μm in diameter. These would be a fairly large bubble size if they were formed from hydrogen evolution reaction. They are more likely to have formed elsewhere in the flow system, such as during pump start-up, despite the system being flushed for several minutes before current was applied. Bubble entrapment has been known to be a major hindrance in both etching [11] and deposition [20] pattern transfer experiments in a similar flow cell.

Figure 6.1(a) also illustrates that there are effects on the deposit in the region surrounding where the bubble was entrapped due to the flow of electrolyte around the bubble. Another interesting observation is the formation of streaky deposit patterns from the bottom edge. A more detailed view of the deposit surface of areas (i), (ii) and (iii) indicated in figure 6.1(b) is shown in figure 6.2(a).

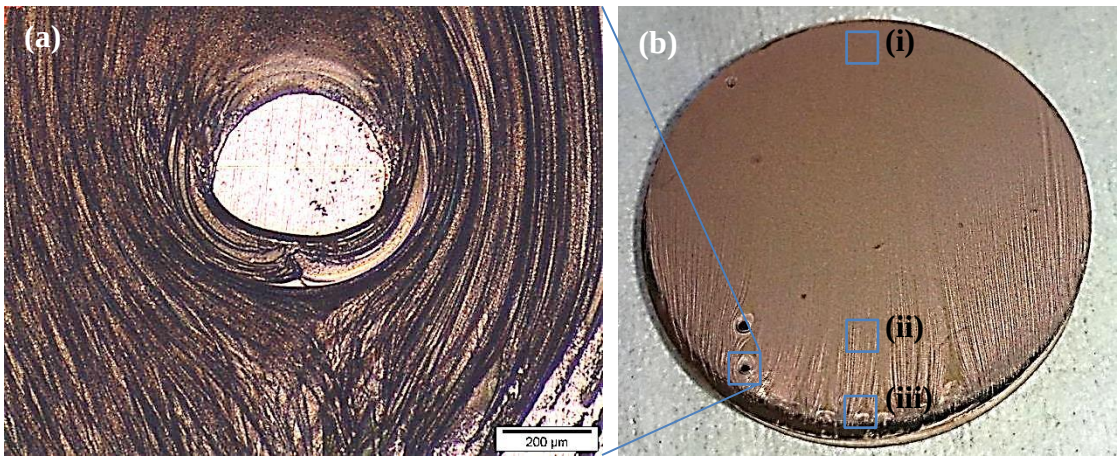

Figure 6.1 – (b) Photo of copper disc with copper deposit plated with a fully exposed copper anode at 46 mA/cm^2 for 300 s with an (a) optical microscope image of deposit where a bubble has been lodged within the electrode gap during deposition, mag x5

Despite the fact that a fully exposed copper anode was used, the deposit at the very bottom edge, shown in figure 6.2a(iii), consisted of the formation of copper deposit lines. These develop into more well defined copper lines moving up the electrode, as shown in the image of the deposit 3 mm from the bottom edge in figure 6.2a(ii). There are two different copper deposit types in this region, dull copper lines and brighter copper lines, alternating in parallel to each other across the electrode surface. A more uniform deposit is formed moving further up the electrode, as shown in the image of the deposit at the top of the electrode in figure 6.2a(i).

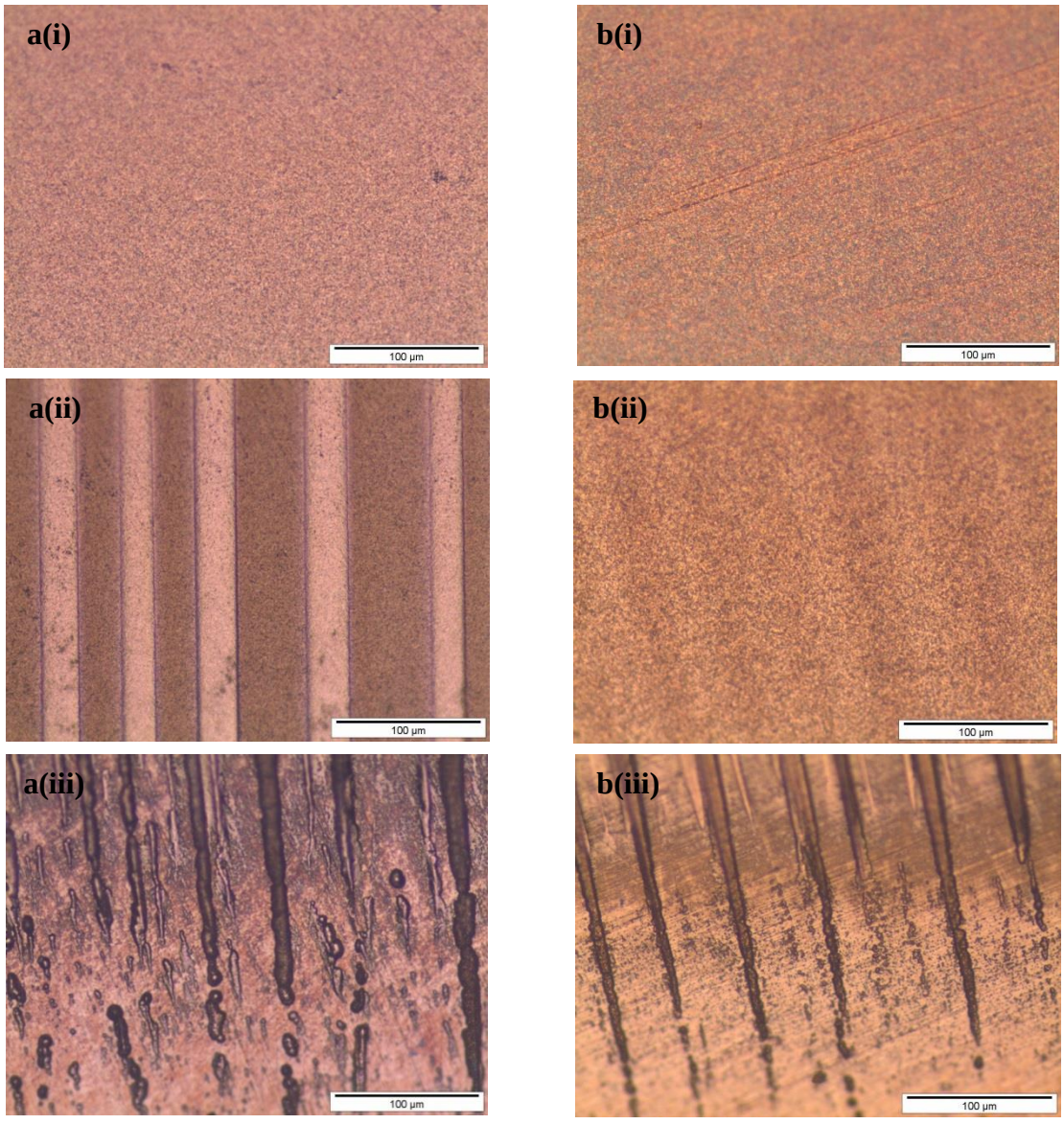

Figure 6.2 – Optical microscope images of copper deposit on a copper substrate plated with a fully exposed copper anode at (a) 46 mA/cm^2 for 60 s and (b) 94 mA/cm^2 for 31 s at various positions on the substrate (i) Near the top edge of the disc, (ii) 3 mm from the bottom edge, (iii) Near the bottom edge (mag x 20)

It is suggested that this deposit formation was caused by flow instabilities within the flow cell. The section of the Perspex electrode holder directly beneath the electrode was analysed by an optical microscope, shown in figure 6.3. Grooves that were formed during the machining of the holder had widths of 25 to 55 μm, similar to the width of the copper deposit lines formed at the bottom of the cathode, illustrated by comparison of figures 6.3 and 6.2a(ii).

This suggests that the flow of the electrolyte directly before the electrode surface may have been disturbed by these machined grooves. For example, the speed of electrolyte flow directly above a groove may be different to the speed of flow directly above a region where no groove is present. A faster electrolyte flow over a region of the electrode surface means there will be a faster mass transport rate of Cu^{2+} ions towards that region of the surface. This results in the sections of brighter copper deposit lines that were observed. Moving further up the electrode, these flows lines moving at different speeds may mix together due to developing turbulence. This means a more uniform electrolyte flow across the top section of the electrode would be achieved, resulting in the more uniform deposit formation observed.

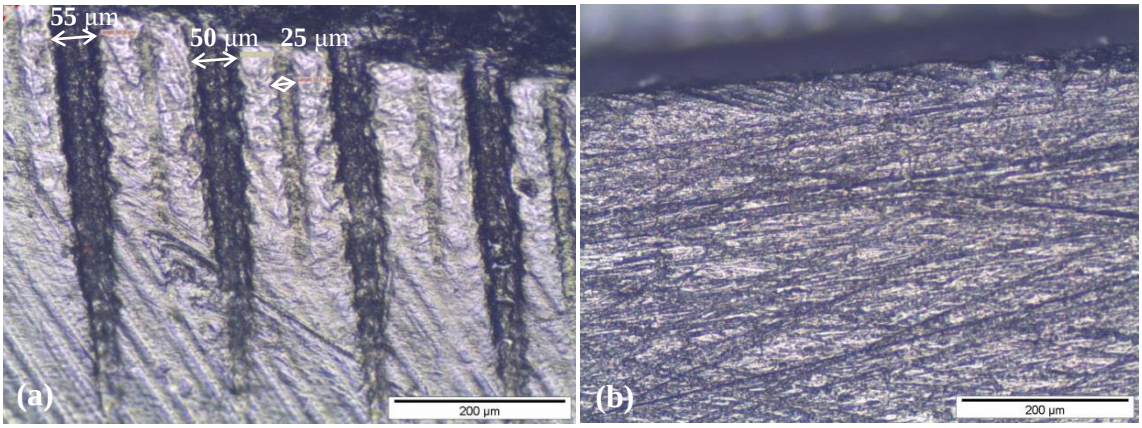

Figure 6.3 – Optical microscope image of bottom edge of the electrode holder, directly below where the electrode disc is positioned, (a) before polishing, showing grooves made during machining of the perspex holder, (b) after polishing, mag x 10.

Figure 6.2b(iii) shows that a similar deposit line formation occurs at the bottom of the electrode when plating at a higher current density of 94 mA/cm^2, thought to have formed for the same reasons as described above. However, the well-defined copper lines that were present at 3 mm from the bottom edge of the electrode at 46 mA/cm^2 (fig. 6.2a(ii)) are less distinguishable in the same region on the deposit plated at 96 mA/cm^2.

Instead very faint lines are observed on the deposit as shown in figure 6.2b(ii). It is unclear why this occurs, but it is thought that this could either be due to a difference in current distribution at higher current densities or slight variances in the hydrodynamics with each experimental run.

The area of the Perspex holder was polished thoroughly with #1200, #2400 and #4000 SiC paper in order to try and alleviate the flow instability problems for the following deposition experiments. The bottom edge of the electrode holder after polishing is shown in figure 6.3(b), showing that the grooves have been removed. This was carried out so that the flow of electrolyte would be more uniform over the electrode disc. It was hoped that less streaky deposits will be plated when deposited pattern features, the results of which will now be discussed.

6.1.2 Deposition with resist patterned copper anode

Copper pattern deposition experiments were carried out on 20 mm diameter copper discs, twice the diameter of discs used earlier in a similar flow cell [20]. The photoresist patterned anode with 100 μm wide exposed copper lines with 500 μm of resist in-between is shown in figure 6.4. The spreading of the photoresist during the spinning process caused an unavoidable 0.67 mm wide rim of thicker photoresist at the disc edge, as shown in the photo in figure 6.4. The pattern did not fully develop in this region; therefore this area was not included when estimating the area of exposed copper surface on the disc, calculated to be 0.395 cm^2. This area was used in the calculation of the current density.

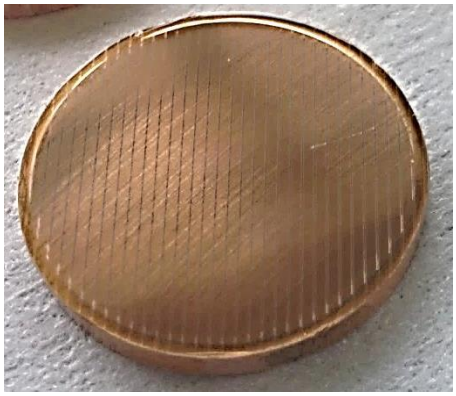

Figure 6.4 – Photo of 20 mm copper anode tool with photoresist linear pattern

Figure 6.5 shows an optical microscope image of the disc and a profilometry across an exposed copper line showing the thickness of the photoresist was approximately 3 μm, as illustrated in figure 6.5(b).

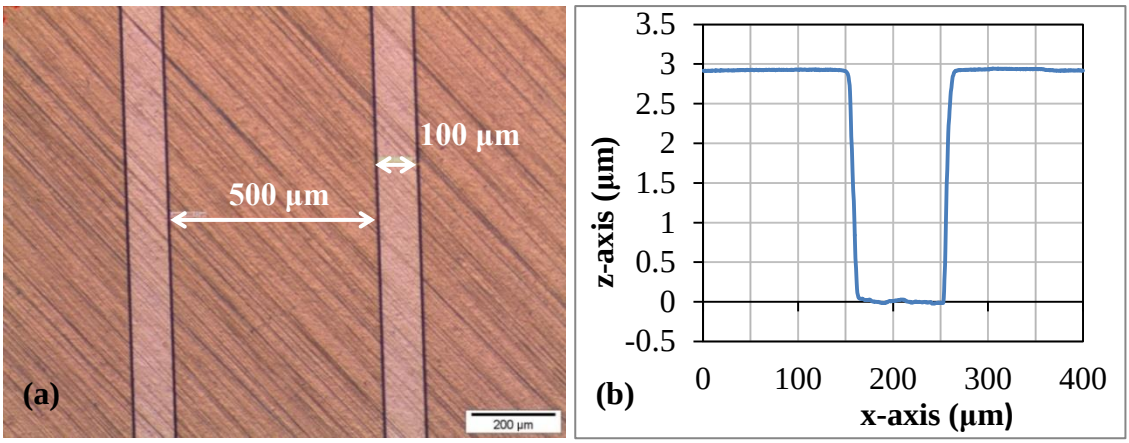

Figure 6.5 – (a) Optical microscope image of copper anode tool with linear photoresist pattern with 100 µm exposed lines of copper. (b) Profilometry of photoresist on the copper anode tool

The deposit pattern that was transferred onto a copper disc at 46 mA/cm^2 using the anode in figure 6.4 is shown in figure 6.6(a). Optical microscope images of the areas indicated in figure 6.6(a) are shown in figures 6.6(i) and 6.6(ii). In the region (ii) reasonably good pattern transfer was achieved. The width of the line is 30% larger than the original anode feature, similar to what was observed in the deposition of the same pattern onto 10 mm diameter substrates [20]. This larger feature width is caused by the spreading of current lines between the anode feature and cathode surface. There appears to be small streaky patterns on the deposit pattern lines which are likely to be due to flow instabilities within the flow cell which are still present despite polishing the electrode holder.

Figure 6.7(a) shows the deposit pattern plated with the same patterned anode at a higher current density of 94 mA/cm^2. The deposited pattern was not as clear as that plated using the lower current density. The deposit is streakier with a number of circular holes suggesting the presence of bubbles trapped on the electrode surface. Despite this, it was still possible to measure some of the deposit line widths, shown in figure 6.7(b). The deposit lines are wider than the lines deposited using the lower current density, some of which were more than 3.5 times greater than the width of the anode features. This suggests that the effect of current spreading is more significant at higher currents.

Often the deposits would appear even streakier than the deposits shown in figures 6.6 and 6.7, or even more bubble entrapment would occur hindering the deposit. It was therefore very difficult to reproduce these pattern deposits by experimental repeats making it impossible to gather a large amount of data.

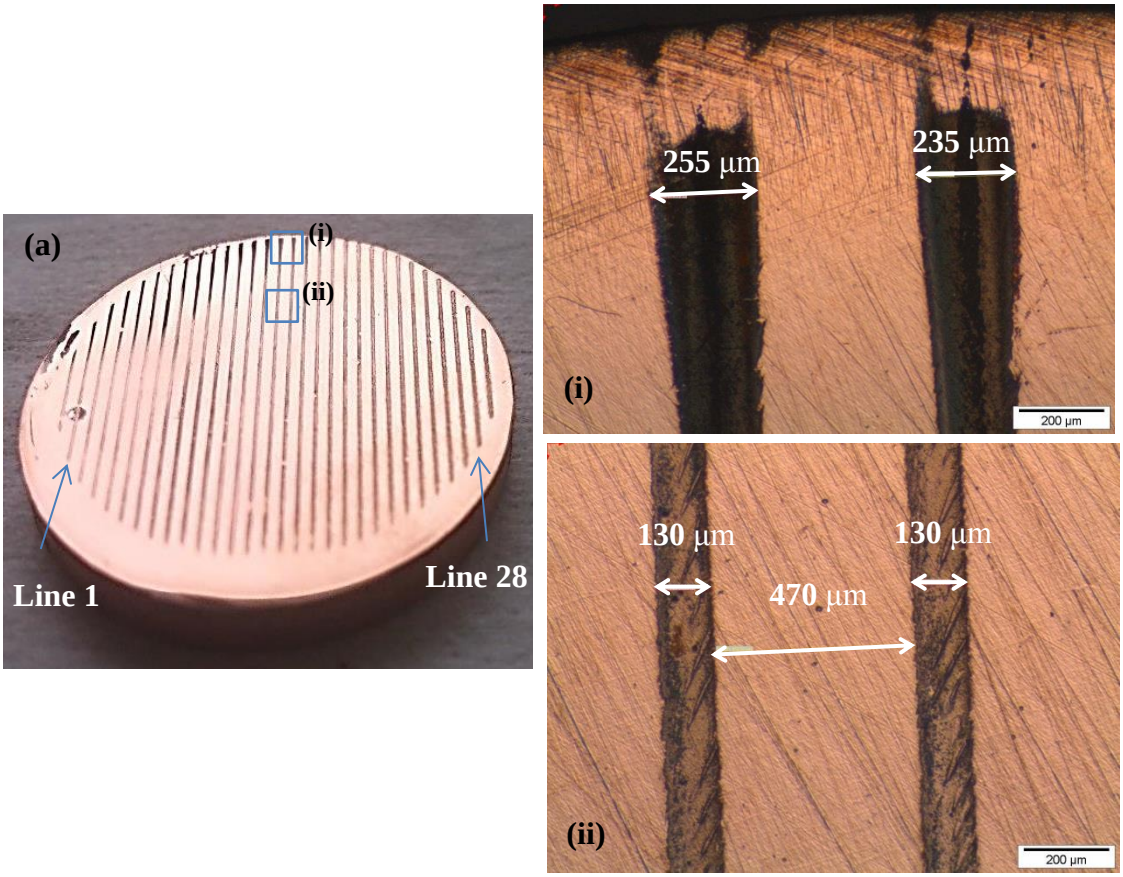

Figure 6.6 – (a) Photo of copper substrate with a deposit of copper lines plated using a patterned copper anode tool with 46 mA/cm^2 for 300 s and an optical microscope image of deposited copper lines (i) Near the top edge and (ii) 3 mm from the top edge of the copper disc (mag x 5)

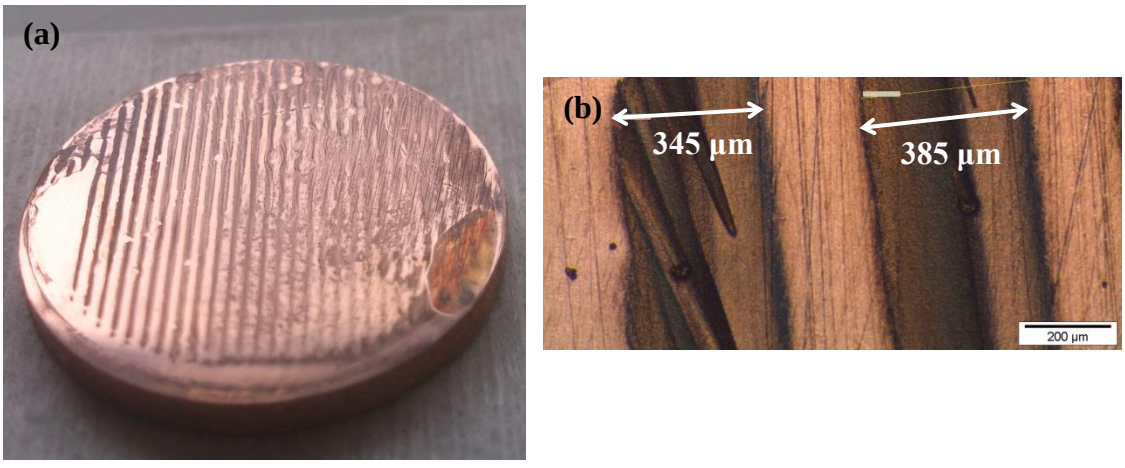

Figure 6.7 – Photo of copper substrate with a deposit of copper lines plated using a patterned copper anode tool with 94 mA/cm^2 for 147 s and an (b) optical microscope image of deposited copper lines 3 mm from the top edge of the copper disc

However, it was still possible to gain useful data on the variation in deposit line widths across the surface of the electrode plated at 46 mA/cm^2 in figure 6.8. At the top of the electrode the width of the lines can be more than 2.5 times greater that the anode feature width, shown in figure 6.6(i). The deposit is much darker in this region suggesting there are higher current densities in this region. The deposit line widths across the entire surface of the disc are shown in figure 6.8.

The lines were numbered left to right from 1 to 28, as indicated in figure 6.6. An optical microscope was used to measure the line widths at 5 different places along each line; the top of the line, 3 mm from the top, in the centre of the line, 3 mm from the bottom, and the bottom of the line. The plot of the line width at these various locations across the disc in figure 6.8 shows a variation within a range of approximately 130 to 250 μm. Not all lines were included for clearer readability.

It can be clearly seen that broader lines were present at the top and bottom of the electrode and the broadest lines were measured at the top middle section of the electrode. There is also a slight broadening of the lines from left to right along the top of the electrode. The narrowest deposit lines were achieved in the region measured 3 mm from the top indicating that this is the region where best pattern transfer is achieved. This widening of features was observed earlier during metal etching [11].

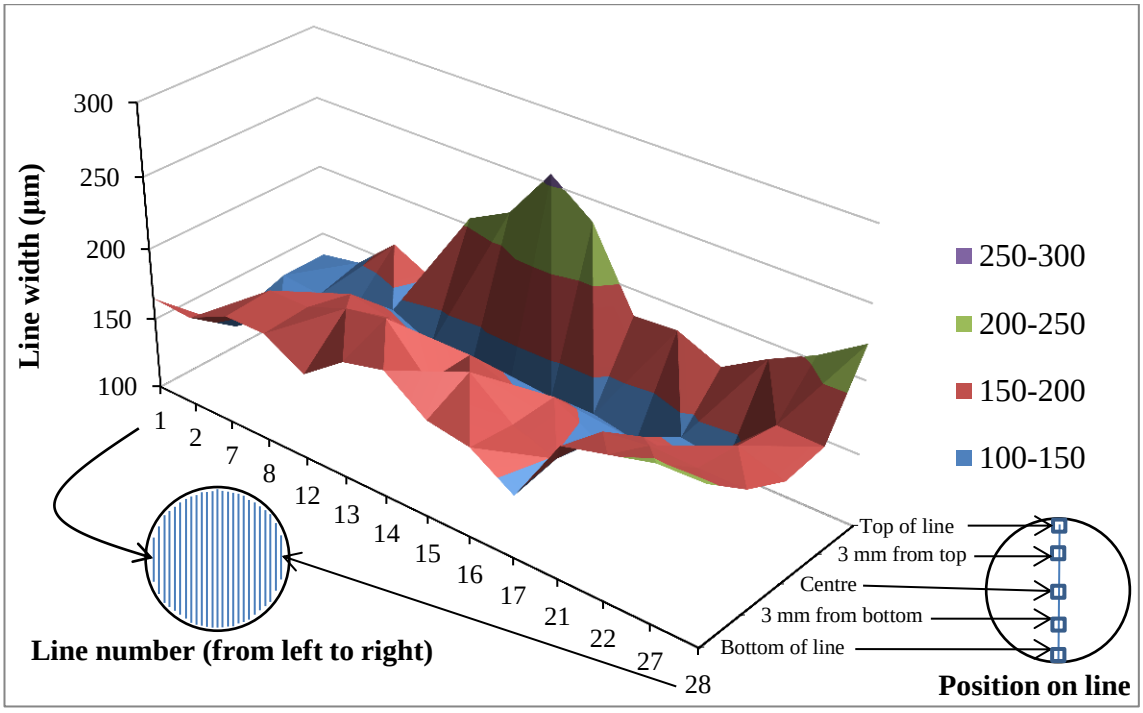

Figure 6.8 – Width of deposited copper lines plated on the cathode with 46 mA/cm^2 for 300s, shown in figure 6.6a, at various locations across the surface of the disc, as shown. Cathode disc was plated using a patterned anode with features sizes of 100 μm.

Profiles were measured across the width of the deposited feature in the middle of the electrode disc at different locations along the length of the line, shown in figure 6.9. It was observed that dendritic deposits were present in the region closest to the top edge of the disc. This is shown by the large dendrite structure shown in the profile of a line measured next to the edge in figure 6.9. Several repeats of this profile measurement were taken and each measurement gave a similar profile shape. An observation of a thicker deposit at the edges of the electrode has been witnessed in previous deposition investigations in a vertical flow channel [39].

Figure 6.9 also shows the decrease in deposit thickness moving down the length of the electrode. At the very bottom of the electrode a very low thickness was measured where very small copper nucleation was observed, suggesting that the current densities in this region were lower. This is thought to be due to a larger electrode spacing at the bottom of the electrode gap compared to the top.

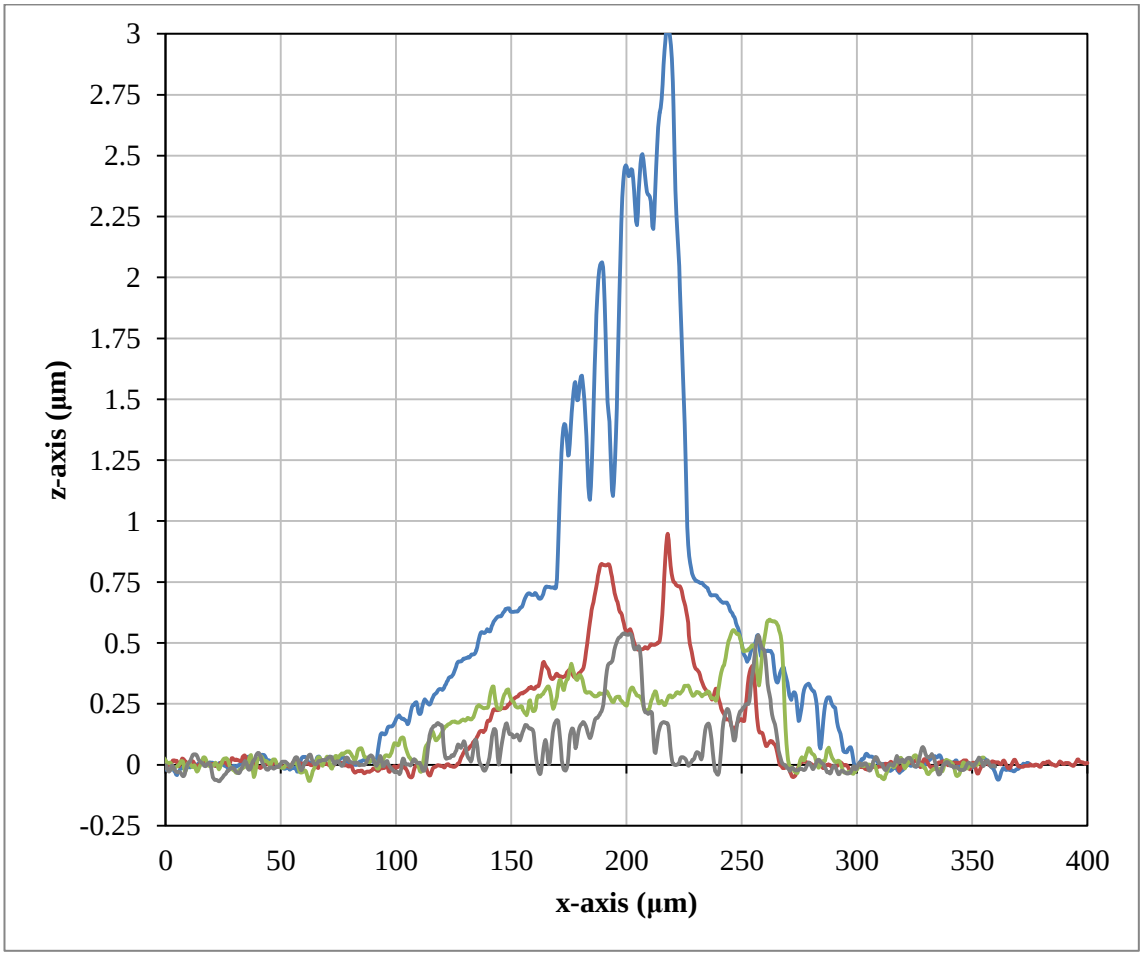

Figure 6.9 – Profilometry across deposited copper lines plated with 46 mA/cm2 for 300 s, shown in figure 6.6a at varying place along the length of the middle line; Near the top edge (blue line), 3 mm from the top edge (red), centre (green) and the bottom edge (grey)

The observations and variation of both the line widths and the deposit thickness of the copper deposit features can be explained by two main reasons; (1) Current distribution across the electrode disc, resulting in higher current densities at the edges compared to the centre, (2) Differences in the spacing between the anode and cathode.

Reason (1) would explain the observation of the wider features at the edges of the electrode. It would also explain the observation of the dendritic and powdery black copper oxide deposit features located at the top of the electrode shown in figure 6.6(i) which would form at high current densities.

Reason (2) involving differences in the electrode gap can be caused by various factors, including the following.

- The curvature of the electrode surface due to polishing causing a difference in electrode gap in the centre compared to the edges, witnessed in previous flow cell deposition experiments [11, 20]
- Repeated polishing of the electrode surface may cause the electrode to be slightly more recessed in its holder than previous experiments, therefore increasing electrode gap
- Electrodes may be positioned in holder so they are slightly angled in such a way that there is a difference in electrode gap along the length of the electrode, causing a difference in the developing mass transfer boundary layer from the bottom edge of the electrode

These could all contribute to a variation in the inter-electrode gap across the electrode, which would affect current spread at different locations on the cathode surface, resulting in the deposit line width variations described above. The fact that the best pattern transfer performance was achieved in-between the centre and top section of the electrode suggests that this region is far enough away from the current distribution and mass transfer effects to be insignificant and also that the electrode spacing was at the correct distance in this region.

The factors described above which contribute to the difference in electrode spacing demonstrates some of the issues with using this flow cell system for the scale-up of the Enface process. Additionally, the geometry of the cell and the constant disassembling and reassembling of the cell for every pattern transfer would not be practical for an industrial large-scale process. Deposition experiments in a more conventional tank-type system were therefore investigated.

6.2 Deposition Experiments in Small-scale Cell

Electrodeposition of copper patterns was carried out in the small-scale 500 mL cell onto 10 mm diameter nickel electrodes in 0.1 M $CuSO_4$ in order to test different deposition modes. The anode tool that was used was simply made from a 10 mm diameter copper disc covered in a non-conductive tape with a 1 x 5 mm rectangle cut out, leaving an area of exposed copper surface. An example of this tool is shown in figure 4.8. The first set of experiments was carried out under silent conditions using direct current.

6.2.1 Electrodeposition using direct current

The first pattern deposition mode was using direct current under silent conditions using the anode tool with a 1 x 5 mm exposed anode feature. The plating current densities that were chosen were a percentage of the i_{Lim} current as copper plating is always carried out at currents which are lower than the limiting current, which in this system is -80 mA/cm^2, measured previously. Plating current densities of 50% i_{Lim}, 75% i_{Lim} and 100% i_{Lim} were used.

Experiments were carried out at 50% i_{Lim} as it is common to plate copper at 20-50% i_{Lim} [20, 133]. The reason why the upper limit has been chosen for these experiments is due to the lower concentration of $CuSO_4$ which is required for the Enface process compared to conventional plating processes. This means a longer deposition time would be required to gain the same thickness in a standard plating bath. Higher current densities may therefore have to be used if this process is to be used in industry so that plating times are reduced.

75% i_{Lim} was used to test the limits of the plating process to test whether pattern transfer could be achieved with Enface at even higher current densities. This percentage of current density is commonly used for copper-foil production and electroforming [134]. Experiments were carried out at 100% i_{Lim} to demonstrate the consequences that occur when plating at the limiting current.

6.2.1.1 Profilometry of deposit features

The profiles of copper deposit features plated on a nickel substrate with a 1 x 5 mm rectangle of exposed copper anode surface are shown in figures 6.10a, 6.10b and 6.10c, which were plated at 50%, 75% and 100% i_{Lim} respectively. There appears to be steeply angled sections at the very edges of the profiles, at either side of the deposit. This was only due to instrumentation issues arising from disc curvature, which was corrected later as per description in the experimental section, see fig. 4.21.

Profiles across the center of copper features plated at 50% i_{Lim} and 75% i_{Lim} under silent conditions show that these deposits have a thickness of 4-5 μm. The deposit plated at 100% i_{Lim} appears to have a very thick rough section in the middle with a thickness of approximately 12 μm. The roughness amplitude (R_a) of the centre of the each copper feature was calculated across a 1000 μm length of the profile from several repeated deposition experiments. The average values of R_a are 0.09 ± 0.05 μm, 0.34 ± 0.26 μm and 2.15 ± 0.23 μm for the deposits plated at 50% i_{Lim}, 75% i_{Lim} and 100 i_{Lim} respectively.

It is well known that as the plating current density reaches values closer to the mass transfer limiting current the surface roughness of the deposit increases [131, 135]. When plating at current densities below i_{Lim} the current distribution tends to be fairly uniform [131], when plating at i_{Lim} however, the effect of mass transfer is dominant due to limitation of the metal ions reaching the substrate [122]. Roughness can develop within the range of current densities approaching the i_{Lim} with noticeable roughness forming at 50% i_{Lim} [131], shown clearly by the roughening of the copper deposits within 50 to 100% i_{Lim} of these copper deposit features.

The profile of the deposit feature plated at 100% i_{Lim} (fig 6.10c) appears to have a very dendritic structure in the middle of the feature. It is known that current density is higher on protrusions than the areas that surround them [135]. Small deposit peaks that initially form will therefore tend to grow at a faster rate. At very high current densities these may grow randomly outwards toward regions of higher concentration of metal ions resulting in the formation of dendritic branches [122]. The roughening of the deposits can be further explained by analysis of the deposit surface morphology.

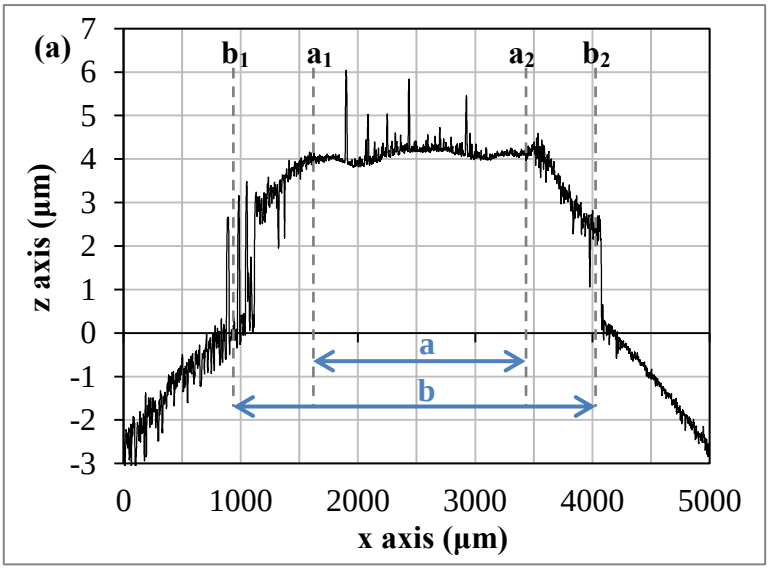

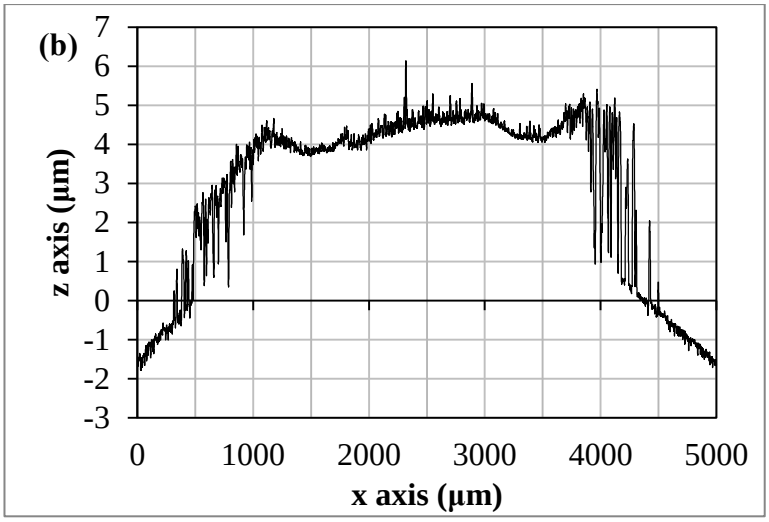

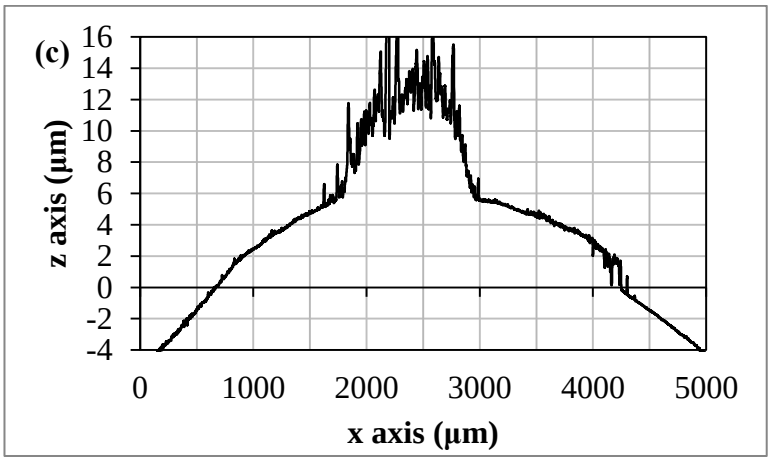

Figure 6.10 – Profilometry of deposited copper features on a nickel substrate plated under silent DC conditions with a 1 x 5 mm of anode feature. (a) Plated at 50% i_{Lim} for 650 s. (b) Plated at 75% i_{Lim} for 450 s. (c) Plated at 100% i_{Lim} for 340 s.

6.2.1.2 Morphology of deposits

SEM and ESEM images of the copper deposits plated at 50% i_{Lim}, 75% i_{Lim} and 100% i_{Lim} are shown in fig. 6.11, 6.12 and 6.13 respectively. An elemental mapping analysis is also shown in figure 6.12 a(ii), measured at the edge of a copper deposit pattern on a nickel substrate. This is the same region as the SEM image in figure 6.12 a(i). The elemental map clearly shows the deposited copper over the nickel substrate demonstrating that the copper patterns covered the nickel substrate surface. The edge of the copper pattern is also well defined. The EDX analysis showed that there was no oxygen present in the copper deposits.

The ESEM images of the centre of the deposits plated at 50% i_{Lim}, 75% i_{Lim} and 100% i_{Lim} are shown in fig. 6.11(iii), 6.12b(i) and 6.13(iv) respectively. Both deposits plated at 50% and 75% i_{Lim} have a closely packed copper grain structure in the centre of the feature, with grain sizes of 0.4 – 2.9 μm and 0.2 - 2.5 μm respectively. However, the ESEM image of the deposit feature plated with 75% i_{Lim} shows that some grains protrude further than those shown in the deposit plated at 50% i_{Lim}. In fact, figure 6.13(iv) shows that the middle of the deposit plated at the highest current density of 100% i_{Lim}, has a very rough and completely dendritic structure.

According to the profiles in fig. 6.10, the widths of the features appear to be quite large with respect to the anode feature width of 1000 μm. For example, it appears as though the width of the feature plated at 50% i_{Lim} is about 3000 μm (distance 'b'), however on closer inspection it was found that this is not the case. There are two distinct sections of the profile; a rough section at the edges (b_1-a_1 and a_2-b_2) and a smoother section in the middle (a_1-a_2). If this is compared with the SEM images of the deposit shown in figure 6.11, it can be shown that the rougher regions (b_1-a_1 and a_2-b_2) consist of a thin rough layer of copper nuclei. The closely packed copper grain structure within the region of a_1-a_2 signifies that the width of the copper feature is closer to 1800 μm (distance 'a') which is 800 μm wider than the anode feature size, caused by current spreading due to curvature in current lines.

The copper nuclei appear to form at the edges of all the deposits, shown in fig. 6.11(ii), 6.12b(ii) and 6.13(ii). The nuclei formation appears to occur along the grooves formed in the nickel substrate during polishing, which can be seen in fig. 6.11(ii) and more clearly in fig. 6.12b(ii). Nucleation is more likely to begin within these grooves because there is a higher surface area of nickel substrate for the copper nuclei to form.

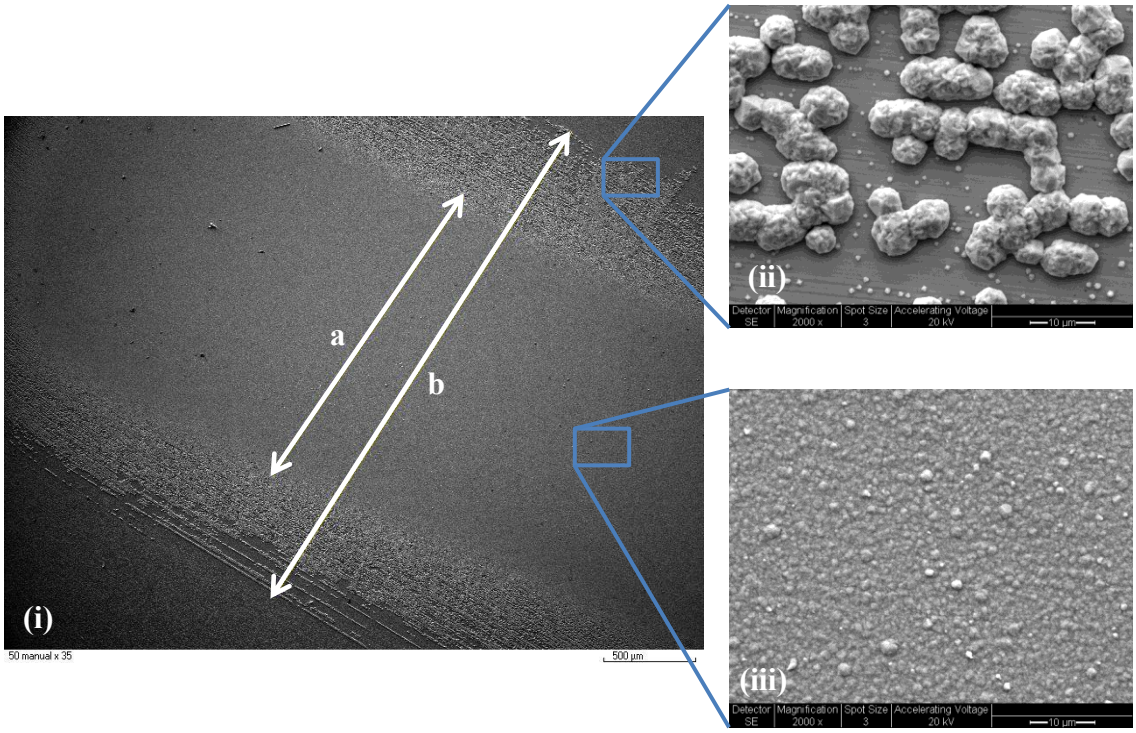

Figure 6.11- SEM images of copper deposit on a nickel substrate plated under silent DC conditions with 1 x 5 mm of exposed anode plated at 50% i_{Lim} for 650 s (i) SEM image, mag x 35 ; a = 1830 µm; b = 2954 µm. (ii) ESEM image, mag x 2000, deposit pattern edge. (iii) ESEM image, mag x 2000, deposit pattern centre.

These edge nuclei have not been recorded in previous pattern transfer investigations [9, 20] when anode tools fabricated with photoresist were used. It is possible that there is a slight de-lamination of the insulating tape at the edges of rectangular feature when it is being cut out with the surgical scalpel. It is therefore suggested that current leaking at the edges of the Kapton tape mask could occur during plating. This could affect the current distribution on the cathode in such a way that low micro-currents are present at the edges of the copper features being plated, resulting in the small copper nuclei formation observed.

By further analysis of the ESEM image in 6.11(ii), two different sized copper nuclei form at the edge of the deposit with diameters of approx. 0.5 – 1 µm and larger nuclei of diameters of approx. 5 – 8 µm. Most of the larger nuclei appear to have an area surrounding them that is depleted of smaller nuclei, which suggests that these large nuclei have been formed via Ostwald ripening.

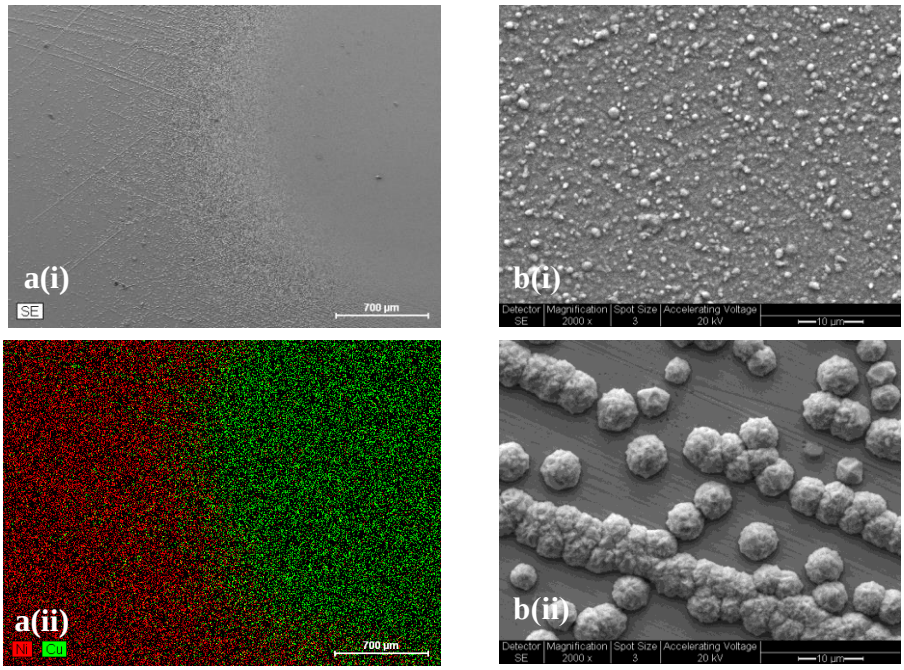

Figure 6.12 – a(i) SEM image of the edge of copper deposit pattern on a nickel substrate plated under silent DC conditions at 75% i_{Lim} for 450 s, mag x 50. a(ii) EDX elemental map analysis of the copper deposit shown in 'a(i)' ; b ESEM images of deposits shown in 'a(i)', mag x 2000 (i) Centre of deposit pattern (ii) Edge of deposit pattern.

The morphology at the edge of the deposit plated at 75% i_{Lim}, shown in figure 6.12b(ii), shows that copper nuclei is again present at the edges of the copper pattern feature. However, there are no small nuclei present, as with 50% i_{Lim}, only large nucleation approximately 4 – 6 µm in diameter. It is possible in this case that the large nuclei have 'consumed' all the smaller nuclei surrounding them via Ostwald ripening as some of these smaller nuclei were found on the substrate further away from the copper pattern feature. However, the electrode was left in the solution for some time after plating had taken place, therefore the small nuclei could have dissolved back into solution during this time.

The edge of the deposit plated at 100% i_{Lim} , shown in figure 6.13(ii) shows large nuclei (4 – 8 um diameter) and many small nuclei (0.2 – 1.0 um diameter). The reason for the high number of small nuclei is because high current densities cause an increase in the deposition potential, which increases the number of active sites [116] therefore creating a high number density of nuclei population [116, 135].

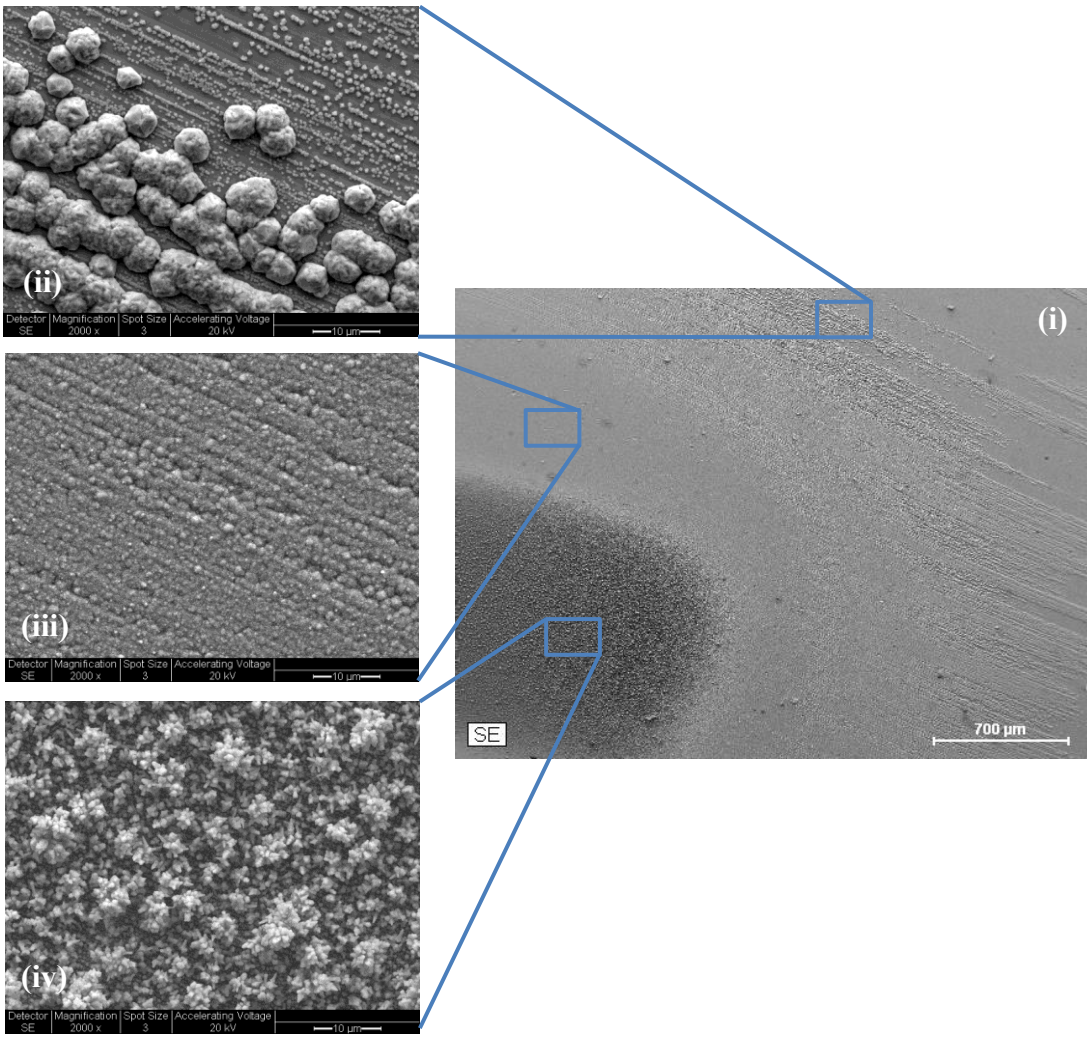

Figure 6.13 - ESEM images of copper deposit on a nickel substrate plated at 100% i_{Lim} for 340 s with 1 x 5 mm of exposed anode. (a) Lower sections of pattern deposit, mag x 50 ; (b) Outer section of deposit pattern, mag x 2000 ; (c) Middle section of deposit pattern, mag x 2000 ; (d) Centre of deposit pattern, mag x 2000.

The morphology of the other areas of the deposit plated at 100% i_{Lim} in figure 6.13, there appears to be two other deposit morphologies as well as the small copper nuclei at the edge. There is a thin copper layer which is a continuation of nucleation growth at the edges (fig. 6.13(iii)) and black dendritic structures (fig. 6.13(iv)). The occurrence of these three different zones is due to the difference in current distribution; during plating the current density appears to be higher in the centre of the pattern feature and lower at the edges. The current density in the centre is high enough for dendritic copper to form when plating at 100% i_{Lim}.

Additionally, some pitted holes of diameters of 5 – 15 μm were found at the top section of the copper deposit pattern feature, shown in figure 6.14. It is most likely that they have been formed due to hydrogen bubbles which are likely to evolve at 100% i_{Lim} because the system is operating very close to the hydrogen evolution potential region. This would cause simultaneous copper deposition and hydrogen evolution to occur, resulting in anchored hydrogen bubbles, seen previously in other copper deposition studies [136]. It is possible that some bubbles of hydrogen generated at the electrode could become trapped within the inter-electrode gap and cause pitting on the copper surface as depicted in figure 6.14. Both the occurrence of hydrogen bubble evolution and dendritic copper formation show that plating at 100% i_{Lim} will not be suitable for subsequent deposition experiments. The following pattern transfer experiments were therefore carried out at 50% and 75% i_{Lim}.

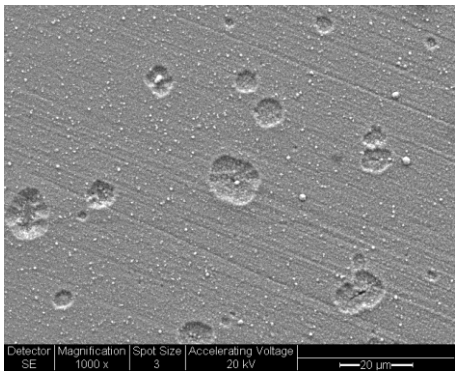

Figure 6.14 - ESEM images of copper deposit on a nickel substrate plated at 100% i_L for 340 s with 1 x 5 mm of exposed anode showing some pitting of the very top section of the deposit, mag x1000

During the silent DC experiments described above, etched copper from the anode would sometimes get trapped within the narrow gap between the electrodes, contributing towards convection flow restriction. When using DC deposition with CUS the lodging of cavitation bubbles would also often occur and build up within the electrode gap. Other deposition modes for pattern plating using the Enface technique had to be investigated to contribute towards the development of the scale-up of this process. A deposition mode which used pulsed US agitation was therefore investigated.

6.2.2 Electrodeposition under pulsing current and ultrasound

A regime was proposed by which US pulses were implemented in the form of short US bursts and were combined with long current pulses. If the current is pulsed in long pulses (seconds), and a short burst of US is made during the off-time of the current pulse then ultrasound is not being used during current plating, but the Cu^{2+} ions are still being replenished within the inter-electrode gap by the US agitation. Also, this deposition mode reduces the overall amount of energy required to power the ultrasound source during the deposition.

Initially experiments were carried out with long current pulses under entirely silent conditions. When plating with 50% i_{Lim}, current pulses of 200 s with an off-time of 25 s was used. When plating with 75% i_{Lim}, current pulses of 150 s was used with an off-time of 25 s. The length of the current pulse is approximately the time that instabilities were observed during entirely DC conditions, discussed later. The off-time was chosen as 25 s as this was slightly longer than the time calculated for the ions to diffuse from outside the gap to the volume of fluid within the inter-electrode gap.

The same anode tool, with a 1 x 5 mm feature of exposed copper surface, was used to deposit features under silent pulsed current and combined pulsed current and US conditions, shown in the photograph in figure 6.15. The profiles of these deposits are shown in figure 6.16 which were used to calculate the roughness across the center of the feature as for the other profiles. The deposit thickness, calculated current efficiency and deposit roughness for the three deposition modes (Silent DC, Silent long current pulses and combined current and US pulses) is shown in table 6.1.

Figure 6.15 – Photo of deposit features plated in small-scale cell with 1 x 5 mm rectangular anode feature. (a) 75% i_{Lim} silent pulsed, (b) 75% i_{Lim} pulsed US, (c) 50% i_{Lim} pulsed US, (d) 50 % i_{Lim}, silent pulsed.

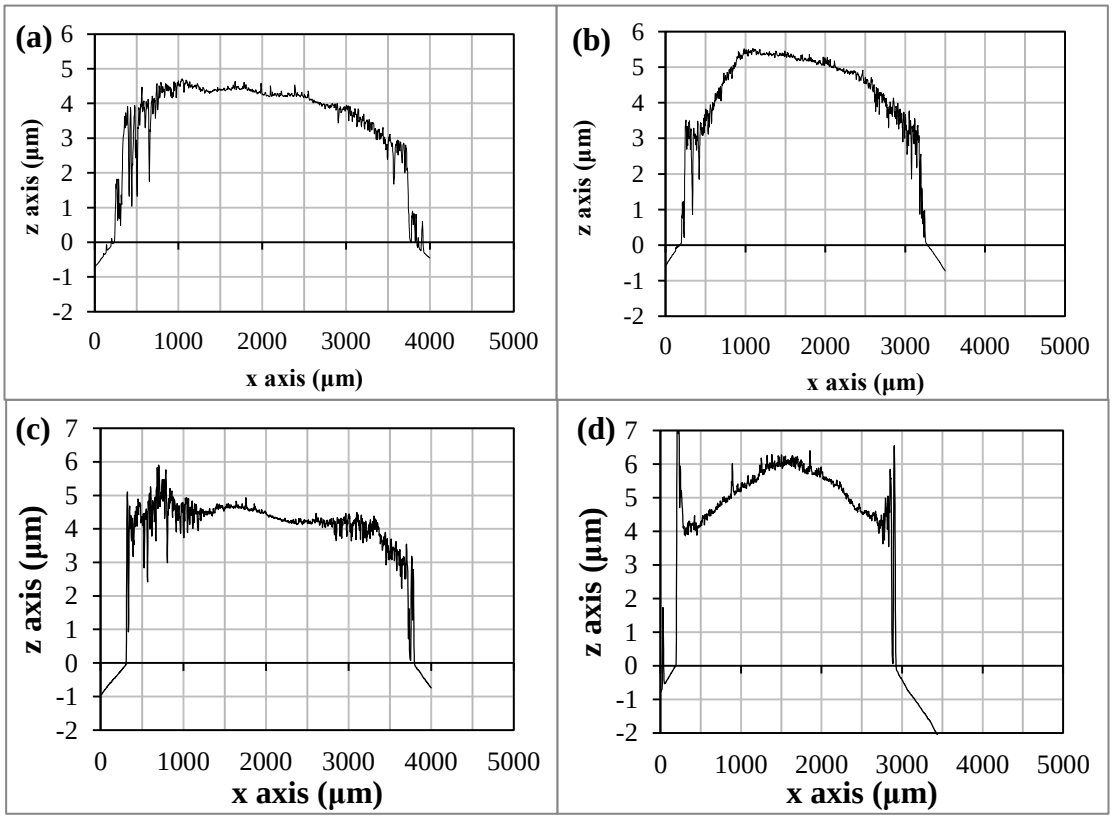

Figure 6.16 – Profilometry of deposited copper features on a nickel substrate with 1 x 5 mm of anode feature plated using long current pulses. (a and b) Plated at 50% i_{Lim} with 200s on-time with 25s off-time under (a) silent conditions and (b) with 10s seconds of ultrasound during the off-time ; (c and d) Plated at 75% i_{Lim} Long current pulse plating at 75% i_{Lim} with 150s on-time and a 25s off-time under (c) silent conditions and (d) with 10s seconds of ultrasound during the off-time, p = 9 W/cm^2 , d_p = 30 mm.

Table 6.1 – Values of deposit thickness, calculated current efficiencies and deposit roughness for different deposition modes plated at 75% i_{Lim}

Deposition Mode	Deposit Thickness (µm)	Current Efficiency (%)	Roughness, Ra (µm)
Silent DC	4.54 ± 0.80	87 ± 10	0.34 ± 0.26
Silent Current Pulsed	4.63 ± 1.73	92 ± 25	0.06 ± 0.01
Current and US Pulsed	5.94 ± 0.82	100 ± 9	0.15 ± 0.06

The average height of the profile across the center of each deposit was used as the measurement of the deposit thickness which was then used to calculate the current efficiencies, displayed in table 6.1. There appears to be a slight increase in the current efficiency when using 'Silent Current Pulses' compared to the 'Silent DC' conditions, but it is difficult to make a comparison between these modes as there is a large overlap in the errors. However, when the combined current and US pulses are used there appears to be an increase in current efficiency to values close to 100%.

Obtaining values of current efficiency higher than 100% may be caused by lower deposit thicknesses in other areas of the feature, or the deposit may be porous which would increase the thickness. It could also be an indication that there is an increase in deposition rate. Other studies which have combined ultrasound with copper electrodeposition have observed significant increases in the current efficiency [122] and also increases in the plating rate by approximately 10% [125].

The roughness of the deposits are 0.06 ± 0.01 μm and 0.15 ± 0.06 μm plated under silent conditions and with US during the off-time respectively. These roughness values are lower than the R_a of the deposits plated under DC conditions and both these values of R_a would be accepted for industrial plating applications. The decrease in deposit roughness when using current pulses occurs because of the relaxation of the diffusion layer during the current off-time [137, 138].

The slightly higher deposit roughness when plating with ultrasound was initially thought to be attributed to effects of bubble collapse which result in the formation of micro-jets. It is known that this can cause pit formation in the deposits surface feature [60]. However, the true reason for the increase in roughness may lie in the deposit surface morphology.

Figures 6.17a and 6.17b show ESEM images of the center of deposits plated using 50% i_{Lim} with long current pulses, with and without US respectively. These are the same deposits of the profiles shown in figures 6.16a and 6.16b. A closely packed copper grain structure has been deposited, reasonably similar to the deposit plated under silent DC conditions in figure 6.11(iii). However, there appears to be some very small nuclei with diameters less than 1 μm present on the copper grains. This suggests that both nucleation and grain growth are occurring simultaneously when using current pulses. There appears to be more of these very small nuclei present on the deposit surface plated with US during the off-time, which is thought to contribute to the slight increase in roughness.

The nuclei formation at the edge of the copper feature, observed in the DC plating experiments (fig. 6.11(ii)), is also evident when using long current pulses with and without US, shown in the ESEM images in fig. 6.17a(ii) and 6.17b(ii) respectively. However, a higher amount of smaller nuclei are observed compared to DC plating.

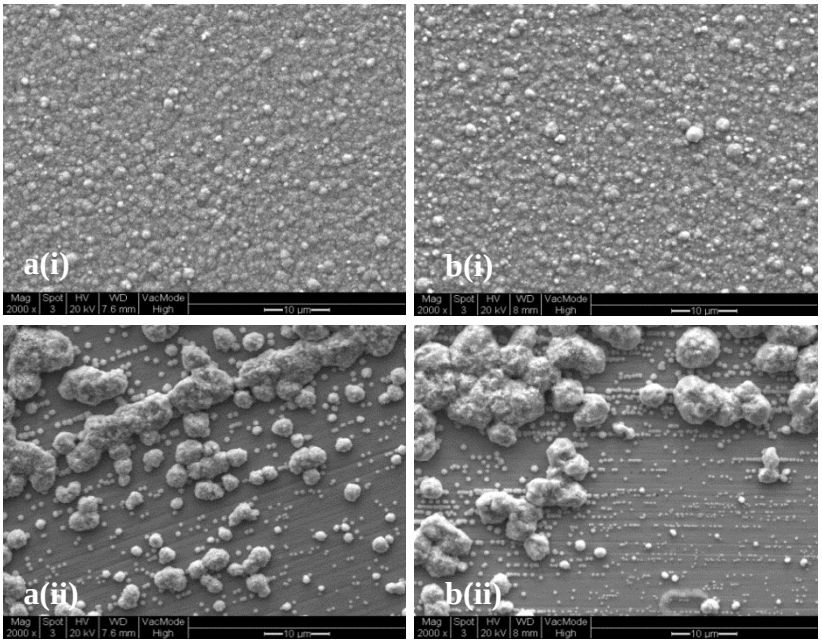

Figure 6.17 – ESEM images of deposits plated at 50% i_{Lim} on a nickel substrate with a 1 x 5 mm of anode feature plated using long current pulses with 200s on-time with 25s off-time, mag x 2000. (a) Silent conditions ; (b) with 10 s of US during the off-time ; (i) centre of the deposit feature ; (ii) edge of the deposit feature.

All of these observations, showing the effect of these different deposition modes on the deposit surface roughness and morphology are caused by the difference in the mass transfer of ions to the cathode surface. When the current is switched off, during the long current pulse mode, the concentration of Cu^{2+} adjacent to the cathode surface will be increased due to the diffusion of ions from the bulk solution outside the electrode gap to the volume of solution within the electrode gap. If current is switched off for a relatively long period of time it is possible that the ion concentration at the electrode surface can even be restored to the bulk concentration of the electrolyte solution [98]. Just before the current is switched back on, the diffusion layer next to the already deposited copper will have been replenished with fresh Cu^{2+} ions which are then reduced when current is re-applied. Repeating this to create a pulsing current process is known to develop an overall smoother deposit than DC conditions [135, 137, 139, 140] This is because any small deposit protrusions will not grow as fast as in DC conditions, shown by Romanov [141] where a shorter time of dendrite appearance was observed under pulsed current compared to DC conditions.[1]

1. The smoothing of the deposit surface can also take place during the off-time for some time after the DC current has been switched off, suggesting that freshly deposit metal surface is unstable as further reaction is taking place after current switch off [131]

The high surface concentration of copper caused by the effective diffusion during the current off-time in pulse plating copper deposition has also been known to increase both nucleation and grain growth [136]. This explains the observation of simultaneous nucleation and growth on the grains in the center of the deposit (fig. 6.17a(i)). The even higher concentration of ions at the electrode surface achieved when using US bursts may cause the increase in the number of nuclei formed on the deposit in the feature center, observed in fig. 6.17b(i).

At the edges of the feature, there is a higher nuclei population density when using long current pulses, as opposed to silent DC plating, which is further increased with US bursts seen by the comparison of figures 6.11(ii), 6.17a(ii) and 6.17b(ii). These observations also support the increased concentration of Cu^{2+} at the electrode surface.

There are also other interesting differences observed in the nuclei formed at the edge when using the different deposition modes. The two distinct sizes of copper nuclei, i.e. small nuclei (0.5 – 1 μm) and large nuclei (5 – 8 μm) that were observed when plating under silent DC conditions (fig. 6.11(ii)) are not observed when current pulses are used. Instead, a range of sizes of copper nuclei are formed with diameters between 0.5 - 9 μm, shown in fig. 6.17a(ii). Additionally, it can be noticed that the depleted areas of the smaller nuclei around larger nuclei observed under DC conditions don't seem to be present in the deposits plated with current pulses (fig. 6.17a(ii)). However, on the top surface of some of the larger nuclei at the edge there appears to be small micron sized nuclei formation, similar to the small nucleation observed on the surface of the center of the deposit. These observations suggests the edge nuclei formed using long current pulses may have grown predominantly via the additional Cu^{2+} supplied by the more efficiently replenished diffusion layer near the deposit surface as opposed to the Ostwald ripening growth regime observed for the DC plated deposit.

The pattern transfer experiments performed in the small-scale cell suggests that the preferred deposition mode for Enface is a combined regime of current pulse with pulsed US agitation. It has been shown that this method produces smoother deposits than when plating with and without CUS under DC conditions, and also effectively removes bubbles and etched metal lodged within the inter-electrode gap during plating. However, before determining whether this deposition mode is suitable for plating patterns on a larger scale, the potential responses for each deposition mode must first be examined to assess which mode provides the most stable potential response.

6.2.3 Potential responses

In order to determine if indeed there is an increase in Cu^{2+} deposition by using current and/or US agitation, potential measurements can be made. The response in cell potential was measured during plating in order to test the stability of the different deposition modes. The author has previously illustrated and discussed these results in recent papers [67, 105, 106]. The cell potential was measured instead of the electrode potential as the anode and cathode are at a narrow distance of 0.3 mm from each other and therefore the placement of a reference electrode would be difficult. The measurement of cell potential is still valid in these experiments as the Ohmic overpotential will be very small due to the narrow electrode gap.

Figure 6.18 shows the potential responses during DC deposition under silent conditions for two applied current densities. The potential peak that is present when the current is applied is an indication of the charging of the double layer. As expected, the potential increases as the applied current density is increased. A decrease in cell potential occurs during the DC current plating, indicated by the arrows in figure 6.18. Several repeats of these plating experiments showed that the average overall decrease in cell potential from the start to the end of plating is 0.044 ± 0.010 V and 0.072 ± 0.024 V when plating at 50% i_{Lim} and 75% i_{Lim} respectively, shown in table 6.2. These repeated experiments also established that this potential instability occurred at 394 ± 20 seconds and 122 ± 55 seconds with applied currents of 50% i_{Lim} and 75% i_{Lim} respectively, shown in figure 6.19. The ratio of these times for each current is approximately 1:3.2.

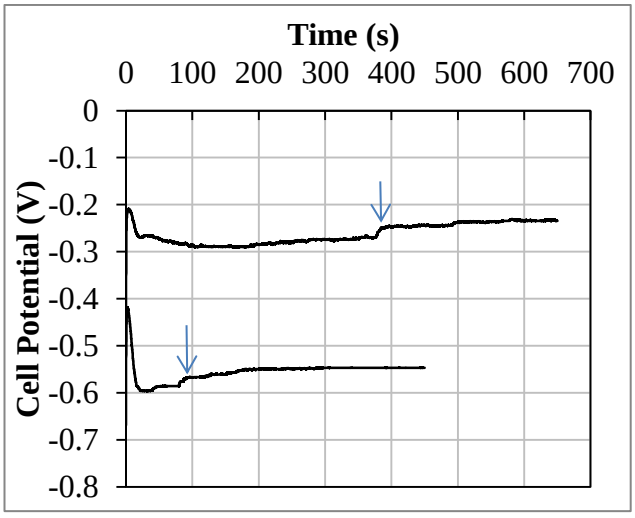

Figure 6.18 - Potential responses during galvanostatic DC plating with 1 x 5 mm of exposed anode area under silent conditions. Line a. Plating at -40 mA/cm^2 (50% i_{Lim}) for 650 s ; Line b. Plating at -60mA/cm^2 (75% i_{Lim}) for 450 s ; Line c. Plating at -80 mA/cm^2 (100% i_{Lim}) for 340 s. Adapted from [106]

Table 6.2 – Comparison of the overall drop in cell potential during plating experiments at 50% i_{Lim} and 75% i_{Lim} plated under silent DC conditions

Current density applied	Repeat	Cell Potential at the start of plating (V)	Cell Potential at the end of plating (V)	Overall decrease in cell potential (V)	Average overall decrease in cell potential (V)
50% i_{Lim}	1	-0.289	-0.234	0.056	0.044 ± 0.010
	2	-0.401	-0.371	0.030	
	3	-0.348	-0.304	0.044	
	4	-0.338	-0.292	0.046	
	5	-0.300	-0.263	0.037	
	6	-0.377	-0.323	0.053	
75% i_{Lim}	1	-0.584	-0.51	0.074	0.072 ± 0.024
	2	-0.676	-0.629	0.047	
	3	-0.736	-0.624	0.113	
	4	-0.713	-0.634	0.079	
	5	-0.586	-0.513	0.073	
	6	-0.596	-0.547	0.049	

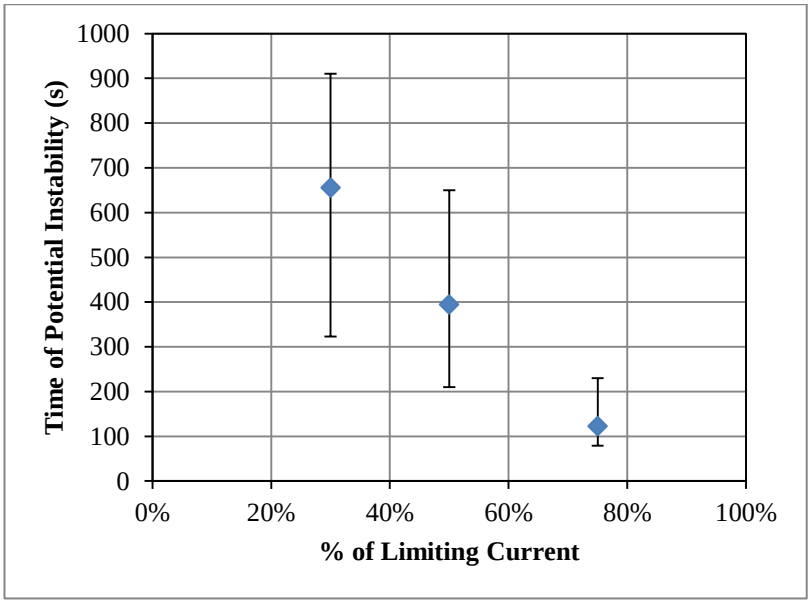

Figure 6.19 – The time at which a potential instability occurs during plating using 1 x 5 mm exposed anode area at 30%, 50% and 75% of i_{Lim}.

The transition time was calculated for each current using the Sand equation, shown in equation 3.20 [112]. It was found that the ratio of transition times for each current was 1:2.25, similar to the ratio of the time of the occurrence of the drop in cell potential. Therefore this potential instability could be related to the depletion of Cu^{2+} within the inter-electrode gap as plating proceeds. The ions would not be efficiently replenished from the bulk solution outside the inter-electrode gap to the cathode surface within the gap due to the narrow geometry which restricts the natural convection flows

One would expect the overall cell potential to increase, and not decrease. However, when deposition proceeds under mass transfer limitation the deposit surface will roughen. Roy and Landolt [130] studied the potential transients during pulsed current copper deposition. They discovered that at the start of deposition there was a noticeable shift in cathodic potential during the transition from Cu deposition to hydrogen evolution reaction. However, towards the end of plating the potential shift due to hydrogen evolution 'disappeared' caused by an increase in deposit roughness.

The deposit roughness of copper features plated at 50% i_{Lim} for 200 seconds and 650 seconds were therefore compared. The values of R_a for these two cases are shown in table 6.3, illustrating that there is clearly an onset of roughening as plating continues. Since surface roughening will result in an increase in surface area, the average current density would decrease, thereby contributing towards the decrease in cell potential.

Table 6.3 – Roughness of deposits plated using 50% i_{Lim} at plating times before and after the occurrence of the drop in cell potential

Plating Time (s)	**Deposit Thickness (um)**	**Roughness, R_a (um)**
200	1.60 ± 0.62	0.04 ± 0.02
650	3.89 ± 0.78	0.09 ± 0.05

When ultrasound is applied as a continuous wave (CW) during DC current plating erratic potential fluctuations occurred, which are shown in figure 6.20. The fully turbulent flow regime that was previously shown to exist in these narrow ultrasound geometries [51] contributes to this noisy potential response. Between the plating times of 0 to 170s, continuous oscillation of the cell potential occurs within a range of -0.8 V and -1.4 V which are mainly due to the formation and collapse of cavitation bubbles close to the cathode surface. Within this high cell potential range, hydrogen evolution is

expected [9, 20] along with the formation of a rough and powdery deposit. During this time, a thick black dendritic deposit formation was observed on the cathode surface.

After approximately 120 s large cavitation bubbles begin to be entrapped within the gap between the electrodes and its holders which would restrict both the natural convection and ultrasound agitation flow. At 180 s, the potential decreased to approximately -0.4 V, at which point the gap between the anode and cathode was bridged by either dendrites of deposited material or from etched copper from the anode. Copper deposition then proceeded but with an unstable cell potential response.

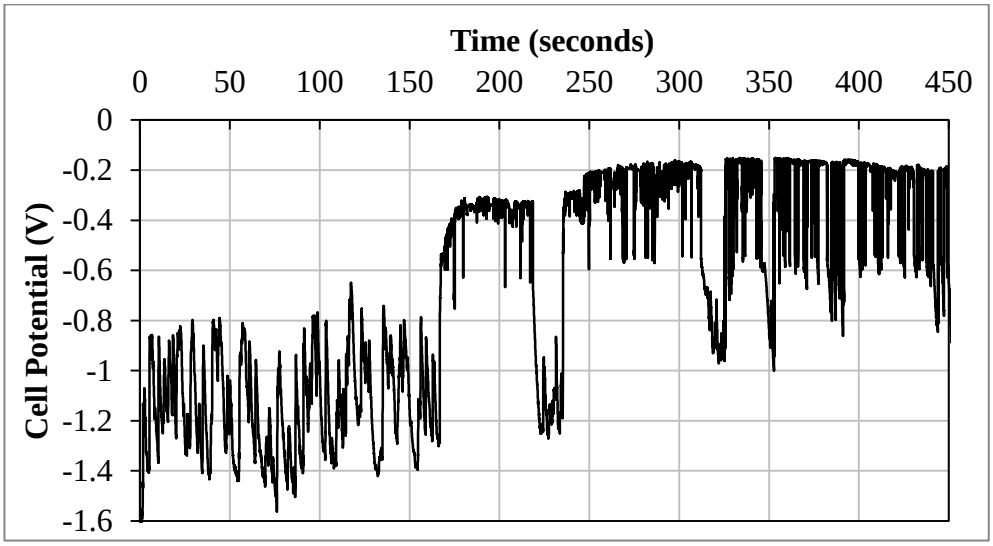

Figure 6.20 - Potential responses during galvanostatic plating with 1 x 5 mm of exposed anode area, plated at 75% $i_{lim, US}$ (150 mA/cm2) under continuous wave ultrasound (CUS), Probe Distance = 30 mm, Ultrasonic Power = 9 W/cm^2. Adapted from [106]

These observations illustrate the issues associated with the use of continuous ultrasound in geometries with narrow electrode gaps and the instabilities that are caused when ultrasound agitation is used during direct current plating. The potential responses during the combined current and US agitation pulses will now be discussed.

The potential response while plating a pattern feature using long 150 s current pulses of 75% i_{Lim} with a silent 25 s off-time is shown in lines (a) in figure 6.21. The length of the current pulse was chosen as 150 s as this is approximately the time that the potential instability occurred during entirely DC conditions.

The potential responses tend to be more stable when using long current pulses as opposed to DC, this can be seen by comparison of the responses in cell potential in

figures 6.21 and 6.18. Several repeated plating experiments, plating at 75% i_{Lim}, showed that the average overall decrease in cell potential during a plating experiment is 0.072 ± 0.024 V and 0.046 ± 0.016 V for silent DC and silent long current pulse plating respectively. This is because of the relaxation of the diffusion layer which occurs during the off-time, allowing time for fresh Cu^{2+} ions to be transported from outside the gap to the electrode surface within the gap.

When ultrasound bursts are induced during the off-time the steady-state potential reached after each current pulse appears to be more constant, illustrated by comparison of lines (a) and (b) in figure 6.21, and also comparison of the values of cell potential in table 6.4. The average overall drop in cell potential when using the combined current and US pulse regime is 0.026 ± 0.015 V. The more stable potential response achieved in this regime is because the transport of metal ions into the volume with the inter-electrode gap is further assisted by the jet-like flow produced by the burst of US waves.

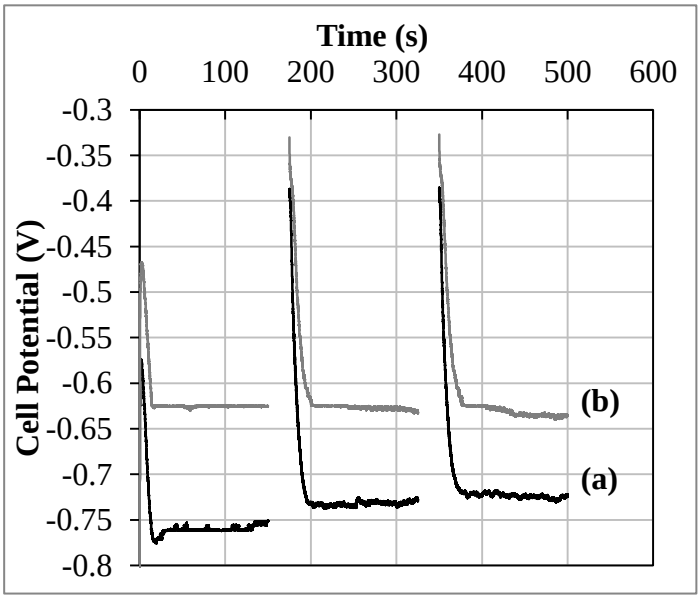

Figure 6.21 - Potential responses during galvanostatic plating with 1 x 5 mm of exposed anode area using long current pulses. (a) Long current pulse plating under silent conditions at -60mA/cm^2 (75% i_{Lim}) with 150 s on-time and 25s off-time ; (b) Plated under the same conditions as for 'a' but with a 10 s burst of ultrasound during the off-time. d_p = 30 mm, p = 9 W/cm^2 [67]

According to figure 6.21, it appears as though there is a difference in the overall plating cell potential between lines a and b by approximately 0.1 V, despite the fact that the same current of 75% i_{Lim} is applied for both cases. There are a few suggestions for the explanation of these differences in potential which could include the following.

Table 6.4 – Comparison of the overall drop in cell potential during pattern plating experiments at 75% i_L for two different deposition modes; Silent long current pulses and combined current and ultrasound pulses

Deposition Mode	Repeat	Steady-state cell potential (V)			Overall drop in cell potential (V)	Average overall drop in cell potential (V)
		Pulse 1	Pulse 2	Pulse 3		
Silent Current Pulses	1	-0.759	-0.732	-0.724	0.035	0.046 ± 0.016
	2	-0.606	-0.541	-0.549	0.064	
	3	-0.815	-0.782	-0.776	0.039	
Pulsed Current and US	1	-0.625	-0.628	-0.635	0.010	0.026 ± 0.015
	2	-0.722	-0.709	-0.694	0.028	
	3	-0.871	-0.910	-0.897	0.039	

(1) Increase in Cu^{2+} concentration near the cathode surface due to US flows

(2) Differences in the area of plating on the cathode itself due to:

(a) Differences in exposed anode area

(b) Slight differences in inter-electrode spacing

(3) Increase in deposit roughness causing a larger area of material to be deposited

Taking the repeated experiments into account, the average steady-state cell potential of the first current pulse is -0.727 ± 0.088 V and -0.739 ± 0.101 V for silent and pulsed US conditions respectively. The similarity in these potentials along with the error values suggests that the overall steady-state potential during plating is not significantly affected by whether US pulses are used or not, and is therefore more likely to be dependent on point (2) and (3) stated above.

The anode area for each experiment is 0.505 ± 0.054 cm^2, the error of this would cause there to be a variance in the applied current density of approximately ± 5 mA/cm^2 which would contribute towards the difference in the cell potential that is measured during plating. Moreover, if there are slight differences in the spacing of the electrodes for each experiment, this would cause a difference in the area of where copper is plated on the cathode due to an increase in current spreading at larger electrode gaps, therefore further contributing to differences in the current density. However, the spacer used to separate the electrodes was accurate to ±5 um and would therefore not make a significant deviation in the 0.3 mm inter-electrode for each experiment.

At the beginning of this chapter, the flow cell geometry was shown to be unsuitable for scaling up for industrial applications for the following reasons; (1) Time consuming loading and unloading procedure, (2) Maximum flow velocity may not be enough to provide sufficient mass transfer for substrates of a greater size, (3) There was a ±60 μm variation in electrode gap across the substrate between several experimental runs, (4) The pattern deposition experiments were not reproducible.

Pattern transfer of copper pattern features was achieved in the small-scale cell using Enface with US agitation. Current was applied either by DC or long current pulses and US agitation was applied either continuously or using US bursts. The combined current and US pulse mode was the most suitable deposition mode because; (1) It gave the smoothest deposits with a values of roughness acceptable for industry, (2) It improved deposited adherence (3) It provided the most stable cell potential response, (4) It effectively dislodged cavitation bubbles and etched metal that were entrapped within the inter-electrode gap. The combined pulse deposition mode could therefore be a suitable deposition mode for a large-scale version of the process with ultrasound agitation. This deposition mode was therefore used to deposit patterns onto larger substrates using the 18 L US tank system.

Chapter 7. Results: Deposition of patterns on large-scale A7 size substrates in ultrasonic tank

7 Deposition of patterns onto A7 substrates in ultrasonic tank

In order to investigate the scale-up of the Enface process the US tank system, shown in figure 4.13 and 4.14, was used to deposit copper pattern features onto A7 size polished copper substrates. Pattern features were deposited in 0.1 M $CuSO_4$.using the electrode holders described in figures 4.11 and 4.12 and A7 size copper anode tools. The tools were fabricated using photoresist, rather than the previous Kapton tape masks.

Initially, mm-scale features were plated to first prove that patterns of this magnitude could be deposited on substrates of this scale. The scalability of the system was quantified in terms of the deposit thickness uniformity across the substrate and across each feature. The uniformity of the deposit roughness across the substrate was also analysed. Following these experiments, μm-scale features were deposited to test the resolution of the system on these larger size substrates.

7.1 Measurement of Electrode Gap

Before deposition of copper patterns onto the A7 substrates was carried out, a method was developed to estimate the gap between the electrodes at different locations across the surface of the plate. There are differences in electrode gap across the electrode surface due to variations in plate thickness due to rolling and polishing, as well as the curvature of the plate due to the imposed pressure when they are clamped between the spacers.

Measurement of the gap between the two electrode plates was required to check the distance between the plates at different locations. In order to do this a polished copper plate was placed into its holder. Silicone rubber was applied at various locations on the surface of the plate, as shown in figure 7.1. Another polished copper plate was placed in the opposite holder and the PTFE spacers were positioned and the holders were clamped together. The silicone was then left to dry, after which the holders were then taken apart. This exposed the dry silicone on the copper plate, shown in fig. 7.1.

The thickness of silicone rubber was then measured using an *Olympus BX41 microscope*. Figure 7.2 shows the thickness of the dry silicone at different locations on the plate. The average electrode gap, calculated from the average of all the silicone thickness measurements, is 270 μm with a standard deviation of 40 μm. The areas with the widest gaps are closest to the PTFE spacers, and the smallest gaps are those which are furthest away.

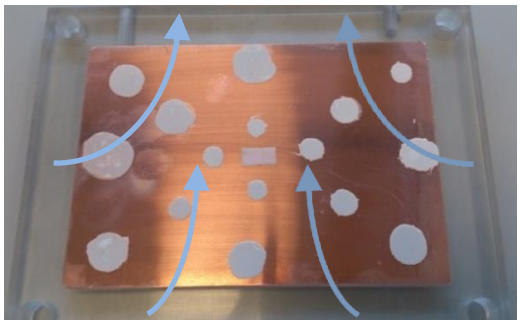

Figure 7.1 – A7 copper plate in electrode holder with silicone rubber on the surface, after being left to dry while electrode holders were screwed together.

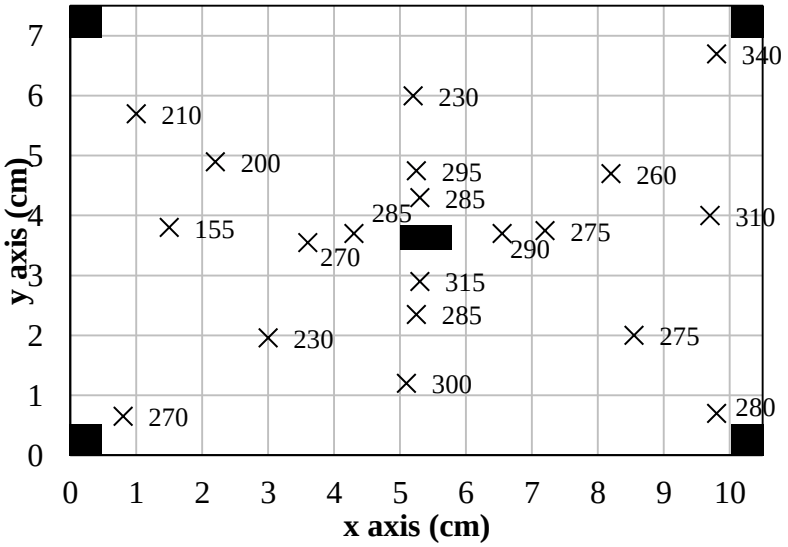

Figure 7.2 – Thickness of silicone rubber (μm) on the surface of a copper plate after being left to dry while electrode holders were screwed together. The thicknesses can be estimated as the distance between the electrode gap at various locations on the A7 copper plate substrate. The black areas indicate the placement of the PTFE spacers.

The variation in electrode gap on this scale of substrate will have various effects on pattern transfer. Locations with wider electrode spacing will have larger current spread, resulting in larger differences in the widths of the deposited pattern features compared to the patterns on the anode tool. This would in turn cause thinner deposits to be plated. The mass transfer of the electrolyte will also be affected by the variation in the distance between the electrodes as the forced convection flows, shown by the arrows in figure 7.1, may be restricted within areas with smaller electrode gaps compared to areas with wider electrode spacing. This may cause differences in electrolyte flow across the electrode plate, resulting in concentration differences, leading to variations in deposit thickness.

7.2 Deposition of mm-scale features onto A7 substrates

Square features of dimension 10 x 10 mm were deposited onto A7 size polished copper substrates in 0.1 M $CuSO_4$. This was achieved using an anode tool made from a copper plate with a layer of spray photoresist and 8 square features of exposed copper, each 10 mm x 10 mm in dimension, arranged in the pattern shown in figure 4.16. The pattern of square features was designed to test the uniformity of 'large' features across both the feature scale and also across the substrate scale for A7 size substrates.

A ruler was used to estimate the area of exposed anode surface by measuring the size of the exposed copper square features, the total exposed anode area of each tool was 8 cm^2. This anode area was used to calculate the required current to apply a current density of 20 mA/cm^2. This is the standard current density for an industrial copper plating process. The nominal thickness of the deposit features based on the anode area is 5.0 μm for a plating time of 677 seconds, assuming 100% current efficiency.

Profiles of the deposit features were measured to test the difference in profile shape, deposit thickness and roughness at different locations across the substrate. US powers of 30, 40 and 60 W/L were used to assess the effect of US using CUS under DC plating conditions at 20 mA/cm^2. A separate experiment using pulsed US (PUS) with current pulses was carried out to compare with the DC plating mode with CUS.

The combined pulse regime is displayed in figure 7.3 US pulses at 40 W/L combined with current pulses of 20 mA/cm^2, with current applied during the US off-time. Ideally, US pulses should be shorter than the current pulse, however this was the only pulse regime which could be operated. The total current on-time for the PUS experiments was the same as for the plating time used for the CUS experiments of 677 s, with an overall plating time of 34 minutes to accommodate the 10 s current off-time.

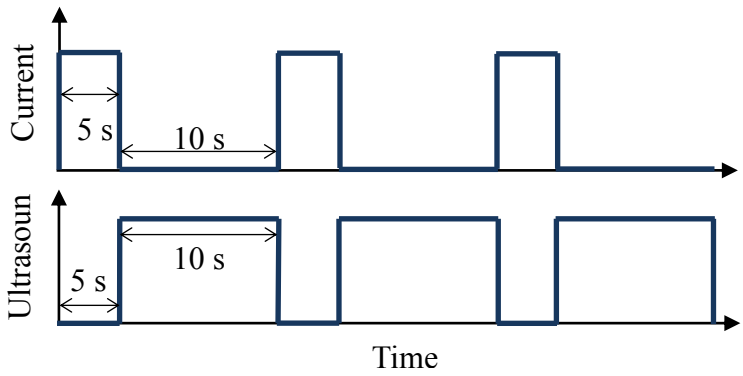

Figure 7.3 – Current and ultrasound pulse waves used for pulsed ultrasound electrodeposition in the ultrasound tank with A7 size substrates

A photo of an A7 copper plate with 10 mm x 10 mm square features plated onto its surface at 20 mA/cm^2 for 677 seconds with a US power of 30 W/L is shown in figure 7.4. The squares are well-defined and were matt in appearance. An optical microscope image of the centre of one of the copper squares is shown in figure 7.5a and illustrates the densely packed copper of the deposits. The profiles in figure 7.4 were measured across the centre line of each square feature, shown by the blue arrow. The deposits have a thickness of 4-5 μm and the edges of the features have reasonably vertical walls. The feature width was measured as the distance between the walls at either side each feature profile. The average deposit feature width was 10.7 ± 0.4 mm; 0.7 mm larger than the anode feature width due to current spread.

It is clear that rough, dark deposits are present on the features close to the edge and corners of the A7 plate, particularly for features B, C and D in figure 7.4. This is due to higher current densities being present near the edges of the electrode due to current distribution across the substrate. It is important to make a distinction between current distribution at the feature-scale and current distribution at the substrate-scale.

7.2.1 Feature scale analysis of deposits plated with CUS

Most features have a reasonably flat horizontal deposit feature surface, such as features A, F and G. However, a number of features appear to have a slightly higher deposit thickness at the feature edge, evident in features B, C, D and H. This is due to the current distribution across each feature, where higher current densities would be expected at the feature edge. Feature E appears to be higher at one end than the other, likely to be caused by a variation in the electrode gap across the feature. The edge of the feature closest to the middle spacer has a lower deposit thickness, as the electrode gap is larger at closer distances to the spacer therefore the current density is lower.

Figure 7.6 shows copper square features plated with a higher US power of 60 W/L along with a profile of each feature. The walls of each profile, again are reasonably straight and the copper squares in the corners of the plate appear dark and rough, similar to the observations seen when using the lower US power of 30 W/L. However, the shape of the profile of each feature plated does not appear to be as flat as was observed at the lower power. An uneven wavy pattern is evident in the shape of the profiles, particularly in the profiles of features A, B, C, D and H.

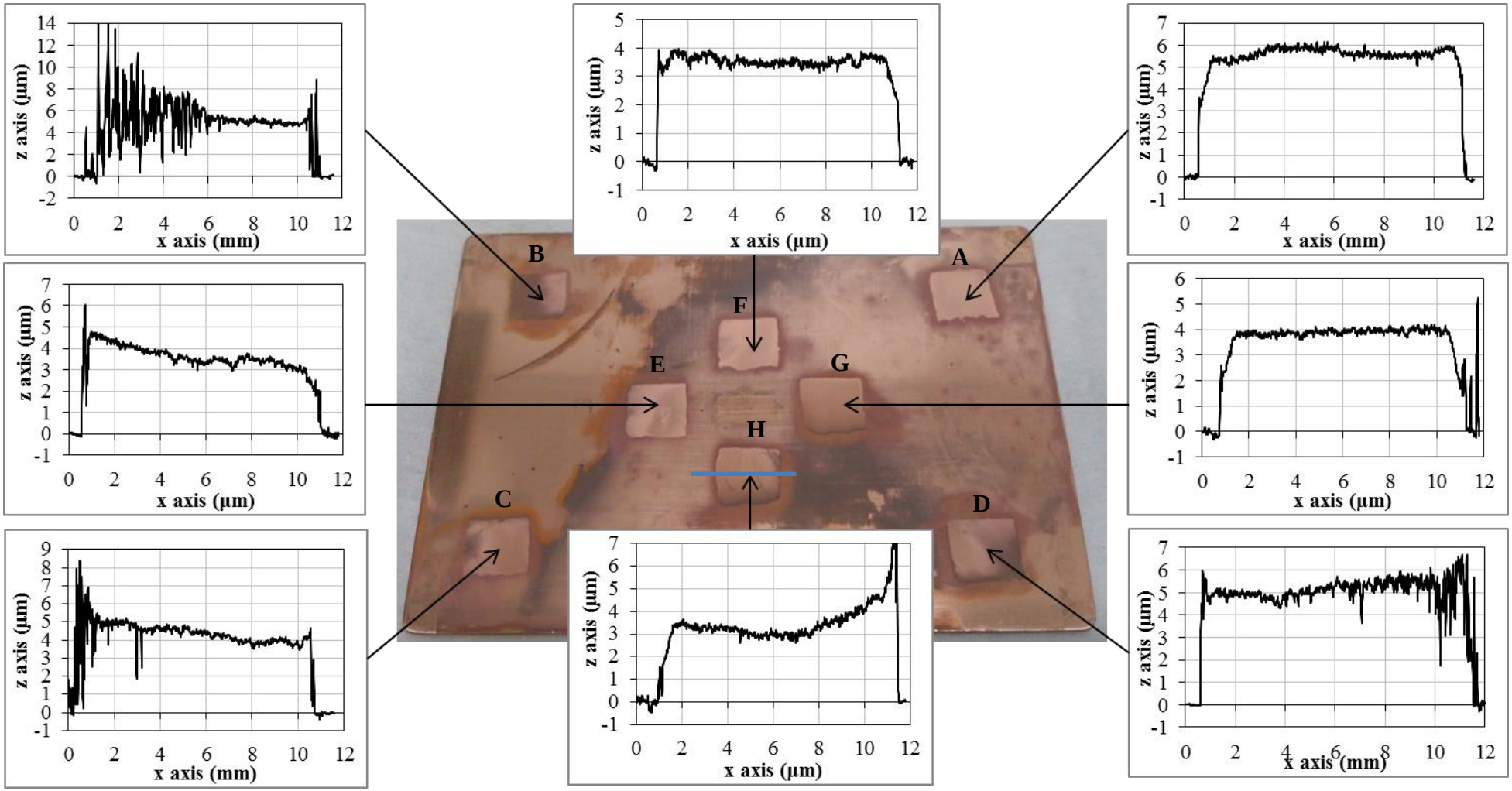

Figure 7.4 – A7 size copper cathode substrate after plating in ultrasonic tank; plated with a DC current of 20 mA/cm^2 for 677 seconds, with all 3 generators on at a power of 30 W/L ; Profilometry taken across the middle of the square deposit features, indicated by blue line

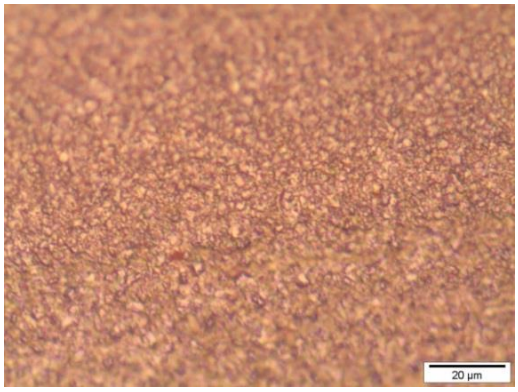

Figure 7.5 - Optical microscope images (mag x50) of copper deposits plated with a DC current of 20 mA/cm^2 for 677 seconds, with an US power of 30 W/L (a) the centre of a copper deposit square feature, (b) a hole in a copper deposit, square A

When the square deposits in figure 7.6 are scrutinized in more detail a wavy pattern was observed on the deposit surface. This is most clearly observed on the surface of feature H in figure 7.7 where a wave pattern of lighter and darker deposit is visible. Although the causes are difficult to state, this formation could have occurred due to the flow regime at higher ultrasound powers. Standing waves could be observed in the solution during sonication using the higher power. These standing waves may be occurring over the regions where copper deposition is taking place, which would result in different deposit thicknesses observed in the profile of square H presented in figure 7.6. This could contribute to the wavy patterns on the surface of the deposit features shown in figure 7.7. The width of each individual wave pattern is approximately 5 mm, which matches with the size of half the wavelength of a 30 kHz ultrasound wave. This effect of standing waves has been known to form wavy patterns on nickel deposits during sonication [60].

Optical microscope images revealed that a few holes were present in some of the deposit features; examples of this are shown in figure 7.8a with a diameter of 20 µm and also in figure 7.8b with diameters of approximately 10 µm. These are similar to the magnitude of the diameters of cavitation bubbles produced by ultrasound devices [52]. The holes are therefore attributed to the collapse of cavitation bubbles close to the deposit surface. The depth of these holes could reach the thickness of the deposit. This is shown in the profile of square F in figure 7.6 where the stylus of the profilometer traversed over a hole in the deposit which was large enough for the stylus to move down to the bottom and the hole, showing that the surface of the copper plate was reached.

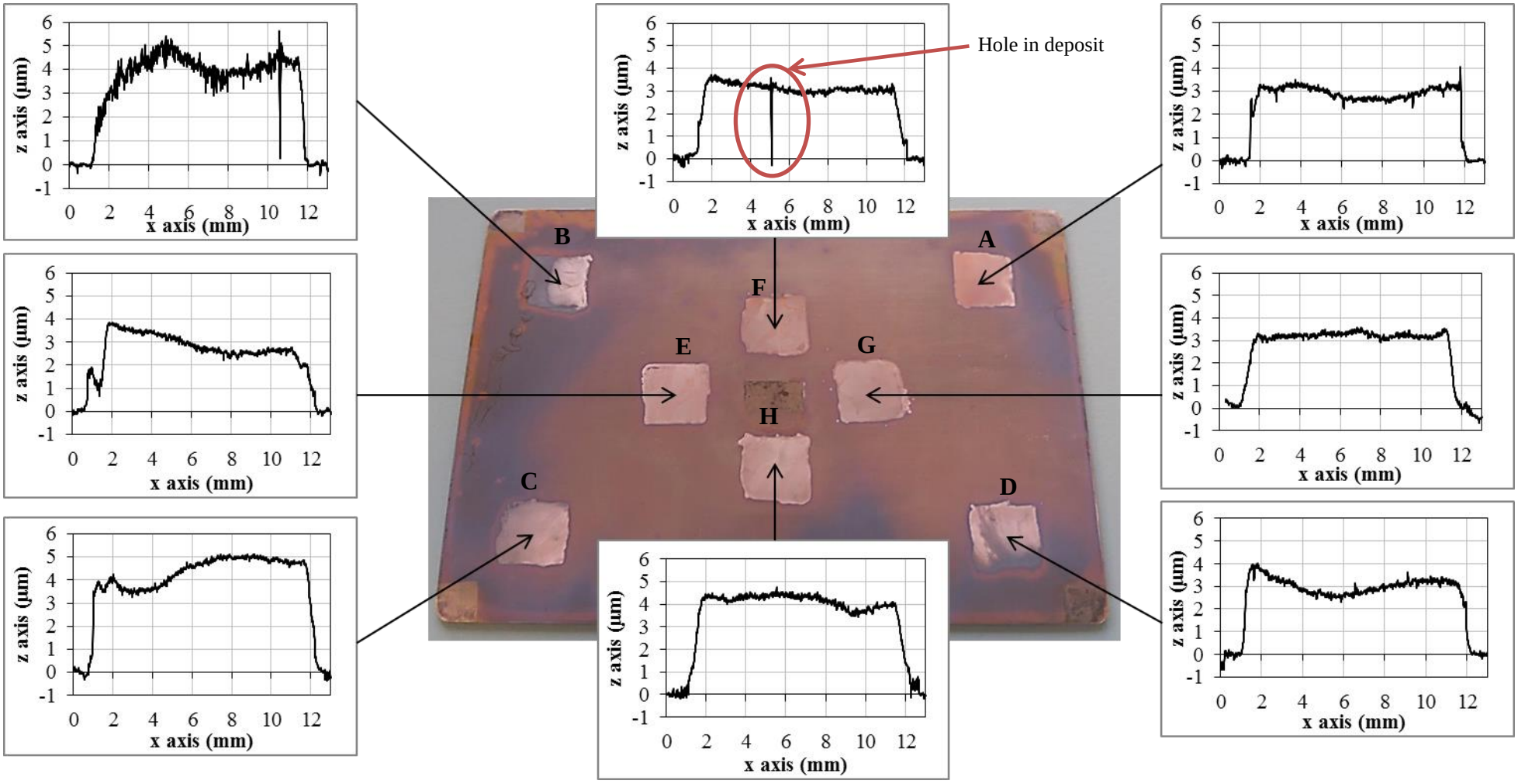

Figure 7.6 – A7 size copper cathode substrate after plating in ultrasonic tank; plated with a DC current of 20 mA/cm^2 for 677 seconds, with all 3 generators on at a power of 60 W/L ; Profilometry taken across the middle of the square deposit features.

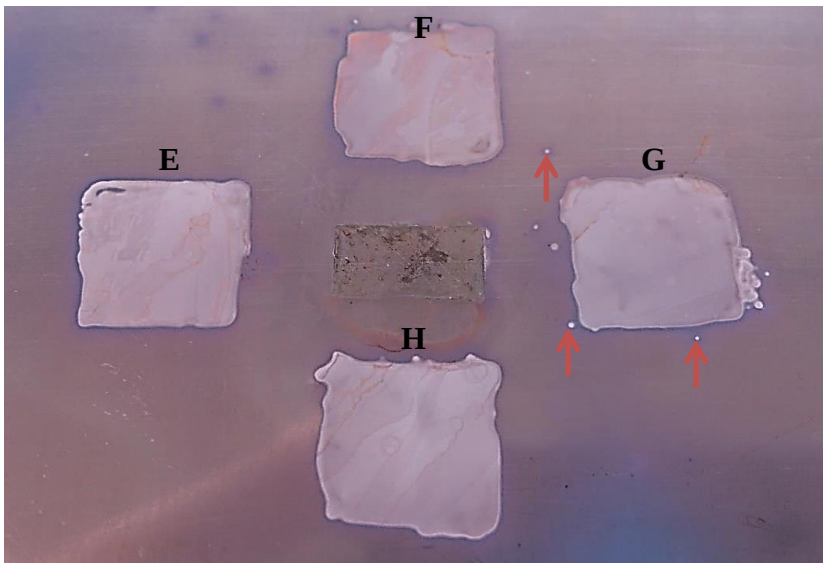

Figure 7.7 – Photo of the copper deposit square features in the centre of the plate shown in figure 5 plated with an US power of 60 W/L

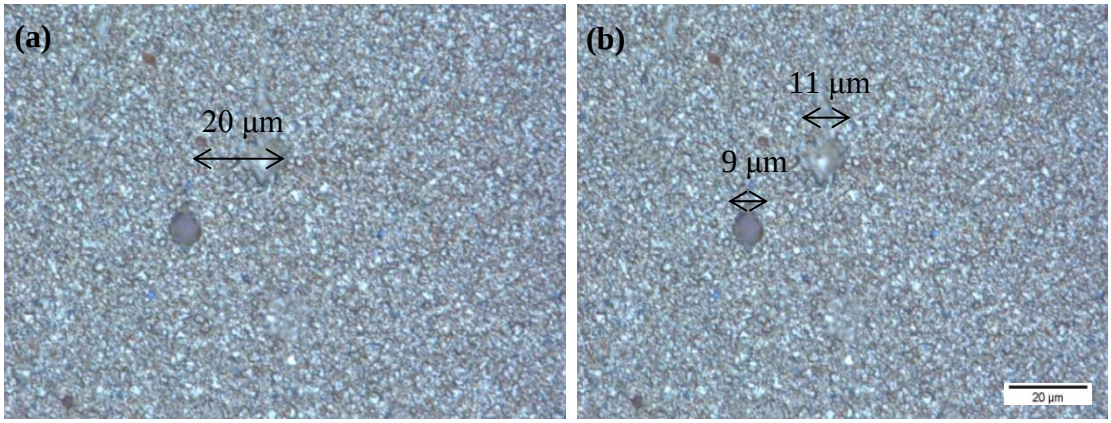

Figure 7.8 - Optical microscope images (mag x50) of copper deposits plated with a DC current of 20 mA/cm^2 for 677 seconds, (a) Deposit plated with an US power of 30 W/L at position A showing a hole in the copper deposit, (b) Deposit plated with an US power of 60 W/L holes at position F.

7.2.2 Feature scale analysis of deposits plated with PUS

Figure 6.30 shows a plate with square features deposited using the combined current and PUS regime, described in figure 7.3. The copper deposit squares are again matt in appearance and well-defined. The shape of the pattern features are not as square as those in figures 7.4 and 7.6, but this is only because the edges of the exposed copper features on the photoresist tool used for this particular deposition experiment were poor.

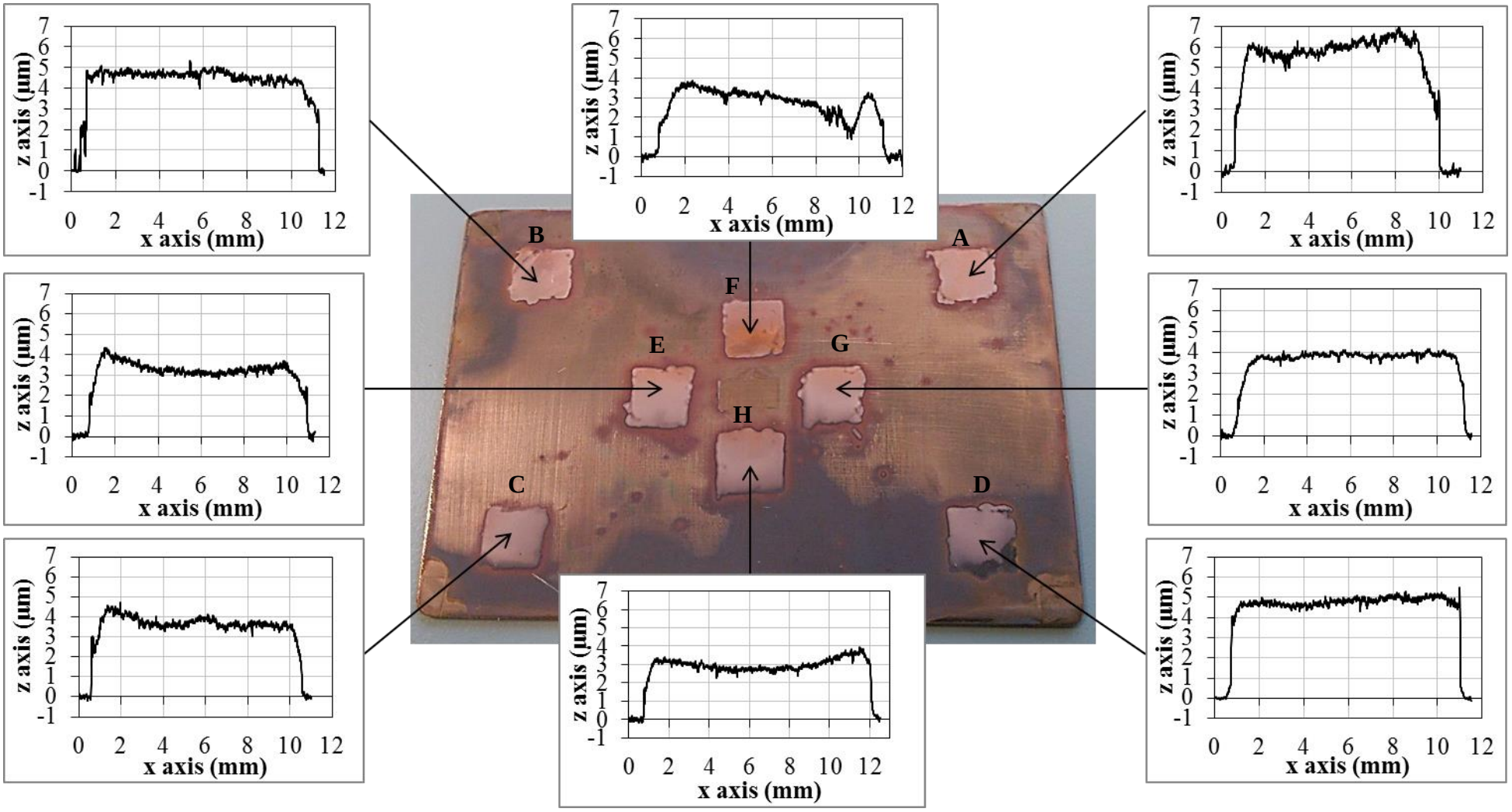

Figure 7.9 – A7 size copper cathode substrate after plating in ultrasonic tank; plated with current pulses of 20 mA/cm^2, with all 3 generators using a pulsed ultrasound power of 40 W/L ; Profiles taken across the middle of the features

The shapes of the profiles of features plated using PUS have reasonably straight walls. However, the profiles appear to be less flat than those plated using CUS at the lower power. There are more profiles that with a thicker deposit at the edges of the feature compared to the centre, particularly evident for features A, C, E, F and H. This is thought to be due to there being a more primary current distribution during deposition using the combined pulsed current and PUS regime.

There are also larger differences in profile height between features across the substrate. The deposit thickness can vary by 50% in some cases, for example between feature A and F in figure 7.9. The profile of square F is quite different to the other squares, possibly due to the effects of cavitation, but could also be because the middle spacer is positioned directly below the location of this square feature. The spacer may restrict the flow of electrolyte from the bottom to the top of the plate and therefore result in a lower concentration of ions in the region directly above the spacer where the feature is being plated. This may cause a thinner deposit to be plated in the middle of square F, as shown in the profile, and also a thinner average deposit of the feature compared to the other squares.

7.2.3 Feature size

The widths of the features, measured from profile widths, were used to estimate the area of the features. The average area of each deposit square feature was 1.14 ± 0.09 cm^2; in other words, a 14% increase in deposit feature surface area compared to the anode feature area. This larger deposit feature size with respect to the anode feature is due to current spread. The current spread will vary at different locations across the plate due to the variations in electrode gap that were measured (± 40 μm). This will contribute towards both current variations across a feature as well as the differences in current distribution across the entire plate.

7.2.4 Deposit thickness of square features

The total surface area of deposit features on the cathode surface (A_f) was calculated for each experiment. This was used to calculate the actual applied current density based on the area of cathode features (i_f), which could be used with the Faraday equation to find a more accurate nominal deposit thickness ($d_{dep,\,100\%,f}$) for each deposition mode. For example the nominal thickness of the experiments plating features with 30 W/L of CUS was 4.44 μm, assuming 100% current efficiency. The $d_{dep,\,100\%,f}$ for each deposition mode is shown in table 7.1.

The average thickness of deposit features ($d_{dep,m}$), measured from feature profiles, are shown in table 7.1 for deposits plated at different US powers under CUS conditions and using the PUS mode. This data is visualized graphically in figure 7.10 where the deposit thickness of the square features at each location on the copper plate is displayed for each deposition mode.

The errors associated with the values of $d_{dep,m}$, approximately ± 1 μm, are due to variations in current distribution across at the feature-scale (across a feature) and also at the substrate-scale (across the substrate), both effected by the variation in electrode gap.

The values of the average $d_{dep,m}$ of all squares on the plate in table 7.1 suggested that there is a decrease in deposit thickness as the US power is raised, also shown in figure 7.10. This is thought to be due to the increased amount of pitting that occurs on the photoresist of the anode tool caused by increased cavitational activity creating a larger area of anode surface exposed to the electrolyte solution. Copper is deposited opposite these pits on the cathode surface, resulting in a larger area where copper deposition is taking place on the copper cathode plate, thereby decreasing the overall current density.

Table 7.1– Average deposit thickness of square features at different locations on an A7 electrode plated at different ultrasound powers ($p_{W/L}$), where A_f is the average total area of the deposited features over three experimental repeats ; i_f is the current density based on A_f ; $d_{dep,\ 100\%,f}$ is the nominal deposit thickness based on i_f; and $d_{dep,m}$ is the measured deposit thickness.

$p_{W/L}$ (W/L)	A_f (cm^2)	i_f, (mA/cm^2)	$d_{dep,100\%,f}$ (μm)	$d_{dep,m}$ of all squares, ABCDEFGH (μm)	$d_{dep,m}$ of squares, ABCD (μm)	$d_{dep,m}$ of squares, EFGH (μm)
30	9.0	17.8	4.44	4.81 ± 1.03	5.00 ± 0.84	4.62 ± 1.2
40	9.2	17.4	4.36	3.90 ± 0.71	3.96 ± 0.85	3.85 ± 0.60
60	9.3	17.2	4.29	3.64 ± 1.07	3.46 ± 1.16	3.81 ± 1.00
40 (P)	9.1	17.6	4.41	4.67 ± 1.09	5.36 ± 0.84	3.98 ± 0.86

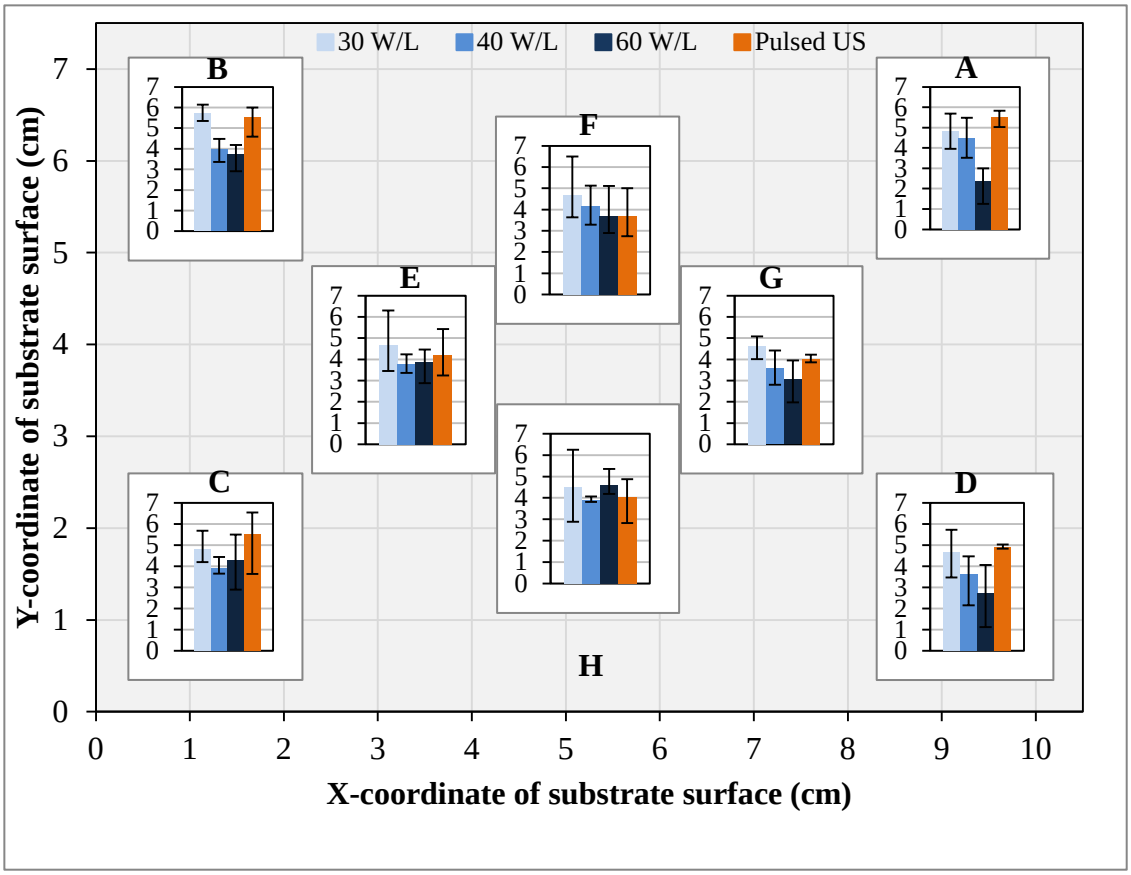

Figure 7.10 – Thickness (μm) of copper deposit square features at various locations on an A7 size copper substrate. Deposits plated at 20 mA/cm^2 with a total current on-time of 677 seconds, under DC plating conditions with CW US at 30 (light blue), 40 (blue) and 60 (dark blue) W/L and using the combined pulsed current and PUS regime using an US power of 40 W/L (orange).

A comparison of the difference in deposit thickness of features located at the corners of the plate (ABCD) and those in the middle of the plate (EFGH) are also displayed in table 7.1. This allows the deposit thickness uniformity on the substrate-scale to be analysed.

When plating with 30 W/L the deposit features of the corner squares have a higher deposit thickness than those in the centre of the plate. This is due to the slightly higher current densities that will be present at the edges of the cathode plate. The variation in electrode gap will also contribute to the current distribution variation. The electrode gap was approximately 20 μm narrower at the location of the features in the corners (ABCD) than the location of the features in the middle (EFGH). This would result in higher current densities at locations ABCD and therefore thicker deposits.

There doesn't appear to be as much difference between the thickness of deposits in the corners and the centre of the plates when using higher US powers. It is suggested that this is due to the resist damage that occurs at higher powers, causing deposition in other areas of the plate other than where the square features are being plated. This will not only decrease the current density being applied but will also alter the variation in current across the plate.

It can be seen from table 7.1 that when plating using the combined pulsed current and PUS mode, the thickness of deposits at the corners of the plate are approximately 1.4 μm higher than those is the middle; a more significant difference than when plating under DC with CUS. This is because a more primary current distribution is achieved using the pulsed deposition mode. The difference in deposit thickness between the features at the edge compared to those in the middle for the PUS experiments can be visualized more clearly in figure 7.10.

7.2.5 Current Efficiency

An estimation of the current efficiency of copper deposition can be made by multiplying the $d_{dep,\,m}$ by the A_f and comparing this to the $d_{dep,100\%,f}$ multiplied by the A_f. The current efficiency for each deposition mode is shown in figure 7.11. Some values of current efficiency were calculated to be higher than 100%.

This is thought to be mainly due to current variations at different locations on the plate, as described above. The main source of current variations across the plate will be caused by the variation in electrode gap of ± 40 μm between the plates. Variation in current distribution across the plate will result in higher deposit thickness in some areas of the plate contributing to calculations of current efficiency that are higher than 100%. However, the average current efficiency across the entire plate gives values of efficiencies that are close to 100%, shown in figure 7.11.

The apparent decrease in the current efficiency as the US power is raised is caused by damage to the photoresist as described above, resulting in thinner deposit features. Interestingly, it appears as though a higher current efficiency is achieved when using the pulsed deposition mode compared to DC conditions. However, this is likely to be due to the higher thickness at the feature edges and also the features nearest the plate edge, which would contribute towards a higher average deposit thickness overall.

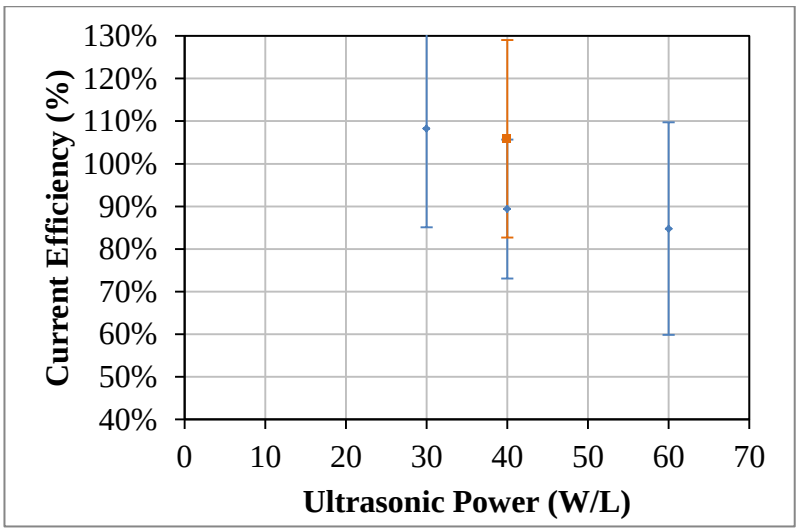

Figure 7.11 – Current efficiency of copper deposition of square features, based on deposit thickness, plated at various US powers under DC with CW US conditions (Blue) and combined current and US pulse conditions (Orange)

7.2.6 Deposit roughness

The roughness amplitude (R_a) of the deposits was measured to test the roughness uniformity of the features across the plate. The measurement could also be used to compare deposit roughness of the features plated with the different deposition modes. Each R_a measurement was calculated over a 3000 μm region. Measurements were taken at 3 different locations of each profile. The average of these 3 measurements gave the average roughness across the feature for that plating experiment. The average R_a of a feature was calculated over 3 experimental repeats. The values of the average R_a for each feature location is shown in figure 7.12 for the difference deposition modes. The average R_a across the entire plate (i.e. at all locations) is shown in table 7.2, along with the average R_a across features in the corners only (ABCD) and the average R_a across features in the middle only (EFGH).

The average R_a of features at all locations on the plate in table 7.2 suggests that there is a slight decrease in increasing the power from 30 to 40 W/L. However, the errors in roughness values indicated in table 7.2 shows that the differences in roughness at these two powers are larger than the error margins. If a small increase in roughness for the lower power does exist however, then this may be because the small increase in US power could result in increasing the flow velocity of the US waves without significantly increasing the cavitational activity. In other words, increasing the US power from 30 to 40 W/L may not significantly increase the amount of pitting but will increase the concentration of Cu^{2+} ions near the cathode surface due to the higher flow rate of electrolyte, resulting in marginally smoother deposits.

Table 7.2 – Roughness (R_a) of deposit square features at different locations on an A7 electrode plated at different ultrasound powers

$p_{W/L}$ (W/L)	Average R_a of all squares, ABCDEFGH (µm)	Average R_a of corner squares, ABCD (µm)	Average R_a of middle squares, EFGH (µm)
30	0.16 ± 0.08	0.17 ± 0.12	0.11 ± 0.04
40	0.11 ± 0.05	0.13 ± 0.05	0.09 ± 0.04
60	0.18 ± 0.13	0.17 ± 0.13	0.19 ± 0.14
40 (PUS)	0.11 ± 0.06	0.12 ± 0.05	0.11 ± 0.07

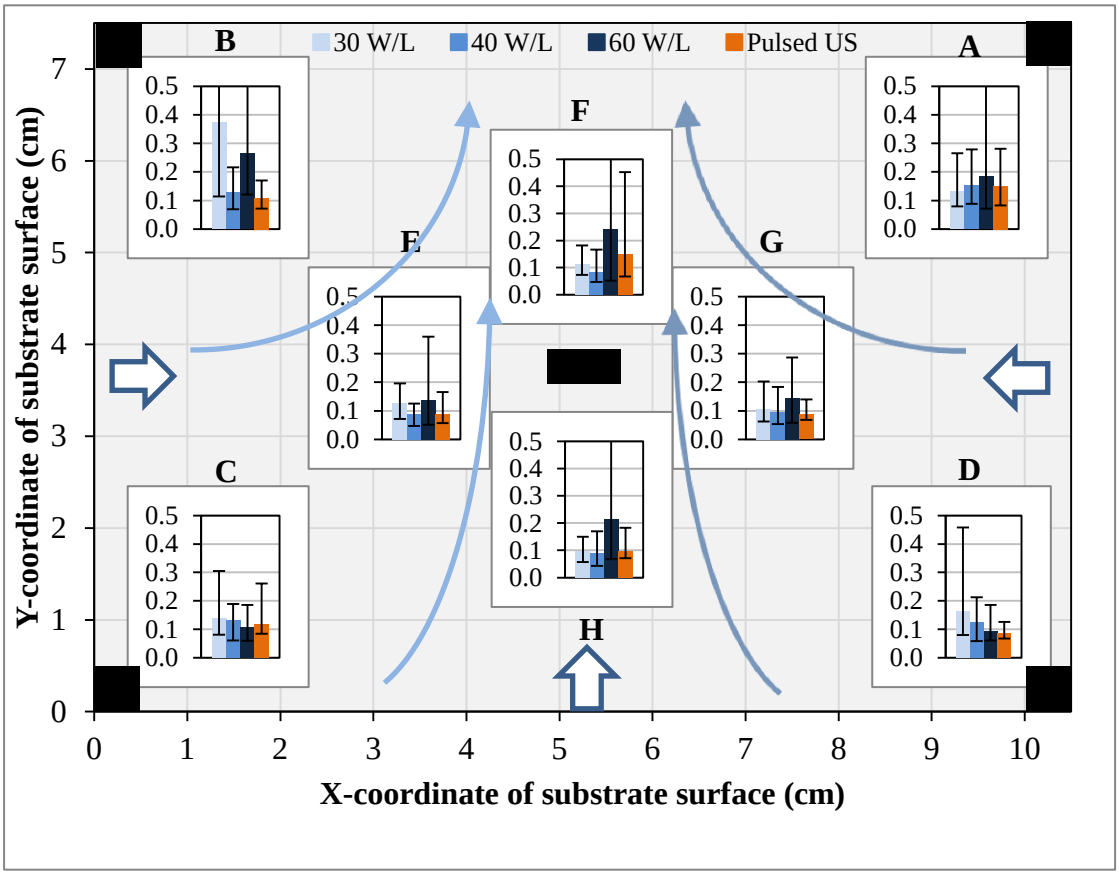

Figure 7.12 – Roughness (µm) of copper deposit square features at various locations on an A7 size copper substrate. Deposits plated at 20 mA/cm^2 with a total current on-time of 677 seconds, under DC plating conditions with CUS at 30 (light blue), 40 (blue) and 60 (dark blue) W/L and using the combined pulsed current and PUS regime using an US power of 40 W/L (orange). Black squares show the location of the placements in the PTFE spacers.

It is possible that the difference in roughness at these two powers could also be related to the operation of the US transducers. 30 W/L is the lowest possible operating power for this US tank and the transducers would therefore occasionally switch off intermittently for a fraction of a second during operation. At these specific moments when the transducers switch off, the limiting current will be lowered during that short period of time. The current is being applied at a constant value continuously and therefore the deposition will be occurring closer to the limiting current density at these occasions. This could result in a slightly rougher deposit.

For the deposits plated at 30 W/L and 40 W/L, the average roughness of the deposits in the corners of the plate were found to be approximately 0.05 μm higher than the average roughness of deposits in the middle of the plate. This is related to the higher current density near the edges of the electrode due to the variation in current distribution across the plate. This causes the slightly darker deposits due to the increased roughness as observed in figure 7.4.

When using the higher power of 60 W/L there is a significant increase in roughness. There is also a larger variability in roughness values across the substrate. These findings are attributed to the increased number of pits which are formed in the deposit, observed with an optical microscope. This is thought to be mainly caused by the higher intensity of cavitational activity, known to occur as the US power is increased [52].

No significant difference in roughness was observed between the deposits plated in the corners and the middle of plate exposed to 60 W/L of US power, as was observed with the lower powers. This suggests there is high cavitational activity in all areas of the plate when using this higher power, resulting in a roughening of the features in each location.

There are other factors which can affect the cavitational activity other than the increase in US power. To study this in more detail a measurement of the distribution of the cavitational activity across the plate was required, which was estimated by considering the amount of pitting in the deposits. The number of pits detected on each deposit feature using an optical microscope is displayed in table 7.3 for an experiment carried out at 30 W/L. Figure 7.13 shows a schematic of this data with a black dot for each pit that was observed.

Table 7.3 – Number of pits in each deposit feature observed using an optical microscope for an A7 size electrode plated at 20 mA/cm^2 for 677 s, with an US power of 30 W/L

Position of square deposit	Number of pits located on deposit feature surface
A	4
B	8
C	9
D	15
E	14
F	35
G	28
H	28

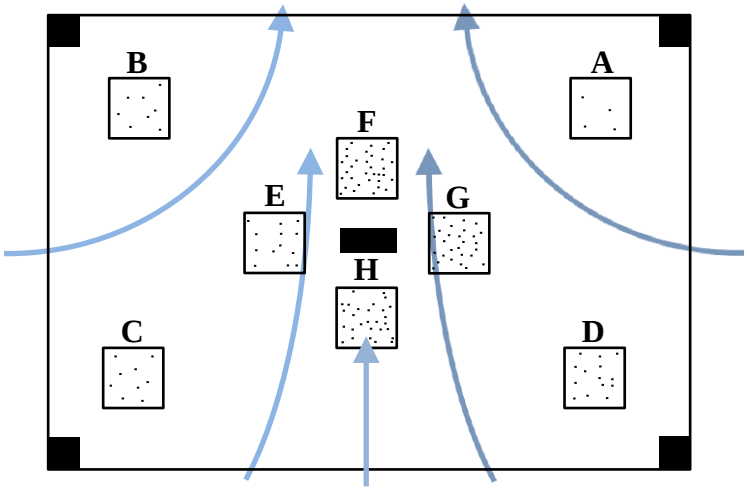

Figure 7.13– Schematic of the number of pits observed in each deposit feature, illustrated by number of black dots, for an A7 size electrode plated at 20 mA/cm^2 for 677 s, with an US power of 30 W/L. Blue arrows illustrate the suggested flow pattern of the US agitation

The features that contained the highest number of pitting were those located in the middle of the plate (EFGH), the highest amount of pitting occurring at feature F. This was caused by either blockage of the deposit due to cavitation bubbles or bubble collapse close to the surface of the deposit. It is most likely due to bubbles collapse as the size of the pits were 10-20 μm, which will be approximately the size of the bubbles which means they are small enough to flow through the electrode gap of 300 μm.

A high amount of pitting in the middle of the plate suggested that a build-up of cavitation bubbles occurred in this region. This is most likely due to electrode gap

variation. The regions where there are narrower electrode gaps would restrict the flow of ultrasound waves, and therefore restrict the flow of bubbles, more so than in regions where the electrode gap is larger. The blue arrows in figure 7.13, indicate how one would expect the flow of the ultrasound waves to flow across the plate, based on the fact that transducers are located at the bottom and the sides of the electrode holder. The liquid flow is therefore entering the gap from different sides of the holder. These flows would meet in the middle of the plate which could result in a build-up of cavitation bubbles in that region before they flow upwards towards the top of the electrode gap.

The roughness of deposited features plated using the combined pulsed current and PUS regime is also shown in table 7.2. Similar values of roughness were measured when using the CUS with DC conditions and the combined current pulse and PUS deposition mode using the same US power of 40 W/L. It would be expected the PUS regime would decrease the roughness of the deposits, as for the case for the deposition experiments in the 500 ml cell. However, the electrodes are exposed to US for a longer period of time under pulsed US mode compared to CUS in the US tank. This is because the PUS experiments in the US tank were carried out with 10 s of US on-time and 5 s US off-time, the only US pulse times that could be applied, with current being applied during the US off-time only (shown previously in fig. 7.3). The total current on-time was the same as for the plating time for the CUS experiments. This means that during the PUS experiments in the US tank the electrodes were exposed to US for twice the length of time than when using the CUS mode in the tank. A longer US exposure time means a longer exposure to cavitation bubble collapse, which may roughen the surface. The combination of pulsed current and the longer US exposure time on deposit roughness may counteract each other, resulting in no significant change in the R_a value.

Square mm-scale features were successfully deposited onto the A7 size substrates using an ultrasound power of 40 W/L with both deposition modes; DC with continuous ultrasound or the combined pulsed current with pulsed US regime. A small amount of current spreading occurred meaning the deposit features were only 14% larger in width than the anode features which is acceptable. The deposit thickness uniformity and deposit roughness uniformity of the square mm-scale features was ±18% and ±40% across the plate. This is within the acceptable limits for industrial application, the Enface process is therefore scalable for mm-scale features on A7 substrates.

7.3 Deposition of linear µm-scale features on A7 substrates

Linear features were deposited onto A7 copper plates using the dry photoresist tool which was shown in figure 4.19 in the experimental section. This was the first time linear features were deposited using the Enface technique onto a substrate of this scale. The tool had 77 parallel lines of exposed copper surface with a length 66 mm and a width of 210 ± 10 µm with a pitch of 1210 µm and therefore a spacing of 1040 ± 10 µm, as shown previously in figure 7.14a.

The total area of exposed copper anode features (A_a) was 10.6 cm^2. A current of 211 mA was applied for each experiment to achieve 20 mA/cm^2 based on the anode area. The DC experiments using CUS were carried out at 40 W/L with a plating time of 677 seconds, achieving a nominal deposit thickness of 5.0 µm based on A_a. The plating experiments using PUS used the same regime as described in figure 7.3 with a US power of 40 W/L with the same total current on-time of 677 seconds.

An image of two deposited linear features is shown in figure 7.14b and the surface of the deposits in figure 7.15 shows a closely packed copper grain structure. The average width of the linear features was 540 ± 120 µm; 2.5 times the width of the average anode linear feature width showing a significant effect of current spread at these µm-scale features.

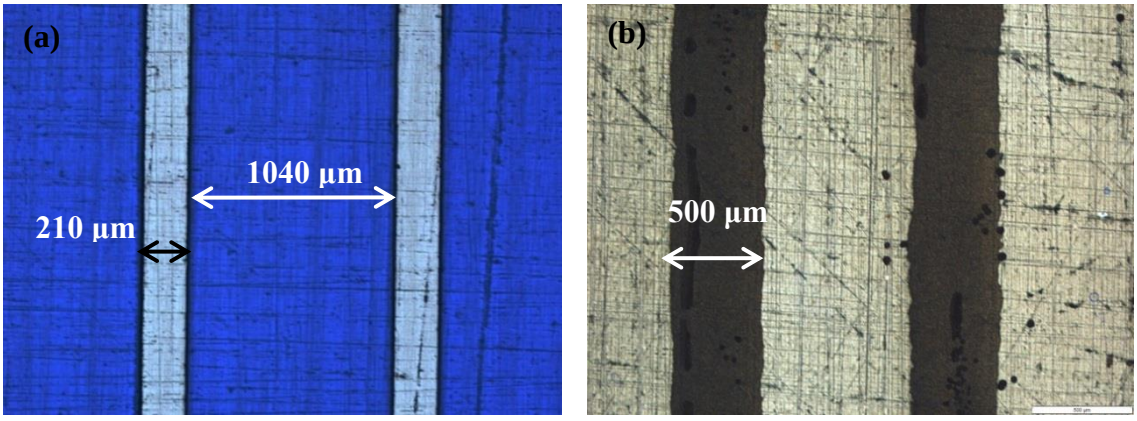

Figure 7.14– Optical microscope images with magnification x5. (a) Dry photoresist pattern on the anode tool (b) Deposited linear pattern features plated at 20 mA/cm^2 under DC conditions with CUS at a power of 40 W/L

Figure 7.15 - Optical microscope image of surface of a deposited linear pattern features plated at 20 mA/cm^2 under DC conditions with CUS at a power of 40 W/L. (Mag x 100)

Figure 7.16 shows an A7 copper plate with deposited linear features plated under DC conditions with a current density of 20 mA/cm^2 using CUS at a power of 40 W/L, along with profiles of the features. The profiles of the lines were measured over two linear features at each location corresponding to the earlier locations for square features (see fig. 7.4). There was a 2-4 μm variation in deposit thickness and the shapes of the profiles are different at across the plate. The average thickness of deposits was 1.9 μm, which was 40% of the nominal thickness based on the anode area. This large difference in deposit thickness indicates that the feature width would be much larger compared to the anode.

It is possible that the plating time could have been adjusted based on a prediction of the larger deposit feature width to achieve a higher deposit feature thickness of 5 μm. In this case, more than double the amount of plating time would be required to achieve a thickness of 5 μm. However, this may result in even more current spreading occurring and also a longer exposure to US agitation. Alternatively, a higher current could also be applied, but this could result in a rougher deposit and also the applied current is limited to what current densities can be applied in industry.

7.3.1 Feature scale analysis of deposits plated with CUS

The profiles show that there is non-uniformity in the shapes of each of the profiles in figure 7.16. The profiles of the linear features in locations A, B, C, and E are reasonably well defined. These features appear to have a thicker deposit in the centre of the feature compared to the edges of the feature due to variation in the current distribution across a feature. The features also appear to be rough at the feature edge. The profiles of linear features in locations DFGH are not as well-defined due to the occurrence of deposition in between the linear features, shown in figure 7.17.

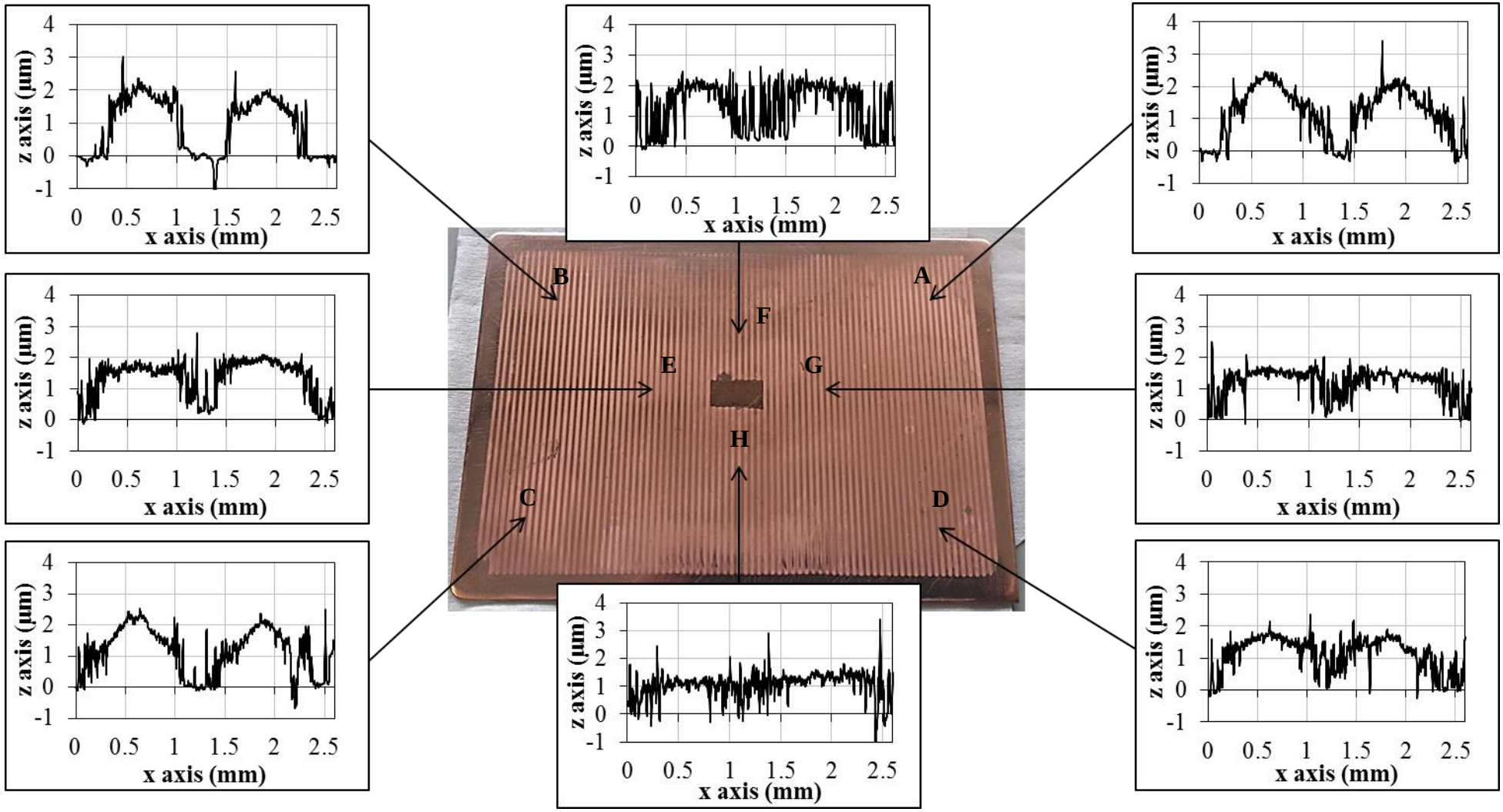

Figure 7.16 – A7 size copper cathode substrate after plating in ultrasonic tank using dry resist tool with linear pattern features; plated with DC current density of 20 mA/cm^2, with all 3 generators using a CUS power of 40 W/L ; Profiles taken across two features

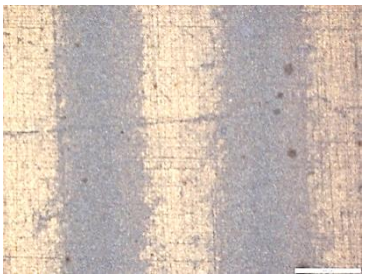

Figure 7.17 - Optical microscope image of linear features within location E, plated at 20 mA/cm^2 under DC conditions with CUS at a power of 40 W/L, (Mag x5)

During a repeat of the plating experiments the profile shape shown in figure 7.18 was observed for features in location B. The current distribution across these tapered shaped features is different to the current distribution across the features shown in the profiles in figure 7.16. This shows that there are variations in each plating experiment.

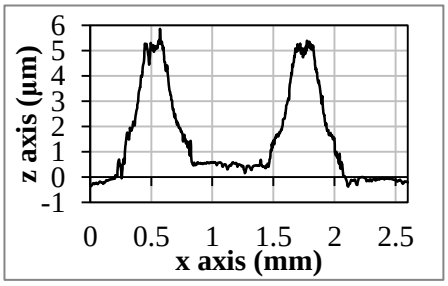

Figure 7.18– An example of a profile of thicker copper linear features plated at location B with a DC current density of 20 mA/cm^2, with all 3 generators using 40 W/L of CUS

7.3.2 Feature scale analysis of deposits plated with PUS

Figure 7.20 shows linear features plated under combined pulsed current and PUS conditions described in figure 7.3. The profiles in figure 7.20 again show that relatively thin deposits were achieved (with thicknesses of approximately 1-2 µm). Non-uniformity in profile shapes is again observed and the profiles are less well-defined than the features plated with CUS. This is because there was even more deposit present in the spaces between the features, as shown in figure 7.19.

Figure 7.19 - Optical microscope image of deposition between linear features, located below area H, plated at 20 mA/cm^2 under PUS conditions at 40 W/L (Mag x5)

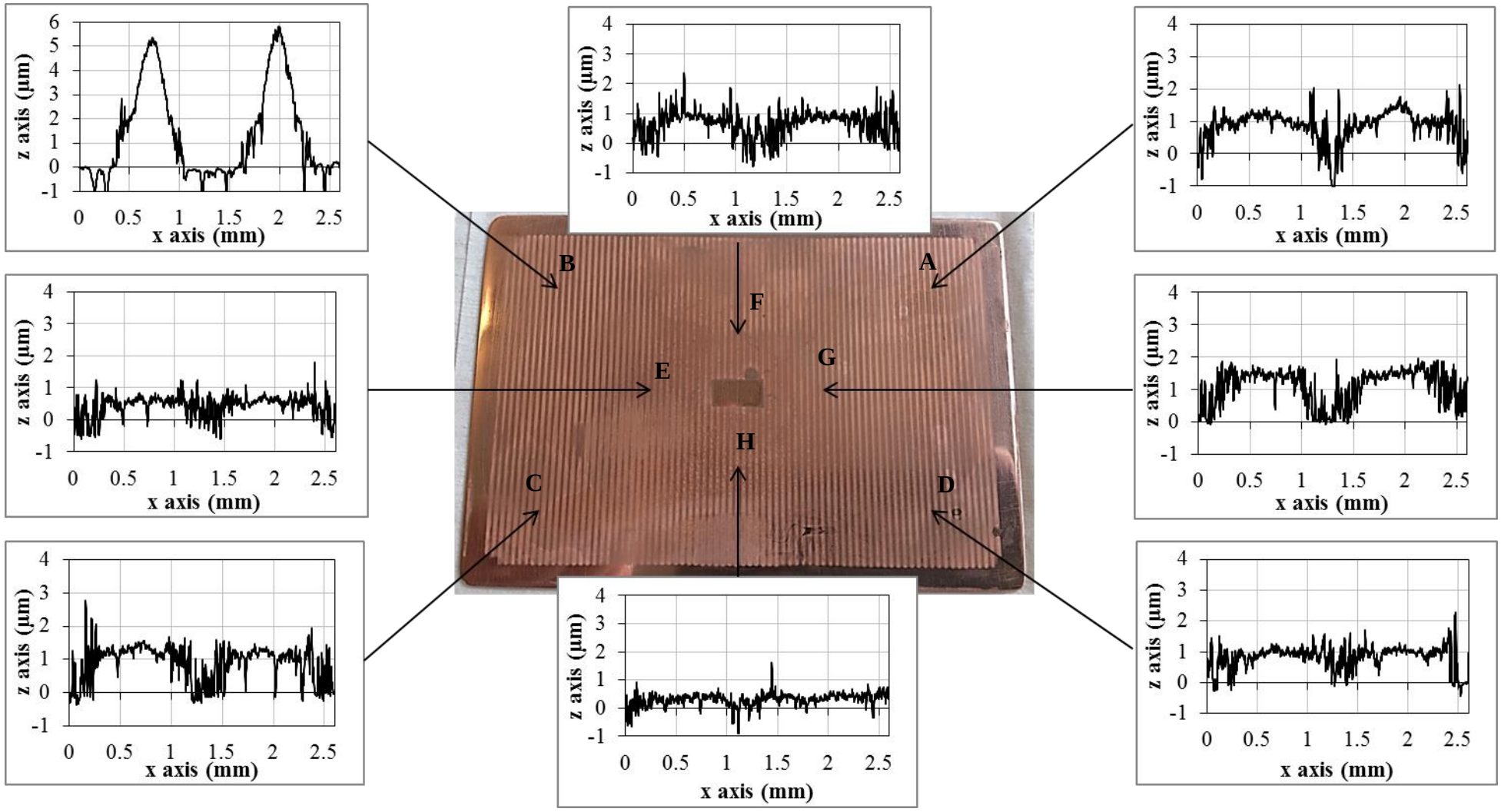

Figure 7.20– A7 size copper cathode substrate after plating in ultrasonic tank using dry resist tool with linear pattern features; plated with pulsed current density of 20 mA/cm^2, with all 3 generators using a PUS power of 40 W/L ; Profiles taken across two features

The majority of the profiles appear to be thinner in the centre, and thicker and rougher at the edges compared to the CUS experiment. This is due to the more primary current distribution when using the PUS regime. The profile of the linear features in location B is very different, showing there can be a large variation in profile shape and thickness across the plate. The variation in deposit thickness needed a more detailed analysis. Before this can be carried out, the size and area of the linear features is required.

7.3.3 Feature size

Measurements from optical microscope images showed that the widths of the linear features were approximately 540 ± 120 μm and 510 ± 130 μm for the CUS and PUS plating modes respectively. This is approximately double the size of the anode feature width. The surface area of the deposited features (A_f) for the deposits plated with the CUS and PUS modes is 27.3 cm^2 and 25.8 cm^2 respectively. This is approximately 2.5 times larger than the anode feature area (A_a). This illustrates the extent of current spread for each pattern in terms of the increase in feature width with respect to the anode. This feature broadening with smaller μm-scale features has been observed previously in nickel pattern deposition [21].

7.3.4 Deposit thickness of linear features

The area of the deposited features (A_f) was used to calculate the nominal deposit thickness based on deposit surface area ($d_{dep,100\%,f}$), as for the square mm-scale features. The value of $d_{dep,100\%,f}$ was 1.93 μm for the CUS mode and 1.86 μm for the PUS mode. A detailed view of the variation in deposit thickness at each location is shown in figure 7.21, which shows that thicker deposits are formed in all areas of the plate when using CUS compared to PUS conditions.

Table 7.4 displays the average $d_{dep,m}$ of the linear features over all locations. This is useful for comparing the differences in feature thickness between the two deposition modes at the feature-scale. Higher values of the average $d_{dep,m}$ of lines deposited over all locations were obtained when using the CUS mode compared to PUS conditions. This is thought to be related to the effect of longer exposure of US on the photoresist anode tool for the PUS mode, due to the longer ultrasound pulse on-time (10 s) compared to the off-time (5 s). After several plating experiments after plating with the PUS mode, it could be seen that edges of the line features on the anode were gradually becoming damaged by the cavitational bubble collapses. This widened the lines of exposed

copper, increasing A_a which in turn increases A_f and lowers the current density that is applied, forming thinner deposits. Therefore, in some part the large decrease in thickness arose from increase in feature size, resulting in decrease in thickness due to a fall in current density.

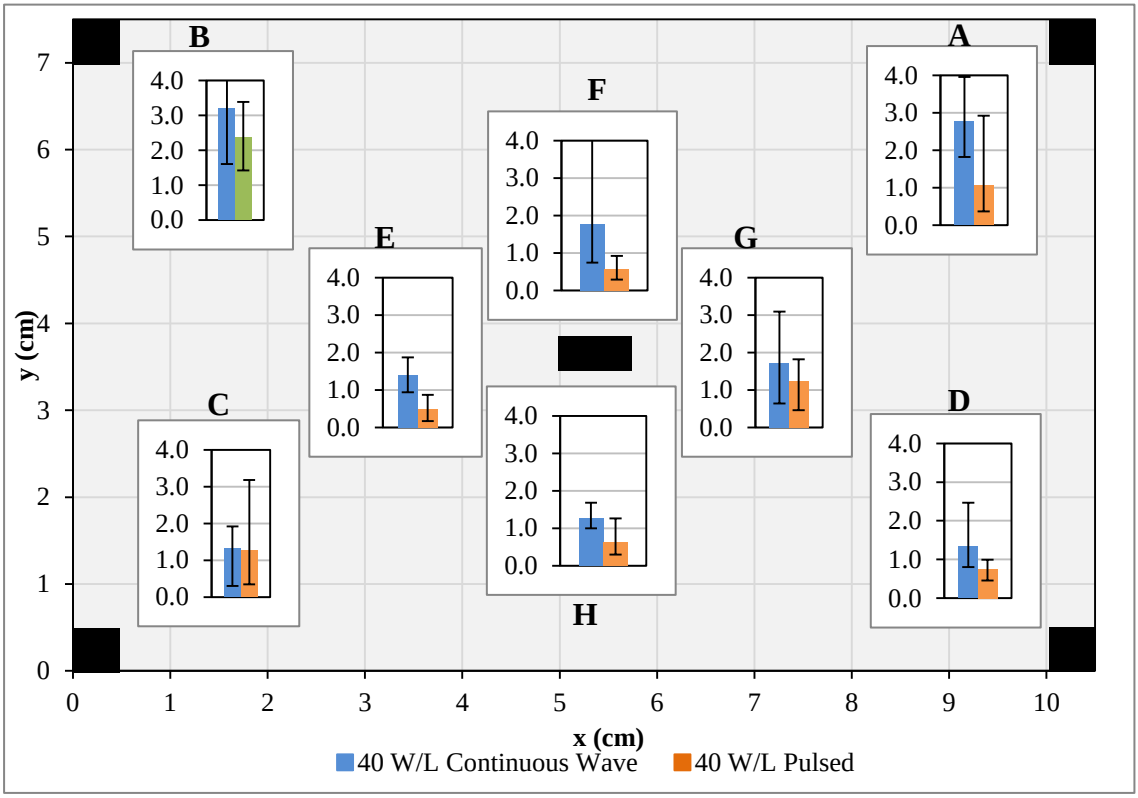

Figure 7.21– Thickness (µm) of copper deposit linear features at various locations on an A7 size copper substrate. Deposits plated at 20 mA/cm^2 with a total current on-time of 677 seconds, under DC plating conditions with CUS at 40 W/L (blue) and using the combined pulsed current and PUS regime using an US power of 40 W/L (orange). Black squares show the location of the placements in the PTFE spacers.

Table 7.4 – Deposit thickness of linear pattern features at different locations on an A7 electrode plated at different ultrasound powers

$p_{W/L}$ (W/L)	A_f (cm^2)	i_f, (mA/cm^2)	$d_{dep,100\%,f}$ (µm)	$d_{dep,m}$ of all lines, ABCDEFGH (µm)	$d_{dep,m}$ of lines, ABCD (µm)	$d_{dep,m}$ of lines, EFGH (µm)
40	27.3	7.7	1.93	1.87 ± 1.13	2.20 ± 1.26	1.53 ± 0.89
40 (P)	25.8	8.2	1.86	1.04 ± 0.84	1.36 ± 1.00	0.73 ± 0.51

Table 7.4 displays the estimation of the current density that was applied based on the A_f. The values suggest that the applied current density is similar for both CUS and PUS modes, however, this does not take into account the area of copper that was deposited in between the lines which would increase the value of A_f.

A comparison of the deposit thickness of features located at the corners of the plate (ABCD) and those in the middle of the plate (EFGH) again allows the analysis of deposit thickness uniformity on the substrate-scale. Table 7.4 also showed that deposited line features at the edges of the plate were thicker than those deposited in the middle. This was seen previously for the square mm-scale features and is caused by current variation across the plate due to higher current density at the edges and variation in electrode gap across the plate. However, it is difficult to interpret these differences in deposit thickness due to the large variation in thicknesses that were measured, shown by the errors in table 7.4. This is due to both the difference in electrode gap variation for each plate and also the variation in electrode gap for each experiment.

Figure 7.21 shows that the thinnest deposits are located in regions F, E and H, i.e. areas closest to the middle spacer. This occurred due to the substrate-scale current density variation problems. Figure 7.20 also shows that the widest deposit lines appear close to these regions. The thin deposits in these areas may also be due to the tool being affected first in these areas because of higher cavitational activity occurring in these regions, as shown previously in figure 7.13, affecting the resist.

Figure 7.21 also shows there are thicker deposits measured at the corners of the plate for both cases due to the current distribution across the plate, resulting in higher current density where deposits are plated near the edges. The deposition of squares showed a greater difference between the deposit thickness at the edges compared to the middle when using PUS rather than CUS. For the deposition of the lines however, this is not the case because the differences in electrode gap and line widths due to photoresist damage has a much more significant effect on the deposition compared to the more primary current distribution effect created by the long current pulse regime.

7.3.5 Current efficiency

The current efficiencies were calculated for the two deposition modes using the nominal deposit thickness based on the deposit surface area, and the average deposit thickness measured at all locations across the plate. The current efficiency is 96% for

the CUS mode and 56% for the PUS mode, which is a very large change in efficiency. However, the large variation in deposit thickness of the linear μm-scale features makes calculation of current efficiency difficult. Additionally, the thickness of the deposits observed in between the line features when using the PUS mode, as shown in figure 7.19, would not be accounted for in the current efficiency calculation resulting in further inaccuracy of the efficiency.

7.3.6 Deposit roughness

The average roughness amplitude (R_a) was measured over a 500 μm region of the feature profiles. The average R_a of the deposits plated using the two different plating modes are shown in table 7.5. Figure 7.22 shows the roughness of the deposits at each location for deposition of linear features using both the CUS and PUS modes.

Table 7.5 shows that a decrease in deposit roughness of the linear features is observed when using the combined current pulse and PUS regime compared to the DC deposition more with CUS. This is due to a higher concentration of ions near the electrode surface using the current interruption technique. It is interesting that smoother deposits are formed using this technique, despite the longer exposure to US when using the PUS mode.

The values of deposit roughness in table 7.5 also shows that for the DC mode with CUS there is marginally rougher deposits at the corners, as seen previously for the deposition of square features. This is due to higher current densities that will be present near the edges of the plate. When the PUS mode is used however, better uniformity of deposit roughness is observed, i.e. the lines deposited at the corners have similar roughness to those in the middle of the plate when using the PUS mode.

Table 7.5 – Roughness (R_a) of deposited linear pattern features at different locations on an A7 electrode plated at different ultrasound powers

Ultrasound Power (W/L)	Average R_a of lines, at ABCDEFGH (μm)	Average R_a of lines in corners, ABCD (μm)	Average R_a of lines in the middle, EFGH (μm)
40	0.114 ± 0.059	0.129 ± 0.069	0.098 ± 0.036
40 (Pulsed)	0.075 ± 0.030	0.076 ± 0.035	0.073 ± 0.026

The better uniformity in deposit roughness at all locations on the plate can be visualised more clearly in figure 7.22. The roughest deposit features were located in the top corners of the plate in locations A and B when plating with CUS under DC conditions due to the higher current density. This is similar to what was observed for the square mm-scale features.

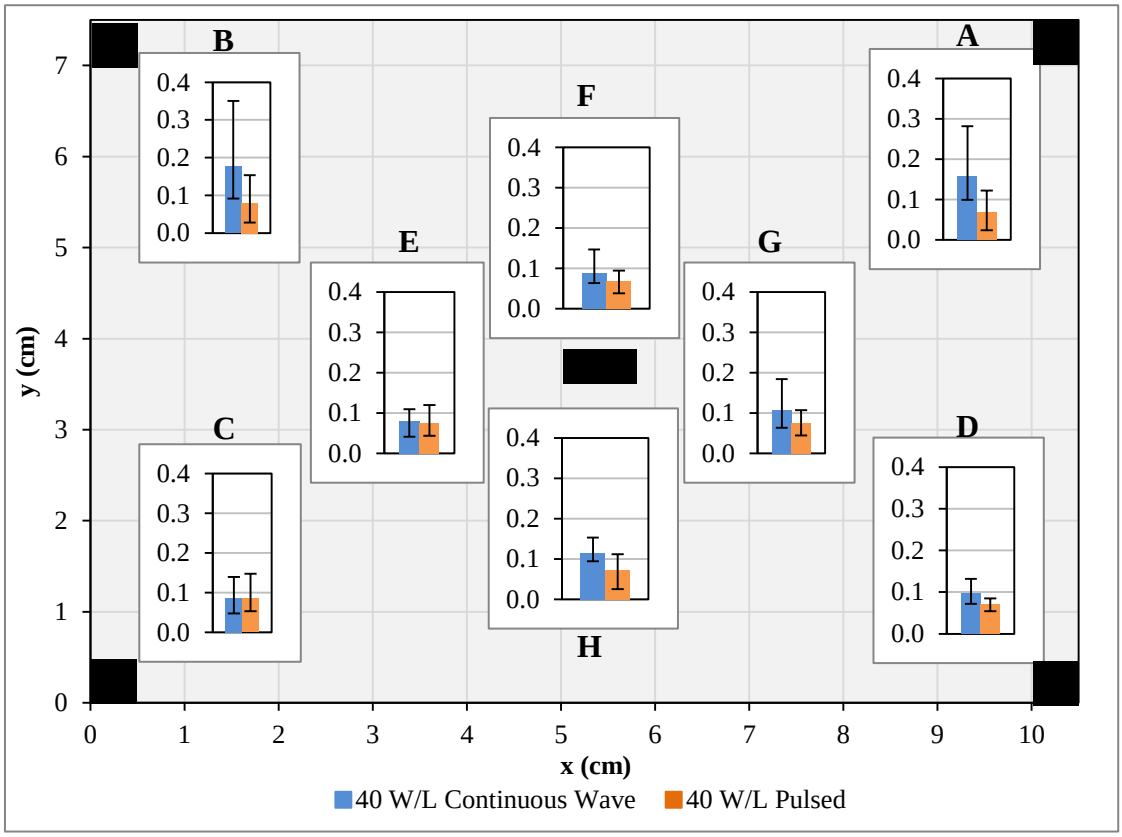

Figure 7.22 – Roughness (µm) of copper deposit linear features at various locations on an A7 size copper substrate. Deposits plated at 20 mA/cm^2 with a total current on-time of 677 seconds, under DC plating conditions with CUS at 40 W/L (blue) and using the combined pulsed current and PUS regime using an US power of 40 W/L (orange). Black squares show the location of the placements in the PTFE spacers.

It has been shown that it is possible to deposit linear µm-scale features onto A7 size substrates. The smoothest deposits were achieved with the PUS regime and the variation in deposit roughness of the features across the plate was ±40% which is acceptable in industry. However, a large amount of current spreading occurred resulting in deposited features which were 2.5 times greater in width than anode features. This also meant that very thin features were deposited. A very large variation in the deposit thickness across the plate of ±80% was measured. The quality of these µm-scale features deposited on A7 size substrates are therefore not acceptable.

Chapter 8. Discussion

8 Discussion

Three different geometries of Enface electrochemical reactors have been investigated, a vertical flow cell, a small-scale 500 ml cell with a US probe and a large-scale US tank system. Extensive mass transfer studies were carried out in these systems, along with deposition experiments where copper patterns were plated using the Enface method. The scalability of the Enface system with ultrasound agitation was assessed in terms of mass transfer enhancement and quality of deposited features. Before stating the final conclusions of the work, there were various issues which were discovered during experimentation which require further discussion.

8.1 Disadvantages of the limiting current technique in narrow gap systems

The first set of experiments was a series of limiting current experiments carried out to compare the mass transfer in each of the 3 systems. These confined reactor geometries appeared to affect the polarization data, particularly evident with the small-scale cell as the electrodes and US probe are placed in close proximity to one another. Potential shifts occur when either the electrodes are brought closer together, or when the distance of the probe to the electrode surface was reduced, causing detection of the limiting current to be difficult. Unobservable limiting current plateau during US agitation has been shown in previous studies [142]. However, few ultrasound investigations have studied these distortions in potentials which occur when using an ultrasound probe [78].

It is possible for current to flow towards probe tip itself, as probe and working electrode are connected electrically through the earth. There are a number of techniques of reducing or eliminating the interaction in potential of the probe. Marken and Compton [78] suggest that a non-conducting material could be used for the probe tip; glass tips are available for some ultrasound probes, however these are not as long-lasting as titanium probes. Another solution is to isolate the tip; therefore the titanium tip will no longer be connected to the working electrode through ground. This has been achieved by Garbellini, Salazar-Banda and Avaca [79] where the titanium tip of an ultrasound probe was insulated from the rest of the probe by use of a Teflon disc. However, there is the possibility of losing power with this method.

Marken and Compton [78] solved the issue of the electrochemical interaction of the probe by controlling the potential of the probe via a bipotentiostat. The probe was connected to the circuit as a second working electrode and then grounded. The bipotentiostat was then used to fix the probe at a certain potential which eliminated current flow through the probe. Bipotentiostats are not however used in industry and wouldn't be suitable for scale-up purposes.

A current distribution model was used to examine the potential distortions. Marken and Compton [78] suggest that an ultrasound probe can act like a second working electrode when placed within an electrolyte solution of an electrochemical cell. The probe surface was therefore modelled as a second cathode. A primary current distribution model of copper electrodeposition was carried out using ElSyca software (ElSy, SA) using a 2D model of the cell. Equations 4.2 to 4.14 in the appendix were used for the model.

Figure 8.1 shows the potential isolines for a h_e of 10 mm and 1.5 mm with a d_p of 30 mm and 15 mm. Significant potential distortions occur when both the probe is brought closer to the electrodes and the electrode gap is narrowed and the current can be seen to flow towards the probe surface. Copper deposition was observed on the probe surface occurred during experiments; further evidence that the probe can act like a working electrode. It is also interesting to note that these distortions are occurring in the region where the copper wire reference electrode was placed in the experiments.

Figure 8.2 shows the current distribution along the top section of the cathode surface. As the probe is brought closer to the electrodes smaller current densities were calculated at the top part of the cathode surface due to the current flowing from the top of the anode to the probe tip.

Table 8.1 shows the changes in potential that were calculated at the cathode for difference values of d_p and h_e. When the probe distance and electrode gaps are brought close together shifts in potential within a range of 0.085 V to 0.22 V in the positive direction can occur according to the values in Table 1. This is similar to the potential shifts that were observed during polarizations experiments, in figure 5.5.

The data from the Elsyca model showed that 17% of the total current flowed to the probe when the probe distance is close at a distance of 15 mm from the electrodes. However, since the limiting current constitutes about 90% of the measured value, which

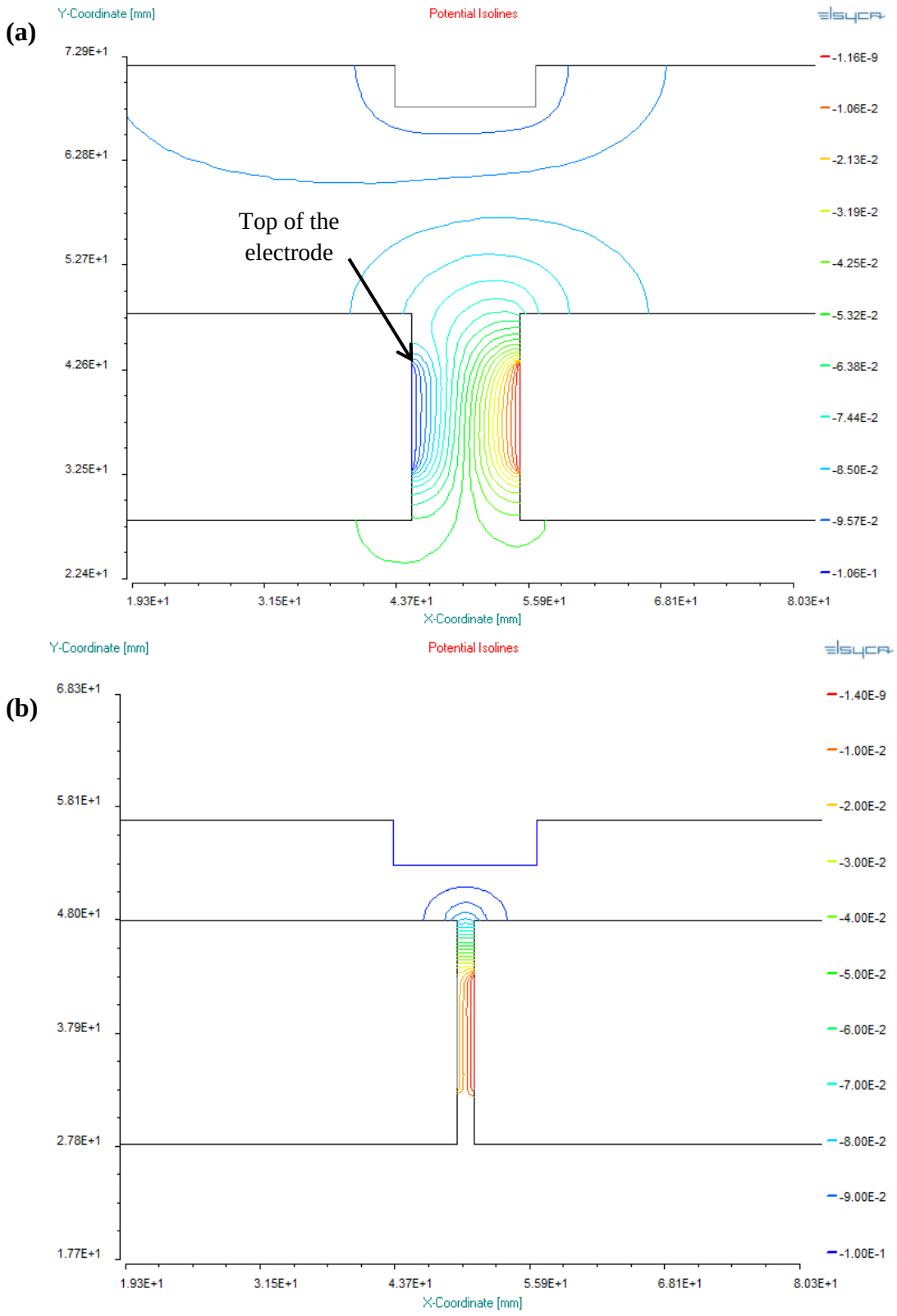

Figure 8.1- Potential isolines within the electrochemical cell with an ultrasound probe placed in the electrolyte solution with cathode (left) and anode (right). Potential applied = -0.1V. (a) h_e = 1 cm ; d_p = 3 cm. (b) h_e = 0.15 cm ; d_p = 1.5 cm.

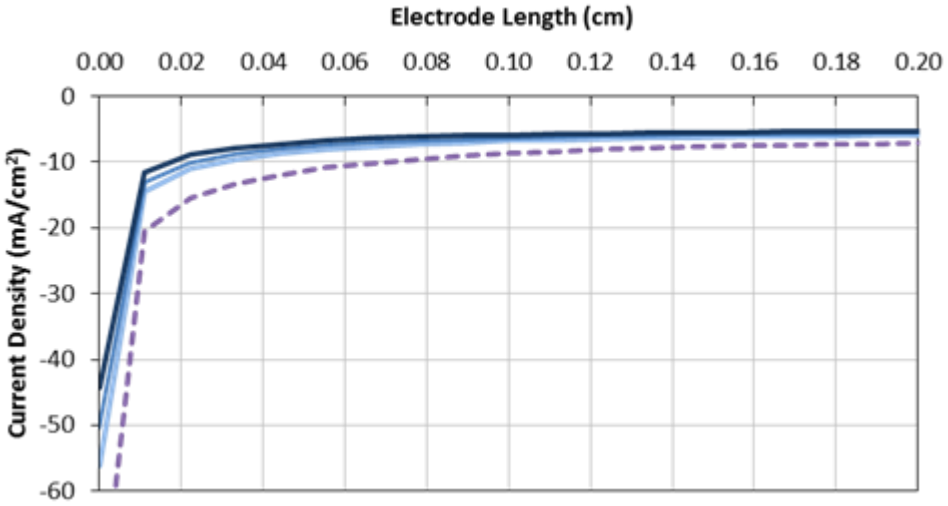

Figure 8.2– Current density distribution along the length of the cathode near the top of the electrode, indicated in fig 8.1, where 0 cm is the top electrode edge. Electrode gap is fixed at 10 mm, Dotted line – No probe ; Light blue line - d_p = 30 mm ; Blue line - d_p = 20 mm ; Dark blue line - d_p = 15 mm

Table 8.1 - Calculated change in potential at the cathode surface for varying electrode gaps and probe distances

Change in Probe Distance, d_p (cm)	Change in Electrode Gap, h_e (cm)	Change in Potential at Cathode (V)
3 to 1.5	1 (constant)	+0.130
3 to 1.5	0.15 (constant)	+0.085
3 (constant)	1 to 0.15	+0.135
1.5 (constant)	1 to 0.15	+0.090
3 to 1.5	1 to 0.15	+0.220

is the experimental accuracy, these calculations show that Sh-Sc-Re correlations are reasonably accurate. In addition, these analyses indicate the well-established limiting current technique has significant limitations when applied to narrow electrode geometries and unusual flows.

8.2 Comparison between the mass transfer in the US probe & US tank systems

Despite the difficulty in measurement of the limiting current it was still possible to retrieve data for the development of mass transfer correlations. *Sh-Re-Sc* correlations were developed for the three systems so that an assessment of the mass transfer could be compared. The predicted mass transfer correlation for the flow cell is shown in

equation 8.1. The correlations that were developed for the ultrasound systems with an electrode gap of 1.5 mm is shown in equations 8.2 and 8.3 respectively.

$$Sh = 1.71\left(Re\ Sc\ \frac{L}{d_e}\right)^{0.359} \tag{8.1}$$

$$Sh = 9 \times 10^{-6}\ \left(Re\ Sc\ \frac{d_e}{L}\right)^{1.38} \tag{8.2}$$

$$Sh = 2.77\ \left(Re\ Sc\ \frac{d_e}{L}\right)^{0.41} \tag{8.3}$$

The correlations show that the flow cell system is mainly controlled by laminar forced convection, whereas turbulent flow was observed in the ultrasound systems. This is ideal for scale up purposes as a higher intensity of stirring is required to ensure that there is sufficient agitation over a large area. The high fluid velocities and intense agitation causes the natural convection flows to be minimized. These systems are therefore mainly controlled by the forced convection flows provided by the ultrasound. The correlations in equations 8.2 and 8.3 illustrate that the US probe system exhibited fully developed turbulent flow but the US tank only provided developing turbulence. This is due to the difference in geometry of the systems.

The small-scale cell is a ‘short electrode system’ which consists of a 20 mm long channel which the US waves flow through. This length is just sufficient for a momentum boundary layer to form from the top of the electrode holder. Turbulent flow will exist near the electrode surface in this system as the electrode is situated near the edge of the electrode holder where turbulences are likely to form due to eddy formation. The large-scale electrode set-up in the US tank is a ‘long electrode system’, with forced convection flow provided mainly from the bottom of the electrode gap, with mass transfer being measured at a 10 mm x 10 mm square feature positioned 45 mm from the bottom edge of the copper plate. The length of the diffusion layer is approximately 10 mm, the same length as the small-scale system. However, the momentum boundary layer is much longer as it has already started to develop from the bottom edge of the electrode holder, 60 mm below where square F is positioned.

The studies by Roy and Pintauro [42] who analysed the convection during copper deposition at an electrode with a length of 75 mm placed within a 25 mm wide flow channel showed that at distances of 37.5 to 70 mm from the bottom edge of the electrode turbulent flow velocities were present, thought to be related to flow instabilities and boundary-layer separation. It was also found that the turbulent flow was

not fully developed near the middle region of the 75 mm long electrode. The reason for this is because the long length of the flow channel means that the flow of the US waves from the bottom of the holder are likely to become less turbulent by the time the flow reaches the position F. This could partially explain the reason for the lower value of b for the mass transfer correlation for the US tank.

The flow of US waves in the small-scale cell from the US probe is similar to a flow from a fluid jet and therefore is suitable to be modelled as a jet-like flow [76]. This fluid flow will be the main contributing factor to the mass transfer enhancement over the cavitational activity. In a US tank however, the flow of ultrasound is more uniform and the cavitational activity may have more of an effect on the mass transfer rather than the fluid velocity.

The deposition experiments showed that there is a high amount of cavitational activity in the region of position F, shown by the number of pits in the deposit in this area. It is therefore likely that this would contribute towards further mass transfer enhancement which results in the thinner diffusion layers at low US powers in the tank compared to the US probe system.

8.3 Issues observed during feature deposition experiments

8.3.1 Issues observed in the small-scale cell

There were some issues which arose during the pattern deposition experiments in the small-scale cell. When long current pulses were applied under silent conditions the 1 mm x 5 mm size deposit feature often peeled off from the surface when the electrode was being rinsed with deionized water. This suggests that there was very poor adherence of the copper deposit to the nickel electrode surface. Figure 8.3 shows an optical microscope image of the nickel surface underneath the area where a copper deposit had been plated. Very small pits of diameter 3 – 4 μm can be observed in the nickel surface, thought to be formed due to hydrogen bubble evolution.

It is thought that the depletion of Cu^{2+} that occurs at the cathode during silent plating conditions could decrease the concentration of Cu^{2+} to an extent where reduction of hydrogen could occur resulting in hydrogen bubble formation. Previous studies on the adherence of copper deposition have shown that the presence of hydrogen beneath

the deposit surface has various negative impacts on the deposition process [143]. One of these is an increase in porosity of the deposit. This would affect the deposit thickness

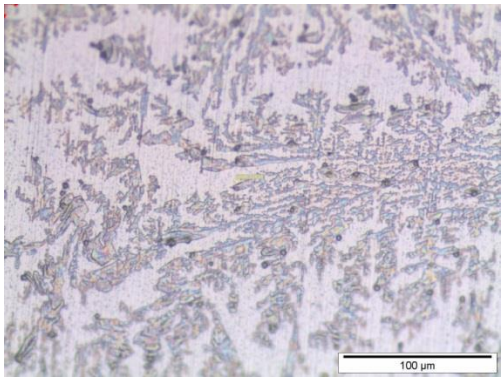

Figure 8.3 – Optical microscope image (mag x20) of nickel substrate after copper deposit was easily peeled away from it immediately after plating at 75% i_L using long current pulses with 150s on-time and 90s off-time under silent conditions.

measurement. Other effects that are caused by the existence of hydrogen beneath a copper deposit includes; a decrease in wettability of copper sulphate solution on the substrate, reduction in contact area and also an increase in the deposit's internal tensile stress [143]. All of these issues would lead to poor adherence of the copper deposit to the nickel substrate.

However, the deposits plated with ultrasound bursts during the off-time always adhered to the surface. One reason for this could be due to the more successful Cu^{2+} ion replenishment within the inter-electrode gap caused by the flow of US waves, resulting in less hydrogen reduction occurring. Another reason could be due to the collapse of US cavitation bubbles which improve hydrogen degassing which has been suggested in previous US studies with copper deposition [143]. This would therefore assist in removing hydrogen bubbles developing within the electrode gap, therefore reducing the effect of the decrease in the deposit internal tensile stress and in turn improving deposit-substrate adhesion.

Additionally, it was also observed that copper being etched from the anode, which often became entrapped within the inter-electrode gap under silent condition, was dislodged from the gap via the US bursts. This eliminates the restrictions in convection flows, further increasing the concentration of Cu^{2+} ions within the electrode gap. The increase in Cu^{2+} ions near the electrode surface may also have caused an increase in copper deposition rate, which could lead to inaccurate calculations in current efficiency.

The patterned anode tool was also an issue in these small-scale experiments. For example, when using the Kapton tape mask, copper nuclei formation occurred at the edges of feature which is not ideal for many pattern plating applications. This addresses the importance of anode fabrication and materials used.

8.3.2 Issues observed in the large-scale ultrasound tank with tool fabricated by spray resist

As mentioned in chapter 7.2, holes in the spray photoresist on the anode tool were found to be present after exposure to the high ultrasound power of 60 W/L or when using PUS at 40 W/L. This is because of the higher cavitational activity that occurs at higher powers or longer US exposure times, resulting in more bubbles collapses close to the photoresist surface. When the PUS mode is used, the copper plates are exposed to US for twice the amount of time than when plating using the CUS mode with DC conditions. This is because the US pulse is longer than the current pulse for the US tank experiments due to the limits of the US tank operation, therefore the electrodes are exposed to US for a longer period of time under pulsed US mode compared to CW US in the US tank. This means that more cavitation bubble collapses could occur using the PUS regime, resulting in more holes being created in the photoresist.

The optical microscope image in figure 8.4 displays an example of one of these holes, approximately 350 μm in diameter. The hole in the spray resist meant there was an area copper surface exposed to the electrolyte solution, which in turn caused etching

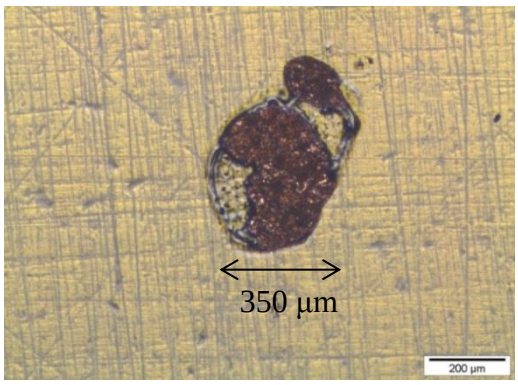

Figure 8.4 – Optical microscope image (mag x 5) of the copper anode plate with spray photoresist with a hole in the photoresist which formed after exposure to an US power of 60 W/L for 677 seconds during plating at 20 mA/cm^2

of the copper tool in that area and small circular deposits to be formed opposite these regions on the cathode substrate. This can be observed on the copper plates in figures 7.4 and 7.6, but can be seen most clearly near square G in figure 7.7, where small deposits are plated with diameters of approximately 600 μm, indicated by the red arrow in figure 7.7. These deposits are slightly larger than the holes created in the anode tool due to the effect of current spreading.

Another issue that was observed is the formation of dark 'stains' in the areas between the copper features, observed in figure 7.4, 7.6 and 7.9. The areas opposite these regions on the anode plate are covered with photoresist, therefore no deposit formation should occur in these places in the cathode plate. However, a very thin layer of Cu nuclei are formed in these regions, shown in the optical microscope image in figure 8.5. The formation of this thin layer was also observed even when no current was applied to the electrode plates.

It is difficult to state the reasons for this nucleation, but it could be promoted by open circuit potential of the cathode during insertion into the electrolyte solution. Shifts in open circuit potential were previously observed when there was a close placement of the electrodes to each other [51]. There were also floating open circuit potentials observed which may be cathodic or anodic.

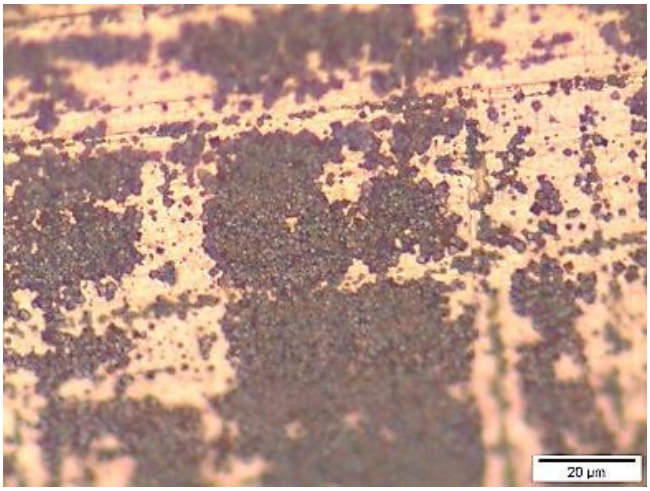

Figure 8.5 - Optical microscope image (mag x 50) of the area opposite an exposed area of the anode tool above square F in figure 3 after applying DC current of 20 mA/cm^2 for 677 seconds with an US power of 30 W/L

8.3.3 Issues observed in the large-scale ultrasound tank with dry resist tool

The dry film resist tools that were used for the linear feature deposition are a much stronger material than the spray resist and were therefore not affected by the cavitation. However, some damage to the resist did occur at the edges of the resist features as shown in figure 8.6, where the edges of the line features of the photoresist have been damaged so much so that the line has widened from 210 µm to 300 µm. This can affect the size of the deposit pattern features.

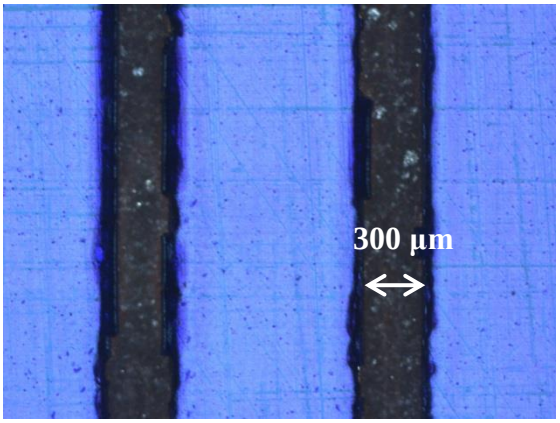

Figure 8.6 – Optical microscope image of a photoresist tool after several plating experiments and exposure to US agitation in the US tank

The photos of the linear features plated using PUS in figure 7.20 shows the deposited line pattern plated over the entire surface of the plate. However, there are some regions where the line widths are very large, particularly in regions below locations H and E, which means that the deposit thickness is exceptionally thin. When using PUS the photoresist tool is exposed to US for a longer period of time than when using CUS. This means that more cavitation bubble collapses will be occurring, damaging the photoresist lines, widening the exposed lines of copper, resulting in wider line features to be deposited on the cathode opposite. This also occurred for higher powers of 60 W/L.

This shows that powers of CUS 60 W/L and PUS 40 W/L and are not suitable if the tool reproducibility is to be improved. When operating at a power of 40 W/L under CUS and DC conditions it is possible to re-use a tool approximately 5 times before the resist becomes too damaged.

8.4 Anode tool fabrication and design

The evidence of resist damage in figure 8.7 shows the importance of choosing the correct materials and methods of tool fabrication for this process as damage to the anode tool can have considerable effects on the deposited patterns. The tool fabrication method used should be able to produce tools that can withstand the aggressive US environment, otherwise the lifetime of the tool will be lowered and therefore the number of possible re-uses of the tool will be reduced. This not just means taking into account the type of resist used, but also the anode plate pre-treatment to ensure the best resist adherence.

The size of the features of resist is also an important factor in tool life-time and reproducibility. A tool was created to test the resolution of the anode tool, with resist line widths of 145 μm and 320 μm. The narrower lines completely de-adhered after exposure to US, whereas only some damage occurred for the wider lines. When resist line widths of 1000 μm, resist damage did not occur until after 5 plating experiments. Therefore, at this point the tool resolution remains at 340 μm and is best at 1000 μm.

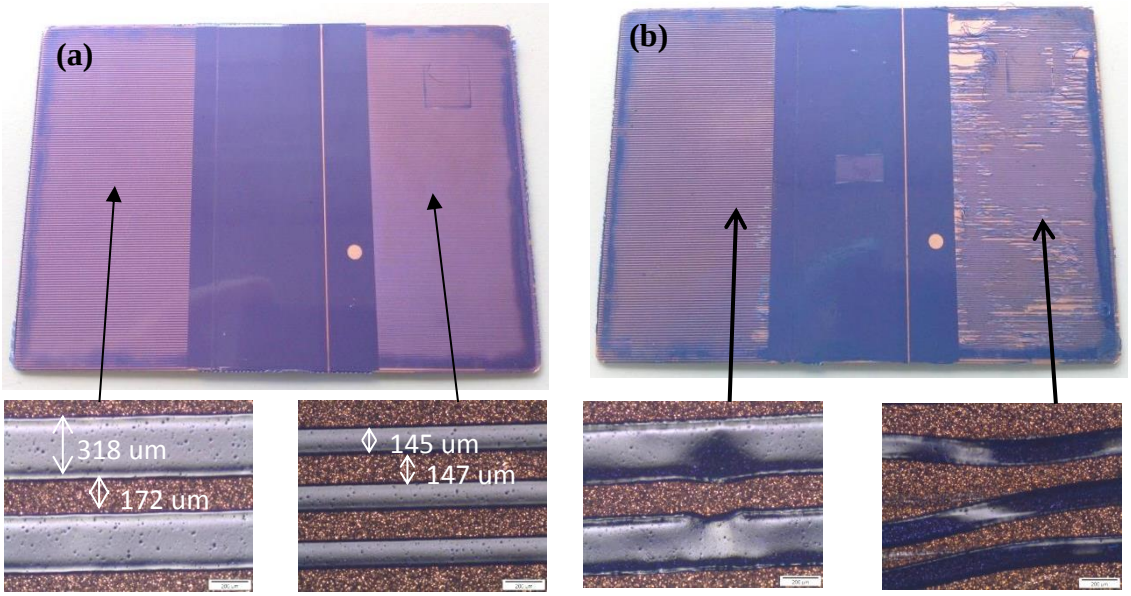

Figure 8.7 – Dry film resist tool with two different size line features, (a) before US exposure, (b) after exposure to 30 W/L of US for 11 minutes

8.5 Summary of the issues and limitations of scaling up the Enface process compared to a conventional patterning process

- The mass transfer of electrolyte can be easily measured and controlled by conventional agitation (e.g. eductors). There are difficulties in obtaining accurate measurement of the mass transfer in the Enface process due to the narrow electrode gap.

- Fully developed turbulence occurs within the narrow electrode gap when using a small-scale US probe system and only developing turbulence occurs in the large-scale US tank between A7 size electrodes. Developing turbulence still provides satisfactory flow of electrolyte across these size plates. However, it is an indication that less turbulent flow could be present if the size the electrodes are further increased. It may not be possible to provided adequate agitation of the electrolyte within the narrow electrode gap if electrode plates larger A7 are used

- The cavitational bubbles collapses cause micro-jetting to occur resulting in pit formation on the deposit features. This may be acceptable for some plating applications where mm-scale features are required. However, the pitting of μm-scale features may be more severely damaged

- Cavitational bubble collapse may also cause pitting on the surface of the tool if the incorrect materials are chosen for tool fabrication

- The dry resist tool used in this work can be used 5 times before the resist becomes damaged. This is reasonably acceptable as photolithography would only have to be carried out once to pattern five substrates. However, the reproducibility may have to be improved before industry would accept this as a worthwhile investment. Increasing tool reproducibility would further increase energy savings and therefore shorten the payback time for installing the process in an industrial production line

- 1000 μm is the smallest resist line width that can be currently used on the Enface tools. This is therefore the limit for the spacing between pattern features that can be fabricated with the Enface method onto A7 size substrates. The PCB industry requires 100 μm spacing between features and is therefore not currently acceptable for this business. However, 1000 μm would still be acceptable for other surface patterning applications.

There are also various other practical aspects which would need to be addressed if this process is implemented fully in industry. This includes the following.

- Copper anode bags are normally used in conventional plating tanks which retain the etched copper within the bags. In the Enface process, copper from the anode tool goes into the solution. This could be solved by:
  (a) Installation of additional solution filtration system
  (b) More replenishment of the plating solution
  (c) Use of insoluble anodes

- The plating industry use well-established acid-copper plating solutions which contain additives to plate copper with certain properties (eg. brightness, conductivity, ductility, etc.). Additionally, Enface uses a lower concentration of copper sulphate, a cheaper solution, but the plating rates will be slower. The following actions therefore need to be carried out
  (a) Studies with a lower concentration of additives used in conventional plating
  (b) Investigation into other plating solution additives
  (c) Development of new plating additives for the Enface process

- The position of spacers between the electrodes limits the regions where pattern transfer can be carried out. These spacers are essential in the design of the Enface tools used in this investigation. Improvements which could be made to the design to solve this are as follows.
  (a) Eliminate the use of numerous spacers by incorporating tools and substrate made from flatter materials (i.e. silicon) in order to have a more uniform electrode gap
  (b) Design a method for more accurate measurement of electrode gap. Feature sizes on the anode tool could then be altered according to the electrode gap at different locations on the plate; therefore sizes of patterns on the tool could be altered to accommodate this so that the desired width and thickness of the pattern feature could be achieved on the substrate.

Chapter 9. Conclusions and Future Work

9 Conclusions and Future Work

9.1 Conclusions

This work focused on the application of ultrasound agitation to the Enface process and investigated whether it was possible to scale-up Enface by using this agitation method. The scalability of the process was determined in a number of methods. The mass transfer was measured and compared in the small-scale and large-scale ultrasound systems to confirm that a similar amount of agitation could be achieved. Pattern transfer onto A7 substrates using the Enface technique was also carried out and the quality of the deposit features was measured in terms of deposit thickness uniformity and deposit roughness uniformity. This would confirm whether the deposit features are acceptable for industrial application.

Three different Enface electrochemical deposition systems were studied; a flow cell, a 500 ml lab-scale cell and an 18 L ultrasound tank reactor. As stated previously, the flow cell geometry would not be suitable for scaling up onto larger area substrates in an industrial setting. The reasons for which include the following:

- Time consuming loading and unloading procedure
- Maximum flow velocity may not be enough to provide sufficient mass transfer for substrates of a greater size
- There was a ±60 μm variation in electrode gap between 3 experimental runs due to differences in each electrode and the method of electrode loading
- The pattern deposition experiments were not particularly reproducible

To test the suitability of US agitation for the Enface system in terms of its mass transfer capabilities, limiting current experiments were first carried out with an US probe in a small-scale 500 ml cell with a narrow electrode gap. The results from the small-scale cell and US probe system were used to design the large 18 L US tank and electrode holders for plating onto A7 size substrates. The outcomes from the mass transfer experiments were as follows.

- Ultrasound agitation was found to significantly improve mass transfer by a factor of 10 compared to silent conditions
- A similar diffusion layer thickness was achieved in the small-scale cell using ultrasound agitation compared with the flow cell system, showing that the same enhancement to mass transfer was attained
- Relatively low powers of 9 – 18 W/cm^2 (24 – 48 W/L) were found to provide the most effective agitation in the small-scale cell
- The mass transfer rates increased as the probe was brought closer to the electrodes. However, potential distortions occurred when the probe-electrode distance was less than 30 mm, this was therefore the minimum probe-electrode distance
- Mass transfer correlations were developed for a side-on probe orientation showing that fully turbulent flows were observed for narrow electrode gaps
- Mass transfer correlations showed that developing turbulence occurred between the electrode plates in the 18 L US tank which provides sufficient agitation for the process
- In the large-scale system, a similar amount of stirring was achieved at the corners of the plate compared to the middle of the plate according to the limiting current experiments

Pattern deposition experiments were carried out in the small-scale cell with different deposition modes to obtain the most suitable method of using ultrasound agitation with the Enface process. The results showed that the combination of pulsing current with pulsed US agitation was the most suitable deposition mode because it,

(a) Gave the smoothest deposits
(b) Improved deposit adherence
(c) Provided the most stable cell potential response
(d) Effectively dislodged cavitation bubbles and etched metal that were entrapped within the inter-electrode gap

Pattern deposition experiments on A7 size substrates in the 18 L ultrasound tank reactor made the following conclusions.

- Square mm-scale features were successfully deposited using either DC with continuous ultrasound or a combined pulsed current with pulsed US regime
- The deposit features were only 14% larger in width than the anode features due to current spreading which is acceptable
- The deposit thickness uniformity and deposit roughness uniformity of the square mm-scale features was ±18% and ±40% across the plate. This is within the acceptable limits for industrial application. It can be confirmed that the process is therefore scalable for mm-scale features on substrates of this size
- Linear μm-scale features were deposited on A7 size substrates for the first time.
- Resist lines on the tool that were less than 1000 μm in width de-adhered from the surface of the tool. Therefore, the patterns can only be a minimum of 1000 μm apart from each other using this type of dry resist tool
- The deposit roughness uniformity of the linear μm-scale features was acceptable with a variation of ±40%. However, the deposit features were also more than 2.5 times greater in width than anode features due to large amount of current spreading therefore very thin features were deposited. Also, the variation in deposit thickness of across the plate was ±80%. The quality of these μm-scale features were therefore not acceptable

The main issue with deposition of μm-scale features using Enface was found to be mainly related to the non-uniformity of the electrode gap across the plate. The variation of the electrode gap across the plate is ±40 μm, which causes a non-uniform current distribution across the plate. This causes the large variation in deposit thickness across the plate. There was also a variation in the line feature width of ±22% which was also caused by the non-uniform electrode gap.

It can therefore be stated that currently the Enface process is scalable for mm-scale features for A7 size substrates. However, the quality of μm-scale deposit features fabricated using the Enface technique at this scale is not presently acceptable and further work would be required to improve the uniformity of these deposit features.

9.2 Further Work

The importance of the electrode gap was realised in these large scale experiments, causing both the feature width variation and differences in deposit thickness of features at varying locations on the substrate. Investigation into substrates and tools made from flatter materials such as silicon is required so that a more uniform electrode gap is maintained between the plates. This would be an important issue to solve if larger size substrates were going to be used to further test the limits of the Enface system.

The modelling of the current spread could also be carried out for different pattern feature designs. It could then be possible to use the model to predict the area of the deposited features. This could be used to calculate the applied current for the required current density needed to achieve the desired deposit thickness.

Pulsed US in the US tank has an on-time which is longer than the off-time, therefore the substrate and tool are exposed to US for a longer period of time, the opposite of what is desired for this regime. Ideally, it would be beneficial to test the process with a more appropriate US pulse time. The effect of different US pulse times should also be investigated in order to find the optimum pulse conditions for this pattern transfer process. Furthermore a deposition which combines ms pulse plating and US pulses should be investigated as this would improve the deposit properties.

A study of the effect of plating additives should also be carried out to further improve the deposit properties. The standard composition of plating additives may not be suitable for this process as these chemical additives have been specifically designed for standard copper plating processes. An investigation into finding the optimum chemistry conditions for this process is therefore also paramount.

The work in this investigation has looked at the effects of relatively high ultrasound powers. The damaging effects of cavitation, which cause pit formation in the deposit and tool materials, can limit the size of deposit features achievable with this process. Very small pattern features may be removed entirely by the micro-jets caused by the cavitation bubble collapse. A US tank with a lower operational power should therefore be investigated to test whether the amount of cavitational pitting will be reduced but provide enough stirring of the solution via the US waves so that the rates of mass transfer of ions needed for the process are achieved. US powers below the

cavitational threshold may also be investigated (less than 5 W/L) to see whether the Enface system could operate under zero cavitational activity.

Another aspect which could be looked at in the future is the design of the tool. It should be noted that photoresist tools are not necessarily needed for every type of tool. 3D printed tools could be investigated in the future. Patterning onto 3D substrates as opposed to just flat substrates should also be studied. This would also widen the possible applications of this novel pattern transfer technique.

Appendices

Appendix A :- Power Density Calibration and Determination

The procedure that was carried out for the calibration of the power density that was delivered to the cell at different amplitudes is as follows:

1. Amplitude was set to the required value.
2. Probe was switched on in the air and the amount of Watts displayed on the Ultrasound Processor Monitor was recorded.
3. The probe was immersed onto the solution in the cell and switched on at the same amplitude. The amount of Watts displayed on the monitor was recorded.
4. The power delivered to the solution was calculated by the difference between the power in the air and the power within the solution.
5. The power density was calculated by dividing by the area of the probe tip (1.33 cm^2).
6. Steps 1-5 were repeated for the next amplitude to be calibrated.

The calculated values are displayed in Table A1. The plot of the power density at different amplitudes is shown in Figure 42.

Table A1 - Calibration calculations for power density delivered to solution at varying amplitudes

Amplitude (%)	Power in Air (W)	Power within electrolyte solution (W)	Power delivered to electrolyte solution (W)	Power Density (W/cm2)
20	0	12	12	9
25	0	17	17	13
30	0	21	21	16
35	1	25	24	18
40	3	31	28	21
45	2	36	34	26
50	3	42	39	29

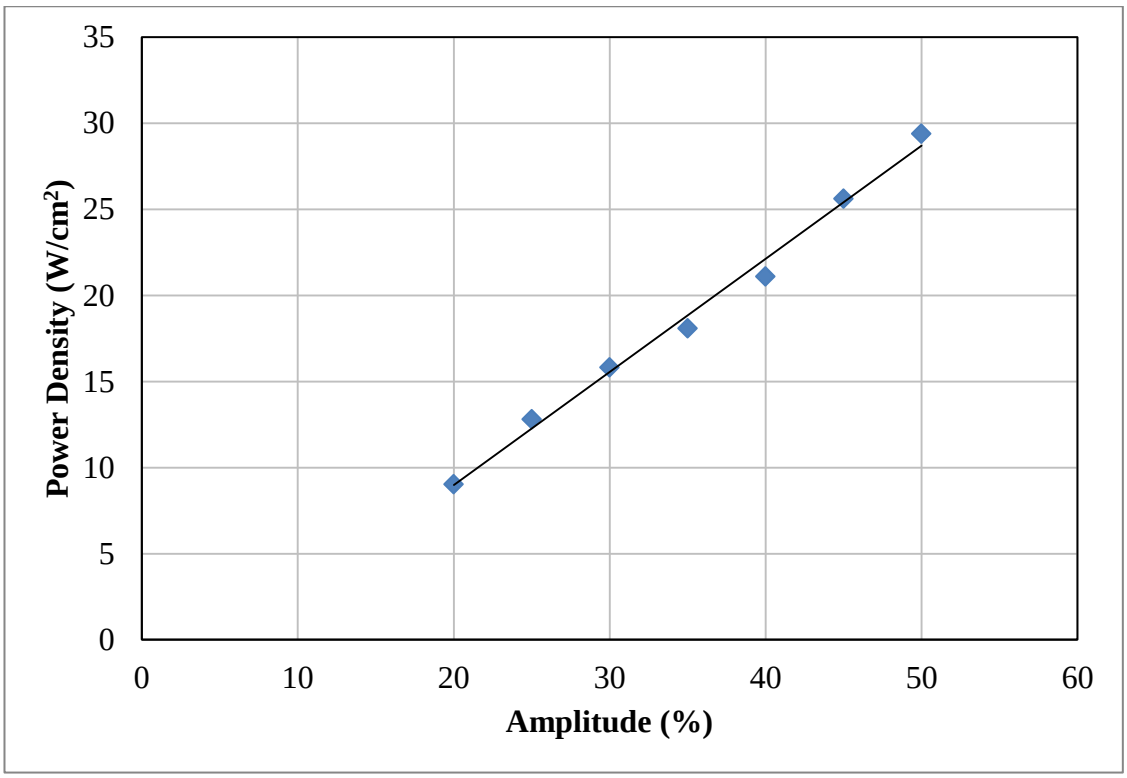

Figure A1 - Power Density delivered to solution of 0.1M Copper Sulphate at varying amplitudes

Appendix B :- Ohmic Drop Compensation

The results from the impedance experiments in the small-scale cell gave the ohmic potential drop for 4 different negative potentials. The values of ohmic drop are shown in table 6, the plot of which is shown in figure 43. It was found that the ohmic resistance ranged from 43 – 49 ohms for potentials from 0V to -1V.

Table A2 - Ohmic values for different potentials obtained from impedance experiments

Potential Applied (V)	Ohmic Resistance (Ohms)
-0.1	43.5
-0.25	44.5
-0.5	46.5
-1	49

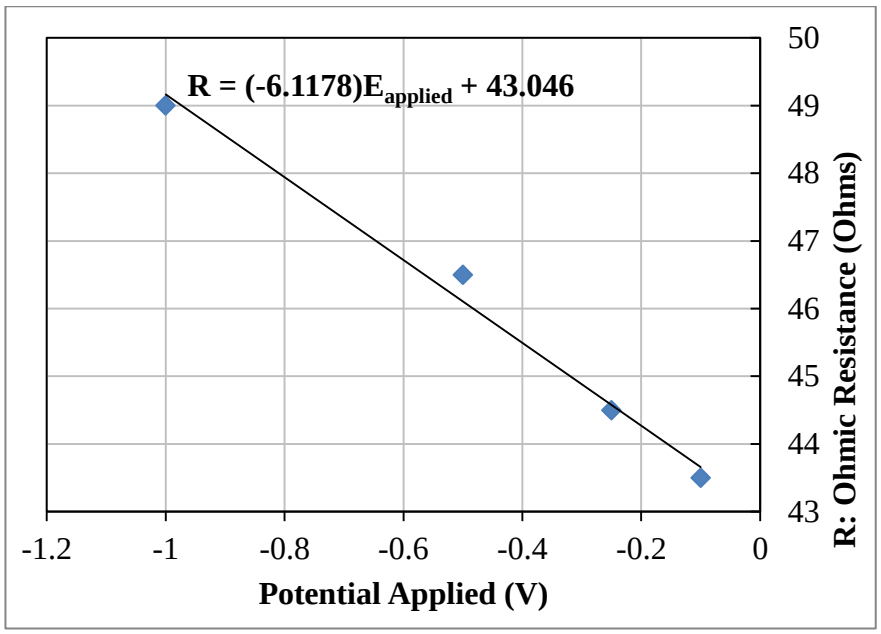

Figure A2 - Plot of Ohmic Resistance at different potentials.

The linear equation from figure 43 was then used to calculate the potential with ohmic drop compensated for silent linear scans. Some example calculations of these are shown in Table 7. The calculated potentials with ohmic drop compensated were then plotted against the current. A comparison of silent linear scans, at 10 mm electrode gap, with and without ohmic drop compensation is shown in figure A3. It can be seen from figure 44 that the ohmic drop becomes more significant at higher potentials as expected. This is due to the constant distance between the reference electrode and the working electrode and the linear relationship of voltage and resistance in Ohm's law.

Table A3 - Example calculations for ohmic drop compensation for 10 mm electrode gap

Potential Applied (V)	Measured Current (A)	Ohmic Resistance (Ohms)	Ohmic Potential Drop (V)	Potential with Ohmic drop Compensated (V)
-0.313	-0.00585	44.914	0.0436	-0.269
-0.315	-0.00590	44.929	0.0443	-0.271
-0.318	-0.00595	44.944	0.0450	-0.273
-0.320	-0.00510	44.959	0.0458	-0.274

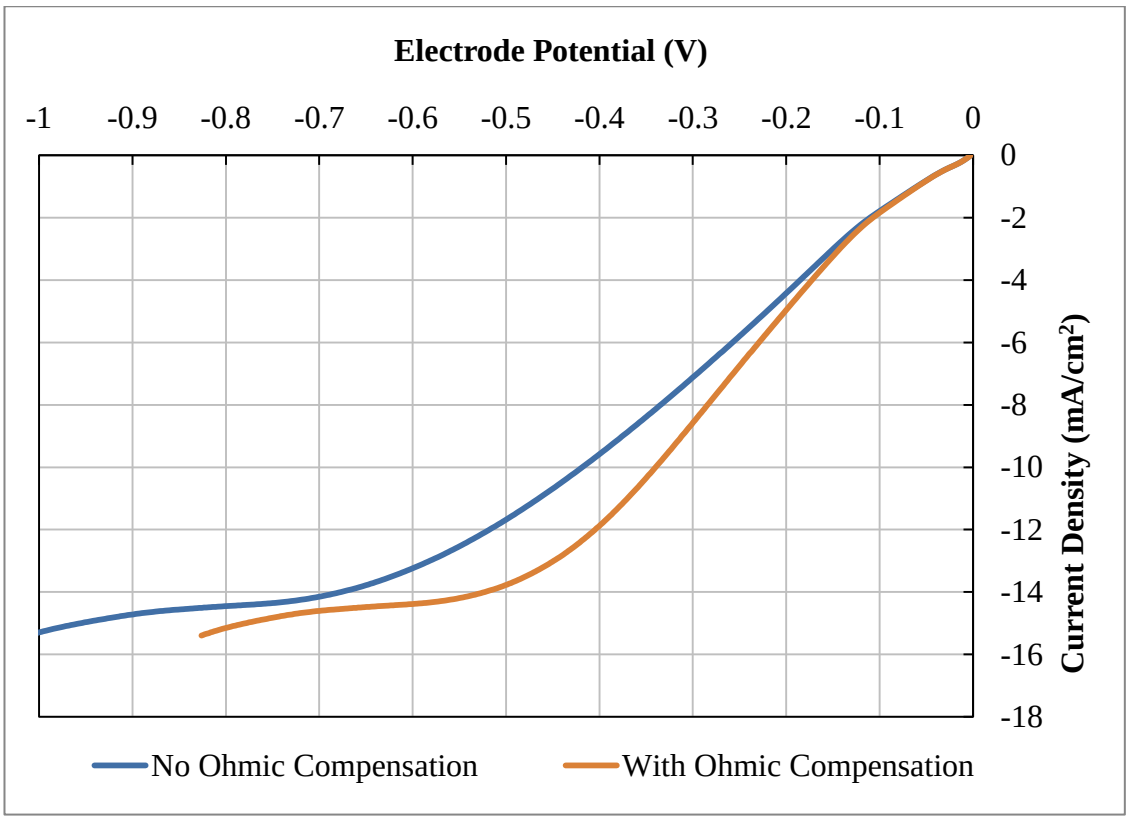

Figure A3 - Silent scans with and without ohmic drop compensated. 0.1M $CuSO_4$ electrolyte ; Scan Rate = 5 mV/s ; Inter-electrode gap = 10 mm.

References

1. Franssila, S., *Introduction to microfabrication*. 2010. 2nd ed, West Sussex: John Wiley & Sons.
2. Madou, M.J., *Fundamentals of Microfabrication and Nanotechnology (Volume II): Manufacturing Techniques for Microfabrication and Nanotechnology*, 2012, CRC Press: Boca Raton.
3. Lee, H.H., *Fundamentals of microelectronics processing.* 1990, New York: McGraw-Hill College.
4. Romankiw, L.T. and E. Sullivan, *Plating Techniques Handbook of Microlithography, Micromachining and Microfabrication, Vol. 2*, 1997, SPIE Press, Bellingham, WA.
5. Rai-Choundhury, P., *Handbook of Microlithography, Micromachining, and Microfabrication Vol 2: Micromachining and Microfabrication (Bellingham, WA*, 1997, SPIE Press.
6. Roy, S., *Fabrication of micro-and nano-structured materials using mask-less processes.* Journal of Physics D: Applied Physics, 2007. **40**(22): p. R413.
7. Roy, S., *EnFACE: a maskless process for circuit fabrication.* Circuit World, 2009. **35**(3): p. 8-11.
8. Adams, T.M. and R.A. Layton, *Introductory MEMS: fabrication and applications*. Vol. 70. 2009: Springer Science & Business Media.
9. Nouraei, S. and S. Roy, *Electrochemical process for micropattern transfer without photolithography: a modeling analysis.* Journal of the Electrochemical Society, 2008. **155**(2): p. D97-D103.
10. *International Technology Roadmap for Semiconductors*. 2012. Technology Working Group Reports Tables 2012 [cited 2012 08/06/12]; Available from: http://www.itrs.net/Links/2011ITRS/Home2011.htm.
11. Schönenberger, I. and S. Roy, *Microscale pattern transfer without photolithography of substrates.* Electrochimica acta, 2005. **51**(5): p. 809-819.
12. Wang, Y., J. Bokor, and A. Lee. *Maskless lithography using drop-on-demand inkjet printing method*. in *Microlithography*. 2004. International Society for Optics and Photonics.
13. Samarasinghe, S.R., et al., *Printing gold nanoparticles with an electrohydrodynamic direct-write device.* Gold Bulletin, 2006. **39**(2): p. 48-53.
14. Müller, A.D., F. Müller, and M. Hietschold, *Localized electrochemical deposition of metals using micropipettes.* Thin Solid Films, 2000. **366**(1): p. 32-36.
15. Whitaker, J.D., J.B. Nelson, and D.T. Schwartz, *Electrochemical printing: software reconfigurable electrochemical microfabrication.* Journal of Micromechanics and Microengineering, 2005. **15**(8): p. 1498.
16. Datta, M. and L.T. Romankiw, *Application of chemical and electrochemical micromachining in the electronics industry.* Journal of the Electrochemical Society, 1989. **136**(6): p. 285C-292C.

17. Landolt, D., R.H. Müller, and C.W. Tobias, *High rate anodic dissolution of copper.* Journal of the Electrochemical Society, 1969. **116**(10): p. 1384-1390.

18. Schuster, R., et al., *Electrochemical micromachining.* Science, 2000. **289**(5476): p. 98-101.

19. Kock, M., V. Kirchner, and R. Schuster, *Electrochemical micromachining with ultrashort voltage pulses–a versatile method with lithographical precision.* Electrochimica acta, 2003. **48**(20): p. 3213-3219.

20. Wu, Q.-B., T.A. Green, and S. Roy, *Electrodeposition of microstructures using a patterned anode.* Electrochemistry Communications, 2011. **13**(11): p. 1229-1232.

21. Widayatno, T. and S. Roy, *Nickel electrodeposition using EnFACE.* Journal of Applied Electrochemistry, 2014. **44**(7): p. 807-820.

22. Compton, R.G., et al., *Voltammetry in the presence of ultrasound: mass transport effects.* Journal of Applied Electrochemistry, 1996. **26**(8): p. 775-784.

23. Walton, D.J., et al., *Sonovoltammetry at platinum electrodes: surface phenomena and mass transport processes.* Journal of Applied Electrochemistry, 1995. **25**(12): p. 1083-1090.

24. Kunnari, E., et al., *Environmental evaluation of new technology: printed electronics case study.* Journal of Cleaner Production, 2009. **17**(9): p. 791-799.

25. Wagner, C., *The role of natural convection in electrolytic processes.* Journal of the Electrochemical Society, 1949. **95**(4): p. 161-173.

26. Wilke, C.R., M. Eisenberg, and C.W. Tobias, *Correlation of limiting currents under free convection conditions.* Journal of the Electrochemical Society, 1953. **100**(11): p. 513-523.

27. Wilke, C.R., C.W. Tobias, and M. Eisenberg, *Free-convection mass transfer at vertical plates.* Chemical Engineering Progress, 1953. **49**(12): p. 663-674.

28. Mason, T.J. and J.P. Lorimer, *Applied sonochemistry.* The uses of power ultrasound in chemistry and processing, 2002: p. 1-48.

29. Newman, J., *The fundamental principles of current distribution and mass transport in electrochemical cells.* Electroanalytical Chemistry, 1973. **6**: p. 279-297.

30. Selman, J.R. and C.W. Tobias, *Mass-transfer measurements by the limiting-current technique.* Adv. Chem. Eng, 1978. **10**(21): p. 1-318.

31. Levich, B., *The theory of concentration polarisation.* Discuss. Faraday Soc., 1947. **1**: p. 37-49.

32. Newman, J., *Effect of ionic migration on limiting currents.* Industrial & Engineering Chemistry Fundamentals, 1966. **5**(4): p. 525-529.

33. Alden, J., *Computational electrochemistry*, 1998, University of Oxford.

34. Subbaiah, T., S.C. Das, and R.P. Das, *Mass transfer rates in an electrochemical cell.* Hydrometallurgy, 1993. **33**(1): p. 153-163.

35. Ward, M., D.R. Gabe, and J.N. Crosby. *Novel agitation for PCB production: Use of eductor technology*. in *Electrochemical Technology Applications in Electronics: Proceedings of the Third International Symposium*. 2000. The Electrochemical Society.

36. Ward, M., C.J. Roberts, and D.R. Gabe, *Effects of air agitation on conductivity in acid copper electrodeposition solutions.* Journal of Applied Electrochemistry, 2000. **30**(4): p. 457-466.

37. Tobias, C.W. and R.G. Hickman, *Ionic mass transport by combined free and forced convection.* Z. Phys. Chem., 1965. **229**(3): p. 145-166.

38. Bazán, J.C. and A.J. Arvia, *Ionic mass transfer in flowing solutions. Electrochemical reactions under ionic mass-transfer rate control on cylindrical electrodes.* Electrochimica acta, 1964. **9**(5): p. 667-684.

39. Roy, S., Y. Gupte, and T.A. Green, *Flow cell design for metal deposition at recessed circular electrodes and wafers.* Chemical engineering science, 2001. **56**(17): p. 5025-5035.

40. Wragg, A.A., *Combined free and forced convective ionic mass transfer in the case of opposed flow.* Electrochimica acta, 1971. **16**(3): p. 373-381.

41. Wragg, A.A. and T.K. Ross, *Superposed free and forced convective mass transfer in an electrochemical flow system.* Electrochimica acta, 1967. **12**(10): p. 1421-1428.

42. Roy, S. and P.N. Pintauro, *Analysis of mixed natural and forced convection copper deposition below the limiting current.* Electrochimica acta, 1993. **38**(10): p. 1461-1470.

43. Kuhn, A. and F. Argoul, *Diffusion-limited kinetics in thin-gap electroless deposition.* Journal of Electroanalytical Chemistry, 1995. **397**(1): p. 93-104.

44. Texier, F., et al., *In situ probing of interfacial processes in the electrodeposition of copper by confocal Raman microspectroscopy.* Journal of Electroanalytical Chemistry, 1998. **446**(1): p. 189-203.

45. Compton, R.G., J.J. Gooding, and A. Sokirko, *Chronoamperometry at channel electrodes: analytical theory of transient behaviour at double electrodes.* Journal of Applied Electrochemistry, 1996. **26**(5): p. 463-469.

46. Tolmachev, Y.V., Z. Wang, and D.A. Scherson, *In Situ Spectroscopy in the Presence of Convective Flow under Steady-State Conditions: A Unified Mathematical Formalism.* Journal of the Electrochemical Society, 1996. **143**(11): p. 3539-3548.

47. Rosso, M., et al., *Onset of current-driven concentration instabilities in thin cell electrodeposition with small inter-electrode distance.* Electrochimica acta, 2002. **47**(8): p. 1267-1273.

48. Zelinsky, A.G. and B.Y. Pirogov, *Electrolysis in a closed electrochemical cell with a small inter-electrode distance. Metal dissolution/deposition in plain electrolytes.* Electrochimica acta, 2009. **54**(26): p. 6707-6712.

49. Meuleman, W.R.A., et al., *Effect of current and potential waveforms on sublayer thickness of electrodeposited copper-nickel multilayers.* Journal of the Electrochemical Society, 2002. **149**(10): p. C479-C486.

50. Nabiyouni, G., et al., *Co-Ni-Cu/Cu multilayers electrodeposited using a channel flow cell.* Journal of the Electrochemical Society, 2002. **149**(4): p. C218-C222.

51. Coleman, S. and S. Roy, *Effect of ultrasound on mass transfer during electrodeposition for electrodes separated by a narrow gap.* Chemical engineering science, 2014. **113**: p. 35-44.

52. Gogate, P.R., A.M. Wilhelm, and A.B. Pandit, *Some aspects of the design of sonochemical reactors.* Ultrasonics Sonochemistry, 2003. **10**(6): p. 325-330.

53. Mason, T.J., J.P. Lorimer, and D.M. Bates, *Quantifying sonochemistry: casting some light on a 'black art'.* Ultrasonics, 1992. **30**(1): p. 40-42.

54. Ramachandran, R. and R. Saraswathi, *Sonoelectrochemical studies on mass transport in some standard redox systems.* Russian Journal of Electrochemistry, 2011. **47**(1): p. 15-25.

55. Curie, J. and P. Curie, *An oscillating quartz crystal mass detector.* Rendu, 1880. **91**: p. 294-297.

56. Cravotto, G. and P. Cintas, *Harnessing mechanochemical effects with ultrasound-induced reactions.* Chemical Science, 2012. **3**(2): p. 295-307.

57. Marken, F., R.P. Akkermans, and R.G. Compton, *Voltammetry in the presence of ultrasound: the limit of acoustic streaming induced diffusion layer thinning and the effect of solvent viscosity.* Journal of Electroanalytical Chemistry, 1996. **415**(1): p. 55-63.

58. Huck, H., *Measurements of the Ultrasound-Diffusion at an Electrode and Its Practical Application.* Ber. Bunsenges. Phys. Chem., 1987. **91**(6): p. 648-654.

59. Labouret, S. and J. Frohly, *Bubble size distribution estimation via void rate dissipation in gas saturated liquid. Application to ultrasonic cavitation bubble fields.* The European Physical Journal Applied Physics, 2002. **19**(01): p. 39-54.

60. Jensen, J.A.D., et al., *Acoustic streaming enhanced electrodeposition of nickel.* Chemical Physics Letters, 2003. **368**(5): p. 732-737.

61. Yeager, E. and F. Hovorka, *Ultrasonic waves and electrochemistry. I. A survey of the electrochemical applications of ultrasonic waves.* The Journal of the Acoustical Society of America, 1953. **25**(3): p. 443-455.

62. Maisonhaute, E., P.C. White, and R.G. Compton, *Surface acoustic cavitation understood via nanosecond electrochemistry.* The Journal of Physical Chemistry B, 2001. **105**(48): p. 12087-12091.

63. Park, Y.S., et al., *Study on the effect of ultrasonic waves on the characteristics of electroless nickel deposits from an acid bath.* Surface and Coatings Technology, 2002. **153**(2): p. 245-251.

64. Suslick, K.S., *Sonochemistry.* Science, 1990. **247**(4949): p. 1439-1445.

65. Benjamin, T.B. and A.T. Ellis, *The collapse of cavitation bubbles and the pressures thereby produced against solid boundaries.* Philosophical transactions of the Royal Society of London. Series A, Mathematical and physical sciences, 1966. **260**(1110): p. 221-240.

66. Suslick, K.S., *Kirk-Othmer Encyclopedia of Chemical Technology.* 1998.

67. Coleman, S. and S. Roy, *Combined pulsing currents and agitation for electrodeposition.* Transactions of the IMF, 2014. **92**(6): p. 316-320.

68. Compton, R.G., J.C. Eklund, and F. Marken, *Sonoelectrochemical processes: a review.* Electroanalysis, 1997. **9**(7): p. 509-522.

69. Mason, T.J., et al., *New evidence for the inverse dependence of mechanical and chemical effects on the frequency of ultrasound.* Ultrasonics Sonochemistry, 2011. **18**(1): p. 226-230.

70. Richardson, K.A., et al., *Towards the electrochemical manufacture of superconductor precursor films in the presence of an ultrasonic field.* Journal of Electroanalytical Chemistry, 1997. **420**(1): p. 21-24.

71. Ohsaka, T., et al., *Effect of intensities of ultrasound sonication on reduction of crack formation and surface roughness in iridium electrodeposits.* Transactions of the IMF, 2010. **88**(4): p. 204-208.

72. Roll, A., Journal of Metallurgy, 1951. **42**(1): p. 197-201.

73. Bard, A.J., *High Speed Controlled Potential Coulometry.* Analytical Chemistry, 1963. **35**(9): p. 1125-1128.

74. Kowalska, E. and J. Mizera, *Influence of ultrasonic fields on processes of electrical oxidation.* Ultrasonics, 1971. **9**(2): p. 75.

75. Lorimer, J.P., et al., *The effect of ultrasonic frequency and intensity upon limiting currents at rotating disc and stationary electrodes.* Electrochimica acta, 1996. **41**(17): p. 2737-2741.

76. Eklund, J.C., et al., *Voltammetry in the presence of ultrasound: a novel sono-electrode geometry.* Electrochimica acta, 1996. **41**(9): p. 1541-1547.

77. Levich, V.G. and S. Technica, *Physicochemical hydrodynamics*. Vol. 689. 1962: Prentice-hall Englewood Cliffs, NJ.

78. Marken, F. and R.G. Compton, *Electrochemistry in the presence of ultrasound: the need for bipotentiostatic control in sonovoltammetric experiments.* Ultrasonics Sonochemistry, 1996. **3**(2): p. S131-S134.

79. Garbellini, G.S., G.R. Salazar-Banda, and L.A. Avaca, *Sonovoltammetric determination of 4-nitrophenol on diamond electrodes.* Journal of the Brazilian Chemical Society, 2007. **18**(6): p. 1095-1099.

80. Sutkar, V.S. and P.R. Gogate, *Design aspects of sonochemical reactors: techniques for understanding cavitational activity distribution and effect of operating parameters.* Chemical Engineering Journal, 2009. **155**(1): p. 26-36.

81. Csoka, L., S.N. Katekhaye, and P.R. Gogate, *Comparison of cavitational activity in different configurations of sonochemical reactors using model reaction supported with theoretical simulations.* Chemical Engineering Journal, 2011. **178**: p. 384-390.

82. Faar P., P.W., *Preface*, in *Pulse Plating*, R.S. Hansel W., Editor 2012, Leuze-Verlag.

83. Puippe, J.-C. and F. Leaman, *Theory and practice of pulse plating*. Vol. 21. 1986: Amer Electroplaters Soc.

84. He, A., Q. Liu, and D.G. Ivey, *Electrodeposition of tin: a simple approach.* Journal of Materials Science: Materials in Electronics, 2008. **19**(6): p. 553-562.

85. Leisner, P., *Chapter 11: Pulse plating of copper on printed circuit boards.* Pulse plating',(ed. WEG Hansal and S. Roy), 2012: p. 189-207.

86. Leisner, P. and W. Hansal, *Pulse plating of chromium.* 2012.

87. Podlaha, E.J. and D. Landolt, *Pulse-Reverse Plating of Nanocomposite Thin Films.* Journal of the Electrochemical Society, 1997. **144**(7): p. L200-L202.

88. Bakonyi, I. and L. Péter, *Electrodeposited multilayer films with giant magnetoresistance (GMR): Progress and problems.* Progress in Materials Science, 2010. **55**(3): p. 107-245.

89. Hansal, W., Roy, S., *Practical Implementation of Pulse Plating*, in *Pulse Plating*, W. Hansal, Roy, S., Editor 2012, Leuze-Verlag. p. 172-183.

90. Hnida, K., J. Mech, and G.D. Sulka, *Template-assisted electrodeposition of indium–antimony nanowires–Comparison of electrochemical methods.* Applied Surface Science, 2013. **287**: p. 252-256.

91. Datta, M. and D. Landolt, *Experimental investigation of mass transport in pulse plating.* Surface Technology, 1985. **25**(2): p. 97-110.

92. Ibl, N., *Some theoretical aspects of pulse electrolysis.* Surface Technology, 1980. **10**(2): p. 81-104.

93. Roy, S., *Mass transfer considerations during pulse plating.* Transactions of the IMF, 2008. **86**(2): p. 87-91.

94. Roy, S. and S. Caprodossi, *Implementation of gold deposition by pulse currents for optoelectronic devices.* Transactions of the IMF, 2009. **87**(2): p. 78-84.

95. Schwartz, D.T., Journal of the Electrochemical Society, 1989. **138**: p. 53C-56C.

96. Schwartz, D.T., P. Stroeve, and B.G. Higgins, *Electrodeposition of composition-modulated alloys in a fluctuating flow field.* AIChE journal, 1989. **35**(8): p. 1315-1327.

97. Tang, P.T., et al., *Dual-bath Plating of Composition Modulated Alloys (CMA) based on a newly developed Computer Controlled Plating System.* SUR/FIN'94, 1994.

98. Roy, S., *Electrodeposition of compositionally modulated alloys by a electrodeposition–displacement reaction method.* Surface and Coatings Technology, 1998. **105**(3): p. 202-205.

99. Birkin, P.R., et al., *Electrochemical measurement of erosion from individual cavitation events generated from continuous ultrasound.* Journal of the Chemical Society, Faraday Transactions, 1998. **94**(22): p. 3365-3371.

100. Deojay, D.M., J.Z. Sostaric, and L.K. Weavers, *Exploring the effects of pulsed ultrasound at 205 and 616kHz on the sonochemical degradation of octylbenzene sulfonate.* Ultrasonics Sonochemistry, 2011. **18**(3): p. 801-809.

101. Riesz, P., D. Berdahl, and C.L. Christman, *Free radical generation by ultrasound in aqueous and nonaqueous solutions.* Environmental Health Perspectives, 1985. **64**: p. 233.

102. Yang, L., J.F. Rathman, and L.K. Weavers, *Degradation of alkylbenzene sulfonate surfactants by pulsed ultrasound.* The Journal of Physical Chemistry B, 2005. **109**(33): p. 16203-16209.

103. Durant, A., et al., *A new procedure for the production of highly reactive metal powders by pulsed sonoelectrochemical reduction.* Tetrahedron letters, 1995. **36**(24): p. 4257-4260.

104. Zin, V. and M. Dabalà, *Iron–chromium alloy nanoparticles produced by pulsed sonoelectrochemistry: Synthesis and characterization.* Acta Materialia, 2010. **58**(1): p. 311-319.

105. Coleman, S. and S. Roy, *Electrodeposition of copper patterns using Enface technique under ultrasonic agitation.* Journal of Applied Electrochemistry, 2015: p. 1-10.

106. Coleman, S.J. and S. Roy, *Electrodeposition of Copper Patterns Using EnFACE Technique under Ultrasonic Agitation.* CHEMICAL ENGINEERING, 2014. **41**.

107. Bard, A.J. and L.R. Faulkner, *Electrochemical methods: principles and applications.* Electrochemical Methods: Principles and Applications, 2001.

108. Nernst, W., *Theory of reaction velocity in heterogenous systems.* Zeit. physikal. Chem, 1904. **47**: p. 52-55.

109. Ota, M., et al., *Measurement of concentration boundary layer thickness development during lithium electrodeposition onto a lithium metal cathode in propylene carbonate.* Journal of Electroanalytical Chemistry, 2003. **559**: p. 175-183.

110. Pletcher, D. and F.C. Walsh, *Industrial electrochemistry*1990: Springer Science & Business Media.

111. Bernstein, J., *Studies on the thermodynamics of bioelectric currents.* Pflügers Arch. ges. Physiol, 1902. **92**: p. 521-562.

112. Sand, H.J.S., *III. On the concentration at the electrodes in a solution, with special reference to the liberation of hydrogen by electrolysis of a mixture of copper sulphate and sulphuric acid.* The London, Edinburgh, and Dublin Philosophical Magazine and Journal of Science, 1901. **1**(1): p. 45-79.

113. Pletcher, D., et al., *Instrumental methods in electrochemistry*2001: Elsevier.

114. Buckley, H.E. and A.C. Walker, *Crystal growth.* American Journal of Physics, 1951. **19**(7): p. 430-430.

115. Pletcher, D., Walsh F.C., *Industrial Electrochemistry*. 2nd ed1993, Glasgow: Chapman and Hall.

116. Grujicic, D. and B. Pesic, *Electrodeposition of copper: the nucleation mechanisms.* Electrochimica acta, 2002. **47**(18): p. 2901-2912.

117. Scharifker, B. and G. Hills, *Theoretical and experimental studies of multiple nucleation.* Electrochimica acta, 1983. **28**(7): p. 879-889.

118. Ostwald, W., *Lehrbuch der Allgemeinen Chemie; Leipzig, Germany, 1896; Vol. 2, Part 1.* There is no corresponding record for this reference.

119. Boistelle, R. and J.P. Astier, *Crystallization mechanisms in solution.* Journal of Crystal Growth, 1988. **90**(1): p. 14-30.

120. Chang, L.M., H.F. Guo, and M.Z. An, *Electrodeposition of Ni–Co/Al 2 O 3 composite coating by pulse reverse method under ultrasonic condition.* Materials Letters, 2008. **62**(19): p. 3313-3315.

121. Floate, S., M. Hyde, and R.G. Compton, *Electrochemical and AFM studies of the electrodeposition of cobalt on glassy carbon: an analysis of the effect of ultrasound.* Journal of Electroanalytical Chemistry, 2002. **523**(1): p. 49-63.

122. Mallik, A. and B.C. Ray, *Residual stress and nanomechanical properties of sonoelectrodeposited Cu films.* Surface Engineering, 2011. **27**(7): p. 551-556.

123. Su, F., C. Liu, and P. Huang, *Ultrasound-assisted pulse electrodeposition and characterization of Co–W/MWCNTs nanocomposite coatings.* Applied Surface Science, 2014. **309**: p. 200-208.

124. Portenlänger, G. and H. Heusinger, *The influence of frequency on the mechanical and radical effects for the ultrasonic degradation of dextranes.* Ultrasonics Sonochemistry, 1997. **4**(2): p. 127-130.

125. Kaufmann, J.G., et al., *Megasonic agitation for enhanced electrodeposition of copper.* Microsystem technologies, 2009. **15**(8): p. 1245-1254.

126. Kobayashi, K., A. Chiba, and N. Minami, *Effects of ultrasound on both electrolytic and electroless nickel depositions.* Ultrasonics, 2000. **38**(1): p. 676-681.

127. Meuleman, W.R.A. and S. Roy, *Transient electrochemical processes during Cu-Ni deposition.* Transactions of the Institute of Metal Finishing, 2003. **81**: p. 55-58.

128. Widayatno, T., *Micropattern transfer without photolithography of substrate: Ni electrodeposition using enface technology.* 2013.

129. Fenech, E.J. and C.W. Tobias, *Mass transfer by free convection at horizontal electrodes.* Electrochimica acta, 1960. **2**(4): p. 311-325.

130. Roy, S. and D. Landolt, *Determination of the practical range of parameters during reverse-pulse current plating.* Journal of Applied Electrochemistry, 1997. **27**(3): p. 299-307.

131. Ibl, N. and K. Schadegg, *Surface roughness effects in the electrodeposition of copper in the limiting current range.* Journal of the Electrochemical Society, 1967. **114**(1): p. 54-58.

132. Gogate, P.R., et al., *Cavitation reactors: efficiency assessment using a model reaction.* AIChE journal, 2001. **47**(11): p. 2526-2538.

133. Walsh, F.C. and C.P. de León, *Versatile electrochemical coatings and surface layers from aqueous methanesulfonic acid.* Surface and Coatings Technology, 2014. **259**: p. 676-697.

134. Veilleux, B., A.M. Lafront, and E. Ghali, *Influence of Gelatin on deposit morphology during copper electrorefining using scaled industrial cells.* Canadian metallurgical quarterly, 2002. **41**(1): p. 47-62.

135. Barkey, D.P., R.H. Muller, and C.W. Tobias, *Roughness development in metal electrodeposition I. Experimental results.* Journal of the Electrochemical Society, 1989. **136**(8): p. 2199-2207.

136. Hu, C.-C. and C.-M. Wu, *Effects of deposition modes on the microstructure of copper deposits from an acidic sulfate bath.* Surface and Coatings Technology, 2003. **176**(1): p. 75-83.

137. Ibl, N., J.C. Puippe, and H. Angerer, *Electrocrystallization in pulse electrolysis.* Surface Technology, 1978. **6**(4): p. 287-300.

138. Tsay, P. and C.-C. Hu, *Non-anomalous codeposition of iron-nickel alloys using pulse-reverse electroplating through means of experimental strategies.* Journal of the Electrochemical Society, 2002. **149**(10): p. C492-C497.

139. Popov, K.I., M.D. Maksimović, and M.S. Simić, *The effect of periodic reverse current on the surface roughness of metal deposits and the maximal deposition rate.* Surface Technology, 1982. **16**(3): p. 209-218.

140. Romanov, V.V., *Vestn. Elektropromishlenosty 9 (1960); VV Romanov.* Zh. Fiz. Khim, 1961. **34**: p. 2692.

141. Romanov, V.V., *Causes of the formation of sponge zinc in the electrolysis of zincate solutions.* Zh. prikl. khim., 1963. **36**(5): p. 1057-1063.

142. Reisse, J., et al., *Sonoelectrochemistry in aqueous electrolyte: a new type of sonoelectroreactor.* Electrochimica acta, 1994. **39**(1): p. 37-39.

143. Touyeras, F., et al., *Electroless copper coating of epoxide plates in an ultrasonic field.* Ultrasonics Sonochemistry, 2001. **8**(3): p. 285-290.